Experimental Investigations of Granular Matter Flow Regimes leading to Insight into Lahar Flow Dynamics

A thesis presented in partial fulfilment of the requirements for the degree of

Doctor of Philosophy

in

Earth Science

at Massey University, Manawatū, New Zealand

Adam Charles Neather

2016

Abstract

The flow of granular material governs numerous natural processes including the aeolian dynamics of sand dune formation, sub-aerial and submarine mass flows, the collective dynamics of ice blocks floating on the ocean, avalanches of debris and snow, as well as volcanic granular-fluid flow processes, such as pyroclastic density currents, volcanogenic debris flows and lahars.

Lahars are a particularly important type of granular flow, in regards to its possible effect on human life; they are debris and water-based flows, initiated by volcanic processes. A fascinating aspect about granular matter is the co-existence of behaviour similar to two or all three of the classical states of matter (solid, liquid, gas) and their frequent transitions between these behaviours. Despite the ubiquity of these transitions in nature and industry, the fundamental physics of granular matter remains a mystery, to the extent that a unified theory to describe the motion and behaviour of granular matter is still absent.

This study is an attempt to simulate lahars and their erosion/deposition mechanics in the laboratory by making use of a rotating drum. A rotating drum can be treated as an analogue for a lahar because it allows for erosion and deposition to occur as an active region of material flows over a passive, erodible bed. In nature these processes are transitory and highly dynamic, but an experimental analogue allows for the processes to be observed in a steady system.

Results include detailed maps of the various regions in a flowing granular material cor-

related to the speed of rotation of the flows. The changing status of the active and passive regions allows for measurements of the erosion mechanics within the drum. Also, potentially identified are two new phenomena; high speed rotations appear to include features similar to Kelvin-Helmholtz instabilities, and enclosed regions of sub-rotation, which are referred to as self-enclosed circulation cells (SECCs).

Acknowledgements

I would like to thank my supervisors, Prof. Shane Cronin, Dr. Gert Lube and Prof. Jim Jones for their support and enthusiasm. My examiners, Prof. Ian Fuller, Dr. Stephen Tallon (Callaghan Innovation), and Prof. Indresan Govender (University of KwaZulu-Natal), should also be thanked for the useful feedback on this thesis.

I would also like to thank the engineers Clive Bardell, John Edwards, Daniel Farley, David Feek, Olaf Griewaldt, Nav Prasad (SEW Eurodrive), Ian Thomas, Anthony Wade and everyone at Triple R Engineering, Ltd. for their help designing, building, maintaining and modifying all the fun toys I got to play with during this project.

Special thanks to my family, Joan and Daniel Neather, for their continuing love and care. This thesis is dedicated to them.

Additional thanks (in no particular order) to: Shane Cronin and Debbie Sparkes for being my financial fairy god-mothers; Miles Grafton for proof-reading an embarrassingly early version of this document; Luke Fullard for the MATLAB code he wrote that greatly sped up the analysis; Eric Breard for supplying the pumice material; Anja Moebis for teaching me how the pycnometer works; Kate Arentsen, Janene de Ridder, and Julia Rayner for making sure the wheels of bureaucracy turned smoothly; Liza Haarhoff for the inexhaustible office supplies; Donald Bailey for his image processing knowledge; Mark Morris, Felicity Samuel and all the staff at the Massey Health Centre for putting Humpty Dumpty together again; Matt Hewerdine, Liam Malone, Chris Sanderson, Tom Robertson, Scott Engerbretsen, and everyone at the Manawatū Duelists for understanding the allure of tiny plastic soldiers; Jonathan Barnard for taking up the torch; Ian Furkert for being able to source any piece of scientific equipment, often at a

moment's notice; Matthew Willey for running the local Sceptics in the Pub group; Lionel Wilson and Georg Zellmer, corner-fighters; David Wiltshire for advice on how to light and film the experiments; Manuela Tost for being the world's greatest office-mate; a slightly inebriated Marco Brenna (*in vino veritas*); Wayne Treanor and Gareth Tasker of Hexanine, Palmy's greatest punk/metal band; Nick Look and Matt Irwin for working their IT voodoo; Angela Woodley for ensuring I wasn't homeless; Jonathan Proctor and Braden Walsh for letting me drive; Magret Damaschke and Gaby Gomez for looking at an active volcano and thinking "that'd be a nice place to go for a walk, let's bring Adam"; Rafael Torres-Orozco for his expertise and help in finding the ash sample; Dianne Reilly and everyone at International Student Support; The Bad Cave, Nexus Games, and Mark One Comics, for helping me scratch the itch; David Stevens and everyone at Radio Control for letting me pollute the airwaves with my taste in "music"; Thalia Evans, the world's most patient shipping agent; and all the lovely staff at the campus coffee and book shops.

Apologies to anyone who feels they should be listed here but aren't - your omission was not intentional, and should be seen as a reflection of my poor memory, rather than your lack of contribution.

Declaration

I hereby declare that this thesis is my own work and effort and that it has not been submitted anywhere for any award. Where other sources of information have been used, they have been acknowledged.

Adam Neather, August 2, 2017

Jim Jones

Shane Cronin

Gert Lube

"One can scoop up poppy seeds with a ladle as easily as if they were water and, when dipping the ladle, the seeds flow in a continuous stream."

- Titus Lucretius Carus, ca. 90 to 55 BCE

Quoted in Sands, Powders, and Grains: An Introduction to the Physics of Granular Materials *(Springer, New York, 2000) by D. Jacques.*

"If you sneeze into it, and it goes everywhere, then it's a powder."

- Dr. Marco Brenna, 28th November 2012

Quoted at the Geological Society of New Zealand annual conference BBQ.

Contents

List of Figures

List of Tables

Chapter 1

Introduction

1.1 Overview

Granular materials are collections of discrete solid particulates [Marks and Einav, 2015] in an interstitial fluid [Hsiau and Shieh, 1999], such as air or water. The flow of granular material governs numerous natural processes including the aeolian dynamics of sand dune formation [Pähtz et al., 2015; Pelletier, 2015; Sutton et al., 2013], sub-aerial and submarine mass flows, the collective dynamics of ice blocks floating on the ocean, avalanches [Daerr and Douady, 1999] of debris and snow [Cronin et al., 1996; Reiweger et al., 2015], plate tectonics [Ferdowsi et al., 2013], tectonic faulting [Reber et al., 2014], as well as volcanic granular-fluid flow processes, such as pyroclastic density currents, volcanogenic debris flows and lahars. Esoteric examples of phenomena governed by granular processes include the rings of Saturn [Campbell, 2006], red blood cells *vis a vis* the flow of blood [Gidaspow and Chandra, 2014; Luo and Bai, 2015; Massoudi et al., 2012], segregation in breakfast cereal [Rosato et al., 1987], the rate at which buildings can be evacuated during an emergency [Pastor et al., 2015], and the locomotion of burrowing snakes [Sharpe et al., 2014].

This study uses naturally-sourced materials in a laboratory-scale setting to investigate the flow behaviour of granular materials, with a focus on understanding the erosive behaviour of the aforementioned lahars, which are gravity-driven mud flows with a volcanic origin (*e.g.*, Jenkins et al. [2015]).

1.1.1 Granular Material Behaviour

A fascinating aspect about granular matter is the co-existence of regimes with behaviour similar to the three classical states of matter (solid, liquid, gas) [Jaeger et al., 1996], and their frequent transitions between such regimes. Said regimes can even appear to be extant at the same time in the same sample of material [Warnett et al., 2014]. Of these regimes, it is the intermediary liquid-like phase [Bonamy et al., 2009] that is least understood [da Cruz et al., 2008]. Despite the ubiquity of granular processes in nature

and industry [Warnett et al., 2014] a unified theory to describe the behaviour of granular matter is still absent [Ancey et al., 1999; de Gennes, 1999; Höhner et al., 2015; Lu et al., 2014]. This contrasts markedly with our understanding of solids, liquids and gases, where the equations of statics have been known for centuries and the theory of linear elasticity, the Navier-Stokes equations and the kinetic theory of gases have had almost a century of investigation. Key to the development of such a theory is the transition of granular material between static and flowing regimes [Bagnold, 1966; Daerr and Douady, 1999; Forterre and Pouliquen, 2008; Jop et al., 2006; MiDi, 2004; Reynolds, 1885].

While granular matter displays some similarities to non-Newtonian fluids [Khalilitehrani et al., 2014], it differs from fluid materials [Bonamy et al., 2002] in a few key ways; most importantly, the affect of temperature, whilst crucial in gases and liquids, is near irrelevant in granular materials [de Gennes, 1999; Jaeger et al., 1996; Mehring, 1929]. A granular material can remain static when placed on an inclined plane, unlike a true fluid [Bonamy et al., 2002]. While gaseous/liquid substances will tend to become more disordered with time, a granular material that is vibrated or stirred is capable of naturally sorting itself. The largest particulates tend to migrate towards the top of the container in a process called "kinetic sieving" or "percolation of fines" [Cagnoli and Romano, 2013], and sometimes also referred to as "the Brazilian nut effect" [Halidan et al., 2014; Rosato et al., 1987] - density of the particulates in question also has an effect on segregation [Chou et al., 2011]. Contrast this with the pseudo-random nature of Brownian motion [Einstein, 1956]. (Brownian motion, first observed by Brown [1828], is the movement of particulates in a fluid due to the collisions of the particulates with the moving atoms or molecules that form the interstitial fluid.) In addition, the future behaviour of a granular material is affected by its past [Njobuenwu and Fairweather, 2015; Santos et al., 2016], *i.e.*, how it has been agitated, which is in stark contrast to the behaviour of a fluid, which is history independent. Additionally, a granular material is capable of choking [da Cruz et al., 2008] under a number of flow conditions, including motion along a wall-bounded flow channel with changing width or direction [Yu

et al., 2014]. Choking occurs if the mass flux through a channel passes a critical point, resulting in the formation of a blockage [Ahn et al., 2008; Yarushina et al., 2015].

It is also known, at least in a laboratory setting, that the addition of an interstitial fluid to a granular material greatly changes its behaviour [Chou and Hsiau, 2012; Chou et al., 2014; Jain et al., 2004; Louati et al., 2015; Tegzes et al., 2003]. In fact, a possible definition of a "dry" granular material could be one in which the interstitial fluid, should one exist, makes negligible effects on the resultant granular flow's mechanics [Ding et al., 2001a; Girolami et al., 2015; Tegzes et al., 2003]. On the other hand, the experiments of Rowley et al. [2014] achieved liquid-like behaviour in a granular bed via a constant injection of gas (also referred to as gas fluidisation [Geldart, 1973]) - this constant re-supply of the fluid phase is unlikely to happen in a natural scenario, however. In contrast with true fluids, due partially to the self-supporting nature of granular materials and also to friction with the side-walls, the pressure in an infinite tube of a granular material would reach a limited value and then stop increasing [Campbell, 2006]; this is in stark contrast to the increasing pressure with depth of a liquid [Jaeger et al., 1996] - this is known as the Janssen effect [Janssen, 1895][1]. Finally, forces within a granular material (compared to other types of materials) are uniquely transmitted, and are not evenly distributed throughout the material [Campbell, 2006]. All these factors produce a material that can behave like a fluid and a frictional material on the same time scales [Reber et al., 2014]. For a practical example of the differences between true liquids and granular materials, consider the work done by Pacheco-Vázquez et al. [2014] who studied the effects of liquids and granular materials inside a bouncing sphere. While a ball containing a liquid would bounce erratically, a grain-filled ball would settle into an equilibrium state.

[1] While known as the Janssen effect, Sperl [2006] points out that earlier work exists demonstrating the same phenomena. Sperl also provides a translation of Janssen's work into English

1.2 Summary and Aims

Granular matter is not well understood quantitatively [Geldart, 1973; Holyoake and McElwaine, 2012; Jain et al., 2002, 2004; Makse et al., 2004] due to the complexity of describing such materials [Kuwagi et al., 2014], despite significant effort from researchers for some time (*e.g.*., Beverloo et al. [1960]; Coulomb [1773a,b]; Janssen [1895]; Jenike [1964a, 1967]; Mehring [1929]). Though the primary aim of this project is to aid the understanding of erosion and deposition in dry and wet natural flows, the work should also inform researchers engaged in the study of the motion of particulates materials in general, and in turn industrial applications such as powder drying in the pharmaceutical industry, and communition machines in the mining business, etc. [Ding et al., 2001b].

The fundamental physical problem of describing granular flows has traditionally been tackled by considering the existence of a quasi-steady flow above a rigid boundary [Daerr and Douady, 1999; Greve et al., 1994; MiDi, 2004; Pouliquen, 1999a,b; Pouliquen and Chevoir, 2002]. The flowing (liquid-like) layer can then be described by introducing an empirical rheology into partial differential equations, akin to the shallow-water model in fluid mechanics [Baran et al., 2011; da Cruz et al., 2005; Jop et al., 2005, 2006; Kumaran, 2006; Mangeney-Castelnau, 2005; Pitman et al., 2003a; Pouliquen et al., 2006; Savage and Hutter, 1989]. Despite some success in validating this hydrodynamic approach for various granular flow systems, there are serious limitations with their applicability to real-world situations where steady flow is seldom encountered [Gauer et al., 2007; Huppert, 2006; Iverson, 1997]. More complex models of flows above an erodible layer have been proposed [Aradian et al., 2002; Douady et al., 1999; Doyle et al., 2007; Lube et al., 2005; Pitman et al., 2003b], but still lack a fundamental theory for the exchange of matter between the solid and the liquid phases. Hence, understanding granular systems and their unsteady behaviour in geophysical and industrial applications remains one of the foremost challenges in this field.

Industrial uses of granular materials often involve rotating drums, which is the experimental equipment of choice for this research because a continuously flowing layer can be viewed in a stationary frame of reference. Drums in themselves have been the subject of a tremendous amount of study (*e.g.*, [Davies et al., 2004; Ding et al., 2001a, 2002; He et al., 2007; Kawashima and Yang, 1988; Parker et al., 1997]), due in part to their relatively simple geometry [Kingston and Heindel, 2014], though like granular materials they, too, lack full comprehension [Schlick et al., 2015; Yang et al., 2008]. Due to the often industrial nature of this work (*e.g.*, Jaeger et al. [1996]), the studies have focused on granular materials involving spherical particles (*e.g.*, Dubé et al. [2013]; Lu et al. [2015]; Taberlet et al. [2004] and drums rotating at a steady velocity. This work will also add to the rotating drum literature by making use of non-spherical (*i.e.*, closer to natural) granular materials and changing rotational velocities in order to investigate the affect of acceleration on the granular material.

Using laboratory-scale granular flows to further our understanding of natural processes is not completely without precedence - see, for example, Cheng [2012]; Daerr and Douady [1999]. It is hoped that the insights gained in this study will help with lahar modelling and prediction, and help inform future danger mitigation endeavours.

1.2.1 Research Approach

This research will aid in the understanding of granular flows as they occur in nature, with a focus on lahars, by using equipment commonly found in industrial research. This will be achieved by moving experiments away from the idealised situations found in industrial granular material research towards more "natural-like" set ups. This will include the the use of naturally-found materials and the addition of water to a selection of the experiments.

The inspiration for this research came from a desire to understand the erosion and deposition mechanics of a lahar. Lahars are covered more in the next chapter.

1.2.2 Controlling Erosion and Deposition

This research aims at quantitatively understanding erosion and deposition processes in unsteady granular flows. This study investigates such processes in laboratory experiments using a rotating drum. This setup allows forcing an initially steady, and hence balanced, granular flow into unsteady motion by accelerating it. The rate of acceleration will variably drive the equilibrated system towards erosion or deposition.

This thesis encapsulates three main research objectives:

1. Characterise granular flow regime transitions in dry granular systems using solids with a natural range in particle shape, size and roughness.

2. Determine the role of the main parameters that control the erosion and deposition in variably unsteady granular flow situations.

3. Quantitatively determine the influence of specific gravity and fluid drag on granular flow regime transitions by comparing dry and wet systems.

This thesis is structured into ten chapters to address these objectives:

- Chapter 2 gives a brief literature review of the research field of granular flows with an emphasis on debris flows and lahars, whose hazards are the primary motivation for this work.

- Chapters 3 and 4 introduce the experimental and analytical methodologies of the research with a focus on the computer-controlled rotating drum apparatus, which was specifically designed for this work. It also reports on the experimental procedures used and results gained to characterise the granular materials that were deployed in this study.

- Chapters 5, 6, 7 and 8 report the experimental results of rotating drum experiments using four different types of dry granular material under variable kine-

matic conditions. By using observations, digital image analysis and automated measurements of the two-dimensional cross-view velocity fields this study complements existing knowledge by studying natural sand and volcanic ash (supplemented with pumice and millet); additionally presented is systematic comparison of flow dynamics in quasi-steady and highly unsteady (accelerating) flow situations. Chapters 5 and 6 focus on the volcanic ash under constant and dynamic velocities. Chapter 7 compares materials and includes potentially new phenomena, including the description and characterisation of a new energy dissipation process in dilated dry granular flows. Chapter 8 analyses the changing behaviour that occurs if the interstitial fluid (air) is replaced by water. This process occurs at high flow velocities leading to the formation of shock-like wave phenomena.

- Chapters 9 and 10 present a discussion of the major findings presented in this thesis, and an overall summary, including an outlook for future work in this area.

Chapter 2

Literature Review

2.1 Overview

This literature review presents an overview of the current state of knowledge around lahars and their related dangers, the usage of a rotating drum and the interrogation there of for quantitative data, and the mathematical modelling of granular materials.

Lahars are a type of granular flow extant in nature, and are extremely dangerous [Iverson and Ouyang, 2015; Jenkins et al., 2015]. When secondary causes of death, such as starvation (resulting from loss of farmland, for example) are removed, lahars are second only to pyroclastic flows[1] for total number of deaths from volcanic hazards[2]. Lahars claim 13.7% [Blong, 1984] of the volcanic event-related deaths in the twentieth century, for a total of approximately 30,000 fatalities [Witham, 2005].

Models that make attempts at predicting lahar dynamics and destructive behaviour are still in their infancy. Particularly enigmatic are highly dynamic erosion and deposition processes, such as the erosion/deposition stripes discussed by Procter et al. [2010a]. The importance of understanding the influence of erosion and deposition on resultant lahar behaviour (flow velocity, volume and runout distance) has been revealed in a number of detailed field studies [Doyle et al., 2009, 2011; Fagents and Baloga, 2006; Lube et al., 2012]. However, development of models from field data alone is hampered by the dangerous and unpredictable nature of lahars and other natural granular flows. Laboratory-scale analogue experiments can aid in filling this knowledge gap; they allow an investigator to examine flows while maintaining control over input parametres. This reduces complexity, while still providing important insights into natural behaviour. As an introduction to the scientific problems addressed in this thesis, presented here is a literature review on both the dynamics and hazards of real-world lahars, and the physics of granular flows.

[1] A pyroclastic flow is a flow involving hot gases and tephra (fragmental material produced by a volcanic eruption), usually initiated by eruption column collapse.

[2] Where "hazard" is defined as "a natural process or phenomenon that may have negative impacts on society" - Gill and Malamud [2014]

2.2 Introduction

Granular flows, as well as being prevalent in industry, are also found in geophysical processes, such as landslides, mud flows, and lahars. These events vary widely, with different fluid phases involved, and wide ranges of particulate sizes [Castro-Orgaz et al., 2015]. Lahars are a particularly important type of granular flow, in regards to their possible effect on human life [Neall, 1976]. Lahars are a two-phase flow, consisting of a mixture of rock and other debris (the solid phase) from a volcanic event, and water (the liquid phase) from one or more sources (see below) [Smith and Fritz, 1989; Smith and Lowe, 1991]. Lahars, like other natural granular flows, exhibit behaviour in the intermediate "liquid-like" regime [Jiang et al., 2014], as outlined in the previous chapter.

2.2.1 Lahars

"['Lahar' is] a general term for a rapidly flowing mixture of rock debris and water (other than normal streamflow) from a volcano. A lahar is an event; it can refer to one or more discrete processes, but does not refer to a deposit." - Smith and Fritz [1989].

To occur, a lahar requires the following: a water source; abundant unconsolidated debris, such as volcanic ash; steep slopes; and a triggering mechanism [Pistolesi et al., 2014]. It also helps to have minimal vegetation on the flanks of the volcano, which would otherwise assist in keeping the soil in place, and obstruct flow of the larger entrained solid objects. (However, a large enough debris flow will denude slopes of vegetation [Iverson, 1997; Miyabuchi et al., 2015].) In geology, a lahar is a type of granular flow [Iverson et al., 1998]. These flows are suggested to be primarily erosive, eroding the channel bed at slopes as low as 3 to 10° [McCoy et al., 2013].

Potential triggering mechanisms include the following; rain induction (such lahars are small but frequent [Rodolfo, 1991; Thouret et al., 1998]); rapid melting of ice/snow

[Cronin et al., 1996; Makse et al., 2004]; a "dam break" situation, in which a barrier of sediments or a crater lake fails [Canuti et al., 2002] (failure of a lake dam appears to be the most efficient mechanism for generating a fast lahar with high peak discharge [Cronin et al., 1997a]); and finally, sub-glacial eruption [Muñoz-Salinas et al., 2007]. In some cases, ground water can also contribute [Pierson, 1985].

2.2.2 Lahar Composition

Lahars can range from hyper-concentrated flows (sediment concentration of 20-60% by volume, or 40-80% by weight) [Pierson, 2005] to debris flows (10-25% water, just enough for the mixture to flow). Many non-cohesive (typically clay-poor [Major, 1997]) lahars begin in a way that is analogous to flood waters [Doyle et al., 2010], and they may behave as a "mobile dam", pushing "clean" stream/river water ahead of themselves (see Figure 2.2.1) [Cronin et al., 1999; Lube et al., 2012]. It is worth noting that a singular definition of "hyper-concentrated flow" has not been reached [3] - see Pierson [2005]. Some authors have tried to define hyper-concentrated flow by when the rheology of the water/solid particulate mixture changes from Newtonian to non-Newtonian fluid, which is governed by the amount of fines in suspension. A Newtonian fluid is one in which any applied shear force will result in flow, with a linear relationship between the two; a non-Newtonian fluid will have a non-linear relationship. (A Bingham fluid will have a linear relationship between shear force and flow speed, but the line will not pass through the origin. See Figure 2.2.2). In addition, some definitions of hyper-concentrated flow state that it begins when the proportion of sand in suspension rapidly increases relative to the suspended fines [Pierson, 2005]. Lahars can be non-cohesive (< 4% clay) to cohesive (>4% clay), rain- and eruption-triggered [Lecointre et al., 2004] (*i.e.*, rapidly formed). Lahars have a typical flow velocity on the order of metres per second, discharges of hundreds to thousands of cubic metres per second, and the largest particulates can be on the order of tens of metres across [Lavigne and

[3] As a further example, in Chinese scientific publications, "hyper-concentrated flow" refers to a slightly different type of flow [Pierson and Costa, 1986] to that detailed in the Western literature.

Thouret, 2002], with larger particulates being more likely in fine-rich debris flows [Caballero et al., 2014]. However, all of this is highly variable; consider that de Bélizal et al. [2013] gives a total volume for *all* 240 of the lahars from Merapi, Indonesia in 2011 to be 2.5 $\times 10^7$ m^3, while Naranjo et al. [1986] estimates the volume of the lahar deposits from the *single* Nevado del Ruiz event to be 3 to 6 $\times 10^7$ m^3.

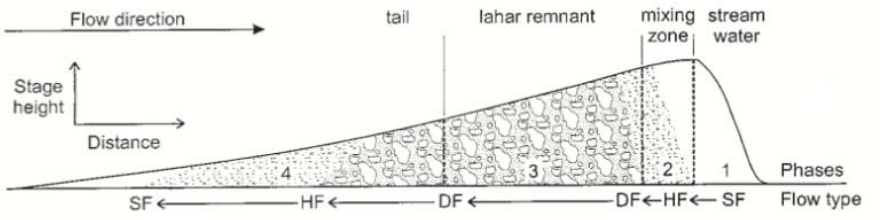

Figure 2.2.1: A modified version of a diagram originally presented in Cronin et al. [1999], showing a cross-section of a typical lahar structure. SF = Stream Flow (clean water), HF = Hyper-concentrated Flow, DF = Debris Flow.

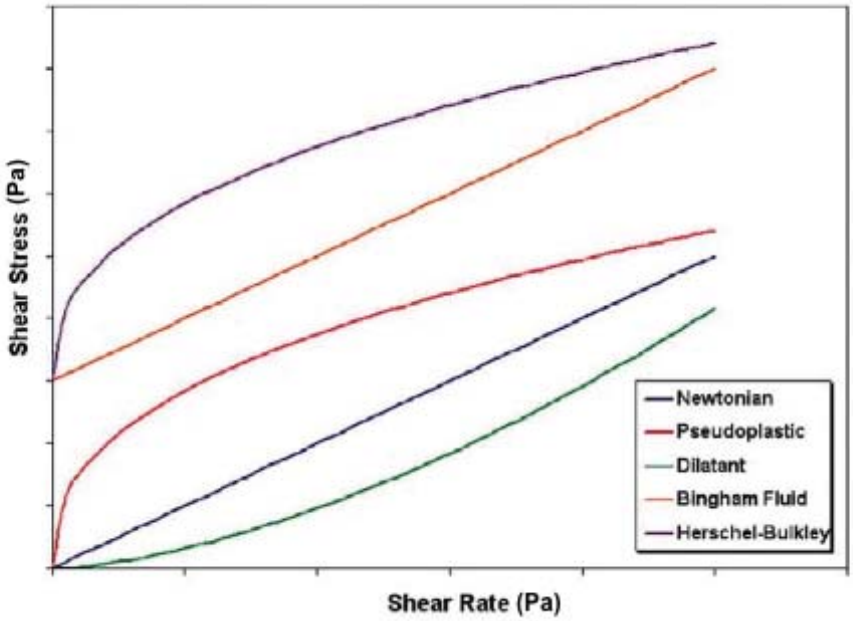

Figure 2.2.2: A demonstration of a selection of flow behaviour types as a function of the applied shear stress and resulting shear rate. The intuitive behaviour most commonly encountered in daily life is the Newtonian fluid. This version originally published by Carter [2012]. Other examples of this chart in the literature include Wilkinson [1960] and Perry and Chilton [1973], among many.

Hyper-concentrated flows can begin during intense rainstorms on hill-slopes and channels, from lake-breakout floods, glacier-outburst floods, dilution (gain of water) or selective deposition (loss of sediment) from debris flows, and input of large amounts of

solids into water floods by landslides [Wilcox et al., 2014].

2.3 Dangers

There are several reasons why lahars are dangerous:

1. They can involve large volume of water; they can travel large distances at high speeds (up to tens of metres per second [Havens et al., 2014; Lavigne et al., 2000; Makse et al., 2004; Muñoz-Salinas et al., 2007]).

2. With multiple initiation methods [Lecointre et al., 2004], lahar initiation is trivial and hence unpredictable [Manville and Cronin, 2007; Paterson et al., 1980; Starheim et al., 2013].

3. The size of a volcanic eruption has little bearing on the likelihood or size of a resultant lahar [Pistolesi et al., 2014] - *i.e.*, as volcanic events can be hard to predict, in turn so are lahars.

4. Lahars do not need a volcanic event to occur [Rodolfo et al., 1996] - they can happen much later (in which case the lahars are "secondary", rather than "primary" [Pistolesi et al., 2014]), possibly up to centuries after the initial eruption [Miyabuchi et al., 2015], and as such the population may enter a state of thinking that the worst is over [Gill and Malamud, 2014].

5. They (or similar phenomenon, such as landslides) can occur in various geological environments [Caballero et al., 2014].

6. Populations often live in lahar-prone locations due to the rich volcanic soil (particularly in developing nations), with 9 to 12% of the world's population [Small and Naumann, 2001] living in volcanically active areas or in zones with the potential for such activity.

7. They have great capability to damage buildings and infrastructure due to entrained solids, which can be on the order of metres in diameter [Pistolesi et al., 2014] and two hundred tonnes in weight [Neall, 1976], though large amounts of damage can occur even for lahars with relatively fine-grain solid fractions [Miyabuchi et al., 2015].

8. Lahars can often be hot [Grattan and Torrence, 2002] and acidic [Kempter and Rowe, 2000].

9. Volcanically active regions are often (coincidentally) frequently those that experience violent rainstorms, giving rise to the perfect situation to form multiple lahars over long periods of time [de Bélizal et al., 2013].

2.3.1 Specific Cases

Specific cases of well-documented lahar disasters include: Tokachidake, Japan (1926) [Uesawa, 2014]; Ruapehu, New Zealand (1953) [O'Shea, 1954; Stilwell et al., 1954]; Mount Saint Helens, United States (1980) [Major and Mark, 2006; Pierson, 1985]; Nevado del Ruiz, Colombia (1985) [Naranjo et al., 1986; Pierson et al., 1990]; and Mount Pinatubo, Phillipines (1991) [Pierson et al., 1996]. Death tolls for these disasters range between single figures and the tens of thousands. The largest event recorded is detailed next.

Nevado del Ruiz

The eruption of Nevado del Ruiz volcano ("Nevado" means "snowy" in Spanish, and refers to the volcano's permanent ice-cap) on the 13th of November 1985 is the largest volcanic disaster since the 1902 eruption of Mount Pelée, Martinique, and killed approximately 25,000 people [Naranjo et al., 1986].

The main eruption occurred at around 2100 hours (local time) [Naranjo et al., 1986; Pierson et al., 1990], and produced an eruption column that reached 31 km above sea

level [Naranjo et al., 1986]. The hot pyroclastic material from the eruption (approximate volume: 0.01 km^3) that was deposited on the mountain melted around 10% of the ice-cap; the resulting water incorporated solid materials from the flanks of the volcano and developed into lahars (approximate volume: 0.1 km^3). These lahars were confined by valleys, and therefore maintained high velocities (a mean of 17 m s^{-1} [Pierson et al., 1990]) and had devastating results up to 100 km from the volcano [Pierson et al., 1990]. These lahars were four times larger at their furthest extent than they were when initiated due to bulking (entrainment of additional solid masses).

At 74 km from the volcano, the town of Armero was "virtually obliterated" [Pierson et al., 1990] - see Figure 2.3.1. This resulted in over 20,000 deaths, around 75% of the town's total population; Pierson et al. [1990] reports 23,000 lives lost, while Naranjo et al. [1986] records 25,000 fatalities. Despite the large-scale loss of life due to this event, the actual eruption of the volcano was a relatively small one [Pierson et al., 1990]. This illustrates the dangerous nature of lahars; their destructive properties cannot be ascertained from the eruption alone, rendering them difficult to predict even in the short term immediately after a volcanic eruption.

2.3.2 Danger Mitigation

Various methods are used to monitor volcanic activity. These include seismographs, which measure the vibration of the ground; pressure pylons [Makse et al., 2004]; remote cameras, used to visually monitor a site that may not be easily accessible; pitot or "gas-bleed" tubes, which measure the pressure in a flow (though these struggle with the destructive nature of lahars). For a project that uses a wide variety of methods to monitor a volcano, see Vazquez et al. [2014]. It is even possible to monitor volcanic activity from orbit using satellites [Torres et al., 2004].

Sabo dams (Fig. 2.3.2) attempt to redirect or slow lahars and other types of natural granular flows [Jiang et al., 2014; Lavigne et al., 2000]. However, care must be taken in

Figure 2.3.1: A photograph showing the aftermath of the Nevado del Ruiz lahar events in 1985. In this image, houses have been submerged and/or severely damaged in the town of Armero. Image was found online - http://hazards.umwblogs.org/, last accessed 15th October 2015.

their construction, as it is possible that they turn many small lahars into one large one, causing much more damage than would otherwise have occurred. Attempts have also been made to drain crater lakes before an event occurs, reducing the amount of water available to form lahars. See, for example, the lake-draining efforts of Mount Kelut, in Java [Zen and Hadikusumo, 1965].

Temporary refuges [Grattan and Torrence, 2002; Newhall and Punongbayan, 1996] can be constructed: these often take the form of artificial hillocks. Built in areas with no easy access to high ground, these hills are built with flat tops, and are used between emergencies as market places or sports fields. Local communities must be sure that they have plenty of supplies available should a lahar event occur, as they can be stranded on these hills for some time before rescue is possible. As natural debris flows, such as lahars, rarely achieve depths greater than a few metres [Grattan and Torrence, 2002], even a low hill or slope can serve as a sanctuary from a lahar.

Figure 2.3.2: A sabo dam on the Lamat River, Indonesia, during construction in 1994. Sabo dams are used to impede a natural granular flow, hence reducing its destructive capability. Originally presented by Lavigne et al. [2000].

2.4 Debris Flows

Debris flows are highly viscous[4]. Debris flows can be laminar (in which flow can be thought of as a series of parallel layers that do not interfere with each other) with a flow velocity order of 1 m s^{-1}, or turbulent (in which flow is chaotic, and features eddies and rapid localised variations in velocity), with a flow velocity on the order of 10 m s^{-1}. The behaviour of debris flows are governed by two main factors; clast interaction and matrix characteristics [Caballero et al., 2014]. "Anti-dune" waves can form in debris flows if the flow speed is greater than the wave speed, *i.e.*, the Froude number (Fr) is greater than one; these waves move upstream, counter to the flow. A typical lahar has a Fr value of over 1 [Lavigne and Thouret, 2002], during the main phase of the flow; however, it may reach as low as 0.7 [Lube et al., 2012].

The Froude number determines whether or not a flow is tranquil or rapid, with 1 being

[4]Viscosity being the measurement of how a fluid reacts to an applied shear force - the more viscous the material, the greater the shear force required to achieve a given shear rate. An effective viscosity is also present in granular materials.

the critical value. It is given by

$$\mathrm{Fr} = \frac{v}{\sqrt{gD}} \tag{2.4.1}$$

where v is the velocity of the flow, g is acceleration due to gravity, and D the depth of the flow, where the ratio describes the relative magnitudes of the inertial and gravity forces. For a rotational system, it can also be given by

$$\mathrm{Fr} = (\omega^2 r)/g \tag{2.4.2}$$

where ω is the rotational velocity of the system, in radians per second. Here, in the case of a rotating drum, the Froude number is the ratio of the centrifugal to gravitational forces [Qi et al., 2015]. It may be useful for the reader to compare the Froude number to the more familiar Mach number, the ratio of vehicle speed to the speed of sound in the surrounding fluid [Knighton, 1998, p.97] - both are comparisons of two velocities in order to determine if a system is in a sub- or super-critical state. When the subject of interest is the active layer of the transverse motion of a granular material, the first Froude number (Equation 2.4.1) is applicable, while the drum as a whole is described by the second (Equation 2.4.2); however, they are interlinked in a rotating system.

2.5 Difficulties when Studying Lahars

"The complexity of lahar events lies in the multiple origins for sediment-laden flows and the transformations that occur from one flow type to another during movement." - Smith and Lowe [1991].

Knowledge of lahars is limited [Lube et al., 2004] as observations are rare [Tost et al.,

2014]. This is due to destructive and unpredictable nature of phenomenon [Major, 1997; Roche et al., 2010; Uesawa, 2014] and because direct, in-situ, field measurements are difficult to obtain [Jenkins et al., 2015; Kingston and Heindel, 2013] in such a dynamic and unstable environment [Wilcox et al., 2014]. Field measurement methods have their own difficulties; for example, bucket sampling (collecting samples of a lahar by buckets submerged in the flow by an investigator on a bridge) has difficulty in measuring sediment density as a function of depth. Additionally, field measurements generally have a low spatial and temporal resolution [Koken et al., 2013]. Also note that until recently (see, for example, [Cronin et al., 1997a,b, 1999]) the rheology of lahars has been studied entirely from their resulting deposits [Pierson and Costa, 1986; Smith and Lowe, 1991]; this is clearly limited in application [Middleton and Hampton, 1976] though some valuable data can be gleaned from such deposits [Caballero et al., 2014]. Finally, sometimes even the source of the water that triggers lahars is under discussion; for example, the Taisho lahar generated by the 1926 eruption of Tokachidake volcano in Japan could have been triggered by a variety of water sources, or combination of several [Uesawa, 2014].

2.6 Analogue Experiments

While subject to considerations of scale, laboratory analogues allow individual processes to be analysed and measured with greater accuracy than is possible in the field [Koken et al., 2013] and side-step any *a priori* assumptions requisite in simulations [Reber et al., 2014]. It is considered key to understanding granular flows that numerical models are validated with experimental data [Deen et al., 2014].

2.6.1 Rotating Drums

While rotating drum experiments are common in the literature (see, for example, Chou et al. [2014]; Ding et al. [2002]; Mellmann [2001]; Santomaso et al. [2003]), they often focus on industrial applications [He et al., 2007; Jones et al., 2003] (despite the ubiquity of particulate flows in nature [Wu et al., 2014]), steady rotational velocities [Orpe and Khakhar, 2004; Renouf et al., 2005] and/or a narrow range of flow regimes [Cheng, 2012; Jain et al., 2002, 2004; Ngako et al., 2014]. Previous studies have also been limited by the technology available: for example, while we will be able to get video footage of the entire drum, Bonamy et al. [2002] were only able to film part of the material through a small porthole, and Orpe and Khakhar [2004] made use of streaks in their footage to analyse velocity, which will be of lower accuracy than PIV (more on particle image velocimetry later; see Section 4.2). There is also a tendency to work at the lower rotational velocities: investigators that do venture into higher velocity regimes are usually more interested in the heat conduction through the granular material (*e.g.*, Gui et al. [2013], Komossa et al. [2014], Nascimento et al. [2015] and Ngako et al. [2014]), *i.e.*, the drum is to be used as a drying apparatus for materials with industrial or pharmaceutical applications. Other high-speed investigations are concerned with the grinding of powders, or studies of rotating drum equipment durability [Kelly and Spottiswood, 1982]. Our drum will be smooth-walled, and not include flights (blades placed on the drum wall) [Debacq et al., 2013; Sunkara et al., 2015] as natural debris flows move under gravity, rather than by forcing from external mechanisms.

Rotating drums are frequently found in industry and industrial research [Kawashima and Yang, 1988; Parker et al., 1997; Ding et al., 2002; Davies et al., 2004; He et al., 2007]. They are used for a variety of purposes, including comminution in the mining sector, powder drying in pharmaceutical processing [Ding et al., 2001b] and waste reclamation [Ngako et al., 2014]. They have been extensively used in research due their relative ease of construction and various advantages, including the ability to non-invasively interrogate the flowing material inside the drum via a variety of methods [Bonamy et al.,

2002] (*e.g.*, radioactive particle tracking, magnetic resonance imaging (MRI) [Cheng, 2012; Deen et al., 2014], and positron emission particle tracking (PEPT); see Dubé et al. [2013], Jain et al. [2004] and references therein; see Section 2.6.2). Additionally, rotating drums allow a material to flow indefinitely, allowing for a large amount of data to be collected [Hsu et al., 2014] - compare this with the "one shot" methodology of flumes [Iverson et al., 2010]. Flume experiments also tend to use a single discharge rate, and involve flows with supercritical Froude numbers [Chatanantavet and Lamb, 2014] - rotating drums afford the investigator more fine-grained control over the Froude number. It is expected that rotating drums, as well as being invaluable in the sphere of industrial research due to the wide variety of processes involving granular materials [Wu et al., 2014], can also be used to create analogues of natural flows in the lab. Consider the accepted typical structure of a flow inside a rotating drum (Fig. 2.6.1) [Ding et al., 2001b; Mellmann, 2001] of an active layer above a passively rotating layer. This is similar to a lahar or other natural flows where a flowing material consisting of a fluid (water or air) and a solid particulate material passes over an erodible bed.

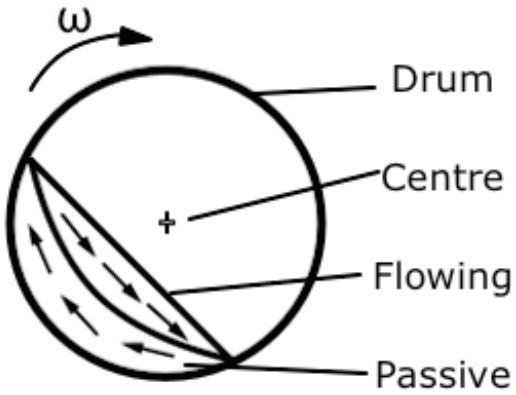

Figure 2.6.1: The typical structure of a granular material in a rotating drum (rotational velocity ω). Under the right conditions, a flowing layer forms on top of a passively rotating layer; these can be considered analogous to a natural granular material flowing over an erodible bed. Based on a diagram originally presented in Mellmann [2001].

The empirical and mechanistic analyses that these researchers have applied to rotating drum is discussed in Section 2.7. First, however, the methods that they use to experi-

mentally interrogate the flows are presented.

Note that while Komatsu et al. [2001] demonstrates that the passive layer, usually considered to be static does in fact flow at extremely low velocities, it is assumed for the purposes of this work that the static approximation holds.

2.6.2 Methods of Non-invasive Interrogation

One of the difficulties of quantitatively studying granular flows is obtaining measurements without interfering with the flow itself. Other workers in this field have employed various methods to obtain data from granular flows without affecting the flow. (See Dubé et al. [2013]; Jain et al. [2004]; Yamane et al. [1998] and references therein.)

PIV (Particle Image Velocimetry) and PT (Particle Tracking)

"PIV means the accurate, quantitative measurement of fluid velocity vectors at a very large number of points simultaneously." Adrian [2005]

PT and PIV are methods of analysing video/imagery of a flow in order to extract data about the flow, including previously unobserved phenomena [Adrian, 2005]. PIV and the related methods were made possible by the advances in computing power over the last couple of decades [Pore et al., 2014]. PIV has become the standard in measuring the velocity of granular flows [Boudet et al., 2007] and has over 30 years of development and usage behind it: the accuracy and usage of PIV has increased over the years with the increased access to computational power, and the shift from film to digital photography [Adrian, 2005]. Note that Particle Tracking is sometimes also referred to as Particle Tracking Velocimetry (PTV) [Dubé et al., 2013; Jain et al., 2002].

PT identifies individual particles and tracks them using a Lagrangian method. PIV, on the other hand, uses Eulerian pattern matching; it looks for changes between the two images as a whole, rather than finding individual particles. The Lagrangian method

treats individual particles as unique points, while the Eulerian considers the provided image as a whole, finding differences between the image n and n+1 to calculate changes in particulate positions, and hence velocities, vorticity, etc. [Zhang and Chen, 2007]. While the Lagrangian method is computationally less intensive for static velocity cases, the Eulerian method becomes more efficient in the dynamic cases [Zhang and Chen, 2007]. As such, the Lagrangian method is better for simulation of granular materials, while analysing images of large numbers of particulates via PIV is better achieved via a Eulerian method, in the opinion of this author.

PIV divides an image up into a grid of over-lapping cells. The analysis assumes that the particles which are nearest to each other between successive frames (using a least squares method on the x and y co-ordinates) are the same particle, and hence the mean displacement within a cell is calculated [Adrian, 2005]. Each particle identified is given a "weight" which determines how likely it is to be a specific particle in a previous image. Particles which appear from off-screen are given a "fee" for moving into view, which is compared to "dummy" particles. It is possible to change the weighting of particulates, for particles already on screen, and the "fee" for particles being compared to off-screen dummy particles. This cost determines how likely one identified particle at time $t = t_1$ is to be the same particle as was previously found at $t = t_0$. When studying a flow, it is advisable to adjust the cost to favour two particles with similar speeds (partially overcoming any issues with making sure each particle in image n is linked with it's most likely subsequent position in image $n+1$). Finally, each particle at time t_1 should only match with one particle at the previous time step, t_0.

The algorithms used in PIV output the velocity; depending on the algorithm used, it is possible to find either the velocity of individual particles or the flow as a whole. (Until calibration is completed, the velocities will be measured in pixels per frame.) The algorithms can also be used to find the vorticity of a flow, *i.e.*, how turbulent the flow is. In addition, assuming that the density of the particulates is known, it is possible to find mass flux.

RPT (Radioactive Particle Tracking)

In this method, a sample of granular material is seeded with a set of radioactive tracer particles. Dubé et al. [2013] made use of RPT in their research. The position of each particle as a function of time can be found via an array of detectors placed around the experiment. The tracers typically emit gamma rays, and the number of rays counted by each detector can be used to reconstruct the path of particular tracer, and by extension the motion of the granular material as a whole.

This method allows for internal flow dynamics to be studied, but care has to be taken with radioactive materials. In addition, steps must be taken to make sure that the radioactive tracer particles have the same mechanical properties as the host material, such as comparable density, size, and frictional properties. The accuracy of RPT is defined by the sensitivity of the detectors, as well as the half-life of the radioactive material chosen. A combination of the two factors that results in the detectors being saturated will produce erroneous results, as will choosing a material that is of low radioactivity.

MRI (Magnetic Resonance Imaging)

Frequently associated with medical applications, this method is of a high spatial resolution [Kawaguchi, 2010; Köhl et al., 2013] and interrogates the internal structure of a flowing granular material by tracking emitted protons. It has been used in rotating drum studies as early as 1993 [Nakagawa et al., 1993]. In fact, one of the first studies of non-spherical particles in a rotating drum was studied using MRI [Yamane et al., 1998]. MRI methods score over the RPT method as it involves no radioactive materials [Yamane et al., 1998]. However, the size of the drum is limited [Pore et al., 2014] by the size of the MRI scanner available. For example, an MRI scanner was available for this project, but would have limited the size of the drum to about 10 cm in diameter. While it would have been theoretically possible to use particulate matter of a small enough

mean diameter, this would have further reduced the choice of suitable particulates; finding a granular material of the requisite size that would not be subject to Van der Waals or electrostatic forces [Petean and Aguiar, 2013] would be difficult[5]. Additionally, MRI-based methods are limited to non-metallic materials [Pore et al., 2014] (for example, mustard seeds [Yamane et al., 1998]), which would be difficult to guarantee when using natural materials such and sands which may have an iron content. MRI also struggles with achieving sufficient resolution in the time dimension [Kawaguchi, 2010]. Considering the above, the option was rejected.

However, other researchers have successfully used MRI in rotating drum investigations, including Kawaguchi [2010] and Nakagawa et al. [1993].

PEPT (Position Emission Particle Tracking)

Developed at Birmingham University [Parker et al., 1993, 1994, 2002] and based on the medical technique of positron emission tomography [Lim et al., 2003], this method uses a tracer particle irradiated by a beam of ^{3}He ions from a cyclotron. The resultant radioactive decay, and its position, is recorded by a pair of positron cameras [Lim et al., 2003; Parker et al., 2002].

Access to the equipment required to irradiate or samples and track the position emission was not available for this study.

Other Methods

Boateng and Barr [1997] used a fibre-optic probe to gather information on the flow inside a rotating drum. While this methodology is not strictly non-invasive [Pore et al., 2014], it is mentioned for the sake of completeness. Kingston et al. [2015] used X-rays to track specially treated particles in a double-screw mixer. While they were able to track

[5]The Van der Waals force is the attraction between dipoles.

the material in three-dimensions, the preparation steps needed changed the properties of the particles in question, and the study was limited in terms accuracy in the time dimension.

Jain et al. [2002] use PT over PIV as they claim the former gives better results, but their PT calculations are based on PIV, so the accuracy of their numbers would be limited by the accuracy of the latter method in either case. Other authors, such as Orpe and Khakhar [2004] use a methodology called streaklines, in which a camera is set with a long exposure time. The resultant blurs recorded by the images can be used, knowing the time the lens is open for, to calculate the speed of the particulates the blurs represent. However, the accuracy of this methodology is limited when compared to high-definition footage combined with PIV analysis.

For this study, the method used is high-speed video combined with PIV. This method allows for accurate measurements of the velocities of the particulates in the flow, whilst remaining relatively inexpensive to implement. This method also does not require careful pre-treatment of particles (beyond washing, see Section 3.3), as in the PEPT or RPT methods, and has no safety concerns like the latter. MRI was considered, but was rejected due to size constraints. PIV allows for the construction of highly detailed velocity maps from actual experiments, rather than from simulations [Yamane et al., 1998].

2.7 Mathematical Descriptions and Modelling

Accurate modelling is essential in order to facilitate understanding of both industrial processes involving particulates and granular flows in nature [Marinack Jr and Higgs III, 2015].

2.7.1 The Inertial Number, I

If we assume that the particles in the granular material in question are rigid, *i.e.*, incompressible, and that the system can be considered large-scale, *i.e.*, the distance between the containing walls is large compared to the diameter of an average particle, then the following equation [Forterre and Pouliquen, 2008] holds:

$$I = \frac{\dot{\gamma} d}{\sqrt{P/\rho}} \tag{2.7.1}$$

where $\dot{\gamma}$ is a characteristic time of the system derived from macroscopic deformation, d the typical particle diameter, P the pressure, and ρ is the typical density of a particle. The inertial number is the square root [Jop et al., 2006] of the Coulomb number [Ancey et al., 1999] (which is sometimes also referred to as the Savage number after Savage [1984]). The Coulomb number, Co, is given in Ancey et al. [1999] by Equation 2.7.2.

$$Co = \frac{\rho R^2 \dot{\gamma}^2}{\Sigma} \tag{2.7.2}$$

here, R is the radius of the particle and Σ is the bulk stress minus the fluid contribution, also referred to as effective shear.

The inertial number was initially proposed by da Cruz et al. [2005]. Low values of I relate to the solid-like [Ancey et al., 1999] regime, while large values are associated with the dynamic regime [da Cruz et al., 2005; Forterre and Pouliquen, 2008; Renouf et al., 2005]. Intermediate values correlate with the dense (liquid-like) regimes. It can be interpreted as a ratio of time scales [MiDi, 2004]: a microscopic time scale, measuring the time it takes for a particle to fall into a hole of size d under pressure P, to a macroscopic time scale measuring the mean deformation, $1/\dot{\gamma}$. The microscopic time scale is modified if an interstitial fluid is introduced [Mansard and Colin, 2012]. Forterre and

Pouliquen [2008] demonstrate that the inertial number is also related to the friction factor, f_f, (the ratio of the shear stress and normal stress in a granular system; in a pile of grains this is the tangent of the slope of the pile, *i.e.*, the angle of repose) and the volume fraction. The volume fraction is the volume of the container currently occupied by the grains; while this is the same as the filling factor at a velocity of zero, this will change as the velocity, and hence the shape, of the flow changes due to regions of in/decreased density.

However, the inertial number is not perfect. While it may allow us to identify the transition between liquid- and gas-like regimes, it does not accurately predict the transition between the solid-like and liquid-like regimes [Forterre and Pouliquen, 2008].

Despite the progress reported here, there remains no model which can describe the entire range of granular material properties [Marinack Jr and Higgs III, 2015] from the solid-like manner to dilute (is able to flow) regimes [Douady et al., 1999; Forterre and Pouliquen, 2008]. The difficulty lies in tying microscopic properties to macroscopic behaviour [Shinbrot et al., 1999a,b; Warnett et al., 2014].

Non-dimensional numbers such as I are common in granular material studies, as their comparisons of like quantities in the form of ratios allows the investigator to determine what dominates material behaviour. Other non-dimensional numbers will be utilised during this thesis, particularly the Reynolds and Froude numbers. Non-dimensional numbers are powerful tools, particularly in granular matter research, as they allow for cross-comparison between different size regimes, and allow the researcher to scale their findings to other systems.

2.7.2 Empirical Relationships

Despite the lack of descriptive theoretical equations for flowing granular materials, there has been extensive work done resulting in empirical relationships.

Dimensionless numbers play a key part in the analysis of granular materials, particularly those in rotating drums. As well as the Froude number, Ding et al. [2001a] make use of the Peclet and Savage numbers to describe the behaviour of granular materials in a rotating drum. Similarly, Alexander et al. [2002] makes use of the Buckingham Pi method to create an equation that describes the shape of the interface between the passive and active regions. Mellmann [2001]; Mellmann et al. [2004] uses the Froude number to great effect, especially in giving relationships between the flow regime of the material and the rotational velocity of the drum.

Empirical relationships, however, should suggest a hypothesis for future testing, rather than being end-points in themselves. Tegzes et al. [2003] present excellent work on the statistics of avalanche sizes in a granular materials, but while this suggests future avenues for research, it does not give answers to the fundamental questions of granular material flow.

Research in the literature with dimensionless quantities and empirical relationships that are particularly relevant to this work include the descriptions of mass balance presented in Jain et al. [2002], and the mass flux interchange (or erosion/deposition) as discussed by Orpe and Khakhar [2001]. Orpe and Khakhar [2001] present the equations that describe the erosion/deposition of a granular material in a flowing drum. However, this equation is for a simplified case in which the active region can be described as thick, and becomes significantly more complex when applied to rotating drums.

2.7.3 The Discrete Element Method (DEM)

The discrete element method (DEM) is a Lagrangian mathematical model [Nascimento et al., 2015] used to describe the behaviour of granular systems. In such models, the behaviour of the entire system is the result of the sum of the interactions of each individual particle [Lu et al., 2015; Mateo-Ortiz et al., 2014]; each particulate is modelled

as a "spring and dashpot" (Fig. 2.7.1) [Berger et al., 2015; Jovanović et al., 2014; Kuwagi et al., 2014; Radl and Sundaresan, 2014; Weerasekara et al., 2013], and their interactions (with each other and the wall) are described using a time integration of Newton's Second Law of Motion [Berger et al., 2015; Bernabé and Evans, 2014; Chen et al., 2015; Gopalakrishnan and Tafti, 2013; Jovanović et al., 2014; Liu et al., 2014] without any arbitrary assumptions [Dong et al., 2015], though the particulates simulated are most frequently spherical [Kodam et al., 2010a]. The method was originally developed by Cundall and Strack (1979), and it has been applied to a range of situations, from simulating chute flow to rotating drums [Faqih et al., 2010; Lu et al., 2015]. There are two main sub-types of DEM: event-driven (hard sphere) and time-driven (soft sphere) [Berger et al., 2015; Lu et al., 2015]. DEM models are highly flexible, able to take into account the size, density and shape of constituent particulates, which a continuum solution struggles to do [Yamane et al., 1998] though most studies have focused on spherical particulates [Höhner et al., 2015]. DEM simulations score over experimental studies because they allow the investigator to individually change any characteristic and measure any physical quantity of the system, in ways that may not be possible in reality, and without perturbing the system [Richard and Taberlet, 2008].

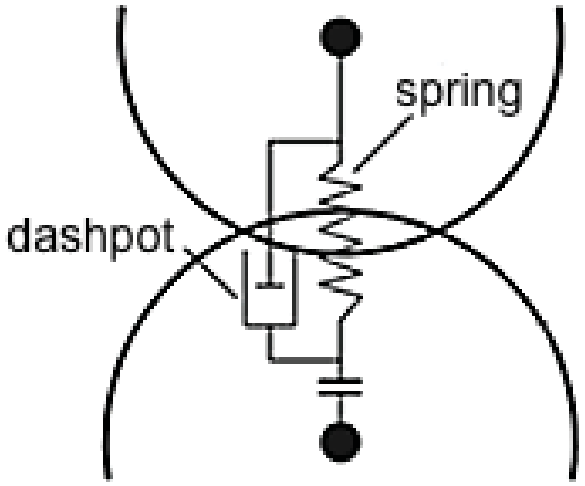

Figure 2.7.1: A cartoon demonstrating the "spring and dashpot" model of particle interaction. The spring represents the attractive forces, and the dashpot the repulsive, for a pair of particles in contact. An edited version of a figure originally presented in a paper by Chen et al. [2015].

DEM programs have been widely adopted [Marinack Jr and Higgs III, 2015] are frequently used to describe systems involving 10,000 to 250,000 particles, with some studies going an order of magnitude higher [Jovanović et al., 2014]. Note, however, that the experiments presented in this study involve a number of particles approximately two orders of magnitude higher than top-end DEM simulations [6]. The computational cost of DEM is very high [Abrahamsson et al., 2014; Cloete et al., 2014; Marinack Jr and Higgs III, 2015; Radl and Sundaresan, 2014; Wu et al., 2014], due to the complex contact detection algorithm - this cost increases directly with number of particles [Nascimento et al., 2015; Santos et al., 2016]. Computational cost increases again for non-spherical particles [Lube et al., 2004]. For example, Qi et al. [2015] presents a DEM study in which 184,608 mono-disperse spherical particles is considered a high number of particles; Richard and Taberlet [2008] presents a DEM study involving 50,000 particles with simulations taking approximately six weeks to run. In addition, DEM has generally been used in two-dimensional simulations [Gopalakrishnan and Tafti, 2013] - flows in nature are, intuitively, rarely two-dimensional.

DEM simulations are frequently combined with computer fluid dynamic (CFD) models. These coupled models are used to describe granular mixtures with an interstitial fluid phase, and are referred to as DEM-CFD models [Gui et al., 2013; Kuwagi et al., 2014; Wang et al., 2013]. The CFD part of the model describes how the fluid moves, while the DEM part covers the collisions of the particulates. It is possible to reduce the computational cost of DEM simulations by treating several particulates in a "parcel"; this method is known as CFD-DPM (discrete parcel method) [Radl and Sundaresan, 2014], but the by-product is a loss of information on the fine structure of the flowing material.

DEM has been used to simulate both generic granular systems and those within rotating drums [Yang et al., 2008]. In the case of rotating drums, the simulation underestimated certain properties of the flow, but scores well at giving investigators quantitative

[6] Assuming a cubic particle 0.5 mm on each side and a typical amount of material in the region of seven litres implies a maximum of 60 million particles with perfect packing.

data on particulate interactions, which are difficult to obtain experimentally.

Note that DEM is also sometimes referred to as PD (particle dynamics) [Bhattacharya and Mccarthy, 2013]. Other mathematical simulations used in the literature include DNS (direct numerical simulation) [Deen et al., 2014], DPM (discrete hard-sphere particle model) [Wang et al., 2014b], which is not to be confused with the discrete parcel method mentioned above, and TFM (two-fluid model) [Ishii and Mishima, 1984].

2.7.4 Other Models for Describing Granular Materials

A full overview of the mathematical models used to describe the behaviour of granular materials is beyond the scope of this thesis. Many other mathematical frameworks exist beyond the ones mentioned above, depending on the system in which the granular material is placed, the forces to which the material is subjected, or even the computer systems available to the reseacher; for example, predicting the behaviour of a particulate system under shear perturbations is best described by the Effective Medium Theory (EMT) [Makse et al., 2004]. For running DEM-CFD models in parallel across distributed memory environments, Wu et al. [2014] describe the Finite Volume Method (FVM). It is also worth noting that while DEM-CFD and CFD-DEM are equivalent (the acronym being simply reversed) [Deen et al., 2014], CFD-DPM (Discrete Particle Model) is slightly different, modelling groups ("parcels") of particles rather than individuals [Radl and Sundaresan, 2014].

2.8 Summary

Granular flow transitions occur in numerous industrial and geophysical flows, but no unified theory has been developed to describe them. Existing research has concentrated on steady velocity experiments with air as the fluid component. This study suggests that it is possible to systematically control the erosion and deposition mechan-

ics of a flow in a rotating drum by changing rotatingal velocity and variably accelerating initially steady granular flows, and by varying the density of particles, grain size and grain roughness. Work extant in the literature supports this hypothesis; Jop et al. [2006], for example, find that the thickness of a flowing region in a granular material depends upon the mass flow rate.

2.8.1 Research Question

This study, then, aims to address the following question: What are the relationships between the manipulated variables of a rotating drum, the material properties, and the resulting erosion and deposition?

Should such a question prove answerable, it should be useful in the area of granular materials in general, said materials in the rotating drum setting frequently encountered in industry, and in providing an increased understanding of the internal mechanics of granular flows in nature. This should help with future endeavours to understand the behaviour of flows such as lahars, and aid with danger mitigation efforts.

The research question will be approached as follows. A variety of materials (Section 3.3) will be placed into a rotating drum. This drum will be rotated at a variety of steady and non-steady (*i.e.*, accelerating) velocities. The material inside the drum will be recorded with a high-speed camera. Processing the resulting footage (Section 4.2) will allow for both qualitative and quantitative analysis of the processes which occur in a flowing granular material. This study will address gaps in the literature with the inclusion of both wet and dry systems, the aforementioned accelerated systems, usage of natural materials, and the analysis of high-resolution footage.

Chapter 3

Experimental Methodology

3.1 Experimental Overview

This project aimed to investigate the effect of changing velocity on a fluid/particulate solid mixture (*i.e.*, a granular material) in a rotating drum. A water-tight drum, 0.15 m in width and 0.25 m in radius, was constructed. The drum was filled with a mixture of fluid and particulate solids, and then rotated at a set velocity. By varying this velocity and studying what happened at different velocities and as the drum accelerates, we can gain insight into lahar flow dynamics - it is hoped that it is possible to draw analogues between this behaviour and the erosion/deposition by a lahar as it accelerates. This is because when a granular material is placed within a rotating drum with the correct angular velocity, there is then created a flowing body on top of an erodible bed (see Figure 2.6.1); with careful scaling, this can be said to be analogous to a lahar or other natural mass flow (*i.e.*, [Orpe and Khakhar, 2004; Tegzes et al., 2003]).

Such a rotating drum experiment has not been previously undertaken; other workers have focused on static (*i.e.*, Mellmann [2001]) and low velocity (*e.g.*, Bonamy et al. [2002]; Chou et al. [2010]) rotational regimes (Fig. 3.1.1), which have limited applicability to unsteady natural flows [Hsu et al., 2014], which tend to be of a higher velocity (Fr > 1, [Lavigne and Thouret, 2002]) and hence turbulent. Schlick et al. [2015] investigates variable velocities but in a simulation and with a sinusoidal, rather than linear, acceleration profile.

The experiments can be summarised as follows.

1. Reproduction of known flow regimes using a dry granular material in a quasi-steady rolling regime. Erosion and deposition will be studied in this regime. (Fig 3.1.1.)

2. Variation of particle types (which will affect the size, friction, density etc. of the material), to investigate their effects on flow regime transitions as a function of Froude number.

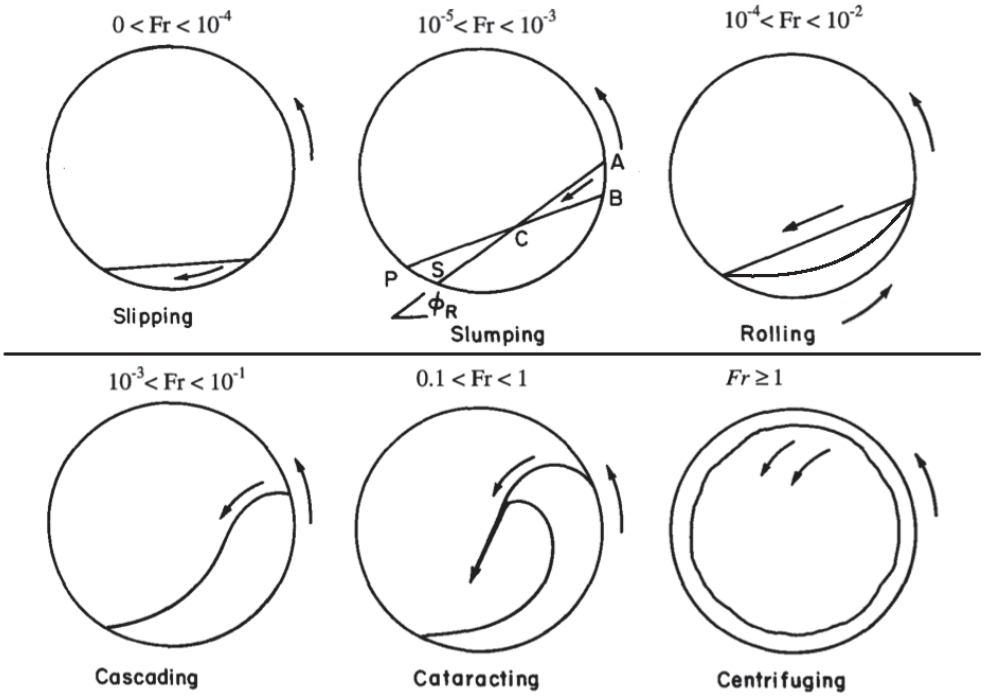

Figure 3.1.1: The various flow regimes possible in a rotating drum as a function of the Froude number, a dimensionless velocity. A modified diagram originally presented in Henein et al. [1983a]. See also work by [Henein et al., 1983b; Mellmann, 2001; Rutgers, 1965a,b].

3. Acceleration of a dry granular material. The erosion and deposition in these experiments will manifest as a change in level of the interface between the flowing and passively rotating layers. (As the bed analogue is eroded, the active region will gain mass and bulk up, moving the interface boundary downwards, and *vice versa*.)

4. Granular-liquid systems. The addition of a fluid phase other than air is expected to change rotating drum flow regimes and granular state transitions [Chou et al., 2011; Kaitna and Rickenmann, 2007]. These experiments will include both under- and over-saturated levels of liquid, with the liquid being water.

While it is hoped that the experiments will be illuminating, they will not be all-encompassing. Choking is an important process in granular flows [da Cruz et al., 2008], but the experimental set up used in this work has been specifically designed to avoid choking, as we are interested in a freely flowing granular material. Secondly, breakage of particu-

lates is a key determinant in the materials resultant behaviour [Caballero et al., 2014] as the process would increase the number of particulates in the system, and granular material behaviour is strongly dependant on the grain size [Abdullah and Geldart, 1999; Tegzes et al., 2003], but this project will avoid particulate breakage in order to reduce the number of variables. This study will focus on the erosion and deposition mechanics, assuming individual particles do not break (though some care will be taken to mitigate and measure this effect). While lahars in nature will undergo de/bulking (losing/gaining of material to/from the local environment), this will not be a feature of the experiments due to the materials used being of a fixed mass. In addition, the rotating drum will only allow us to investigate the nature of lahars already in motion; intuitively, it will not reveal anything as to the formation of lahars, or how they come to an end and leave a deposit. However, rotating drums have proved to be useful in the past for investigating natural phenomena, despite these limitations [Havlica et al., 2015; Hsu et al., 2014; Orpe and Khakhar, 2001].

3.2 Equipment

3.2.1 Rotating Drum

Considering the kind of conditions which this project wishes to replicate, the drum is capable of steadily rotating at velocities of between 1 and 37.5 RPM. It can also accelerate (or decelerate) at a rate of several RPM per second in a linear fashion (see Section 3.4.3). Finally, the system should be able to handle granular materials with a total weight of up to 75 kg. Note that this is an extreme case, in most runs the weight will probably not exceed 22 kg, not including the drum itself. For example, seven litres of beach sand weighs approximately 19 kg.

The materials placed within the drum may be abrasive, acidic, or saline. Hence the materials the drum is constructed from should be water-proof, rust-proof, and resistant

to abrasion. The chosen materials are welded steel for the main part of the drum, with the door (which needs to be transparent for observation) fabricated from toughened glass (similar to equipment used by Chou et al. [2010] and Yamane et al. [1998]) which scores over the more fragile acrylic [Orpe and Khakhar, 2004].

Further details on the drum's specifications are given in the next section.

Rotating Drum Design

The drum is driven by a SEW Eurodrive CMP50S PC-controlled motor-gearbox unit that allows for a range of drum velocities (0 to 37.5 RPM) and accelerations (up to 1 rad s^{-2}) and which also allows for real-time data acquisition of drum velocity. With the given drum geometry this translates to a range in Froude number that encompasses those found in natural granular and granular-fluid flows (see Equation 2.4.2 and Section 2.4). In fact, measurements of the local Froude number in the experiments presented in the results chapters gives values from around 0.5 to 2.5, which is a very good match for those found in natural lahars. The mounting frame of the drum is readily rotatable by 90° allowing the complete filling of the drum with various materials (*i.e.*, a mixture of granular solids and a fluid).

The drum is 304 stainless steel built on a mild steel plate welded on a stainless steel frame and mounted on bearings manufactured by SKF[1] to reduce vibration. The drum measures 0.5 m in diameter, and is 0.15 m deep. Stainless steel was chosen as the construction material as it should be resistant to scratches from rougher particulate materials, rust, and corrosion. In addition, steel enables us to construct the drum to a high degree of accuracy. The dimensions were chosen to balance size and cost whilst at the same time minimizing edge effects for the size of particulates that we are likely to be using. The set up is water-tight, making use of a rubber seal, so both dry and wet experiments can be undertaken. Wet experiments are relatively rare in the literature [Tegzes

[1] `http://www.skf.com/au/index.html`, last accessed 20th October, 2015.

et al., 2003], with most workers focusing on dry experiments (*i.e.*, the interstitial fluid is air) [Chou et al., 2011; Chou and Hsiau, 2012]. It is expected that the wet experiments will be very valuable, as the water content is expected to have marked effects on the behaviour of the system [Caballero et al., 2014; Finger and Stannarius, 2007], due in part to the suppression of the Van der Waals forces and static electric effects [Petean and Aguiar, 2013; Wang et al., 2014a]. The door was constructed from toughened glass, which is resistant to scratching and static electrical effects [Chou et al., 2010]. This was used to observe the flow with a digital high-speed video camera. Flow regimes and flow transitions were then quantified through analyzing particle and fluid velocity profiles. It was assumed that the wall effects[2] [Liao et al., 2013] of a rotating drum experiment are minimal [Jop et al., 2005], and the flow structure seen at the wall can be treated as representative of the internal structure of the material during motion [Girolami et al., 2010; Hill and Kakalios, 1995; Orpe and Khakhar, 2001]. This assumption is valid as the walls of the drum are toughened glass, which is smooth. The annulus of the drum is stainless steel, which is rough enough to produce motion in the granular material as the drum rotates. This produces a situation in which the internal failure of the material (*i.e.*, the onset of a flowing layer) happens before slippage at the wall. In this work, the presence or absence of wall slip will be tested by examining the PIV images.

Lighting

High speed filming, when compared to that with a normal frame rate of around 30 to 60 frames per second, requires a greater amount of lighting, as the shutter on the camera is open for less time. Consulting with David Wiltshire, Massey University's resident photographer[3], it was advised to light the experiment from above. A custom lighting frame was constructed, on which were mounted four 500W halogen lamps (Fig.

[2]Wall effects are when the distance between the edges of the experiment (in this case the back wall and the door of the drum) is too low, leading to interference with the flow mechanics within the material. As the width of the drum is at least several orders of magnitude greater than the typical largest particulate diameter, wall effects should be minimal.

[3]`http://www.massey.ac.nz/massey/expertise/profile.cfm?stref=642630.`, last accessed 20th October 2015

3.2.1).

Halogen lamps have a frequency, and under high-speed filming the resultant footage can appear to flicker. This was minimised in two ways. First, having multiple units meant that the frequency of each lamp would be more likely to be counter-acted by the frequency of its neighbours. Second, Mr. Wiltshire recommended using natural light whenever possible. As such, when the weather permitted, the experiments were run with the large door to the lab open to allow in sunlight. It was found that the artificial light was enough to illuminate the experiments, with natural light reducing flicker as well as any post-processing that was required on the final images.

Happily, it was found that any flickering that was recorded did not effect the ability of the PIV to track the material in the drum. The footage was recorded at a fast enough frame rate that the flickering of the halogen lamps was rendered moot as adjacent frames were lit under near identical conditions.

3.2.2 Annular Shear Cell

A brief note on nomenclature is required before discussing use of the annular shear cell. In the literature, the name Jenike shear cell is often used interchangeably for both linear shear cells and annular shear cells. Some authors use Schulze ring shear tester in lieu of annular shear cell [Louati et al., 2015; Scieszka and Adamecki, 2013]; others use Portishead ring shear cell [Walker, 1967] or Couette cells [Abrahamsson et al., 2014; Höhner et al., 2013; Mansard and Colin, 2012; Reddy et al., 2011]. Note that in this thesis, linear cells will be referred to as Jenike shear cells (after their inventor - see Jenike [1964b]), while their toroidal cousins will be given the designation annular shear cell (ASC).

Figure 3.2.1: The lighting rig constructed for this research. There are four 500W halogen lamps mounted on a custom frame, constructed from spare office shelf mounts. The two lamps mounted to the reverse of the rig were not used. On the left of the image, just visible is the computer used to control the drum motor, and the stack of airtight boxes used to store samples. Photograph taken by the author.

Usage of the Annular Shear Cell

The usage of the annular shear cell in this project was informed by Section 4 of the ASTM International methodology standard D6773 [ASTM, 2008].

A description of the methodology of using an ASC is summarised as follows. A material is loaded into a circular trough (Fig. 3.2.2), which itself is attached to a motor enabling the trough to turn at very slow but steady rotational velocities. The material is subject to a range of shear forces and normal stresses (analogous to pressures), with the trough being rotated both with and against the shear forces, which are supplied by a series of weights attached to an arm that pulls on the trough in a lateral direction due to a pulley. A sensor mounted to the trough measures the amount of force that is applied in a direction congruent with the shear forces. As the direction on the trough is switched between the two possibilities, the measured force will vary between two average values; comparison of these average values and the applied normal stress allows the investigator to find a value for the shear strength of the material.

The maximum normal stress that a material is subjected to is determined by the ASTM standard D6773 [ASTM, 2008] , and is shown in Table 3.1. This stress is also called the consolidation stress.

Table 3.1: This table shows the consolidation stress that a material should be subjected to in an annular shear cell, based on the material's bulk density. (Found in the ASTM Standard D6773.)

ρ (kg m$^-$3)	σ (kPa)
< 300	~ 1.5
300 - 799	~ 2.0
800 - 1599	~ 2.5
1600 - 2400	~ 3.0
> 2400	~ 4.0

Having the correct consolidation stress is important to avoid a material that is over- or under-consolidated. An under-consolidated material is one in which the material has a greater void space fraction than the critical case, while in an over-consolidated system, the particulates themselves have begun to break down [Campbell, 2006] - both

scenarios will produce behaviour from the granular material that will introduce errors into the shear strength measurements by the ASC. The concept of critical consolidation in a material is demonstrated by Figure 3.2.3.

The average of the two peak force values, *i.e.*, the resultant shear stress, is plotted against the applied normal stress (the weights on top of the trough, combined with those hung from the pulley attached to the arm). By making use of Mohr-Coulomb circles analysis (see Section 4.4), it is possible to find the unconfined yield stress (UYS) and major consolidation stress (MCS) (also known as the minor and major principle stresses, respectively) of a particular combination of applied shear stresses and a specific normal stress.

There are limitations to the usage of an ASC. The investigator must make sure that the material is not under- or over-filled in the trough. An under-filled trough will not have enough particles for the system to truly reflect the shear strength of the material. An over-filled system will overflow during use and result in the properties of the system changing with time, rendering the results unusable. An optimal fill level was found by trial and error and marked on the trough for reproducibility between runs. The same fill level was used for both the sand and the ash, as they were similar enough to each other in this regard.

The individual particulates must also not be so wide as to introduce serious edge effects into the system. Each different ASC will have its own tolerances on both of these factors[4]. It is also important to consider the air moisture in the laboratory [Gómez-Arriaran et al., 2015]; if the material itself gains moisture, this can have a significant effect on its flowability[5]. In addition, while the ASC is an improvement over the Jenike shear cells that came before it, the ASC is still subject to operator induced errors; the accuracy of the data obtained from an ASC can vary significantly if care is not taken

[4]The particles in the experiments presented in this thesis were all sieved to sizes (0.25 to 4 mm) well below the tolerances for the ASC used in this project [ASTM, 2008].

[5]Moisture content as a concern was mitigated by several means, including drying the samples in an oven, storing them in airtight containers, and running the experiments in an air-conditioned laboratory.

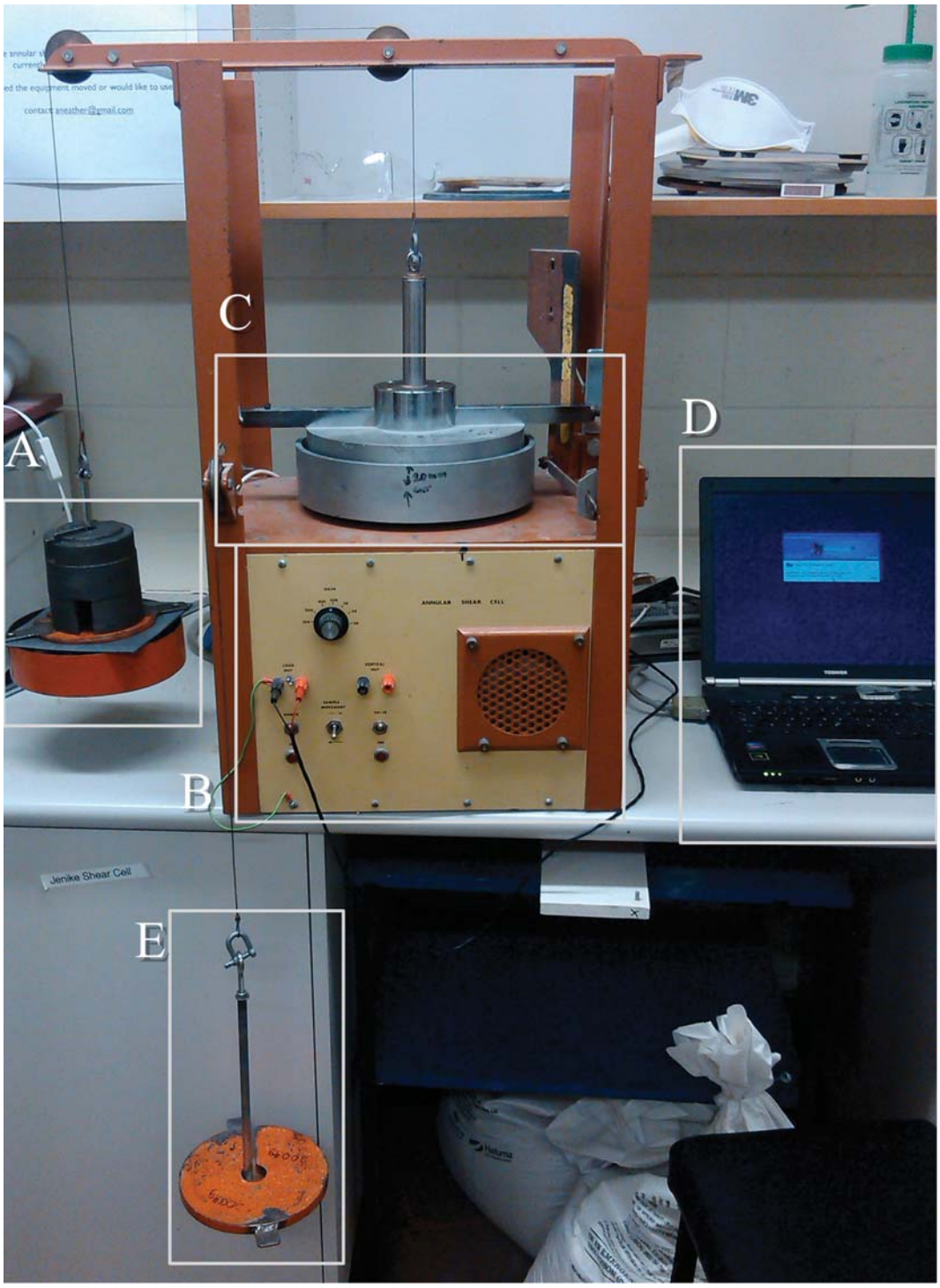

Figure 3.2.2: The parts of an annular shear cell, specifically the one used in this study. A is the counter-weight used to bring the normal stress below that which would be provided by an unladen lid. B is the controls for the unit, and also houses the motor that drives the rotation of the trough, which is seen in C. The data, in the form of a voltage, is recoded by the laptop, D. The weights on E provide the shear stress to the system. Photograph taken by the author.

to follow a strict sequence of steps [ASTM, 2008] - it is for this reason than the ASTM standard was created.

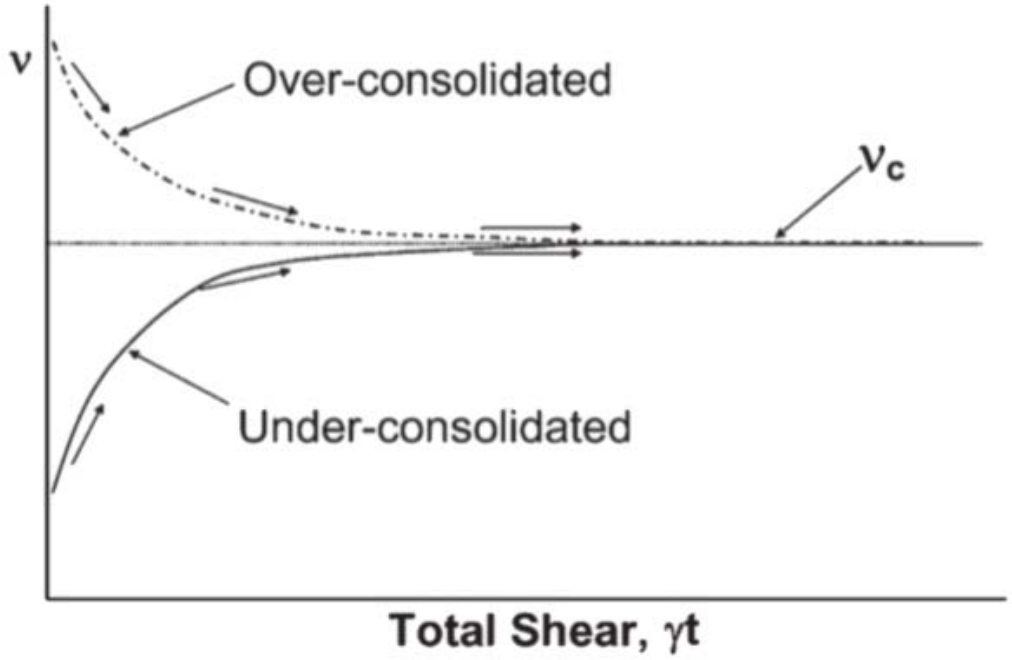

Figure 3.2.3: An illustration of the concept of critical consolidation, ν_c. An under- or over-consolidated material will produce strange total shear strength results. Care must also be taken not to apply too much load to a sample, or the critical consolidation will be change. An edited version of a figure originally presented by Campbell [2006].

The ASC used in this study was constructed as an exact copy of the instrument described by Carr and Walker [1967] at the University of Canterbury, New Zealand.

3.2.3 Video Analysis Computer

As the experiments will be recorded with high speed video, it is necessary to have a high-power computer to analyse the resulting footage. Particle image velocimetry (PIV) requires high processing power, while high-speed footage can occupy large amounts of memory. As such, a computer with the following specifications was obtained.

It was decided that the best solution would be the 21.5" 2011 iMac. This is due to the unit's large screen and ease of running multiple operating systems (OS X, Windows, and GNU/Linux systems), which we may need depending on the software that we decide to employ, and the Mac platform's historical standing as a good one with which to

do image manipulation.

The iMac received was upgraded slightly from the stock model. Specifically, it had 16GB of RAM, rather than the standard 4GB and a 1TB HDD, rather than the standard 500GB. This is due to the following reasons: image analysis/manipulation, particularly when automated, is a RAM-intensive process, and as such it was felt that 4GB wasn't going to be enough. Testing of a commercial PIV package called DigiFlow[6] on a machine with 4GB of RAM resulted in severe slow down. In order to make sure that we are able to produce results in a timely manner, 16GB of RAM was requested. Secondly, high-definition high-speed video can take a lot of HDD space; for example, a standard-length TV programme recorded at standard definition could take up to 700MB: a 500GB HDD will be filled rapidly when generating extensive high speed footage. Even with the expanded HDD, several external drives were used to store raw experiment footage. (Footage was also backed-up to the department server.)

Software

Recording the experiments resulted in files often tens of gigabytes in size for real-time processes of only a few seconds. A suite of software was put together to allow for meaningful quantitative analysis of the footage.

The experiments were recorded to a Windows 7-based computer running Streampix 5[7]. The resultant footage was converted into individual frames, using the .jpeg image format, via Virtual Dub. PIV analysis was obtained by running the required frames through PIVlab, a plug-in for MATLAB[8]. Once this was completed, the PIV data could be interrogated by hand inside PIVlab, or by running the MATLAB code written by Dr. Luke Fullard[9]. The MATLAB code outputs various data from the PIV as either comma

[6] `http://www.dalzielresearch.com/digiflow/`, last accessed 15th October, 2015.

[7] `https://www.norpix.com/products/streampix/streampix.php`, last accessed 26th September, 2016.

[8] `https://uk.mathworks.com/products/matlab/`, last accessed 27th September, 2016.

[9] `http://www.massey.ac.nz/massey/expertise/profile.cfm?stref=681050`, last accessed 27th September, 2016.

separated value files (.csv) or as Microsoft Excel spreadsheets (.xlsx), depending on the complexity of the resultant data set. This outputting in Excel format requires Microsoft Office and running MATLAB in a Windows environment.

3.3 Materials - The Ideal Particulates

There are several criteria that a particulate material needs to meet in order to be suitable for the experiments. These are; size, shape, survivability, colour, availability and minimal inter-particulate forces (which can greatly affect granular flows [Moughrabiah et al., 2012; Shinbrot et al., 2006]).

The size is a consideration because if the particles are too large compared to the vessel through which they are expected to flow, this can introduce wall effects [Liao et al., 2013]. In addition, particulates that are too small may experience inter-particulate interactions due to van der Waals forces [Nguyen et al., 2014] or static electricity [Shinbrot et al., 2006]. It is noteworthy, however, that van der Waals forces can be an order of magnitude stronger than static electric forces, especially in granular systems under stress [Petean and Aguiar, 2013]. Shape of the particulates must be taken into account for two main reasons; firstly, particles that are too smooth (such as the frequently used glass or steel beads [Parker et al., 1997; Chou and Hsiau, 2012; Orpe and Khakhar, 2004; Rodrigues et al., 2014; Santos et al., 2013]), which are too idealised to simulate natural flows [Dioguardi and Mele, 2015; Iverson and Ouyang, 2015; Kingston and Heindel, 2014; Marks and Einav, 2015; Tegzes et al., 2003]) display their own unique flow properties (Lu et al. [2015]), and secondly because shape of particulate has been shown to be a key factor in determining flow parameters [Colbert et al., 2015; Dubé et al., 2013; Kodam et al., 2010b; Liu et al., 2013; Yamane et al., 1998; Zhang et al., 2015] and can even result in the material becoming closely-packed and unable to flow [Reber et al., 2014]. Additionally, little is known about non-spherical particles in a rotating drum [Lu et al., 2015]. As an aid to visualisation, compare a stack of billiard balls to a structure

composed of childrens' wooden building blocks. The former will collapse once any support is removed, while the latter will support itself, until an external force is applied. Furthermore, differences in particle size and density result in segregation due to percolation and buoyancy effects [Cagnoli and Romano, 2013; Chou et al., 2010; Halidan et al., 2014; Kingston and Heindel, 2014; Rosato et al., 1987]. By survivability it is meant that the particles should neither damage themselves (a property known as friability) nor the equipment (*i.e.*, the equipment must be abrasion resistant) whilst undergoing flow; while in nature materials involved in a debris flow will be damaged during transit (in a process known as cataclasis [Caballero et al., 2014]), this is a process avoided in this work for two reasons: to reduce equipment maintenance costs and reduce complexity of analysis of resultant data as it is well known that inter-particulate collisions that damage the particulates can change the behaviour of a granular material [Caballero et al., 2014; Raman, 1918]. Colour is to help with analysis of the flow; if the particulates are available in, or can be made into, two contrasting colours, this will allow easier tracking and differentiation of an individual particle. Availability is simply a matter of practicality; a perfect material needs to be obtainable in large enough quantities and not cost too large a sum of money. Finally, inter-particulate forces must be avoided to accurately replicate lahar flows; the materials swept up in a lahar generally don't attract each other through static electricity or van der Waal's forces.

Various particulates were considered for this work. These include, in no particular order: various types of peas and beans; plastic, steel and clay ball bearings; Lego™ building bricks; jewellery beads, rice, glass beads (such as the Ballotini brand which are typically used to either make paint reflective or to "sand blast" surfaces in industrial cleaning applications); decorative garden pebbles; and various types of sand.

Reasons why some of the list above were not used include: cost (a large enough sample of Lego™ bricks would have cost several thousand New Zealand dollars); inter-particulate forces (plastic ball bearings, such as those used in air guns, would have built a static charge during the experiments); self-destructive properties (such as the

way that rice "polishes" itself when large quantities are stirred); too spherical (such as the perfectly round and smooth glass beads); equipment-destructive (such as the steel ball bearings that would damage the glass door of the experiment); and size (while in most other respects perfect the clay ball bearings, typically used for hydroponic purposes, were not available in small enough sizes).

Particulates that were chosen include samples of beach sand, pumice, volcanic ash and millet seeds. Each sample was sieved between geological mesh sizes -2 ϕ and 2 ϕ (<4 and >0.25 mm, respectively), and then washed to remove fines adhering to larger particulates. The material was then stored in a 70 °C oven for at least 24 hours to remove any moisture content which could change material behaviour properties. Any materials involved in experiments with water were subsequently re-dried before being used again.

These particular materials were chosen for the relative ease with which they could be obtained, as well as being non-spherical, and as such closer to the materials that might be found in natural flows. The beach sand was obtained from the beach at Napier, in the Hawke's Bay region, while the ash was collected from Mount Taranaki[10] in the Taranaki region, and the pumice was originally found at Lake Taupo (all in New Zealand). Specifically the beach sand was chosen as it displays a selection of features deemed desirable for this study, such as non-spherical shape and two-tone visual appearance, as well as being non-self-destructive during flow. The ash was used as it is the closest material to that which would be found in an actual lahar or volcanic debris event (while we do recognise that such an event would have solid materials from a wide range of sources, not just volcanic). Pumice was chosen as it is also a natural material, and is also a very different density to the other materials. This was initially to have as different as possible a density ratio between the solid and fluid-phase during the water-based experiments, but pumice was eventually passed over for this role as the pumice proved especially difficult to wash effectively, and resulted in cloudy water,

[10]Mount Taranaki is also known as Mount Egmont.

rendering PIV of the resultant footage impossible. This is potentially a very rich area of investigation for future researchers, however.

The materials were sieved between the aforementioned mesh sizes to remove any materials that may be too small and be subject to static electric or van der Waals forces, and larger particulates that would be subject to excessive wall effects. A standard minimum and maximum size, albeit with a different intervening distribution, would also help to make the materials comparable with each other, as particulate size is known to greatly effect granular material flow mechanics. Additionally, removal of the smallest particulates aids in keeping the fluid-phase transparent in the water-based experiments.

Sieving was also used to help with making sure that the experiments could be scaled to natural phenomena, such as lahars, by selecting particulate sizes similar in ratio to the drum width as typical materials involved in a debris flow event relative to the channel width. Lahars can be a wide range of sizes and carry a wide size range of particulates. Taking as a "typical" lahar width a value of 130 m, based on data from Procter et al. [2010a], and the largest particulates as boulders, which are given on the Wentworth grain size chart as 256 mm or greater in diameter, this suggests a maximum number of adjacent particles as around 500. All the materials in this experiment were sieved between >0.25 mm and <4, and the drum is 0.15 m in width. This suggests that on average the maximum number of particles that can fit laterally in the drum is 150, which is on the same order of magnitude as the real world case given above. Note that while real-world lahars would probably contain materials finer than those excluded from the experiments, this does not change the fundamental property of both lahars and the analogues being a two-phase flow of a solid particulate material suspended in a liquid.

To further aid with keeping the water clean during wet runs, the materials were washed to remove any fines stuck to the surface of larger particulates. Two methods were employed to wash the materials. The first involves placing the material in a bucket and

adding water to a level deeper than that of the material - any fines in the mixture are removed from their host particles and float in the water - this process can be aided by gentle agitation of the solid materal. It is then trivial to decant this water and dispose of the unwanted fines. The second method was employed only with the pumice, as this was the most cohesive material, and also the least dense. This means that particles that would be large enough to be considered valuable could be washed away using the bucket method, as larger particulates would float in the excess water and possibly be accidentally disposed of. This second method is known as wet sieving and is essentially identical to the standard dry sieving method (which is covered in Section 3.4.2). The only difference is that the material is drawn through the mesh of the sieve not only by gravity but by applied water flow. This removes the very small undesirable fines, whilst using the mesh itself to keep any particulates that would be large enough to be useful.

Other materials were used as part of some experiments, but later abandoned. For example, also studied was a second sample of beach sand, slightly finer than the other sample. This was used in a few experiments, but while from a geological point of view was distinct from the other beach sand, was too close to the other from a mechanical/granular flow view point to be of any use. Experiments involving the pumice with water as the fluid phase were also planned, but abandoned after the first run when the fluid phase became a colloidal suspension, visually opaque and impossible to analyse via PIV: there were simply too many fines in the pumice sample to remove completely via washing. The pumice sample was also friable (self-destructive), so additional fines were being continuously generated. While the solid phase in lahars in nature would presumably be damaged during the event, this is avoided in the experiments to avoid another variable which would be difficult to quantify. Finally, a sample of builders' sand was used to test the experimental equipment, and was planned on being used during the experiments, but the source material had been poorly stored and would have been very difficult to clean properly for actual experimental use. Secondly, it had a very narrow size distribution; while the other samples were sieved to remove parti-

cles that were too large and washed to remove any that were too small, they still show a size distribution that may be considered natural-like [Caballero et al., 2014].

3.4 Experimental Methodology

3.4.1 General Concerns

Features of the experiment which can be varied are as follows;

- the type of fluid used; for this study these are air or water
- the size of solid particulates
- the density of solid particulates
- the density ratio of particulates to fluid (as in nature, the density of the inter-particulate fluid can vary widely, from approximately 1 kg m^{-3} to values in the region of 1700 kg m^{-3} for liquid muds [Hsu et al., 2014])
- the percentage of the drum which is filled by the solid particulate fraction, referred to as the fill factor, f, should be no higher than 50% to avoid a non-flowing "dead zone" [Ding et al., 2002] in the material, whilst also maintaining a weight range of 5 kg to 75 kg to avoid over-straining the motor. For all experiments reported here, the fill factor, f, is kept to ~0.25 (equivalent to seven litres). Fill factor is kept constant as it is a variable of secondary importance when the project is focused on erosion and deposition mechanics [11]
- the angular velocity at which the drum rotates
- the rate of angular acceleration, if any

[11] As Mellmann et al. [2004] points out, many rotating drum studies have $f = 0.5$ which limits their application to industrial studies. Having $f = 0.25$ means our results could be used in further geophysical and industrial research.

- the humidity of the area in which the experiment takes place. Though this cannot be easily controlled by the experimenters, it is something that has to be taken into account, as it can effect the flowability of a powder[Colbert et al., 2015; Stanford and Dellacorte, 2006]. This is only of a concern during experiments in which the fluid phase is air - the water-based experiments will clearly be immune to this. This should not be too much of a concern, as the materials were dried before usage, stored in air-tight containers, and the laboratory was air-conditioned

The overarching aim of the experiments can be summarised thus: To investigate the effect of velocity and acceleration on a fluid/particulate solid mixture in a half-metre diameter rotating drum. It is hoped that such experiments will give insight into how changing topography influences lahar flow, and in turn their erosion and deposition.

3.4.2 Granular Material Characterisation

It is important to know the properties of a granular material in order to be able compare the results for one substance against another. For example, all other things being equal, a material with a higher particulate density would presumably produce different results to one with a lower density.

Key variables that need to be measured include particulate density, bulk (or "tapped" [Abdullah and Geldart, 1999]) density, angle of repose [Chou et al., 2010], particulate size distribution, and the material's internal angle of friction.

Angle of Repose

There are two angles of repose that need to be considered when working with granular material; the static and the dynamic. The static angle is the maximum angle to the horizontal a stable pile of the material in question will attain before an avalanche takes place. The dynamic angle is the angle the slope settles at once an avalanche has taken

place; the dynamic angle is generally shallower than the static [Chou et al., 2014]. For this study, the static angle of repose was measured using a simple system of creating piles of the substance to be tested, and then measuring the height and two diameters, taken at right angles, of the pile. Simple trigonometry using the average of the two diameters and the pile's height gives the static angle of repose. Five piles were created for each material, and an average angle taken. Results are presented in Table 3.2.

Note that the angle of repose is a measurement of an unstressed granular material. While it is useful for cross-material comparison, it is less robust than the internal angle of friction, which is discussed later in Chapter 4, along with the flow function. These two measurements are not included here due to the greater amount of analysis that is required to obtain their values.

Table 3.2: The angle of repose for the various materials used in this study, found by measuring piles of the material in question and simple trigonometry.

Material	*Angle of repose* ±0.3°
Taranaki Ash	32.1
Beach Sand	29.3
Pumice	33.4
Millet	26.6

Particle Size Distribution

In a rotating drum, a size distribution of the particulates in the granular material can affect the flow [Abdullah and Geldart, 1999; Alexander et al., 2002; Liao et al., 2013] and segregation of the material (*i.e.*, the percolation effect [Chou et al., 2010]).

Size distribution of the materials used in this study was undertaken using standard geological sieves. These sieves are graded on an exponential scale known as the ϕ scale. Negative numbers on the ϕ scale relate to the coarsest materials, while the positive numbers denote finer materials (Fig. 3.4.1). For example, -8 ϕ particulates are 256 mm or greater in diameter and would be classified as boulders, while 8 ϕ materials are <8 and ≥ 4 μm across and are referred to as silt [Wentworth, 1922]. Each increment in

the ϕ scale in the negative to positive direction represents a halving of the size of the particulates that will pass through the associated mesh; the conversion between the ϕ scale and millimetres (d) is given in Equation 3.4.1. The sieves used to measure the size distribution of a material are able to be stacked, with the material that passes from one falling into the one below. By arranging the sieves so that the largest meshes are at the top, a material can be separated out into its constituent sizes. If the weight of the sample is measured before being passed through the sieves and the contents of each sieve weighed afterwards, the size distribution of the material in question can be ascertained.

Sediment grain sizes (mm)	Wentworth grade	Phi (Φ) scale
>256	Boulder	−8
>64 to 256	Cobble	−6
>4 to 64	Pebble	−2
>2 to 4	Granule	−1
>1 to 2	Very coarse sand	0
>0.50 to 1	Coarse sand	1
>0.25 to 0.50	Medium sand	2
>0.125 to 0.25	Fine sand	3
>0.0625 to 0.125	Very fine sand	4
>0.0313 to 0.0625	Coarse silt	5
> 0.0156 to 0.0313	Medium silt	6
>0.0078 to 0.0156	Fine silt	7
>0.0039 to 0.0078	Very fine silt	8
<0.0039	Clay	>8

Figure 3.4.1: A table that converts between mm, the Wentworth grade, and the ϕ scale. Image originally presented in Hedrick et al. [2013].

$$d = 2^{-\phi} \tag{3.4.1}$$

Figure 3.4.2 shows the size distributions of the materials used in this study.

Particulate Density

Particulate density is an important characteristic for granular materials [Chou et al., 2010]. The particulate density can be measured at a precision of up to four decimal places using a gas pycnometer. The more accurate the weight measurement supplied

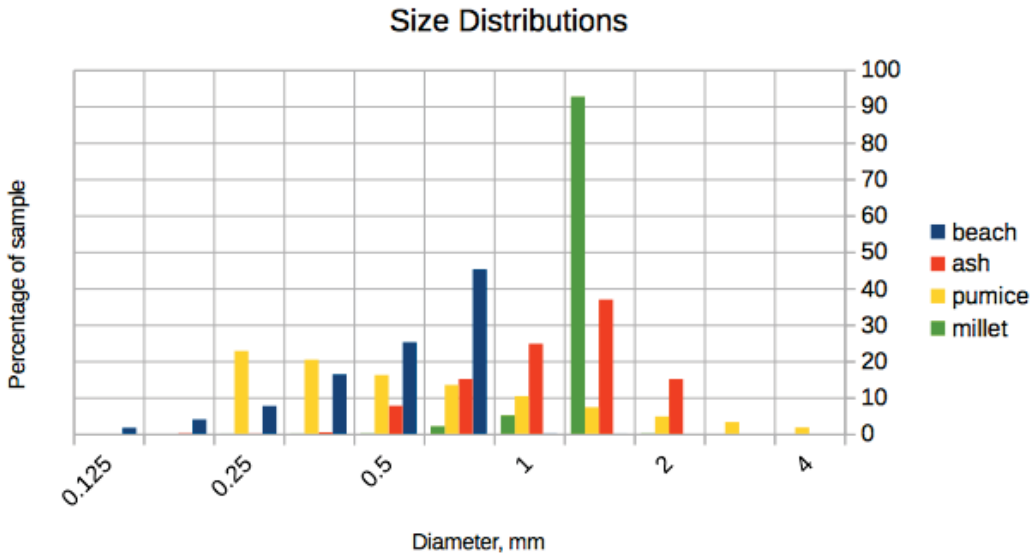

Figure 3.4.2: The size distributions of the materials used in this study. The *x* axis is the mesh size of the geological sieves in millimetres. The *y* axis is the mass percentage of the sample with diameters *greater* than the respective millimetre measurement and *less* than the sieve size above. Blue is the beach sand, red the ash, yellow the pumice, and green the millet. As can be seen from the figure, the beach sand is skewed towards the finer particulate sizes, with a mode between 0.5 and 1 mm (0.707 mm). The ash is relatively normally distributed with a peak between 1 and 2 mm (1.414 mm). The pumice has a wide distribution, skewed towards the fine. Finally, the millet is essentially unimodal at 1.414 mm.

to a pycnometer will obviously aid in the accuracy of the densities obtained. Note that the results from the machine are sensitive to moisture in the air; to allow direct comparison between samples, they must be put through the process on the same day to minimise variation in moisture exposure; it is beneficial to avoid days where it is raining. The size (*i.e.*, volume) of the sample container used when measuring the particulate density must be known accurately, or the pycnometer will give erroneous results.

The pycnometer can be set to analyse the same sample multiple times in order to obtain an average particulate density value. For the machine used in this study, this can be up to 100 times, but accurate results were obtained with 10 repetitions.

The standard deviation required can also be set on this study's pycnometer. As may be expected, the higher the accuracy required, the longer the machine will take to analyse

the sample, and the more prone the final value will be to error. As for the purposes of this work the material density is only used for comparison of materials after other experiments which will be subject to wider error margins than the pycnometer, the standard deviation was set to 0.01%.

The equipment used here was a Quantachrome[12] Ultrapycnometer 1000 nitrogen pycnometer. The particulate densities of the materials are presented in Table 3.3. Note that the density of the pumice was calculated from data provided by Eric Breard, and the millet density was supplied by Dr. Luke Fullard. Size distributions and angles of repose for these materials were found by the author.

Table 3.3: The particulate densities for the various materials used in this study, ±0.01 g cm^{-3}. These were found using a gas pycnometer or supplied with the material by other workers, as covered in the main text.

Material	*Density* (g cm^{-3})
Taranaki Ash	3.03
Beach Sand	2.69
Pumice	1.60
Millet	1.31

Bulk or "Tapped" Density

The methodology for finding the bulk density of a granular material for this study is very simple. The material was poured into a measuring cylinder of a known weight. After this, the combined cylinder and sample was weighed. Finally, to take into account the possible variation in particulate packing, the cylinder is tapped 100 times, causing the material to settle. The final fill level on the cylinder is noted, and this allows for the density of the material to be found. The bulk densities found for the materials used in this study are presented in Table 3.4.

[12] `http://www.quantachrome.com`, last accessed 15th October, 2015.

Table 3.4: The bulk densities, in kg m^{-3} to four significant figures, of the materials used in this study.

Material	*Density* (kg m^{-3})
Ash	1402
Beach	1606
Pumice	897.9
Millet	747.0

3.4.3 Introductory Experiments - Equipment Validation

The initial experiments have rather modest aims; to make sure that the equipment is behaving as expected, *i.e.*, it can achieve the velocities and accelerations required, and that the motor can handle not just the weight of the drum, but of the drum with various contents. In addition, it was checked that the drum was waterproof, which will be necessary for later experiments.

By undertaking a run of experiments with the simplest possible set-up, the aim is to investigate the operational parameters of the equipment. This is in order to help constrain the details of future experimental runs, and so the safety limitations of the drum can be ascertained.

Speed Verification

The first step was to make sure that the drum was rotating at the speed that was requested of it via the software control package, MoviTools. The drum was rotated at a variety of speeds containing builders' sand at a fill factor, f, of 0.25. Analysing the high speed footage in DigiFlow, it was found that the speeds were being achieved with an average error of 1.39% (Table 3.5.)

Table 3.5: Shows the speed that was requested of the system via the control software, and that which was measured in the resulting high speed footage.

RPM Requested	RPM Measured	Percentage Error
2	1.98	0.90
3	2.99	0.48
5	4.96	0.79
10	9.71	2.84
15	14.53	3.10
20	19.94	0.27

Acceleration Verification

Here the aim is to discover if the equipment was a) reaching the required velocities in the requested time and b) whether the acceleration produced was smooth. An overhead transparency was printed with a polar grid; a series of lines each rotated about a common centre, spaced 22.5° apart. This sheet was then attached to the drum's glass door, and used to verify the rotational speed of the drum as a function of time.

The target velocities were chosen to be 10, 20 and 30 RPM, as this represents a wide spectrum of the speeds that will be required of the system. Target times were set at five and 10 seconds. Each of the six resulting runs was filmed at 500 FPS for five seconds longer than the target acceleration time, just in case the target time was not met it would still be possible to find when the target velocity was reached. The fill factor in this experiment was also 0.25.

The results, which show the linear acceleration behaviour required, can be seen in Figures 3.4.3 and 3.4.4. As can be seen in the figures, the equipment was able to meet all the requested accelerations bar the 30 RPM in 5 second target.

3.4.4 Intermediate Experiments - Steady Rotational Velocities

These experiments form the core of this work. The key variables in these experiments are the type of material and steady rotational velocities. These experiments were filmed

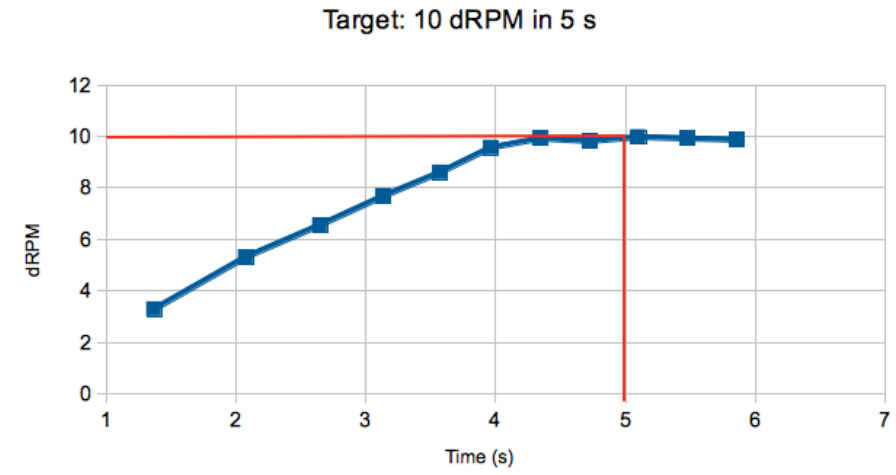

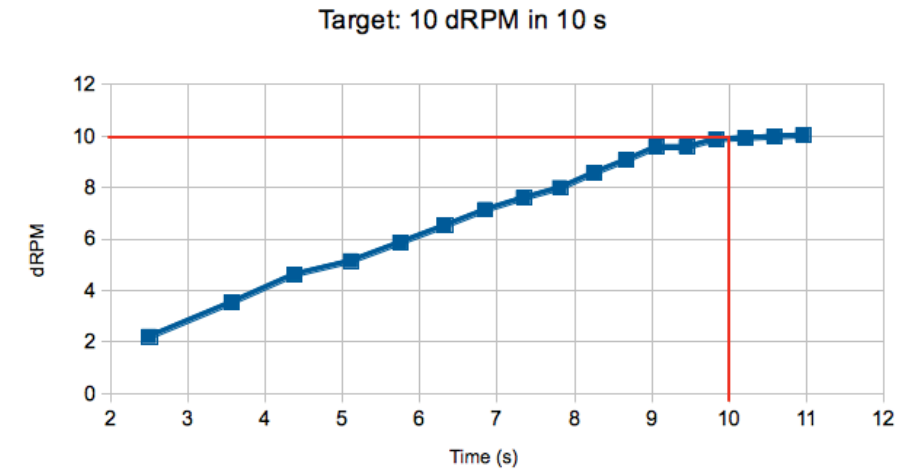

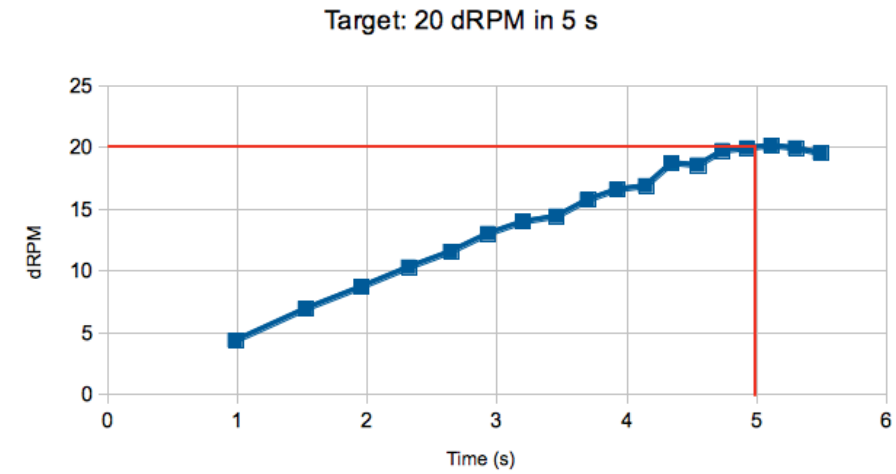

Figure 3.4.3: Graphs showing the speed of the drum against time, for a range of target acceleration regimes (first of two figures). These regimes are defined by the target velocity and the target time to reach this velocity. The equipment is capable of meeting all the requested regimes, bar the fastest 30 RPM in five seconds. The accelerations are considered to be smooth, *i.e.*, linear from these graphs.

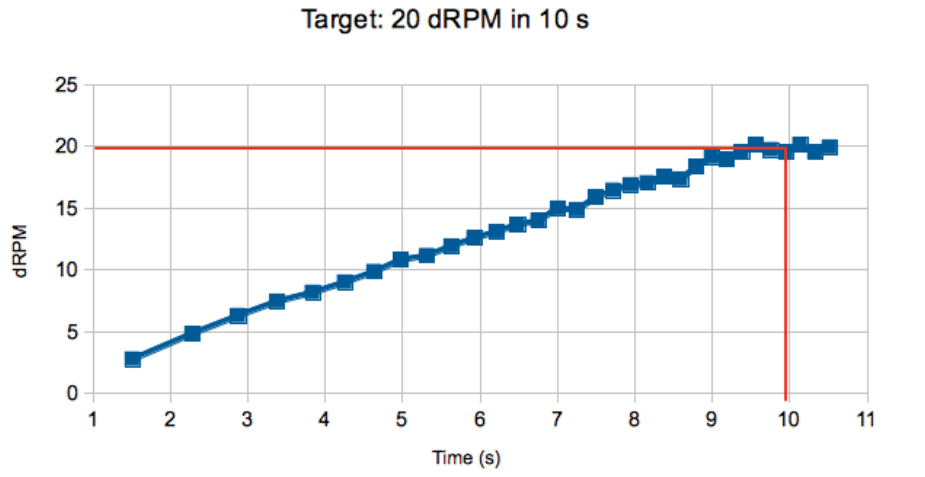

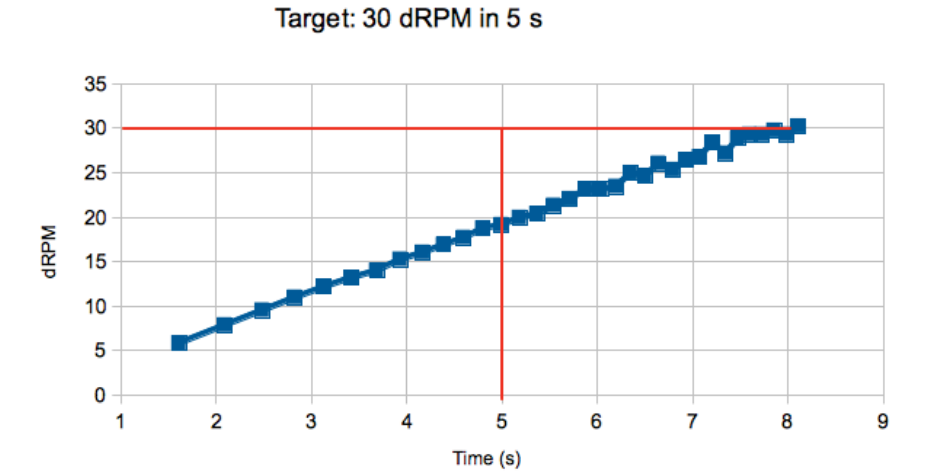

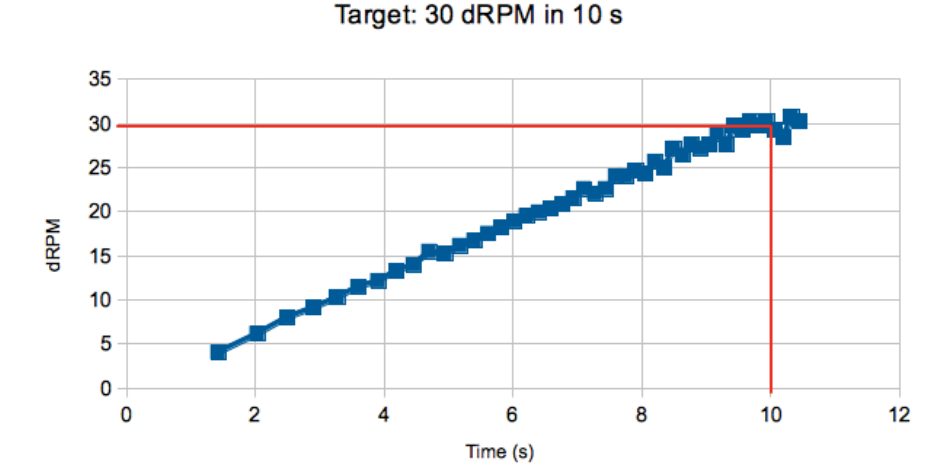

Figure 3.4.4: Graphs showing the speed of the drum against time, for a range of target acceleration regimes (second of two figures). These regimes are defined by the target velocity and the target time to reach this velocity. The equipment is capable of meeting all the requested regimes, bar the fastest 30 RPM in five seconds. The accelerations are considered to be smooth, *i.e.*, linear from these graphs.

at 500 FPS, or 40 times slower than real time[13]. Footage was fed through the PIVlab software and then interrogated to discover rates of erosion, flow velocities, and layer locations, etc. Velocities were chosen to limit the behaviour of the material to the rolling and cascading Mellmann regimes [Mellmann, 2001], as these are best suited to explore the erosion/deposition mechanics of the system [Yamane et al., 1998].

Results from these experiments are presented in Chapter 5, Results I.

3.4.5 Advanced Experiments - Acceleration and Changes in Interstitial Fluid

These experiments are the most novel included in this study. They include accelerational regimes, the introduction of water as the fluid phase, and focus on new phenomena. For these latter experiments, the footage was also filmed at 500 fps

Rotating drum studies involving acceleration are rare in the literature. Schlick et al. [2015] have dynamic velocity experiments, but avoid regimes this study includes. Fiedor and Ottino [2005] vary their velocities with respect to time, but with a sinuisodal, rather than linear, profile. They are also concerned with different mechanics with a granular material to this study; they focus on material stratification.

Fill factors and materials were kept constant for experiments in the Intermediate group, to allow for cross-comparison of results.

Exchanging air for water as the fluid phase in drum gives rise to a drastically different density ratio between particulate and fluid phase, and as such is a closer analogue to flows that may occur in nature.

[13] This compares with lower FPS from previous studies, for example 250 FPS used by [Mellmann et al., 2004].

Acceleration Experiments

The acceleration and deceleration experiments were subject to the profile seen in Figure 3.4.5. For these experiments it was t_1 that was varied. The experiment was stopped after t_2. The time period t_2 itself was included to compensate for any lag in the motion of the accelerating material.

The fill factor, f, as for the other experiments, was set at approximately 0.25, or seven litres of loosely packed material. The materials involved in the acceleration experiments were the sieved volcanic ash, the millet, and coarse beach sand. The camera settings were kept the same as for the static velocity experiments, *i.e.*, they were recorded at 500 fps.

The fluid phase in these experiments was air. Experiments involving water as the fluid phase are detailed next.

Varied Water Level Experiments

In nature, a lahar consists of water and a solid particulate component. The ratio of water to solids can vary widely (between 10 and 60% by volume, see Chapter 1 and Pierson [2005]), and as such a series of experiments was undertaken with varying levels of water, using the beach sand as the solid fraction.

The saturation level of the beach sand was calculated by placing a sample of the sand of known weight in a measuring beaker and then adding water until the water level was equal to that of the sand. The sample was then left for a period to allow air to escape, and then water was added again to bring the water level back up to the sand level. Once the water level was steady, the entire mixture was weighed. Subtracting the weight of the sand and the cylinder, and knowing the density of water, allows the investigator to find the volume of water that was added. Taking this as a ratio with the solid fraction volume gives a dimensionless saturation level for the material.

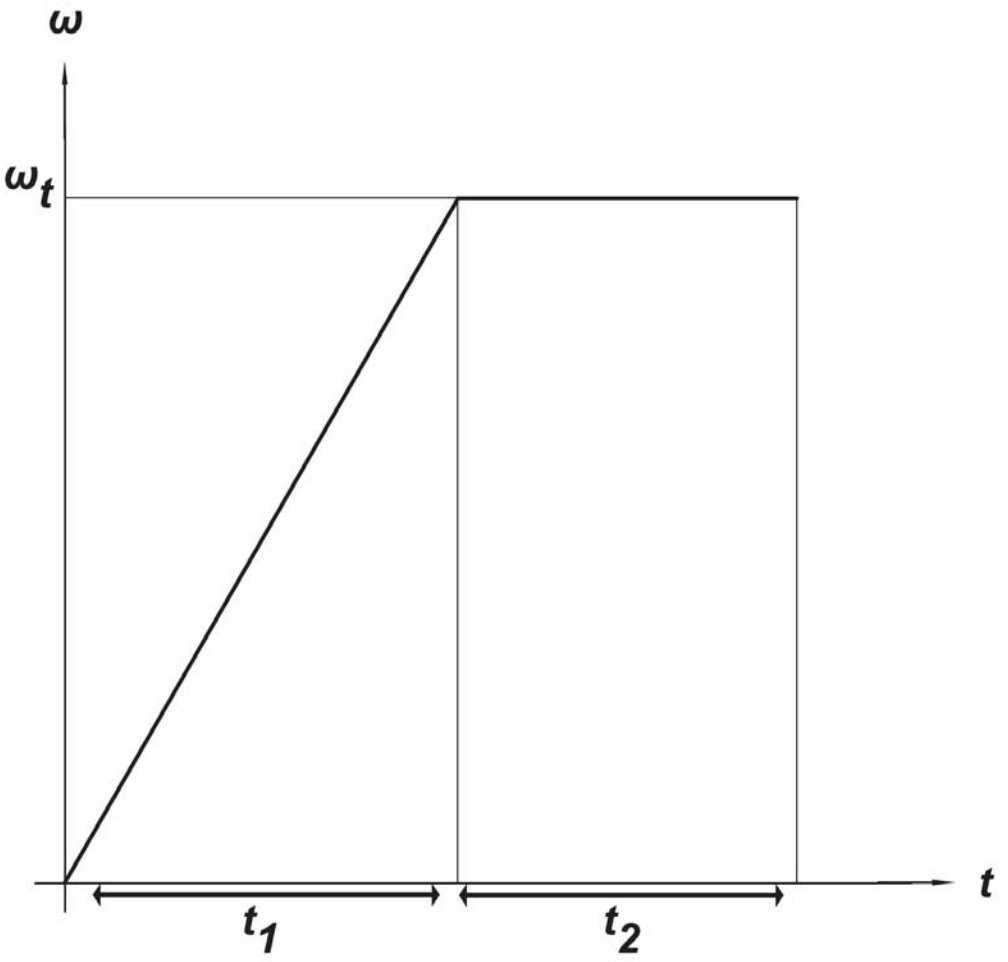

Figure 3.4.5: A representation of the acceleration regime used in this study. The target velocity, ω was varied between 10, 20 and 30 RPM. The target time (t_1) to achieve the desired velocity set to 5 or 10 seconds, to provide a wider range of accelerations. The maintenance time, t_2, was kept at 2.5 seconds.

Experiments were undertaken with levels of water 5% below saturation, at saturation, at +50% (by volume) water above saturation, with equal volumes of water and sand, and with a completely full drum. In the final case, the horizontally positioned drum was left over-night to allow the air content to escape, before attaching the glass door and setting the drum in the vertical rotational position. The fill fraction of the solid material was kept at the standard 0.25.

Chapter 4

Analytical Methodology

4.1 Introduction

As this project is a blend of industrial methodology and geological application, a variety of analytical methods are employed. These range from particle image velocimetry (PIV, Section 2.6.2), which allows the velocities within a granular flow to be measured, to various geological characterisation methods (Section 3.4.2) used to measure the properties of the materials employed. Also covered here are Mohr-Coulomb circles, the static angle of internal friction and the annular shear cell (ASC, Section 3.2.2), and the usage of dimensionless numbers.

In the case of this study, the shear amount of data from the PIV itself presented a challenge. With the help of Dr. Luke Fullard's MATLAB code, the rate of processing the PIV data was greatly increased. What the code does is also explained in this chapter.

4.2 PIV - Particle Image Velocimetry

PIV has already been briefly covered elsewhere in this thesis (see Section 2.6.2); more detail is given here. PIV is a method of analyzing imagery of a flow in order to extract data about the flow, specifically velocities [Adrian, 2005]. PIV uses Eulerian pattern matching algorithms to output the velocity. In order to use PIV, it is necessary to know the size of the frame, *i.e.*, how wide/tall the image the computer is processing is in real terms, so that the distance travelled (and hence velocity, *etc.*) can be found by the program. In addition, we need to know the location of the particles as x and y coordinates. PIV applications look for "blobs" of a certain brightness (which can be adjusted to avoid false positives) and the change in their position between frames.

It is possible to change the weight ("cost" for particles already on screen, "fee" for particles being compared to off-screen dummy particles). This cost determines how likely one identified particle at time $t = t_1$ is to be the same particle as was previously found at $t = t_0$. For simple Brownian motion, we can assume that the blob nearest (using a

"least squares" method on the x and y co-ordinates) to where another blob appeared before to be the same particle. When we're studying a flow, it is necessary to adjust the cost (which can be adjusted to avoid false positives) to favour two particles with similar speeds. Each particle at t_1 should only match with one particle at t_0. In order to perform PIV, the image must not be distorted, such as by the "fish-eye" effect, where the centre of an image is magnified compared to the edges, as this will produce erroneous velocity profiles by adding a parallax effect that will be difficult to quantify.

For this study, the footage was recorded at 500 fps (frames per second) and a resolution of 2048 by 760. Compare this with extant work, such as 30 fps and 640 by 480 resolution [Chou et al., 2010] or 30 fps and 800 by 600 resolution [Chou et al., 2011]. This should allow for much more detailed analysis of the flow of the granular material than previously possible. PIV analysis was undertaken using an open source plug-in for MATLAB called PIVlab [Thielicke and Stamhuis, 2014]. Pairs of images were analysed in a "a-b, b-c" style, rather than the alternative "a-b, c-d". The interrogation windows were set at 64 and 32 pixels, for the first and second passes, respectively. (Interrogation windows are how the image is sub-divided as part of PIV analysis. More accurate results are obtained from smaller interrogation windows and greater number of passes, but at the cost of computational power requirements and time to complete the analysis.) The FFT (fast Fourier transform) window deformation PIV algorithm was chosen over the alternative DCC (direct cross correlation). These settings were arrived at after a period of trial and error, and were chosen for a balance of accuracy (*i.e.*, minimal erroneous vectors) and minimisation of analysis time. After PIV analysis was performed, erroneous vectors were removed (*i.e.*, any that were much larger than the surrounding norm, or pointing in unlikely directions). The data were converted from pixels per time step to metres per second by calibration - the diameter of the drum (0.5 m) was used.

4.2.1 Image Skew Problem and Solution

It was noticed while analysing some of the images that, while care was taken to avoid this problem, the images were skewed slightly but measurably. This was due to the camera being somewhat off-centre while recording the footage (Fig. 4.3.1). This meant that, despite efforts taken during experimental set up, the dot marking the centre of the drum, which is on the back wall, was not marking the exact centre of the glass door, and it is at the glass door that the PIV analysis is run.

To avoid having to do the experiments again, mass automated image editing was investigated, specifically using macros within ImageJ. Consultation with image editing expert Prof. Donald Bailey[1], however, revealed that doing this in a mathematically rigorous and accurate manner would be time consuming. It was decided that, as the skew was minimal, it would be possible to compensate for it by simply changing the location of the centre point when running the MATLAB analysis code (Fig. 4.3.1 B). Testing this gave satisfactory results, and as such the ability to change the centre of the analysis on the fly was added to the MATLAB code.

4.3 Automated Layer Thickness Analysis

The MATLAB code was written by Dr. Luke Fullard, and automates the process of finding the thicknesses of the active layers and the passive region. This allowed the PIV data to be more accurately and rapidly interrogated than it would have been possible to do by hand.

The code draws a series of lines radially from a user-defined point, which in the case of this study should be the point marking the centre of the drum. The angle between each line is also user-definable: for this study the lines were spaced 5° apart. The edge of the drum is defined by the radius and matched to the image being processed by the

[1] `http://www-ist.massey.ac.nz/dbailey/`, last accessed 27th September, 2016.

calibration set during the PIV analysis of the footage. The code then looks for the point along each line where the angular velocity flips sign, *i.e.*, the point at which the flow goes from downhill to uphill, which is used in this study as the boundary between the active layers and passive region. Finding the position of the free surface is a slightly more complex process, as for parts of the footage the point at which the free surface meets the back wall of the drum is visible along with the desired point at which the free surface meets the glass door. The image is converted into binary, *i.e.*, black if below a certain grey scale value, or white if above that same value (see Figure 4.3.3). As the visible free surface is brighter than the bulk material involved in the experiment (due to being lit from above, see Section 3.2.1), correct choice of a critical grey scale value can have the visible free surface marked in white, while the bulk material will be black. The code then just looks for the point along the line from the centre of the drum to the outer edge where the white region returns to black. If no such change from black to white to black again is detected, the code assumes there's no material that intercepts that radial line, and the data are discarded. The final data are output as a comma separated value (.csv) file type (chosen for its interoperability across multiple spreadsheet applications and computer operating systems) or in Excel format (.xlsx) for more complex data sets, which can then be analysed. The thicknesses of each layer are output in metres. To obtain dimensionless measurements, the thicknesses are added together and then the thickness in question becomes the numerator in a ratio with the drum radius.

4.3.1 Area of Active and Passive Regions

The areas of the active and passive regions (these regions are illustrated in Figure 2.6.1) were also found using the code. The profile lines can be spaced at a known angle: where the profile lines met the free surface, the passive/active interface, and the drum wall created a series of trapezoidal regions whose areas are relatively simple to find. For small angles, the difference between these straight-edge trapezoids and ones taking into account the curvature of the the drum wall is minimal. The sum of the ar-

eas of these trapezoids gives the area of each layer with a reasonable amount of accuracy.

As the distinction between the active and passive regions becomes less obvious at the edges of the material, the edges were ignored for the purposes of finding the areas of the regions, see Figure 4.3.2. This was done by eye, using the velocity vector maps to find the end of the distinct active and passive regions, and on a case-by-case basis. As each velocity will cover different amounts of the drum interior, cases would have a different number of profile lines. The author considers this approach valid as the trend in layer areas would be correct even without the less distinct edges if they are ignored in the same manner, and because the edges of the material represent artefacts of the experiments being undertaken in a drum, rather than "true" parts of the active and passive layers. (A geological granular flow would not display these end regions, for example.)

4.3.2 The Centre of Mass/Dynamic Angle of Friction

The code written by Dr. Luke Fullard also finds the centre of mass of the material in the drum. It finds the angle of the line which bisects the area of the material in two from the vertical. Using the same techniques outlined above to find the free surface and the edge of the drum, the code is also capable of finding the midpoint of the bisecting line - this point then represents the centre of mass for a material. The angle of the centre of mass for a flowing material is also the definition for the dynamic angle of friction. The dynamic angle of friction is used in this thesis across materials and velocities (both static and dynamic) to compare the properties of the materials involved.

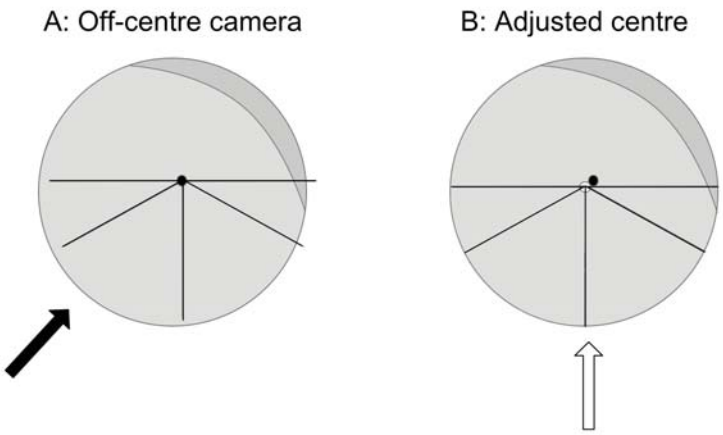

Figure 4.3.1: A cartoon showing an exaggerated example of the image skew problem that affected some of the images it this study. In A, the camera (black arrow) is off-centre, down and to the left. This causes the centre of the drum (the black dot on the back wall) to not be at the centre when considering the glass door. When applying the MATLAB analysis code, the radial profile lines "miss" the edges of the drum. As the image skew is (in reality) small, we can compensate, as seen in B, by moving the point at which the profile lines are drawn, finding an artificial centre of the glass door (the white dot) which "corrects" the placement of the camera (white arrow).

4.4 Mohr-Coulomb Circle Analysis

The ASC described in Section 3.2.2 is used to determine the flowability of a powder or granular material. This is achieved via Mohr-Coulomb circle analysis, which allows the investigator to find the static angle of internal friction (θ_i) and flow function (f_f) of a material [**?**], via measurements of the material's principal stresses. The static angle of internal friction determines when a granular material will or will not flow, and as such is valuable when comparing two materials. A low value of f_f relates to a material with a high flowability, and *vice versa*. While the value of θ_i found depends on the methodology used [Holtz and Kovacs, 1981], using the same methodology across materials mitigates this problem.

The Mohr-Coulomb circles are drawn on a graph of normal versus shear stress for a

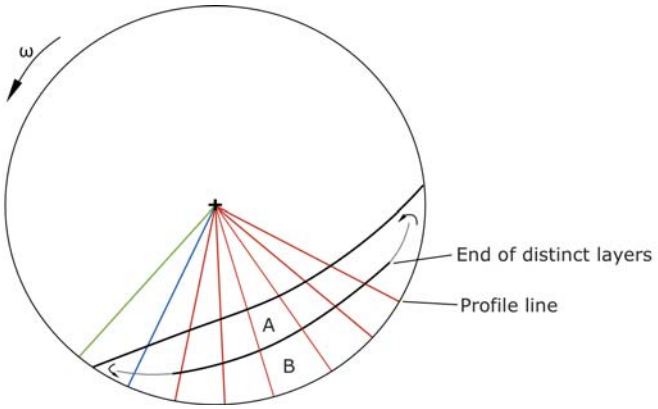

Figure 4.3.2: A cartoon demonstrating the way in which the areas of the passive and active layer were found. The red lines represent the radial profiles. Where two of these profiles meet the free surface, interface, and drum edge forms two sections which can be interpreted as trapezoids, in this figure A and B (and of course the neighbouring sections). The sum of these sections gives the area of the active and passive regions. The grey lines towards the edges of the material represent the place at which the clear distinction between active and passive layers begins to fade - arrows at the very edges show the places at which the distinct layers are gone completely and the material is recycled from one layer into another. The blue line is an example of a radial profile line that passes through the end regions of the flowing material, and is manually ignored. The green line, as it does not meet any material, is automatically rejected by the MATLAB code.

material. The circles are named for the two researchers who collectively discovered the technique - Mohr, who detailed the failure envelope of a material [Mohr, 1887], and Coulomb, who created the Mohr-Coulomb strength criterion, or more commonly the internal yield locus (IYL) [Coulomb, 1773a], which can be considered as the linear approximation of the failure envelope. Two Mohr-Coulomb circles are plotted, one intercepting the origin and tangent to the IYL, and the other tangent to the internal yield locus at the final data point recorded by the investigator. Where these circles meet the x axis (normal stress) gives principal stresses of the system. Of greatest interest are the right-hand intercept points of each circle, which are the major principal stress and unconfined yield stress. These are shown in Figure 4.4.1.

In order to plot the Mohr-Coulomb circles, the IYL must be known. This is found using an annular shear cell (ASC, see Section 3.2.2). Various shears are applied to the system in combination with known normal stresses. Running the motor of the shear cell in both directions alternately allows the investigator to find the shear strength of the ma-

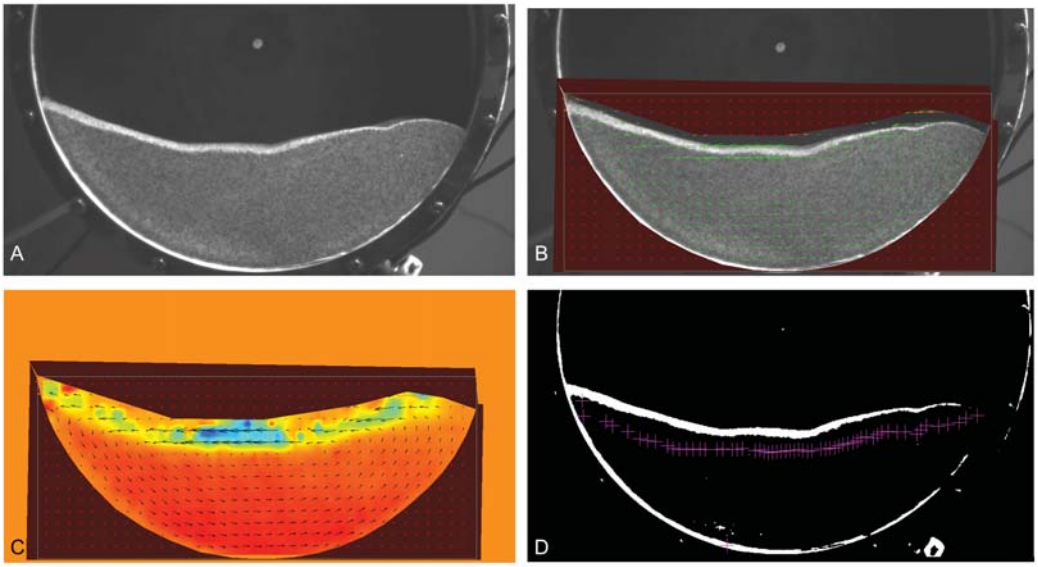

[h]

Figure 4.3.3: Steps in analysing the thicknesses of the flowing layers and the passive region. Images are rotated at ~30°clockwise - this is due to the way the experiments were filmed to ensure the entirety of the material is visible at all velocities. First, the experiment is recorded and the resultant footage is converted into individual frames (A). PIV is run on a group of frames in order to get velocity maps of the materials' motion; this can either be displayed using vectors (B) or colours (C). Using the code written by Dr. Luke Fullard allows the interface boundary to be measured automatically via the PIV data and a binary image (D), though care must be taken by the user to identify possible sources of error. In this figure, these would be the erroneous measurements on the left hand side near the drum wall, and the single point that falls near the drum wall, just before the half-way mark of the interface line.

terial in the shear cell by subtracting the lower value found (with the shear cell turning away from the shear sensor) from the upper value (with the shear cell turning into the shear sensor).

The investigator then plots the found shear strengths against each applied normal stress. Through these points the IYL can be found for each normal stress. The intercepts of the Mohr-Coulomb circles for each case can be found using simple trigonometry, illustrated below (Section 4.4.1).

A different IYL can be generated by changing the pre-consolidation stress, σ_c. The pre-consolidation stress is preliminary normal stress applied to a granular system, and the lower normal stresses applied to the material during the ASC tests are derived from this, say at 20%, 40%, etc. Changing the pre-consolidation stress changes the com-

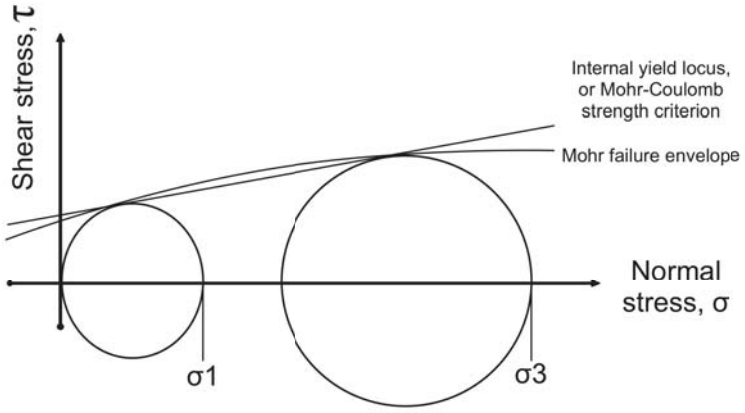

Figure 4.4.1: An example of Mohr-Coulomb circle analysis. The normal and shear stresses are set by the investigator using an annular shear cell (ASC). The major principal stress and unconfined yield stress are given by σ_3 and σ_1, respectively, derived from the intercept between the Mohr-Coulomb circles and the horizontal axis. The internal yield locus is unique to specific pre-consolidation stress, and is the linear approximation of the Mohr failure envelope.

paction of a granular material, and hence its flowability. Each IYL generates different Mohr-Coulomb circle intercepts. Plotting the major principal stresses and unconfined yield stresses found in this manner against each other allows an investigator to find the static angle of internal friction (θ_i) and flow function (f_f) of a material. A family of IYLs is shown in Figure 4.4.2.

The IYL is a linear approximation of the Mohr failure envelope. However, in this project, the linear approximation is shown to be valid by the data found from the ASC. Presented below are the IYL sets for the ash and beach sand (Figures 4.4.3 and 4.4.4).

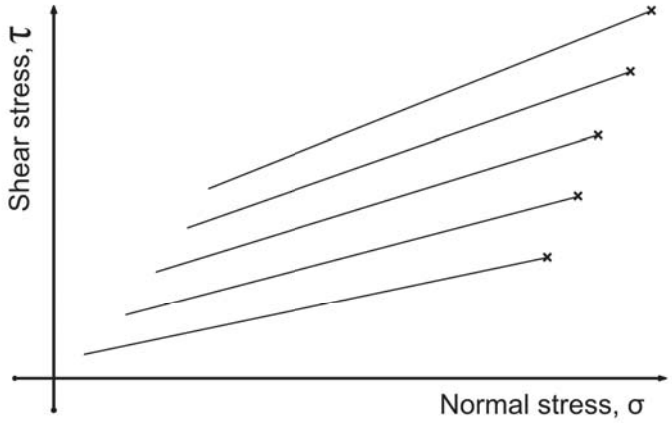

Figure 4.4.2: A demonstration of a family of internal yield loci (IYL). Each loci has its own pre-consolidation stress (σ_c) applied, marked with a cross. The Mohr-Coulomb circles for each IYL will clearly produce a different σ_3 and σ_1 (see Figure 4.4.1). Plotting the multiple σ_3 and σ_1s against each other allows the investigator to find f_f (the flow function) and θ_i (static angle of internal friction); see Sections 4.4.1 and 4.4.2. The numbers f_f and θ_i allow for cross-material comparisons.

4.4.1 Finding the flow function

Intercept of the Left-Hand Mohr-Coulomb Circle

The left-hand Mohr-Coulomb circle is illustrated in Figure 4.4.5. Note that this circle is more accurately described in Nedderman [2005] as the "Mohr circle for the stresses at the surface of the passive Rankine state". In this study, it will be referred to as the left-hand Mohr-Coulomb circle for simplicity.

The generic equations for a circle and a straight line in a Cartesian coordinate system are

$$y = mx + c \tag{4.4.1}$$

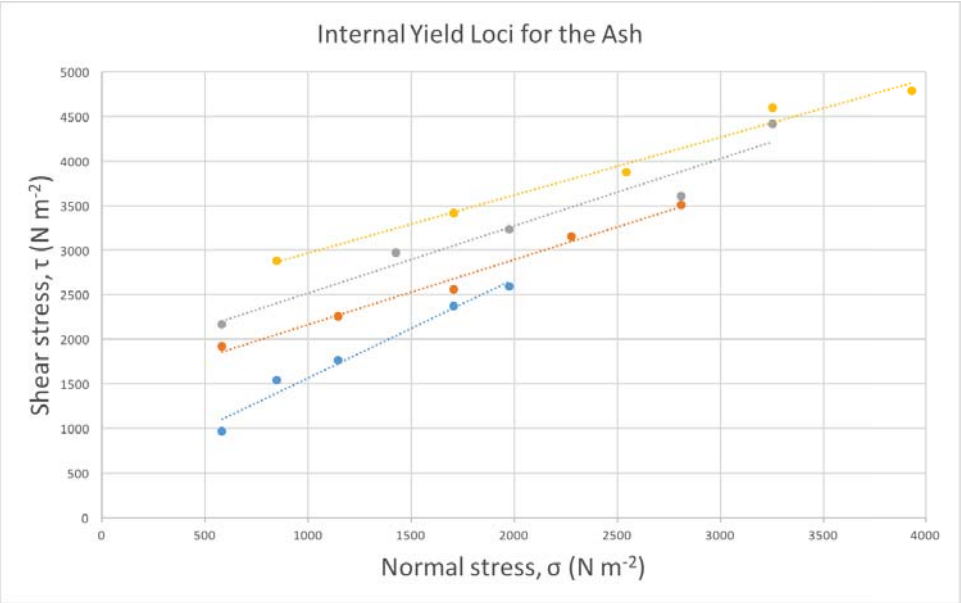

Figure 4.4.3: The family of yield loci for the volcanic ash. Each colour represents a different pre-consolidation stress. The linear lines of best fit clearly show that the Mohr failure envelope can be treated as linear, *i.e.*, as an internal yield locus.

where m is the gradient and c the y-axis intercept, and

$$r^2 = (x-a)^2 + (y-b)^2 \tag{4.4.2}$$

where r is the radius, a the centre on the x-axis, and b the centre on the y-axis. Re-writing these equations for the case of the left-hand Mohr-Coulomb circle gives

$$\tau = m\sigma + c \tag{4.4.3}$$

and

$$r^2 = (x-r)^2 + \tau^2 \tag{4.4.4}$$

because the left-hand Mohr-Coulomb circle's centre lies on the y (τ) axis. Substituting Equation 4.4.3 into Equation 4.4.4 and expanding gives

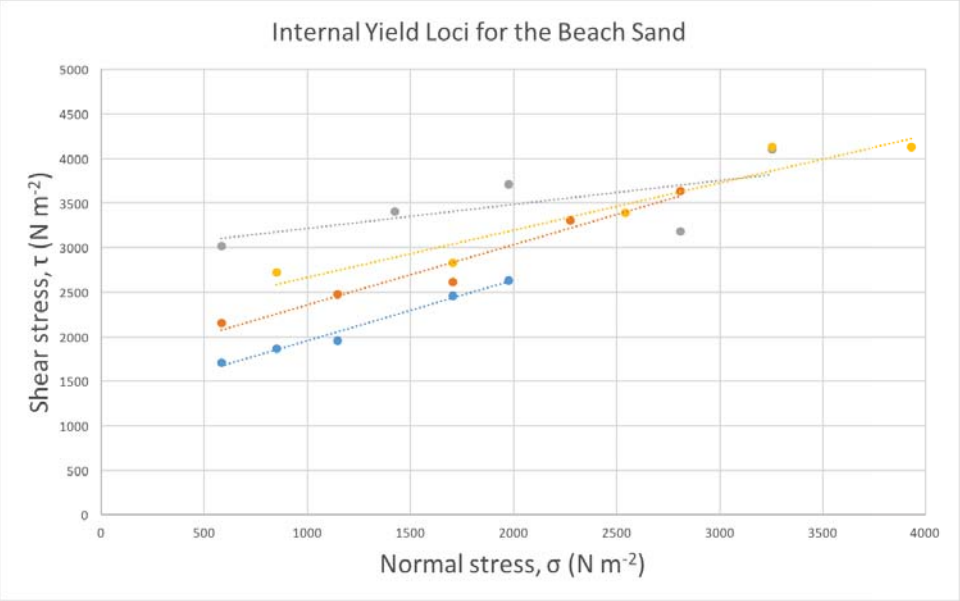

Figure 4.4.4: The family of yield loci for the beach sand. Each colour represents a different pre-consolidation stress. The linear lines of best fit clearly show that the Mohr failure envelope can be treated as linear, *i.e.*, as an internal yield locus (IYL). The grey set for the beach sand appears to be erroneous. Due to this it was ignored for the purposes of finding the f_f and θ_i for the beach sand.

$$(m\sigma)^2 + 2m\sigma c + c^2 + \sigma^2 - 2\sigma r = 0 \tag{4.4.5}$$

as we already know, from Figure 4.4.5 that $\sigma_1 = 2r$, and σ_1 is required, Equation 4.4.5 becomes

$$4(mr)^2 + 4mrc + c^2 = 0 \tag{4.4.6}$$

which can be factorised into

$$(2mr \pm c)^2 = 0 \tag{4.4.7}$$

Equation 4.4.7 can be solved for $2r$, thus:

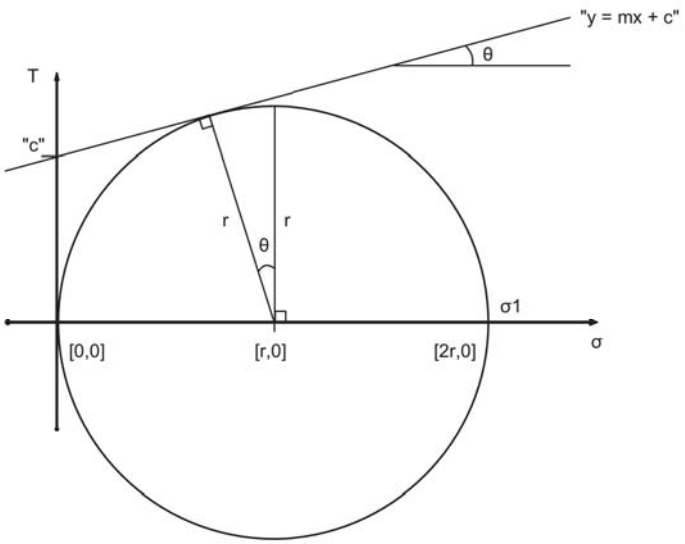

Figure 4.4.5: The left-hand Mohr-Coulomb circle, *i.e.*, the circle which for each IYL gives σ_1 in Figure 4.4.1. This circle passes through the origin and is incident with the internal yield locus line found experimentally - this line can be described with the classical straight line equation. Where the circle intercepts the σ (x) axis is the value of σ_1. The coordinates of this point are necessarily $[2r,0]$, where r is the radius of the left-hand Mohr-Coulomb circle.

$$2r = \frac{\pm c}{m} \tag{4.4.8}$$

As we know that σ_1 is a positive number, we get the final equation of

$$\|\sigma_1\| = \frac{c}{m} \tag{4.4.9}$$

where $\|\sigma_1\|$ is the magnitude of σ_1.

Intercept of the Right-Hand Mohr-Coulomb Circle

The right-hand Mohr-Coulomb circle is illustrated in Figure 4.4.6.

A slightly different approach is required here - it is possible to redraw the situation

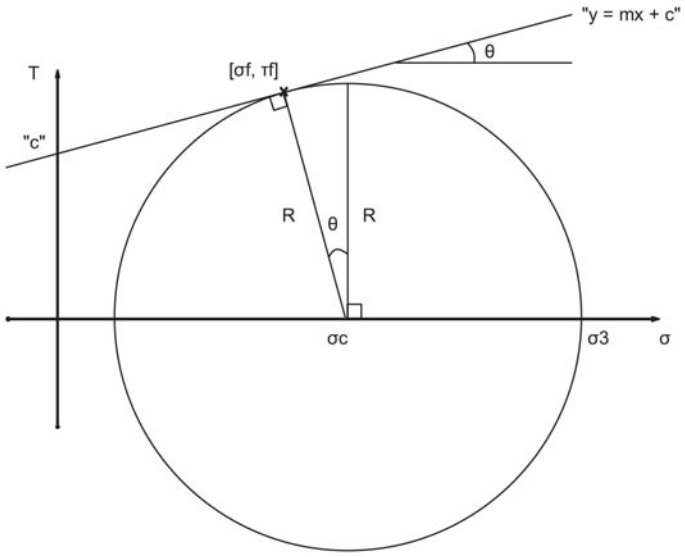

Figure 4.4.6: The right-hand Mohr-Coulomb circle, *i.e.*, the circle which for each IYL gives σ_3 in Figure 4.4.1. This circle is incident with the internal yield locus line found experimentally at the point of the last data point recorded (*i.e.*, the one with the highest normal and shear stresses) - this line can be described with the classical straight line equation. Where the circle intercepts the σ (x) axis is the value of σ_3. From this diagram it can be seen that $\sigma_3 = \sigma_c + R$.

shown in Figure 4.4.6 into the form shown in Figure 4.4.7.

The distance between the points $[\sigma_f, \tau_f]$ and $[\sigma_c, 0]$ is R, the radius of the right-hand Mohr-Coulomb circle. The gradient of the line between these two points, m' is given by

$$m' = -1/m \tag{4.4.10}$$

where m is the gradient of the IYL found experimentally. The equation of the $[\sigma_f, \tau_f]$ to $[\sigma_c, 0]$ line is given by

$$\tau = \sigma m' + c' \tag{4.4.11}$$

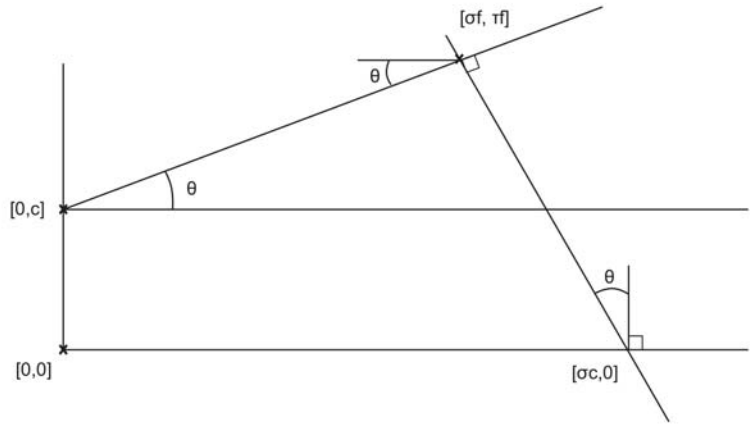

Figure 4.4.7: A simplified representation of the situation described by the right-hand Mohr-Coulomb circle (Fig. 4.4.6). The origin is at [0,0], the intercept of the internal yield locus [0,c], the final data point (which the circle is incident with) is at $[\sigma_f, \tau_f]$, and the centre of the circle is at $[\sigma_c, 0]$. All three angles (marked θ) are known to be equal from simple trigonometric rules.

where c' is unknown. This line must pass through the point $[\tau_f, \sigma_f]$, so the following substitution is valid:

$$\tau_f = \sigma_f m' + c' \tag{4.4.12}$$

Rearranging Equation 4.4.12 to solve for c' gives

$$c' = \tau_f + (\sigma_f / m) \tag{4.4.13}$$

remembering that $m' = -1/m$. So the full equation for the line between points $[\sigma_f, \tau_f]$ and $[\sigma_c, 0]$, using known terms, is

$$\tau = (-\sigma / m) + \tau_f + (\sigma_f / m) \tag{4.4.14}$$

This line must also pass through the point $[\sigma_c, 0]$. Substituting these values into Equation 4.4.14 gives

$$0 = (-\sigma_c / m) + \tau_f + (\sigma_f / m) \tag{4.4.15}$$

Multiplying through by m and rearranging Equation 4.4.15 gives the value for σ_c, the centre point of the right-hand Mohr-Coulomb circle.

$$\sigma_c = m\tau_f + \sigma_f \tag{4.4.16}$$

All that remains is to find a value for R. Remembering that the point $[\tau_f, \sigma_f]$ lies on the circle (and the Pythagorean theorem), R is simply

$$R = \sqrt{(\sigma_c - \sigma_f)^2 + {\tau_f}^2} \tag{4.4.17}$$

As it stated in Figure 4.4.6, finding σ_3 is then simply

$$\sigma_3 = \sigma_c + R \tag{4.4.18}$$

Hence, once an investigator has found the IYL for a certain shear cell run, the unconfined yield stress (σ_1) and the major principal stress (σ_3) can be easily found. Plotting these numbers against each other (Fig. 4.4.8) allows for f_f to be found. The results for this process are presented in Figures 4.4.9 and 4.4.10.

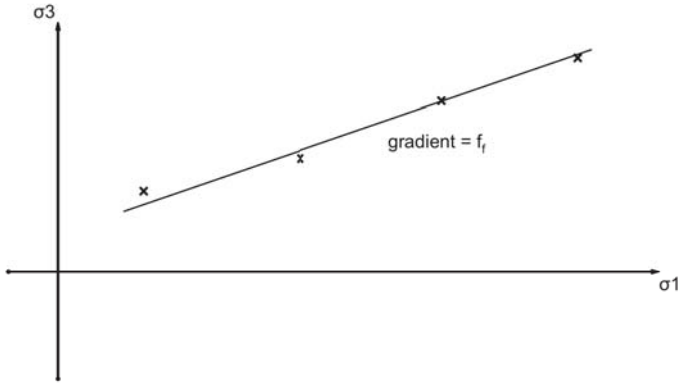

Figure 4.4.8: A cartoon which demonstrates how plotting the major principal (σ_3) and unconfined yield (σ_1) stresses for a certain material against each other gives the powder flow function, f_f, for the material in question. The stresses required are found from Mohr-Coulomb circle analysis of ASC data (Fig. 4.4.1).

4.4.2 The Static Angle of Internal Friction, Flow Factor, and Cohesiveness

The value for θ_i is simpler to find than that of f_f, using one of the graphs used to find σ_1 and σ_3. The angle of the resultant line of best fit for a set of normal and shear stresses gives θ_i, the static angle of internal friction, for the material tested. A low static angle of internal friction implies a material that is easy flowing, while a higher static angle of internal friction indicates a material that is resistant to flowing. For this study, the value of θ_i was found from the ASC data sets of the highest shear and normal loads.

The cohesiveness of a material, the amount of shear that needs to be applied in order to initiate flow, is given by the y-intercept of the same linear line of best fit mentioned above. A lower cohesion indicates a material that is easier to set into motion.

The results for both θ_i and cohesion for the ash and beach sand are presented in Figures 4.4.11 and 4.4.12.

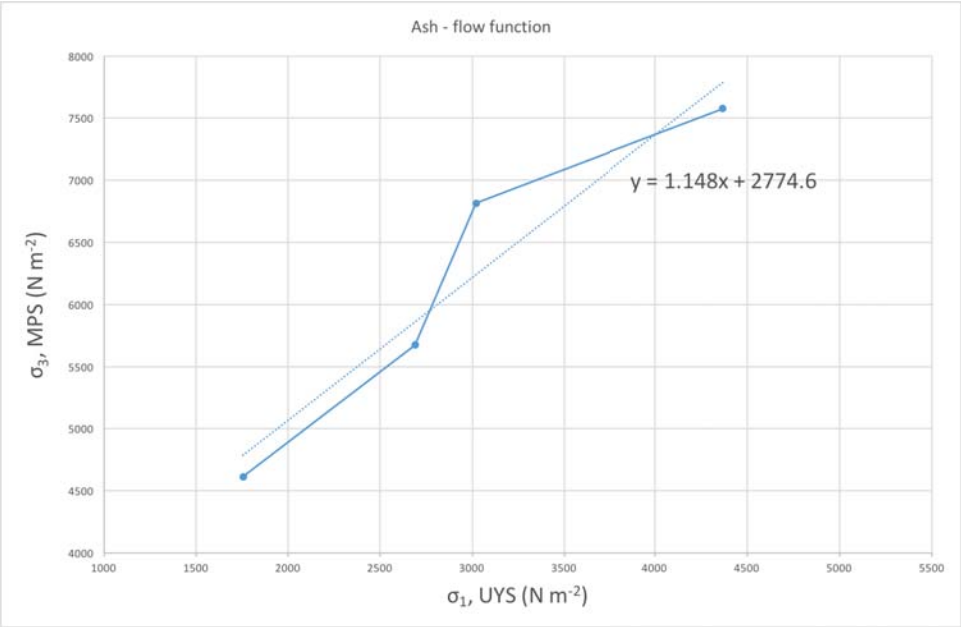

Figure 4.4.9: The results of the Mohr-Coulomb circle analysis for the ash. The unconfined yield stress (UYS, or σ_1) plotted against the major principal stress (MPS, or σ_3). The flow function (f_f) is given by the gradient of the linear best fit, in this case 1.15 to three significant figures.

Using the methodologies outlined above, the static angle of internal friction (θ_i), flow function (f_f), and cohesion were found for the main materials in this study, the ash and the beach sand. The results are presented in Table 4.1.

Table 4.1: The static angle of internal friction (θ_i), flow function (f_f), and cohesion (in N m^{-2}) for the beach sand and ash. These indicate that the beach sand should be more easy flowing than the ash. Data accurate to three significant figures. Found using Mohr-Coulomb circle analysis and the data as presented in Figures 4.4.3 and 4.4.4.

	θ_i (°)	f_f	Cohesion (N m^{-2})
Beach Sand	14.9	1.03	1323.7
Taranaki Ash	18.0	1.15	1415.3

4.5 Dimensionless Numbers

As should already be apparent, the current study is a complex one. In order to understand the phenomena in question, it is necessary to reduce the complexity. This can be achieved via dimensionless numbers, in which variables are divided by a common

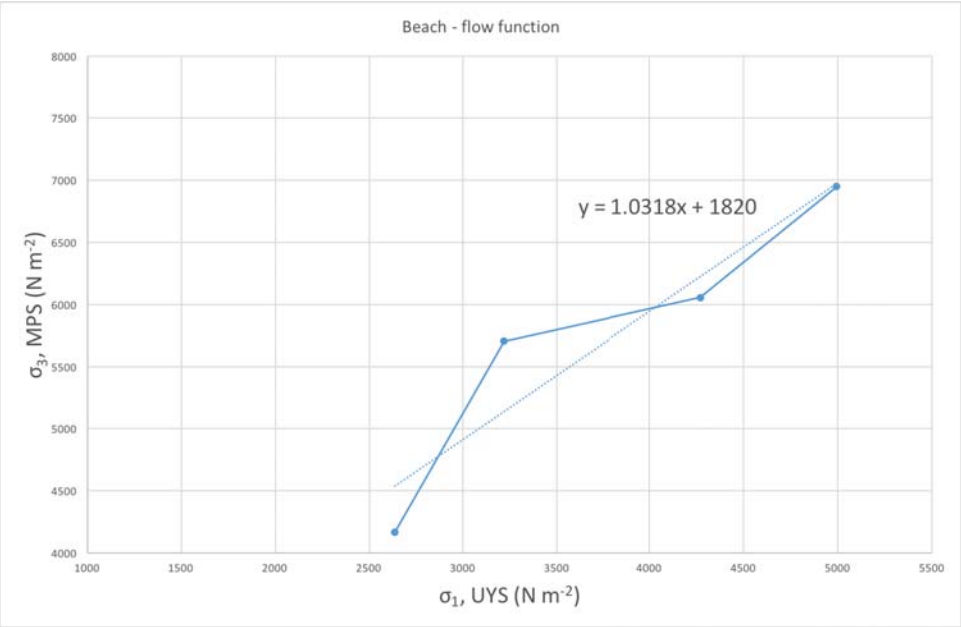

Figure 4.4.10: The results of the Mohr-Coulomb circle analysis for the beach sand. The unconfined yield stress (UYS, or σ_1) plotted against the major principal stress (MPS, or σ_3). The flow function (f_f) is given by the gradient of the linear best fit, in this case 1.03 to three significant figures.

reference number in order to remove the units. Dimensionless numbers are already widely used in fluid dynamics and granular material studies [Ding et al., 2001a; Kuwagi et al., 2014; Qi et al., 2015], such as the inertial number, I, the Froude number, Fr, and the Mach number. For example, the Mach number is the velocity of a vehicle, typically an aircraft, divided by the speed of sound of the fluid through which the vehicle travels. This allows for the expression of the vehicle's velocity as a pure number without a distance per time unit attached.

Note that while these non-dimensional numbers are strictly only defined for steady and uniform flows, a comparison of their relative values should prove useful for scaling unsteady/non-uniform experiments, and hence comparing natural and experimental flows [Hsu et al., 2014; Jiang et al., 2014].

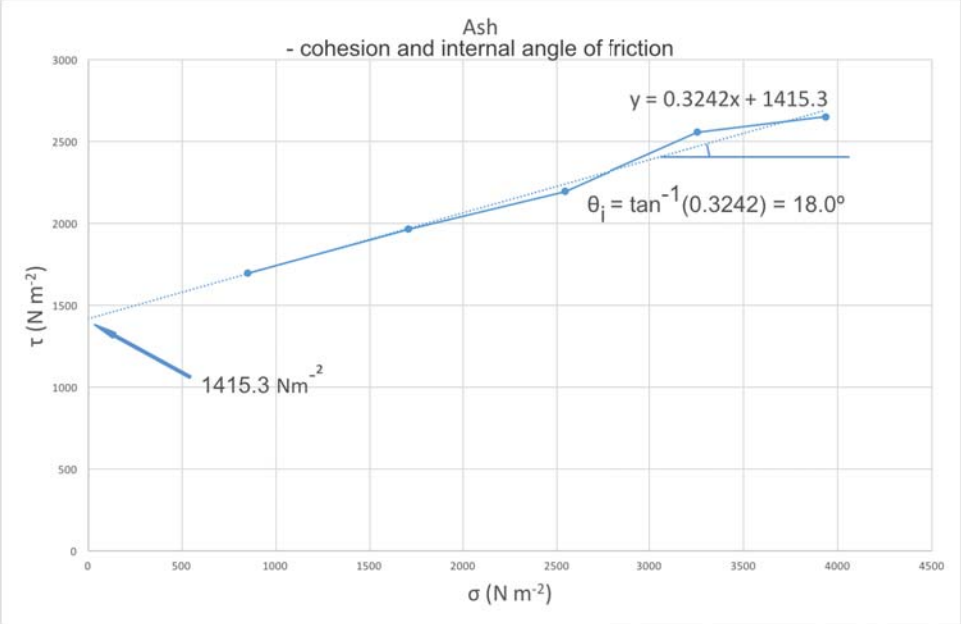

Figure 4.4.11: Finding the the static angle of internal friction and cohesiveness of the ash. The values of σ (normal stress) and τ (shear stress) are set experimentally. The gradient angle is then the static angle of internal friction for the material in question (18.0°), and the y-intercept gives the cohesiveness (1415.3 N m^{-2}).

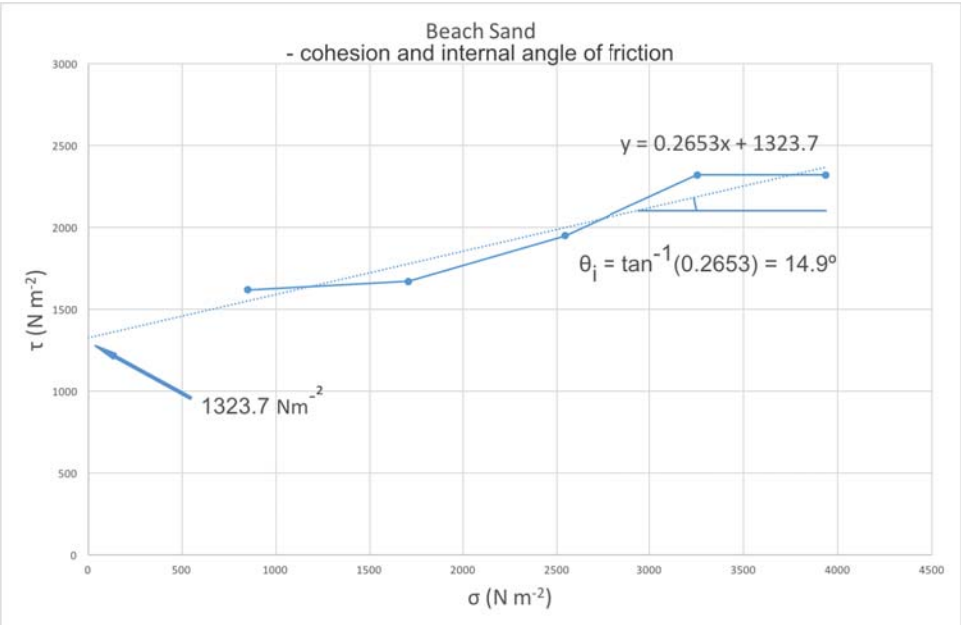

Figure 4.4.12: Finding the the static angle of internal friction and cohesiveness of the beach sand. The values of σ (normal stress) and τ (shear stress) are set experimentally. The gradient angle is then the static angle of internal friction for the material in question (14.9°) , and the y-intercept gives the cohesiveness (1323.7 N m^{-2}).

Chapter 5

Results I - Dry Volcanic Ash under Constant Velocities

5.1 Introduction

Presented in this chapter are the results for a dry material under constant rotational velocities. Results are given in a qualitative fashion, then the chapter moves on to quantitative results - measurements of the thicknesses of the layers involved in a flowing granular material in a rotating drum, followed by velocities and measurements of avalanching behaviour and dynamic angle of friction. Preliminary discussion of these results are given at the end of the chapter. A more general synthesis of the results as a whole is given in the Discussion chapter (this starts on page 170). The equipment used in this study is shown in Figure 3.2.1.

This study also has a number of other findings, which will be presented across the subsequent Results chapters. These include quantitative and qualitative descriptions of the internal structure of a flowing material in a drum of a higher detail than previously extant in the literature, discovery of potentially previously unobserved phenomena, quantitative comparisons of wet/dry flows, and of static velocity/dynamic velocity flows.

This chapter focuses, as previously mentioned, on the results for the constant velocity experiments, in which the material was the sieved volcanic ash. Here the ash is dry, *i.e.*, the interstitial fluid is air. In later chapters, water replaces the air, the velocities are varied with time, and the solid material is switched out. The sieved ash is used at all stages, facilitating cross-experiment comparison of results.

At present, the behaviour of a granular material in a rotating drum is divided into the various accepted regimes [Henein et al., 1983a; Mellmann, 2001]. These are defined by broad ranges of Froude number, crossing several orders of magnitude, and by qualitative descriptions of the visual appearance of the flowing material.

Is it possible to more accurately define the transition between regimes for a material? This chapter presents results for a relatively simple granular system - a dry material

(i.e, the interstitial fluid is air) with a narrow but non-monodisperse size distribution at constant rotational velocities. Bulk material properties (dynamic angle of friction, layer dimensions, *etc.*) are measured and plotted against rotational velocity to investigate the relationship between end-member flow regimes and quantitative descriptions of material behaviour.

Knowledge of layer thicknesses and transitions between different flow regimes will help us to better understand erosion mechanics in a granular system, as a growing active layer (and *vice versa*, a shrinking passive layer) can be considered analogous to erosion in a natural flow. This chapter represents the first step in that growing understanding.

5.1.1 Current Knowledge of the Internal Structure of a Granular Flow in a Rotating Drum

Previous workers in this field have generally divided a granular material in a rotating drum into two main regions; first, a passive layer (adjacent to the drum wall), and secondly, an active layer flowing over the passive (Fig. 2.6.1). The two layers are separated by a line known as the yield line [Dubé et al., 2013].

This study has found that the internal structure can be more complex than this. Under the right circumstances, a granular flow in a rotating drum can consist of (from top to bottom): an avalanche; an active region; an upper and lower sheared layer; and a passive region. The active region is further sub-divided into the zone in which the velocity is relatively consistent across the layer, and a lower region in which the velocity reduces rapidly, as identified by Chou and Hsiau [2012] and Yamane et al. [1998]. The avalanches themselves are often fronted by a "splash" at the moment when the avalanche meets the downhill side of the drum wall. A splash is defined particularly diffuse region of energetically ejected granular material, named for its visual similarity to the spray from an ocean wave.

Note that while Komatsu et al. [2001] demonstrate that the passive layer, usually considered to be static relative to the active region, does flow at extremely low velocities, it is assumed for the purposes of this work that the static approximation holds [Orpe and Khakhar, 2001]. This will simplify considerations of interactions between the active region and the passively rotating layer, as well as being a closer analogue for natural flows with a static bed layer. In addition, this study assumes that the material bulk density doesn't change considerably when flowing. This approximation is valid at the rotational velocities employed in this study [Yamane et al., 1998].

A visual summary of the observations of the ash is presented in Figure 5.1.1. The full notes are given in Appendix A.

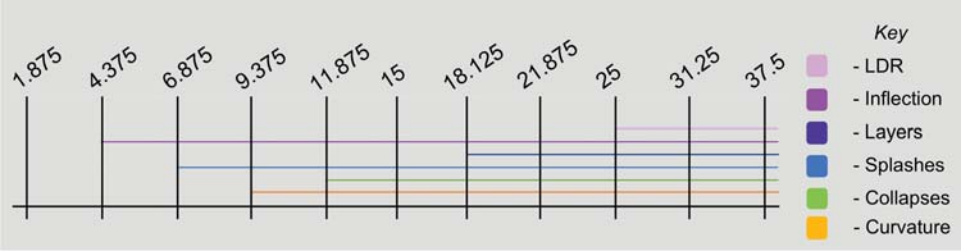

Figure 5.1.1: A summary of the observations by velocity for the ash. Coloured horizontal lines indicate at which experimentally investigated velocities various phenomena are observed in a specific material, on which more details are given in the main text. The phenomena observed are as follows: low-density regions, or LDRs, (pink) are the zones of reduced density seen as a material in the cascading regime nears the cataracting; inflection points (purple) are sharp bends in the free surface; layers (dark blue) refers to the point at which multiple layers beyond two are observed; splashes (light blue) are the ejection of particulates, either individually or as groups, due to an avalanche reaching the drum wall at the downhill end; collapses (green) are the events which give rise to an avalanche.

5.2 Flow Description as a Function of Drum Rotational Velocity

At the lower velocities (around single-digit RPM), two layers are present; a very thin (on the order of 1 cm at the midpoint) active region on top of a passively rotating layer (the passive region), which contains the bulk of the material (approximately 65% or greater,

depending on rotational velocity). As the velocity increases, the free surface begins to curve, and the layer structure becomes more complex. From the upper most part of the granular material downward, we label the layers the free surface, the avalanche, the fast flowing region, the sheared regions (separated from each other by the primary interface, and from the other layers by the secondary interfaces), and finally the passive region.

The active region/passive region interface, *i.e.*, the primary interface, is defined in this study as the point at which the velocity of the granular material goes to zero. This same definition was used by Yamane et al. [1998].

Figure 5.2.1 shows the generalised regions identifiable in the bed as the drum rotates. The magnitude and nature of these change as a function of drum speed. The largest region is the passive region which rotates as a solid body. Figure 5.2.2 shows that as drum speed increases, the relative size of this region decreases. Above the passive region is the active region which flows down hill. Figure 5.2.2 shows that it increases in size as drum speed increases. Within the active region, distinction is made between the parts of the bed which are shearing, *i.e.*, clearly showing a velocity gradient. The top-most active layer is not shearing but is fast flowing, moving at a bulk, relatively uniform, velocity. Both the thickness and the velocity of this layer increase with drum speed. Also changing is the shape of the free surface, which, with only minor curvature at lower rotational velocities, but develops greater curvature and a distinct transition point that defines the boundary between the cascading and rolling regimes of Mellmann [2001].

The free surface is the uppermost part of the flow, where the particulates are exposed. This free surface starts flat at lower rotational velocities, but begins to curve when the rotational velocity increases (see Figure 5.2.2). The fast flowing region, when studied in PIV vector map images, is the region of the flow that moves at the fastest downhill velocity, and has a relatively constant velocity from top to bottom. This region is the very uppermost part of the active region.

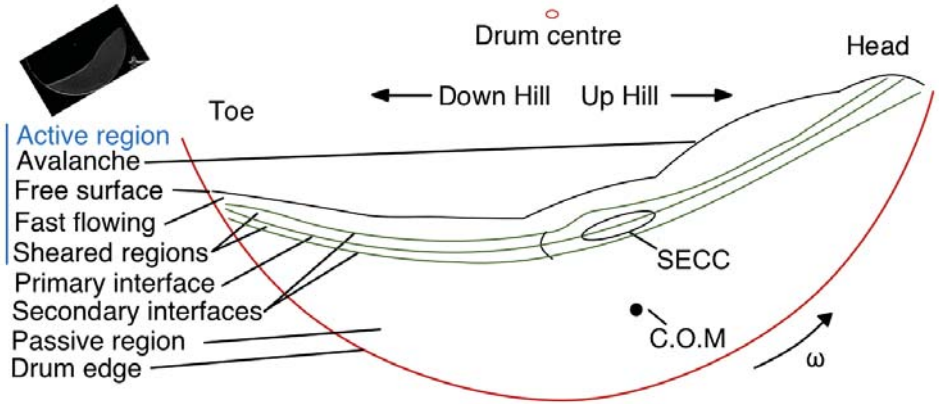

Figure 5.2.1: The designations given to the various layers and other features within the flowing granular material in a rotating drum in this study. The SECC, (self-enclosed circulation cell) is a new phenomena and is discussed in more detail in the next chapter (Section 6.3.1). Note that the angle of the material in this image is not representative of what would be observed in experiments. It has been rotated in a clockwise direction to help with clarity and reduce figure size. The inset (top left) shows an image from the footage used to construct this diagram orientated as it would be observed in reality.

A section of material travels as a discernible body (an avalanche) down hill, above the fast flowing section of the active region. This is the result of the head of the flow collapsing (more on this later - see Section 5.4.3). This body of material distends with distance travelled. If the collapse was energetic enough, it will produce a splash when it meets the downhill drum edge (see Figure 5.2.3 D2 for an example of a splash).

The sheared regions are proposed to be the zone in which erosion and deposition occurs. This study will refer to them as the sheared regions as their behaviour is produced by the shearing of the active region over the passive region. Particulates from the active region are either deposited into the passive region, or passive region particulates are entrained by the active layers.

For a geological flow, the rate of erosion will be dependent on the amount of overburden in the fast active region, its velocity, and the angle of the slope for a material with defined frictional properties and particle size distribution.

The passive region is the part of the granular material that is simply travelling in the rotational direction of the drum. Once this region reaches an unstable point, it falls

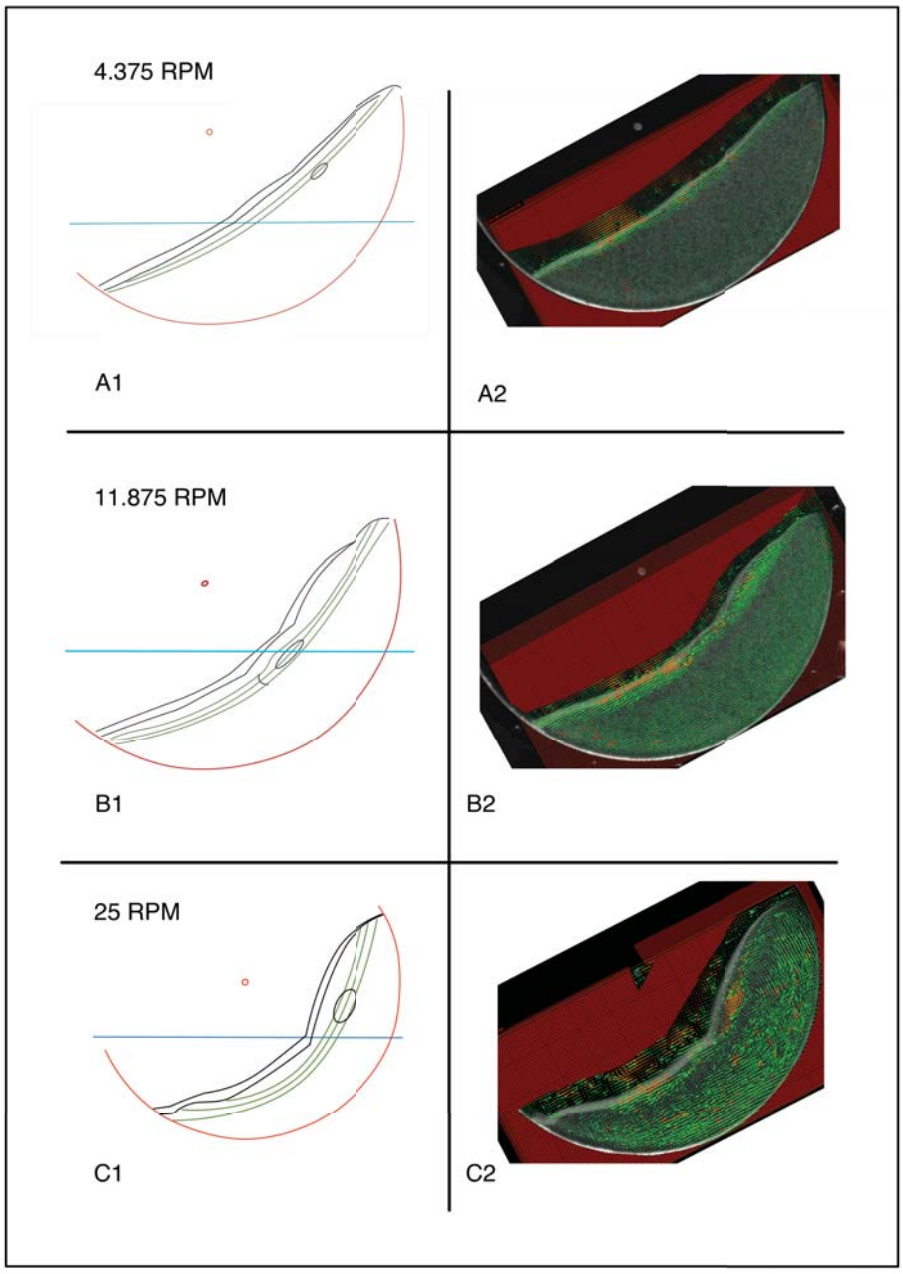

Figure 5.2.2: Layer structure diagrams (1) next to the PIV vector map (2) used to find the layers. Rotational velocity is (A) 4.375 RPM, (B) 11.875 RPM, and (C) 25 RPM. Material is the beach sand, and the fill factor is 0.25. Unusual cropping on the right hand images due to tilted camera. Each vector map was created by running PIV algorithms on two seconds of real-time footage recorded at 500 fps. In the layer diagrams, black represents the free surface (there are two layers here because the surface of the flow is partially visible) and is also used to mark SECCs (self-enclosed circulation cells), green represents the layer interfaces, red shows the centre of the drum and the drum edge. The upper green line shows the change in velocity magnitude between the two zones in the active layer. The middle green line was drawn along the normal to the velocity vector, denoting the transition into the passive region. The lower green line marks the extent of the passive region. This line is not on A1 as it is not distinguishable in A2. In the vector maps, the red zones mark areas not included in the PIV analysis. In general, as the rotational velocity increases, the thickness of the active layer increases, as does the complexity of the layers, and the curvature of the free surface. Note that the author currently has no explanation for the feature to the left of the the SECC in B1.

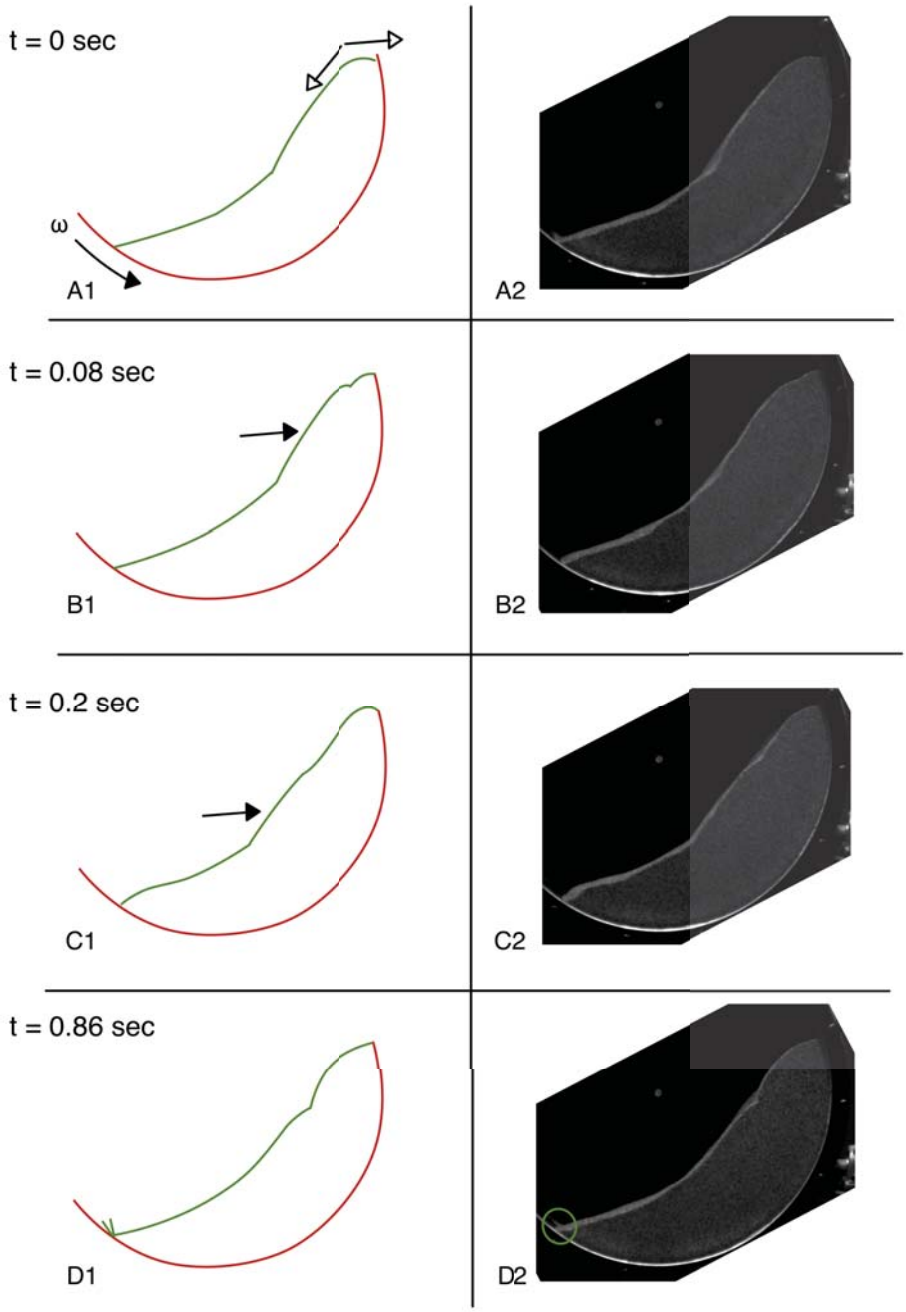

Figure 5.2.3: In this figure the key stages in the life time of an avalanche are shown. Each image pair is the same point in time, with the left hand images showing the shape of the free surface and the right hand images showing the original frame from the high speed footage. Images obtained during a rotational velocity of 15 RPM. Material is the beach sand, and the fill factor is 0.25. Unusual cropping on the right hand images due to the experiment being filmed with the camera tilted. A - [0 seconds] Collapse; the head of the flow collapses on itself, with both the left and right hand side of the peak falling downward (*i.e.*, the right or drumward side is moving counter to the motion of the drum). B - [0.08 seconds] Shear; the avalanche forms from this collapse and causes the head of the flow to feature two peaks for a time. C - [0.2 seconds] Dissipation; the avalanche starts to move downhill, concurrent with its thickness reducing. D - [0.86 seconds] Splash; the avalanche meets the wall of the drum and causes the ballistic ejection of particulates from the bulk mass. Note how at the head of the flow a another avalanche has already formed and is starting its transition downhill.

away from the drum wall and forms the active region layers. The fraction of the material in the passive region depends on the rotational velocity of the drum. The faster the drum is rotating, the lower the fraction of the material in the passive region (see Figure 5.2.4). The fraction in the passive layer changes at a different rate to that in the active region.

5.2.1 Active Region Fraction

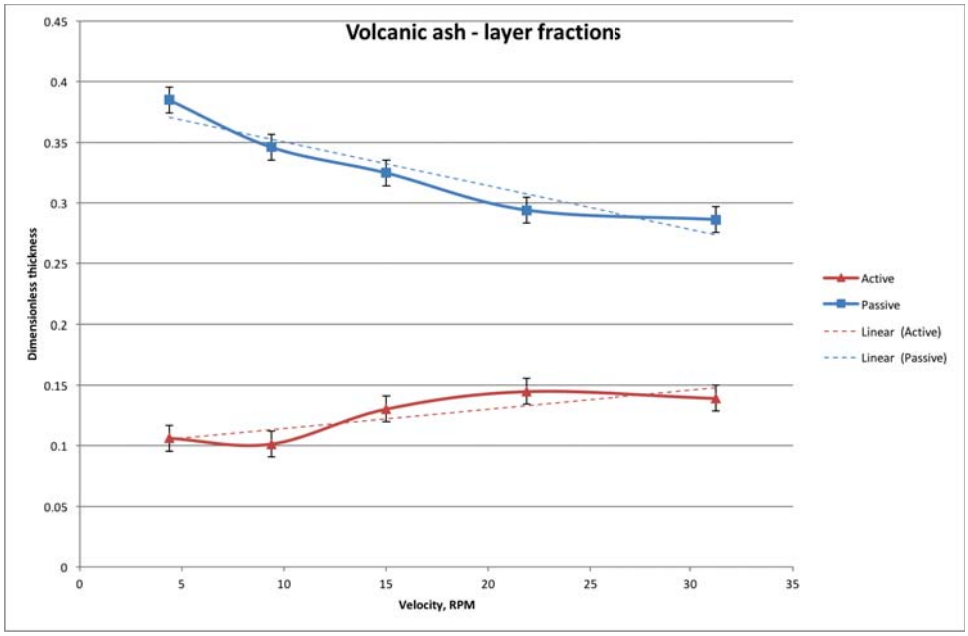

Figure 5.2.4: The dimensionless thicknesses, or layer fractions, for the volcanic ash with a fill factor of 0.25 in all cases. The fraction is found by the average thickness of the layer in question divided by the radius of the drum. Layer thicknesses are calculated from five evenly spaced radii using the methodology given in Section 4.3. The green data are the active region, and the purple are the passive region. Dashed lines are linear best-fit, and intended to draw the eye to the general relationship between the variables rather than conclusively suggest a specific type of mathematical relationship. Vertical error bars are one standard deviation. Horizontal error bars are smaller than the point (see Table 3.5).

The active region fraction is the fraction of the material actively flowing, as opposed to passively rotating with the drum. This was measured by using the MATLAB code created by Dr. Luke Fullard.

While what is observed is what one would expect, *i.e.*, that a greater fraction of the

material is in the active regions the faster the drum is rotated, it is worth noting that the rate at which the passive layer and active layer fractions change are different.

5.2.2 Velocity Profiles

Velocity profiles were obtained for the ash. The PIV data for 1000 frames (two seconds of real-time footage) were interrogated in two-frame pairs along the radial line that passes through the drum centre and the centre of mass for the material at the velocity in question. Presented below (Fig 5.2.5) are the results from these measurements.

The centre of mass line was chosen as it represents a common point across all the materials that has some basis in the properties of the material itself, rather than being an arbitrary point.

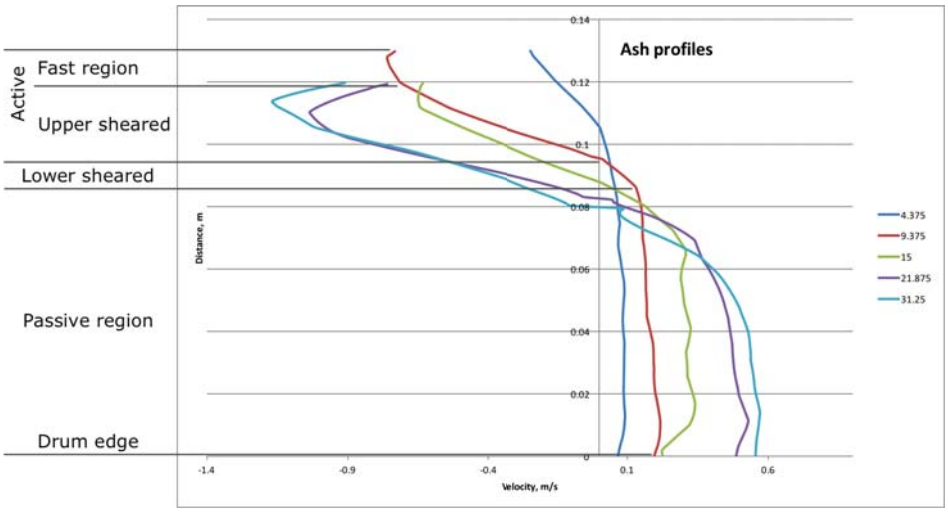

Figure 5.2.5: Velocity profiles for the ash, along the radial line that passes through the material's centre of mass. Velocity profiles are for consecutive pairs of frames for an arbitrary 1000 frame sequence for a range of drum speeds. Distance measures width of the material from the edge of the drum. The drum is rotating counter-clock wise. Legend gives the rotational velocities in RPM.

The layers in a rotating drum (Fig. 5.2.1) are demonstrated in the ash velocity profiles. Looking at the 15 RPM case in Figure 5.2.5 (the green line), the very top of the line (from 0.12 m down to 0.11 m) is the fast flowing region, which is mostly unaffected

by the shear between the active and passive regions. Below that, while in the negative (downhill) velocity region, we have the sheared part of the active region. Below that is the sheared part of the passive region. In the 15 RPM (green) case, the bulk passive region occurs at about 0.065 metres, at which point the material is simply moving with the rotation of the drum. In the 15 RPM case some slippage at the drum wall is visible. However, in the other velocities presented in Figure 5.2.5 do not display slippage - this validates the assumption that slippage is minimal in the experimental system used in this study (previously discussed in Section 3.2.1).

5.2.3 Avalanche Velocity Profiles

To investigate the effects of an avalanche on the internal structure of the material, avalanches were identified in the footage, and their starting frame number was noted. All avalanches across all rotational velocities were measured for a total of 80 frames (0.16 seconds), as this represented a common value that would cover the entire life span of the passing avalanche event across all rotational velocities.

The velocity profiles in this case were determined for PIV data obtained across two frames, to obtain as close as possible to an instantaneous velocity. As before, the velocity profiles were obtained from the radial line that passes through the material's centre of mass for that rotational velocity.

The velocities presented for the passing avalanche data are 9.375 RPM, 15 RPM, and 21.375 RPM. Results are shown in Figures 5.2.6, 5.2.7, and 5.2.8.

Note that the velocity profiles here do not strictly address the question of erosion and deposition within a rotating drum. However, they do address the movement of mass in a granular flow during an avalanche, and this should be of interest to both rotating drum and natural granular flow researchers. They are given here as they present novel insight into the internal mechanics of a granular flow over short time scales not previously extant (to the author's knowledge) in the literature.

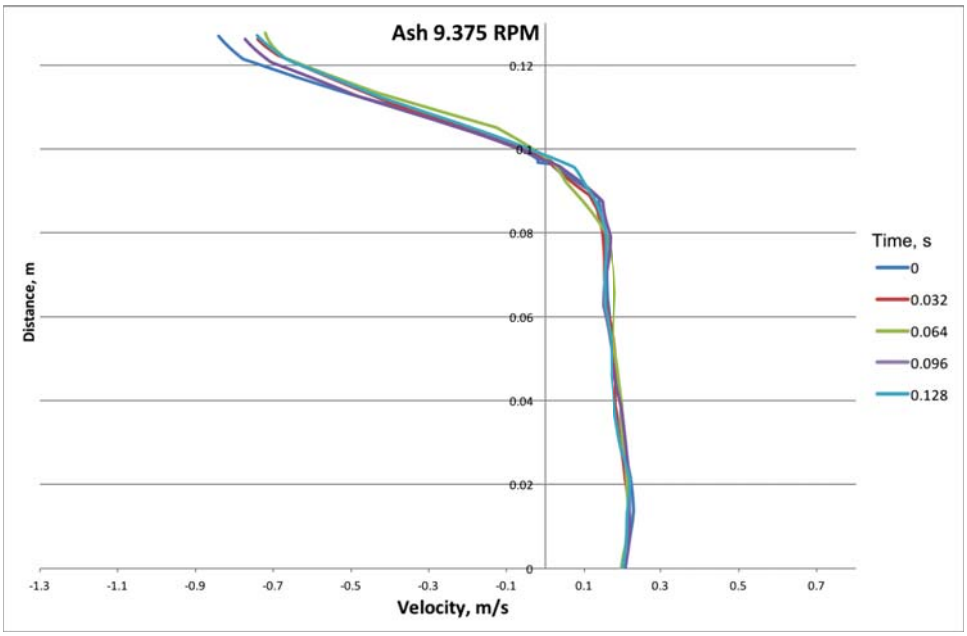

Figure 5.2.6: Instantaneous velocity profiles for a passing avalanche. across the centre of mass line for the ash at 9.375 RPM. Legend gives time in seconds at which the profiles were taken. Time zero is the point at which the body of the avalanche meets the centre of mass line.

5.2.4 Area of Passive and Active Regions

The areas of the active and passive regions were also found as a complementary measurement to the active region fraction depth measurements presented above. The areas were found by using the automated PIV analysis code. The profile lines were spaced 5° apart. Where the profile lines met the free surface, the passive/active interface, and the drum wall created a series of trapezoidal regions whose areas are relatively simple to find (see Section 4.3.1). The areas were non-dimensionalised by the total area of the drum. For such a small angle between profile lines, simple trigonometry shows the difference in area between the assumed trapezoids and the curved-edged reality is less than half a percent. The sum of these areas by region type across various constant rotational velocities are presented in Figure 5.2.9.

As the drum is a constant depth (0.15 m), the areas of the regions can also be treated as representative of the volumes of the respective regions.

As may be expected, the passive region gets smaller with increasing rotational velocity,

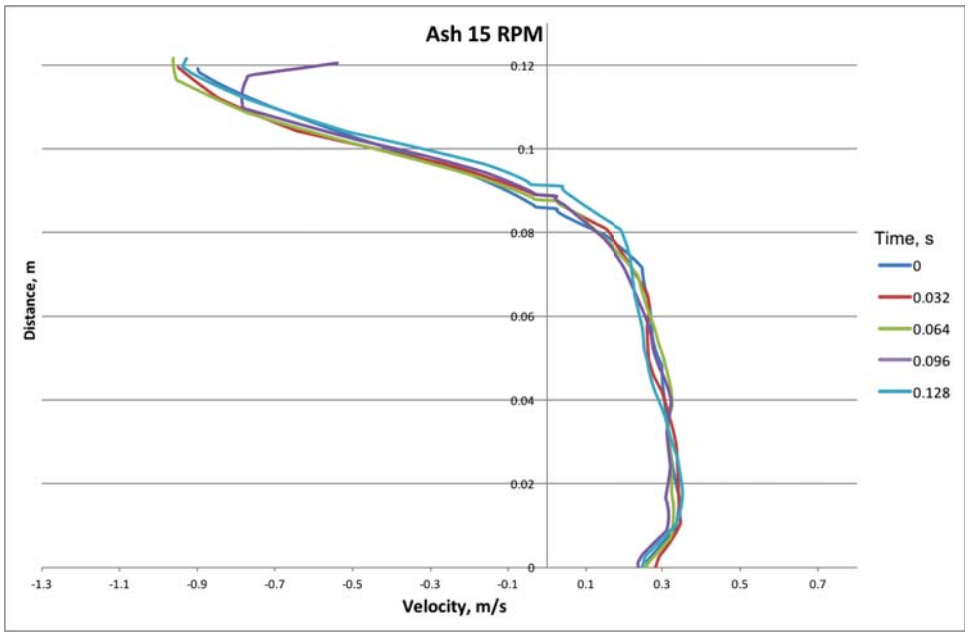

Figure 5.2.7: Instantaneous velocity profiles for a passing avalanche across the centre of mass line for the ash at 15 RPM. Legend gives time in seconds at which the profiles were taken. Time zero is the point at which the body of the avalanche meets the centre of mass line.

and *vice versa* for the active. The total areas is relatively constant, as one may expect. However, there is some variation in the total. This is explored more later; see Section 7.3.4.

5.2.5 Collapse Events

The flows shown in Figure 5.2.2 are not steady. Instead they consist of a series of events where the head of the flow collapses downslope, which is observable as a descending body of material. The way the head "collapses" is sketched in Figure 5.2.10. A more robust term for the collapses may be, in fact, "a head collapse event", but for the sake of brevity the term "collapse" will be used in the rest of this thesis. The period between these collapses shows a negative correlation with rotational velocity (Fig. 5.2.11). However, the correlation is not linear; the periodicity appears to have reached a minimum by approximately 12 RPM. The collapses themselves are often fronted by a splash - a diffuse region of the granular material, named for its visual similarity to the foam on an ocean wave. As such, for this study, the nomenclature has been adjusted and expanded

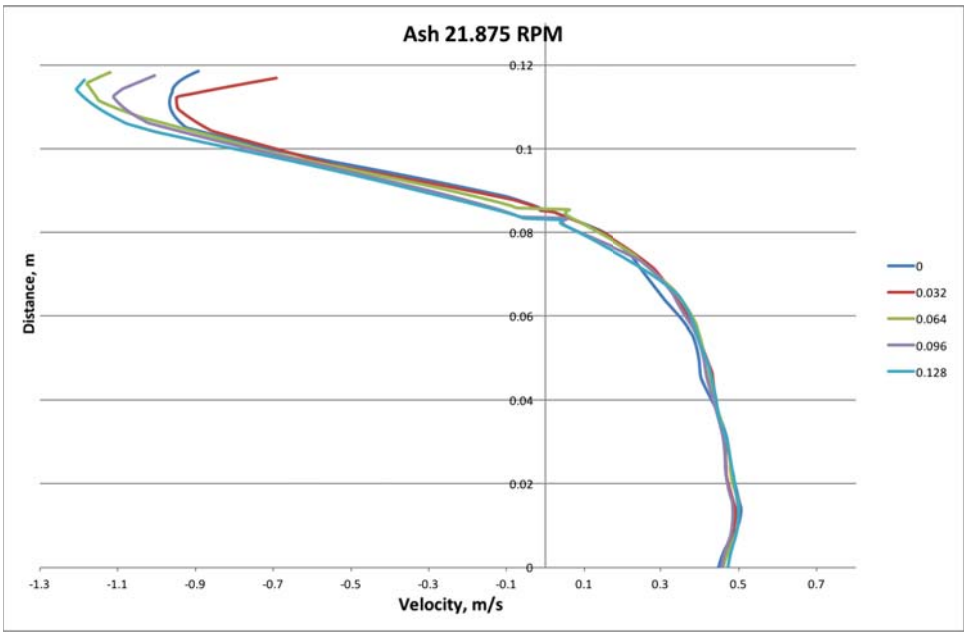

Figure 5.2.8: Instantaneous velocity profiles for a passing avalanche across the centre of mass line for the ash at 21.875 RPM. Legend gives time in seconds at which the profiles were taken. Time zero is the point at which the body of the avalanche meets the centre of mass line.

to reflect this complexity (see Appendix C).

5.2.6 The Dynamic Angle of Friction

The dynamic angle of friction is one of the data outputs of the MATLAB code. This angle is the displacement from vertical of the centre of mass of the material in the drum while the drum is turning (Fig. 5.2.12). The code finds this angle by looking for the point at which the area of the material as measured by the PIV is divided by two. Note that this makes no assumptions about the dilation of the active region as this increase in area will be automatically taken into account.

The dynamic angle of friction for the ash is presented in Figure 5.2.13.

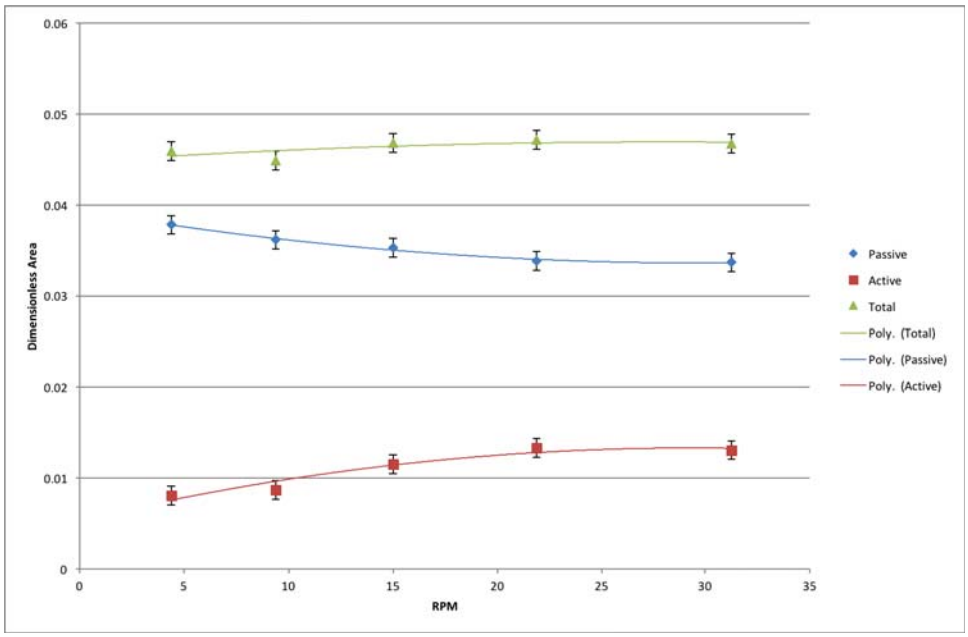

Figure 5.2.9: The area of the active and passive region of the ash at various velocities (x axis). On the y axis is the dimensionless area of the passive region (blue diamonds), the active (red squares), and the total of the two regions (green triangles). Areas are non-dimensionalised by the sum of the two areas. The lines are polynomial best fit. Error in the vertical axis is the standard deviation. Error in horizontal axis is smaller than the point (see Table 3.5).

5.3 Measurements of a Passing Avalanche

For three velocities (9.375 RPM, 15 RPM, and 21.875 RPM), particularly distinct avalanches were visually identified in the footage. The frame number at which the avalanche reached the average centre of mass line was noted, and PIV analysis was run on five groups of two frames, for a total duration of 80 frames, or 0.16 seconds. Velocity profiles were constructed for each of these two-frame groups across all three velocities, and are presented in Figure 5.3.1. Velocities presented in the figure were chosen as representative of the entire range of velocities tested, without overcrowding the image.

5.4 Discussion

Here are discussed the implications of the findings presented in this chapter.

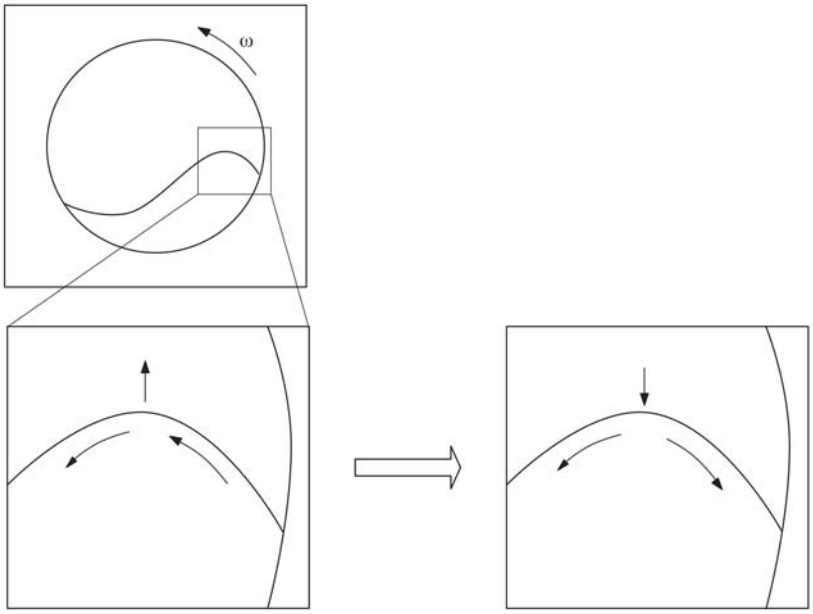

Figure 5.2.10: Illustrates what this study considers to be a collapse event. Initially, the head of the flow moves upward with time, with its side closest to the drum moving with the rotation of the equipment. Eventually, unable to support itself, the head collapses, resulting in a downward motion of the top of the head, and a counter-rotational movement of the material closest to the drum wall.

5.4.1 Active Region Fraction

The active region fraction appears to change differently to the passive region fraction, *i.e.*, it is gaining thickness as velocity increases at a different rate to the way the passive region is losing thickness - see Figure 5.2.9. This may be related to the curvature of the free surface, *i.e.*, the material is unable to cope mechanically with the increased velocity, and begins to dilate around the edge of the drum.

Both the active and passive layers rate of change also drops with increasing RPM, lending credence to the idea presented above that the material is unable to cope via flow in the active layer with further increases of the rotational velocity of the drum.

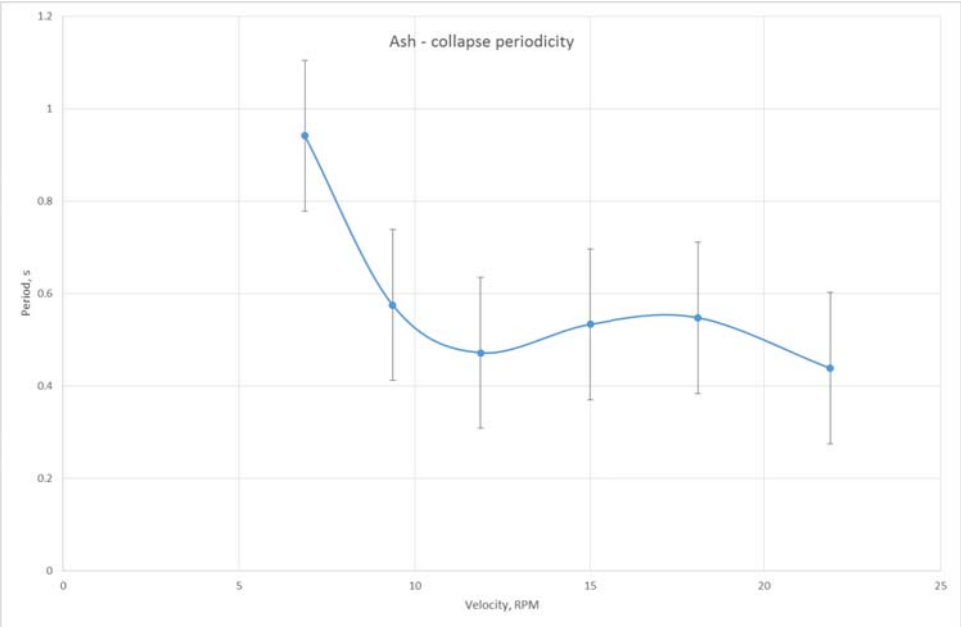

Figure 5.2.11: This is the collapse periodicity versus motor RPM. At around the 12 RPM mark the periodicity levels off (within the error bars), after which the frequency of collapse on set no longer changes significantly. Error bars for vertical data (period) represent the standard deviation. Error for the rotational velocity is smaller than the point. For each velocity, four seconds of footage was observed to find the number of collapses. Note that while some velocities do display collapse behaviour, it was not always measurable, so data presented here may not match presented velocity ranges for collapses presented elsewhere in the thesis. (For example, Figure 5.1.1 and Appendix A.)

Active Region Dilation

The most striking aspect of the flowing region dilation measurements is the fact that the dilation does not reach the maximum value at the corresponding maximum rotational velocity. If the extent of dilation is considered as a compensation mechanism for the increased rotational velocity, one must also take into account the fact that the flow regime within the drum changes within rotational velocity, too. It seems reasonable, then, to surmise that the dilation increases with rotational velocity, until the flow regime changes, in this case presumably from rolling to cascading, at which point the change in the shape that the flowing material (*i.e.*, free surface curvature) also plays its part in the way the mass is transported within the drum.

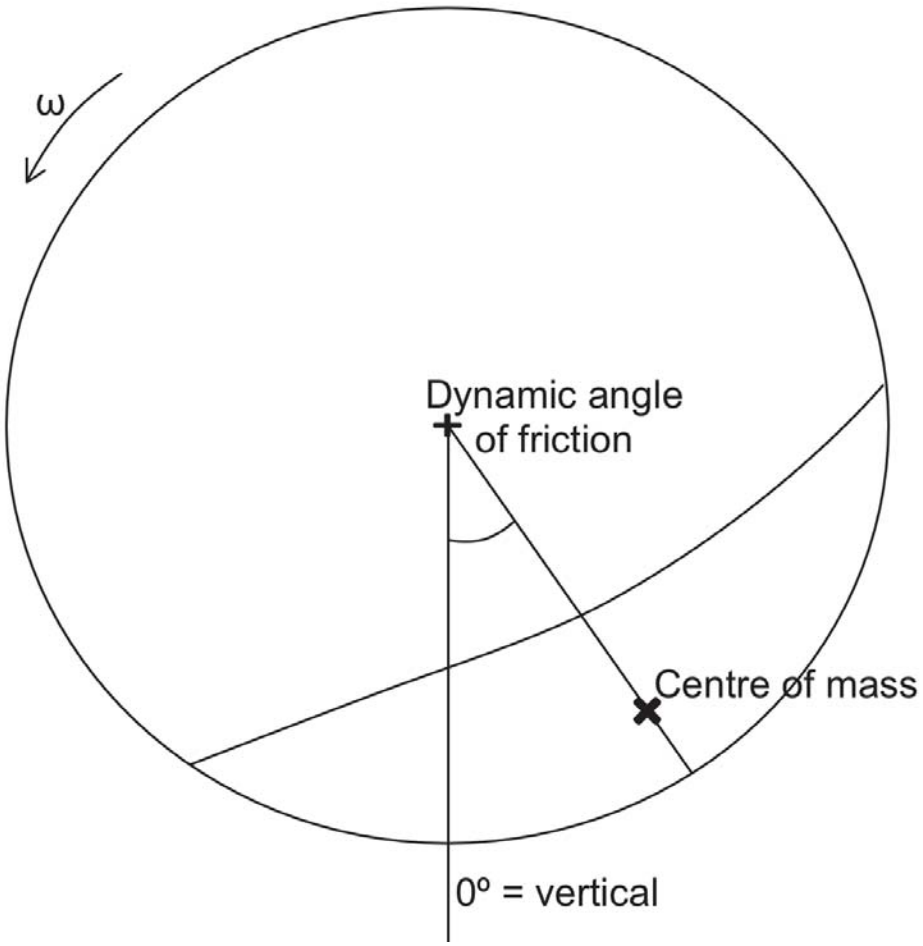

Figure 5.2.12: An illustration of the dynamic angle of friction. It is measured from vertical to the line which passes through the centre of the drum and the centre of mass of the material, while the drum is rotating. The downward vertical direction is where a evenly packed material would have its centre of mass, assuming the drum is stationary. The dynamic angle of friction, then, is a measure of the displacement of the material's centre of mass due to the rotation of the drum.

5.4.2 Dynamic Angles of Friction

The general trend for the static velocity cases is an increase in the displacement, as may be expected. The relationship is not strictly linear, however, featuring a peak and a trough at the 9.375 and 15 RPM. Further illumination into why this occurs may be found when the beach sand material is also tested under similar conditions; it is possibly related to Mellmann regime changes.

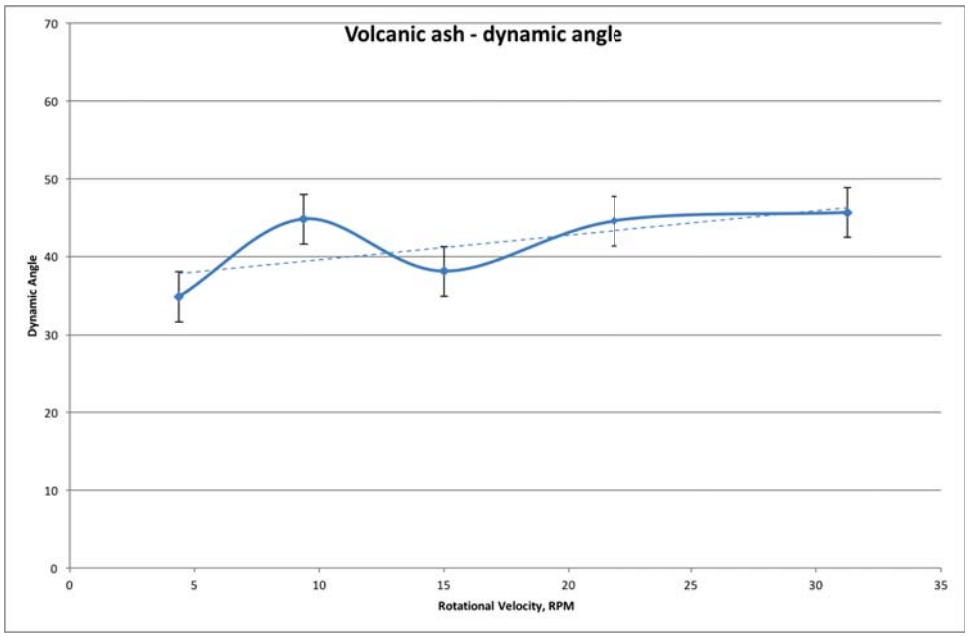

Figure 5.2.13: The dynamic angle of friction for the ash as a function of rotational velocity. Dashed line is the linear best-fit. Vertical error bars represent the standard deviation. Horizontal error is smaller than the point.

5.4.3 Collapse Periodicity

Attempts were made to measure the periodicity of collapse for higher velocities, but these are not easily discernible by eye. It is possible that there is an automated solution using PIV software, but this has not been explored due to time constraints. However, Tegzes et al. [2003] define the transition from the rolling to cascading regime as when the avalanching becomes continuous; *i.e.*, when the period between avalanches becomes a minimum/zero. The periodicity inflection point (Fig. 5.2.11) seems to be related to the transition of the Mellmann flowing regime from rolling to cascading, but not conclusively. It is suggested that this is again related to a mechanical limit of granular material to transfer its own mass. While in the rolling regime, increasing the rotational velocity and hence the rate of mass transfer simply results in more frequent avalanching. The transition to the cascading regime happens when this maximum mass transfer rate is reached; now that the avalanching cannot occur any more frequently, the material has to compensate for the increased rotational velocity in other ways, such as by curvature of the free surface, *i.e.*, by dilating the material around the drum edge.

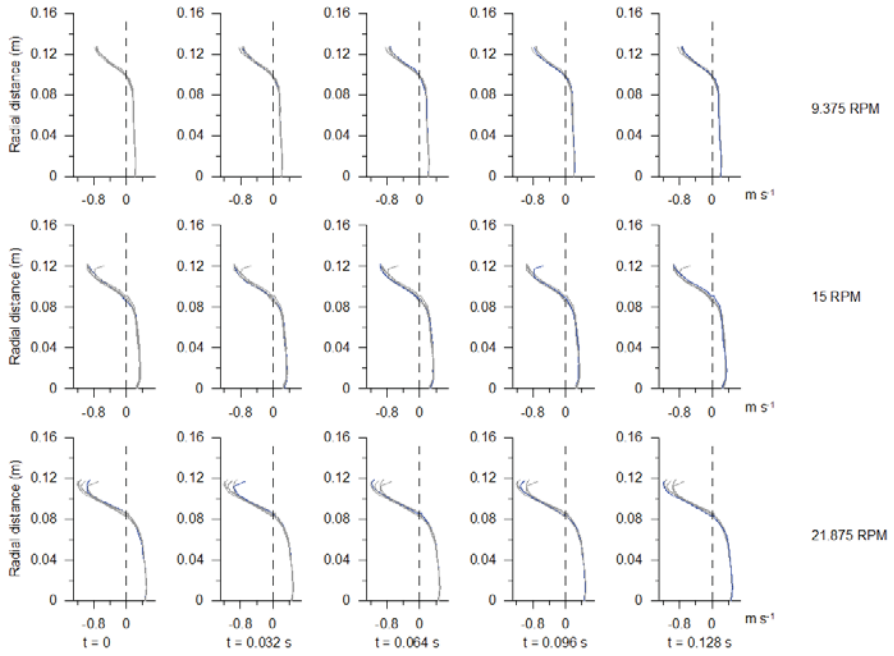

Figure 5.3.1: Velocity profiles through the centre of mass line as an avalanches passes, for a variety of velocities (rows). Time is from left to right. The profiles show the passive region (positive velocity) and active region (negative velocities). All profiles are shown on each graph. The profile for the time in question is highlighted in blue.

5.4.4 The Effect of a Passing Avalanche

A passing avalanche manifests as an increase in velocity of the active region (Fig. 5.3.1). Additionally, the faster velocities are more prone to a curved profile at the free surface end of the profile.

Overall, passing avalanches seem to have a greater effect on the active region, and very little on the passive layer; for example, see Figure 5.2.8. While the profiles at the active end of the flow (left-hand side of the figure) show wide differences in velocity (from a high of 1.2 m s^{-1} to a low of 0.9 m s^{-1}), the passive (right-hand) region's profiles are almost super-imposed.

This has interesting implications for the effects of an avalanche in a natural granular flow. In a lahar event scenario, for example, the collapse of a sabo dam, should the observation above bear true, would have great implications for the amount of material

being transported in a lahar, but not much effect on the erosional capability of the flow. This means that an avalanche in a lahar scenario is of concern for buildings and other structures, as they are likely to be impacted by greater amounts of material, but not much effect on the channel the lahar is flowing in.

5.4.5 The Mechanical Limit and the Dynamic Angle

While the surface curvature and collapse periodicity seems to indicate a mechanical limit to the rate at which a granular material can transfer mass, the dynamic angle (the deflection of the centre of mass) has a linear dependency on the rotational velocity. While this may seem counter-intuitive, if the centre of mass of the material is taken as simply an indication of the velocity of the drum itself, *i.e.*, the material is in whichever flow regime it happens to be in given the rotational velocity of the drum, but the frame of reference for this flow regime changes. The mechanical process of the flow within the drum is separate from the centre of mass deflection.

Chapter 6

Results II - Dry Materials under Variable Velocities, and New Phenomena

6.1 Introduction

This chapter covers the results discovered from the acceleration experiments (as described in Section 3.1). The material used here was the volcanic ash. A variety of acceleration regimes were investigated, and the fluid phase was air. By changing the rotational velocity of the drum with respect to time, we move to a case which more closely simulates the situation found in natural granular flows as changes in topography force a change in velocity.

Also presented here are what are suspected by the author to be newly discovered granular flow phenomena. The new phenomena were (in most cases) observed in all the materials used in this study. The new phenomena are described in this chapter, and their differences in behaviour and appearance are discussed in the next chapter.

6.2 Dynamic Equivalents

Dynamic equivalents were compared to the constant velocity cases by, firstly, assuming that the acceleration profiles were linear. (This was demonstrated earlier in the thesis; see Figures 3.4.3 and 3.4.4.) By dynamic equivalents the author means the points during the accelerating experiments in which the instantaneous rotational velocity is equal to the steady velocities chosen for the experiments presented in the previous chapter. As such, it is possible to create a linear relationship between frame number and an instantaneous rotational velocity. Groups of 20 frames were chosen, evenly distributed around the key frames found from the linear relationship between velocity and frame number. These were then analysed using the same methodology (PIV, MATLAB code, *etc.*) as the constant velocity cases. The results for this comparison between steady velocity and accelerating equivalents are presented in this chapter.

6.2.1 Layer Fractions

As for the constant velocity case, the layer fractions (depth of layer non-dimensionalised by radius of drum) were found for the three chosen acceleration regimes. The results are presented in Figure 6.2.1.

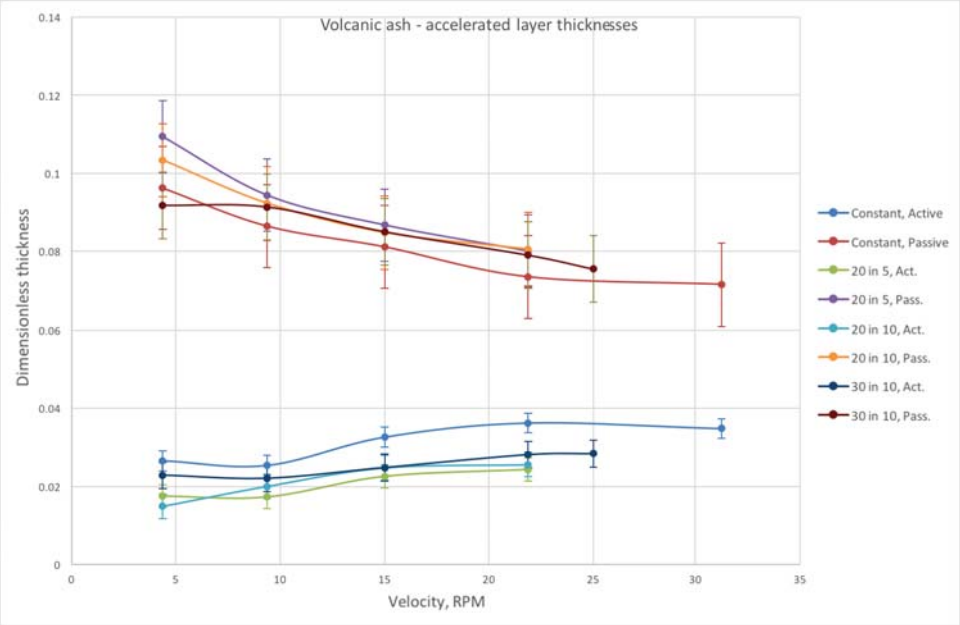

Figure 6.2.1: The layer fractions for the ash, in both constant velocity and accelerating equivalent cases. The acceleration profiles used were 30 RPM in 10 seconds (30 in 10), 20 RPM in 5 seconds (20 in 5), and 20 RPM in 10 seconds (20 in 10). Thicknesses were measured in the standard way, as given in Section 4.3. In the legend, Active (or Act.) refers to the active or flowing layer, while Passive (or Pass.) refers to the passively rotating layer. Layer thicknesses were non-dimensionalised by the radius of the drum. Vertical error bars are the standard deviation for the experiment in question; horizontal are smaller than the point. The accelerated experiments don't have the same extent in the x-axis due to the accelerated cases not replicating all the static velocity equivalents.

6.2.2 Dynamic Angle of Friction

The dynamic angle of friction was measured for the equivalent velocities in the accelerating experiments. Presented here (Fig. 6.2.2) are the results for the ash, in both constant velocity and accelerating cases.

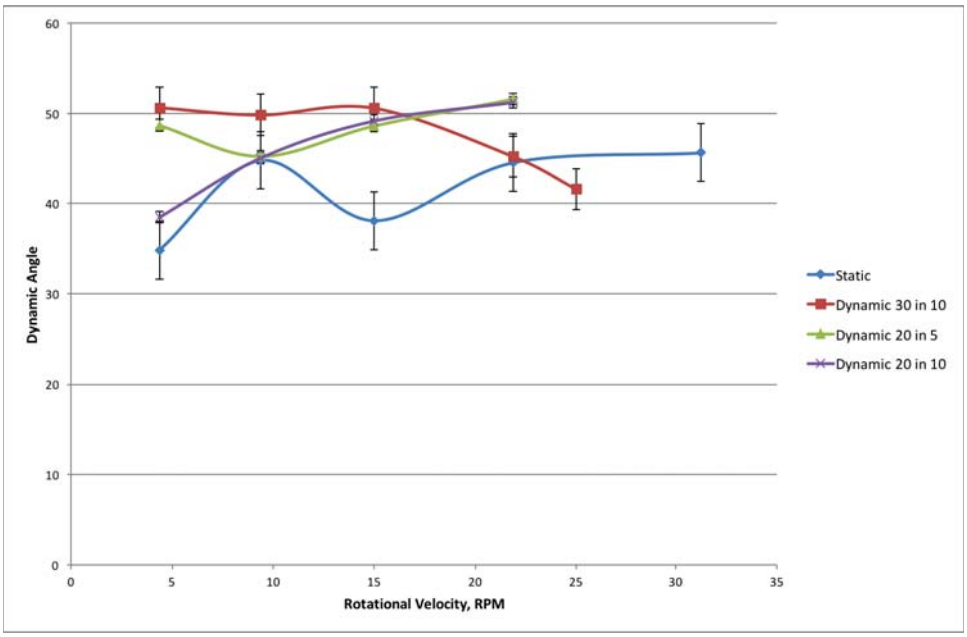

Figure 6.2.2: The dynamic angle of friction for the ash, across the constant velocity case (blue) and for the equivalent velocities achieved during three different accelerating cases; 30 RPM in 10 seconds (red), 20 RPM in 5 seconds (green), and 20 RPM in 10 seconds (purple).

6.3 New Phenomena

This section covers the other results found during this study, that were not explicitly looked for, but represented interesting findings on their own, and hence were considered worthy of reporting. These include the discovery of two potentially new phenomena in granular material flows - the self-enclosed circulation cell (SECC) and a potential Kelvin-Helmholtz instability (KHI).

Note that these phenomena were also observed in the constant velocity experiments, but only after they'd been spotted in a more energetic variations during the acceleration experiments. As such, and for ease of reading, their results are presented here, rather than in the previous chapter.

The self-enclosed circulation cells (SECCs) are the first of two of what are thought to be new phenomena reported in this thesis. They are small regions of what appear to be zones of material rapidly exchanged between the fast flowing and the passively rotating layers.

The SECCs appeared at 15 RPM and higher rotational velocities in experiments involving the sieved volcanic ash.

The second new phenomenon reported here are suspected Kelvin-Helmholtz instabilities (KHIs). These occur in the experiments in which the low-density regions (LDRs) are present (these are defined above, *e.g.* Fig. 5.1.1). Where the low-density region meets the fast flowing layer (i.e., the uppermost part of the active layer), there is an interface between two distinct density regimes. Additionally, these two parts of the flowing material are moving almost normal to each other, creating a situation similar to that which lead to Kelvin-Helmholtz instabilities in fluid dynamics, *i.e.*, fluids of different densities moving across each other, leading to an unstable interface. This normal interaction between the low-density region and the fast flowing layer can be seen in Part 1 of Figure 6.3.5, where the LDR is moving with gravity while the active region is moving downhill.

At first, the interface between the LDR and active layer is indistinct. With time, a clear boundary forms. This will grow upward, into the low-density zone. Eventually the boundary will go through a process visually similar to a bursting bubble, and the clear boundary between the zones will disappear. At this point, the process begins again. More detail on this process is given in this chapter's discussion section; see Section 6.3.2.

Note that a Kelvin-Helmholtz instability is not the only possible explanation for the observed phenomenon, but they will be referred to as such due to noted similarities in formation process. (Other possibilities are discussed later in the thesis; see Section 9.4.1). Validation of the KHI hypothesis presented here is left to future workers.

The ash displayed the KHIs at 37.5 RPM, which was the highest experimental rotational velocity.

The new phenomena are explored more thoroughly below.

6.3.1 Self-Enclosed Circulation Cells

Whilst running the experiments, it was observed that there were zones of enclosed circulation along the flowing/passive boundary (see Figures 6.3.1, 6.3.2, and 6.3.3). These zones were initially expected to be artefacts, an optical illusion rendered by the motion of the material. However, after running PIV analysis on the experiment footage, zones of circulation could be clearly seen in the vector map along the boundary, as were observed by eye (see, for example, inset in Figure 6.3.1). The footage analysed was two seconds long in real time, and comprised 1000 frames per film.

Self-enclosed circulation cells (SECCs) are usually elliptical in appearance. They are not static, but fluctuate around a mean position.

To verify the observation that the SECCs are regions in which material rapidly enters and leaves the flowing layer (*i.e.*, passes between the two main layers of passive and active material), PIV data was interrogated along the major axis of three suspected SECCs in the beach sand (11.875, 15, and 18.125 RPM). The major axis of these elliptical phenomena is the one which lies along the passive/active boundary, as mentioned above. As such, if material is entering and leaving this region, it is reasonable to expect that a vertical velocity profile drawn along the SECC's major axis would have a positive peak on the downhill side (*i.e.*, material is leaving the passive region and entering the active), a relatively flat region coinciding with the passive/active boundary, and then a negative peak on the uphill side (material going from the active to the passive). If, in the cases where there appears to be multiple SECCs, the areas are totalled, then the graph as presented in Figure 6.3.4 is obtained.

On average, an elliptical SECC measures around 1.75 cm in height (minor axis) and is approximately 4.3 cm in length (major axis). Their average area is 2.5×10^{-3} m^2. See Table 9.3, below. The figures were found using the same coarse beach sand as detailed earlier, with a fill factor of 0.25.

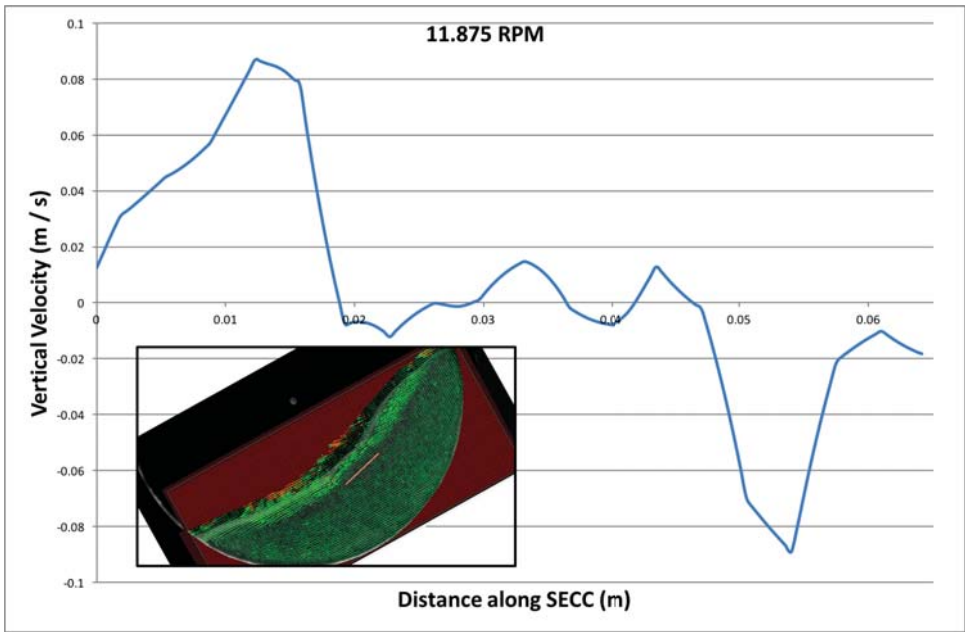

Figure 6.3.1: A velocity profile for the vertical component extracted from PIV data for a SECC observed in the beach sand static velocity experiments at 11.875 RPM. As can be seen the material leaves the active region on the downhill side of the SECC (left in this image), and re-enters on the uphill (right-hand) side. Inset shows PIV vector map for the respective data set - the orange line shows the location of where the velocity profile was taken. Note the slightly different x-axis compared with Figures 6.3.2 and 6.3.3.

6.3.2 Kelvin-Helmholtz Instabilities

This phenomenon was observed during the higher rotational velocity runs of the beach sand, volcanic ash, and pumice - it did not occur for the millet.

This phenomenon appears as a fluctuating interface between the dense passive region of rotating drum granular material flow, and the lower density curtain (low-density region or LDR) of material that occurs as the material starts to enter the cascading regime [Mellmann, 2001]. This interface fluctuates whilst maintaining an average position, then forms a peak at its centre, forming what may approximately be called a bell curve. This curve will eventually "burst" (a colloquialism that we use to describe the moment at which the clearly defined interface boundary rapidly disappears), at which point the interface becomes indistinct. The clearly defined fluctuating interface that was the starting point of this description then reforms, and the sequence begins again (Fig. 6.3.5).

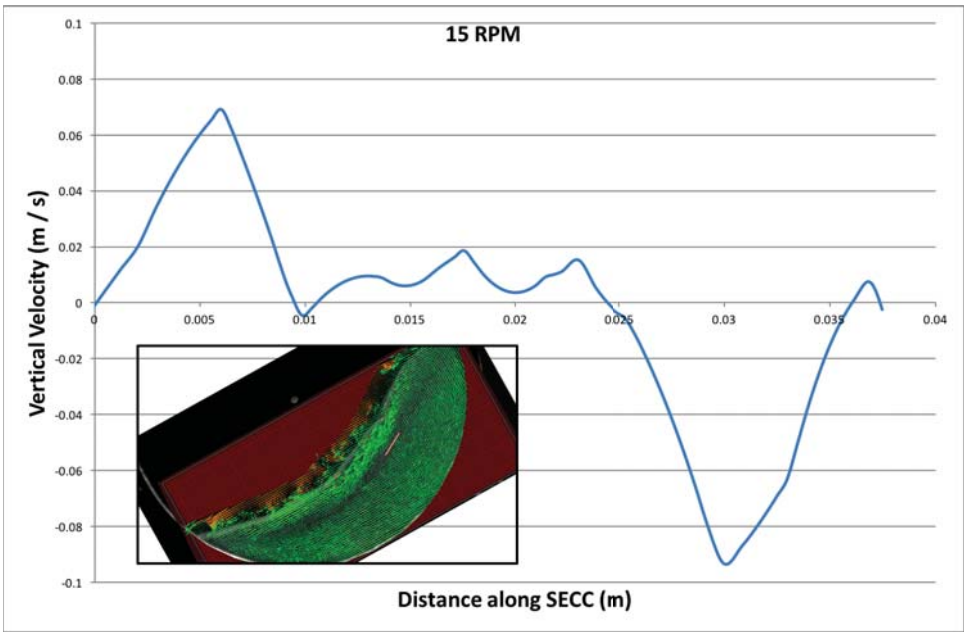

Figure 6.3.2: A velocity profile for the vertical component extracted from PIV data for a SECC observed in the beach sand static velocity experiments at 15 RPM. As can be seen the material leaves the active region on the downhill side of the SECC (left in this image), and re-enters on the uphill (right-hand) side. Inset shows PIV vector map for the respective data set - the orange line shows the location of where the velocity profile was taken.

Once the drum has reached a high enough velocity, then the LDR can form. This happens when the material enters a flow regime between that of the classical Mellmann regimes of cascading and cataracting. The passive region is moving uphill with such velocity that the resultant downhill material becomes less packed. Increasing the velocity still further leads to the observation of the KHI or "shockwave" events in the interface between the main body of material and the LDR. The frequency with which these events occur also increases with rotational velocity.

A cartoon demonstrating the main phases of the life time of an event is shown in Figure 6.3.5, with still images of the same key phases presented in Figure 6.3.6. The interface between the LDR and the bulk flowing material is initially very clearly observable by eye. However, the interface soon becomes indistinct, after which a growing intrusion from the bulk flowing material can be seen. The interface then collapses downwards and the process begins anew.

Measurements of the KHIs were taken from the high-speed footage, using the PIV data

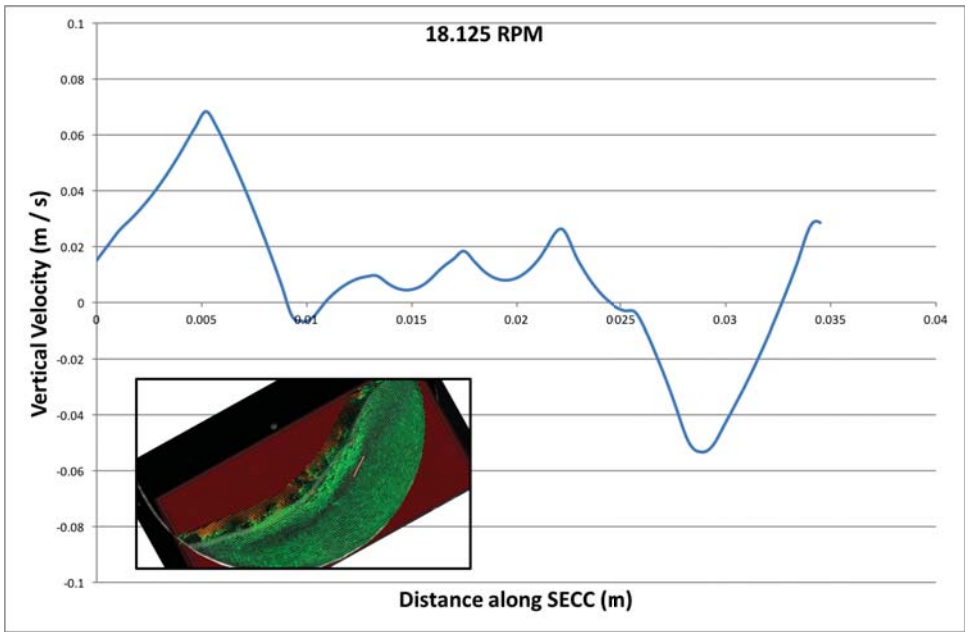

Figure 6.3.3: A velocity profile for the vertical component extracted from PIV data for a SECC observed in the beach sand static velocity experiments at 18.125 RPM. As can be seen the material leaves the active region on the downhill side of the SECC (left in this image), and re-enters on the uphill (right-hand) side. Inset shows PIV vector map for the respective data set - the orange line shows the location of where the velocity profile was taken.

to help obtain lengths, etc. The variables recorded were speed of propagation (the rate at which the intrusion propagates upwards, see Figure 6.3.5), the size ratio (*i.e.*, minor axis divided by the major axis) and the total area occupied at the KHI in question's greatest extent.

The results of these measurements are presented in Figures 6.3.7, 6.3.8, and 6.3.9. For each velocity, five instabilities were identified. Velocity was found by recording the frame numbers at which the instability formed and reached its maximum extent (which gave a time value), and by measuring the maximum height of the instability interface in pixels, then converting into metres. The area was found by treating the instability region at its greatest extent as an ellipse, and as such was calculated by πab, where a and b are the minor and major axes (*i.e.*, as if the KHI were an ellipse). Finally, the size ratio (or circularity) was found by dividing the minor axis by the major (*i.e.*, a/b).

Also measured for a similar range of rotational velocities was the frequency with which a KHI event occurred. This is displayed in Figure 6.3.10.

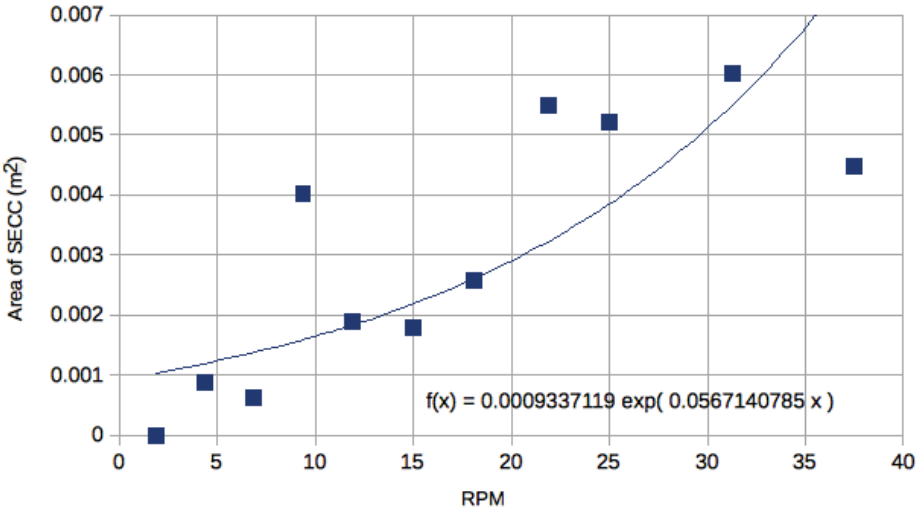

Figure 6.3.4: Plotting the rotational velocity versus the total area of all the SECCs found in the PIV vector map for that velocity. Errors are smaller than the point. Line of best fit is an exponential curve: raw equation is presented on the figure.

6.4 Discussion

6.4.1 Layer Thicknesses

The general trend displayed here is that the faster the acceleration, the greater the lag from the constant velocity case. By "lag" we refer to the way in which the layer thicknesses for the active and passive layers differs at the relevant instantaneous velocities in the accelerating cases when compared with the constant velocity cases. (Fig. 6.2.1.)

6.4.2 Dynamic Angle

It is clear that the accelerating cases have a greater displacement from vertical due to the additional forces acting on the granular material due to the acceleration of the system. In each case, however, the difference between the accelerating and static velocity cases diminishes with increasing velocity. (Fig. 6.2.2.)

The behaviour of the 30 RPM in 10 seconds case, however, is perplexing. While at the

Table 6.1: The attributes of the SECCs, as they appeared for the rotational velocities undertaken in this work. No data are presented for 1.875 RPM, as no cells appeared at this rotational velocity. Note that 15 and 18.125 RPM have multiple SECCs (two and three, respectively). Also note the increased circularity of these multiple cell velocities.

RPM	Minor (m)	Major (m)	Area (m^2)	Circularity
4.375	0.0105	0.0269	0.0009	0.3889
6.875	0.0085	0.0231	0.0006	0.3667
9.375	0.0114	0.1121	0.0040	0.1020
11.875	0.0122	0.0493	0.0019	0.2483
15.000	0.0194	0.0187	0.0011	0.9649
15.000	0.0146	0.0139	0.0006	0.9535
18.125	0.0162	0.0165	0.0008	0.9800
18.125	0.0159	0.0165	0.0008	0.9600
18.125	0.0169	0.0172	0.0009	0.9808
21.875	0.0225	0.0780	0.0055	0.2882
25.000	0.0293	0.0565	0.0052	0.5192
31.250	0.0282	0.0679	0.0060	0.4150
37.500	0.0223	0.0640	0.0045	0.3485
Mean	*0.0175*	*0.0431*	*0.0025*	*0.5781*

lower equivalent velocities the dynamic angle starts at a higher value, it stays relatively constant and drops.

The tendency of the accelerating cases to have higher dynamic angles resulted in interesting behaviour when water was added to the system - temporary centrifuging, which is explored in a later chapter.

6.4.3 SECC Behaviour

This chapter has also presented velocity profile graphs along what we propose to be the major axis of the elliptical phenomenon we refer to as self-enclosed circulation cells (SECCs). A SECC is a region in the flow, found along the active/passive boundary, that appears to be a small zone of material rapidly circulating in and out of the two layers. The purpose of the velocity profiles was to ascertain if this was a feasible explanation for the phenomenon, which could also be simply artefacts of visual observation. If the rapid exchange of material between layers hypothesis is correct, then the vertical component of the velocity along the major axis should present two opposed peaks,

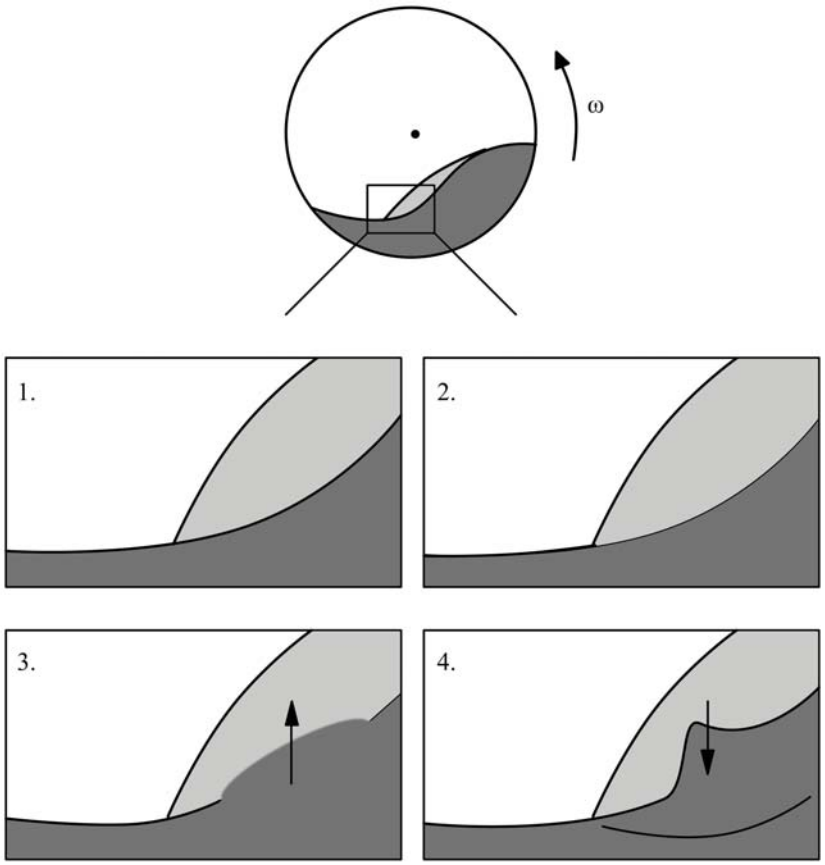

Figure 6.3.5: A cartoon demonstrating the life time of a single event. The events occur as a material flows in a manner that sits between the true cascading and cataracting regimes, as described in Mellmann [2001]. 1. There is a clear boundary between the bulk material and the falling low-density region. 2. The boundary weakens and becomes indistinct. 3. A growing intrusion can be observed. 4. The intrusion suddenly coalesces into a sharp boundary, which settles back down to the state seen in step 1. The process then repeats.

with an intervening flat region. Such a profile is seen in three different SECCs from three velocity cases.

While acting as some confirmation of the SECC hypothesis, the opposing peak velocity profiles (Figures 6.3.1 to 6.3.3) are not conclusive. Further study is needed, and represents a potentially rich area of research. This is particularly true of industrial applications were a high degree of mixing is required, as small zones of what could be called "trapped" material would present a potentially expensive problem.

As the rotational velocity is increased, the measured area of the SECCs also increases,

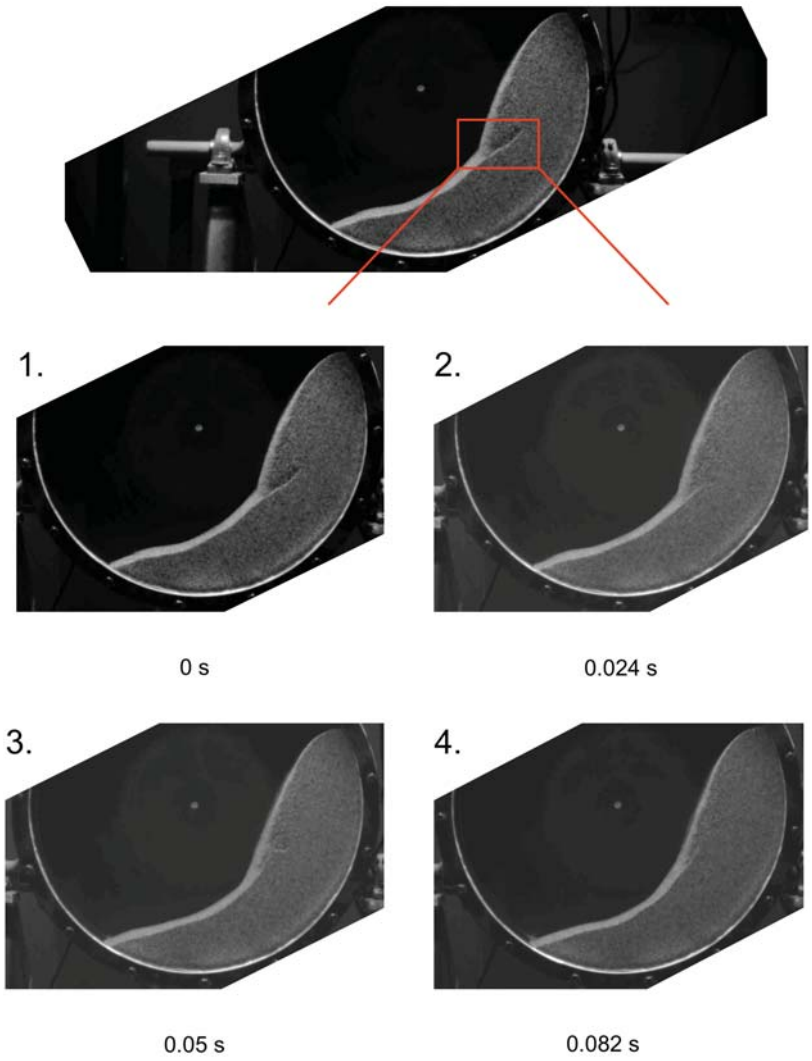

Figure 6.3.6: A KHI event in the beach sand experiments, with a rotational velocity of 31.25 RPM. The stages are the same as those presented in Figure 6.3.5, *i.e.*, boundary formation, boundary dilution, intrusion growth, resettlement. Number below each image is time in seconds.

with an exponential line of best fit. However, there is some scatter of the data points. If the SECCs turn out to be a real phenomena, then further study will be needed to clarify the relationship between area (and by extension, volume and mass) contained by a SECC and the rotational velocity of a drum. Another future avenue for research would be in varying the fill level, and observing quantitatively how this changes the area of the SECCs at a range of comparable velocities.

The mechanics and nature of these SECCs remains a mystery to the author. Initial findings are presented here stimulate discussion and further study of these cells among the community. As a transfer of mass between layers, are they the mechanism by which

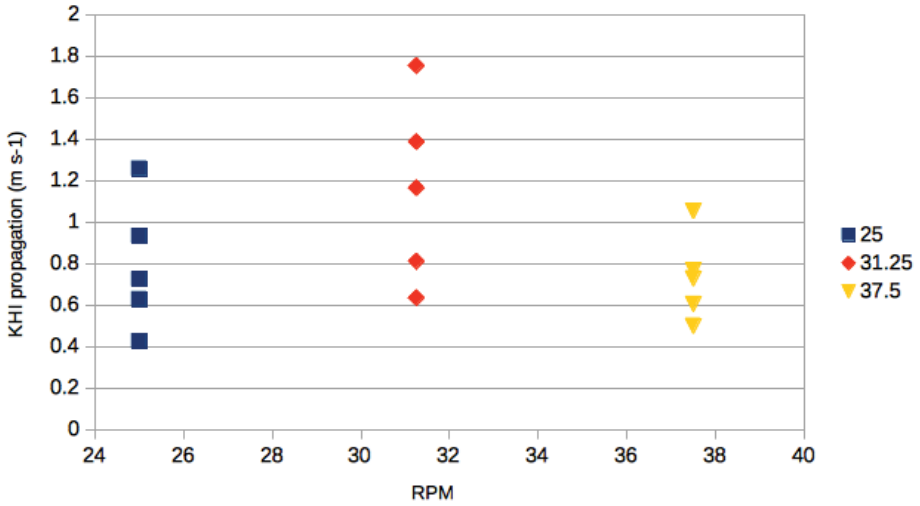

Figure 6.3.7: The findings for the upward propagation velocity of the KHI phenomenon in the beach sand at 25, 31.25 and 37.5 RPM. For each velocity, measurements were taken from five events.

Ding et al. [2001b]'s mass transfer rate E is enacted? It seems feasible. On the other hand, Mellmann et al. [2004] mention "vortices" which they define as regions in which no mass transfer takes place. (It is therefore possible that the SECCs have been observed before, but noted differently.)

6.4.4 KHI Behaviour

There is a recurring trend within the KHI behaviour in the beach sand, as presented in this chapter (Figs. 6.3.7 - 6.3.9). As the rotational velocity is increased from 25 to 31.25 RPM, the instabilities become larger and more energetic in their motions. However, when the velocity is increased to 37.5 RPM, the instabilities become slower and smaller in extent, though still over all larger than they were at 25 RPM. The exception to this is the size ratio (circularity) which drops even further (Fig. 6.3.9) due to the general decrease in vertical extent. It seems reasonable to assume that the higher velocity cases (37.5 RPM) are being dampened by the increased rate of material turn over.

Measurements of the area covered by the shockwave as it travels through the material is also presented in this chapter. The general trend is that the area increases and then

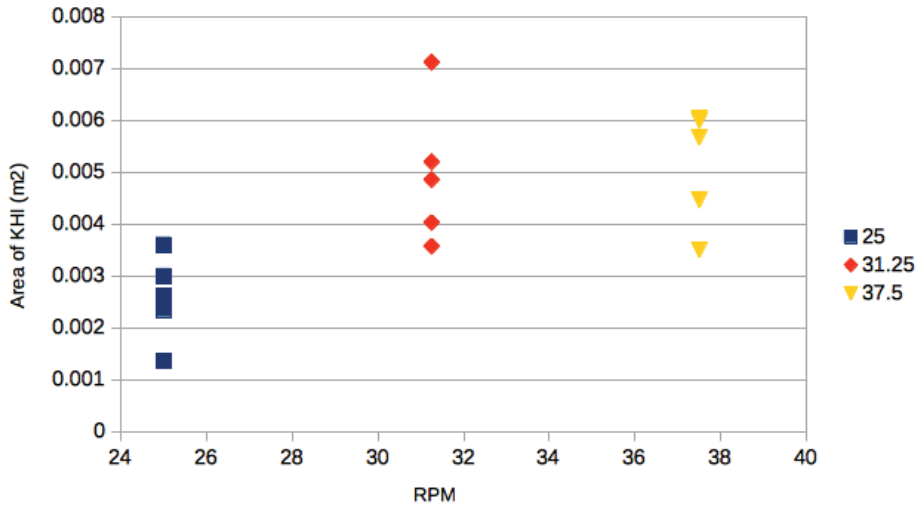

Figure 6.3.8: The findings for the area of the KHI phenomenon in the beach sand at their maximum extent for 25, 31.25 and 37.5 RPM. For each velocity, measurements were taken from five events.

decreases again. It is possible that this is due to a change in flow regime, and part of the increased mass flux required by the increased velocity is being compensated for by the free surface curvature, *i.e.*, the shift from the rolling to cascading regimes. Only three sets of data were analysed for these graphs, though, and expanded data sets in this area may prove illuminating. This is left for future workers.

A much stronger relationship, in this case linear, is shown by the rate at which KHI events occur as a function of rotational velocity.

KHIs are referred to as such due to being a wave-like phenomena in a flowing material with two different densities. However, they may or may not be actual KHIs. This is a potential area for future research.

6.4.5 Implications for Natural Flows

The hysteresis between the constant velocity and accelerating cases has interesting implications when considering the erosive capabilities of lahars. It implies that instantaneous measurements of a lahar are not going to paint a complete picture, and the history of a lahar will also a play a part in its destructive and erosive capabilities.

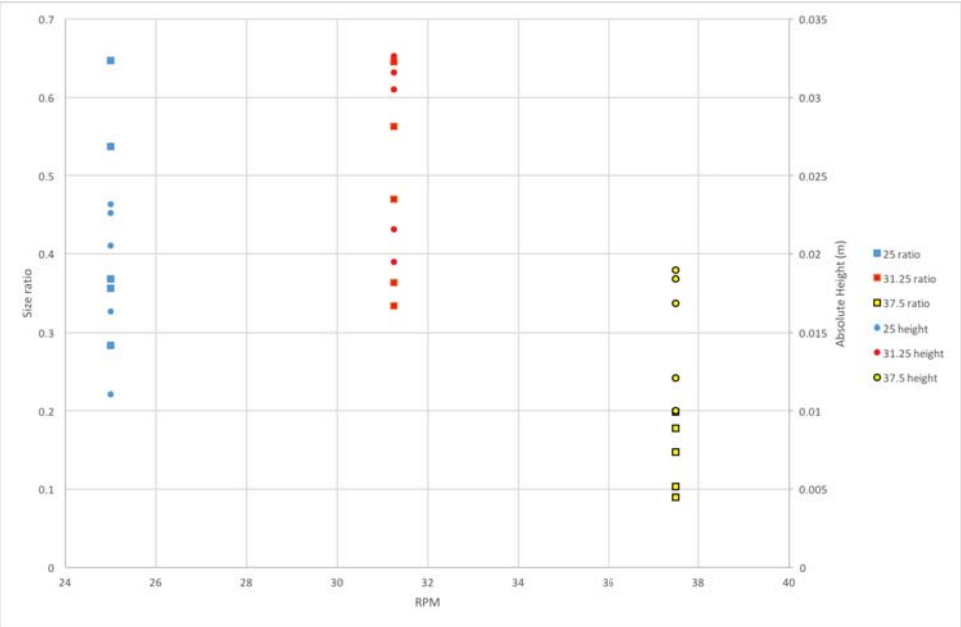

Figure 6.3.9: The findings for the sizes of the KHI phenomenon in the beach sand at their maximum extent for 25, 31.25 and 37.5 RPM. For each velocity, measurements were taken from five events. Squares are the size ratio (left-hand y-axis) of minor over major axis. The circles represent the absolute height, which is plotted on the right-hand y-axis.

Of the new phenomena presented in this chapter, the most applicable to lahars are the SECCs. A natural flow is unlikely to be able to sustain the conditions required to created the KHI phenomena. It is easy to imagine a SECC being created in a natural flow, say after a sudden drop in the elevation of flow channel.

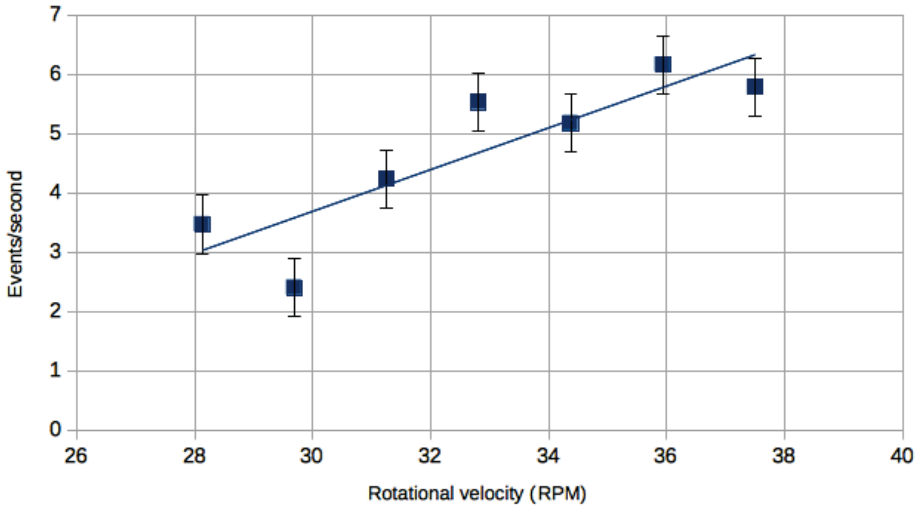

Figure 6.3.10: The frequencies with which KHI events occurred across the five highest velocities for the coarse beach constant velocity experiments.

Chapter 7

Results III - Cross-Material Comparisons: Ash, Beach Sand, Pumice and Millet

7.1 Introduction

This chapter presents quantitative results for the various measurements of the beach sand and volcanic ash presented together, in order to investigate how particulate particle properties (size, shape, density and friction) affect granular flow.

Qualitative comparisons are also made with millet and pumice. These two materials are presented in a primarily qualitative fashion for a variety of reasons. The pumice was initially chosen as it was another natural, volcanically-sourced material that would hopefully aid in the experiments being used to describe real-world granular flows. However, it was found to be extremely self-destructive during experiments. This means that the number of particles in a given experiment would be continually increasing with time; this would also mean the material's size distribution would also be changing continuously. This rendered the material very difficult to analyse satisfactorily with MATLAB/PIVlab - the resultant velocity vector maps produced were often incredibly chaotic and unable to be interrogated further. It was also observed that the pumice would eventually produce large amounts of dust in the drum, which only confused matters when it came to PIV analysis. This dust was presumably the result of two factors: one, the extreme friability of the material eventually producing particles of such small size as to be able of becoming airborne, and two, the difficulty of preparing the material prior to usage in the experiments. The pumice was initially collected in very large amounts with the help of fellow PhD student Rafael Torres-Orozco, but after sieving and washing very little remained. Even after several washes, very fine particulates were being found in the water - the pumice being such a porous material that the dust always had "somewhere to hide", precluding the possibility of a totally clean (*i.e.*, dust-free) sample for usage in the experiments. This difficulty in getting the pumice in sufficient amounts, and its self-destructive tendencies, meant that undamaged samples of the material quickly became scarce. As such, the experiments that were undertaken with the pumice are presented in a primarily qualitative manner.

The millet was added as a fourth material after observing the experiments of Dr. Luke Fullard [Fullard et al., 2017]. Their relative regularity in size compared to the other materials used (see Figure 3.4.2) meant it was thought they might prove an interesting counter-example to the more widely spread size distributions of the other materials (whilst still avoiding the near-absolute uniformity of the glass beads extensively used in the literature). It was also hoped that their organic nature would mean that the seeds would be amenable to being coloured by being soaked in black ink. This would provide the ideal two-tone situation as described in Section 3.3 that would aid the PIV analysis. Sadly the millet proved ink-proof, and so remained a single colour. It was also found that the millet was extremely susceptible to building static charge, which meant that it was impossible to guarantee that the motion observed in the material was due to mechanical processes only. (It essentially failed the minimisation of inter-particulate forces, also discussed in Section 3.3.) As with the pumice, the millet was limited mainly to qualitative descriptions. Both materials were also not suitable for wet experiments, as the millet would absorb the water and change physical properties (as one would expect for a dried seed), while the pumice (especially the very fine dust) would become a suspension in the water, creating a mud or a paste rather than a true particulate solid/fluid two-phase granular system.

7.2 Observation Summary: by Phenomenon

The phenomena observed during the experiments and the velocities they appeared at are illustrated in Figure 7.2.1. Full notes on the behaviour of each material as the rotational velocity increases are given in Appendix A.

Layers

There are two main layers in a granular material in a rotating drum, depending on rotational velocity. These are the passive region and the active region. The latter appears

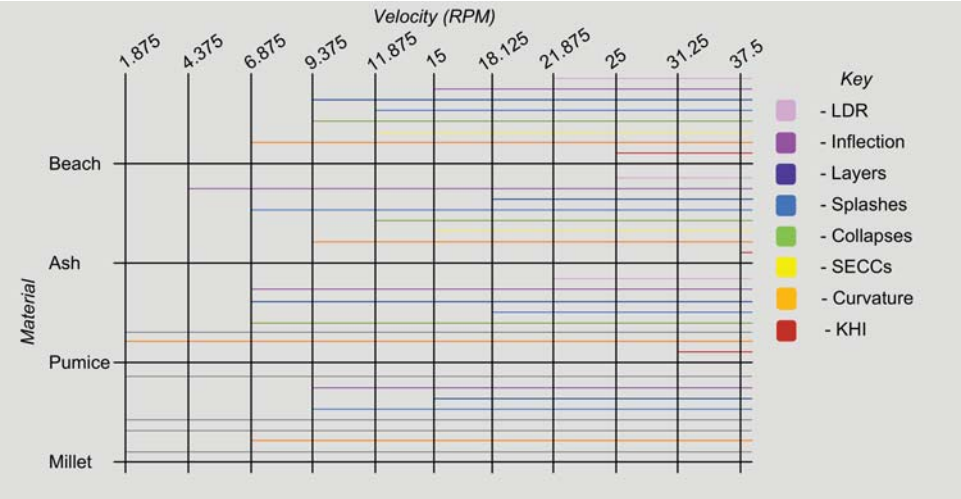

Figure 7.2.1: A summary of the observations by velocity. Coloured horizontal lines indicate at which experimentally investigated velocities various phenomena are observed in a specific material. A thin grey line for a material indicates that the phenomenon in question was not observed. The phenomena observed are as follows: low-density regions, or LDRs, (pink) are the zones of reduced density seen as a material in the cascading regime nears the cataracting; inflection points (purple) are sharp bends in the free surface; layers (dark blue) refers to the point at which multiple layers beyond two are observed; splashes (light blue) are the ejection of particulates, either individually or as groups, due to an avalanche reaching the drum wall at the downhill end; collapses (green) are the events which give rise to an avalanche; SECCs (yellow) is the acronym for self-enclosed circulation cells; curvature (orange) is when the free surface goes from flat to curved, *i.e.*, when the material moves from the rolling to cascading regimes; and KHI (red) are the shockwaves or Kelvin-Helmholtz instabilities observed in some flows.

once the rotational velocity is high enough that the material is in the Mellmann rolling regime [Mellmann, 2001]. This is the Mellmann regime with the lowest rotational velocity of the drum that results in continuous motion of the material travelling downhill, above the passive region (Fig. 3.1.1).

The pumice displays a consistent active region first, at 6.875 RPM. After that, a continuous active region appears in the beach sand (9.375 RPM), the millet (15 RPM) and finally the ash (18.125).

Collapses (Avalanches)

Collapses were defined earlier in this thesis (see Section 5.2.5). These occur periodically, and are when the head of the flow grows in height until it rapidly collapses, causing an avalanche to travel downslope.

They appear earliest in the pumice, at 6.875 RPM, followed by the beach sand at 9.375 RPM. Finally collapses are observed in the ash at 11.875 RPM. Interestingly, the millet never displays collapse events, with the head of the material always flowing smoothly into the active region.

Splashes

In this work "splash" refers to the ejection of one or more individual particulates from the main body upon the event of an avalanche meeting the downhill end of the drum wall (Fig. 5.2.3).

The material that displays splashes at the lowest velocity is the volcanic ash, with small splashes involving few (singe digit) particulates. This occurs at 6.875 RPM. Splashes are then displayed in the millet (9.375 RPM), the beach sand (11.875 RPM) and finally the pumice (18.125 RPM).

Curvature

As the rotational velocity was increased in each experiment, eventually the free surface begins to display curvature - *i.e.*, the material is moving from the rolling to cascading phases [Mellmann, 2001] - see Figure 7.2.2. As with other phenomena, this occurs at different rotational velocities for different materials.

The pumice displays curvature the earliest, at 1.875 RPM - essentially as soon as the drum starts turning, the pumice will be in the cascading regime. The beach sand and

millet enter the cascading regime next, both at 6.875 RPM. The ash displays a curved free surface last, at 9.375 RPM.

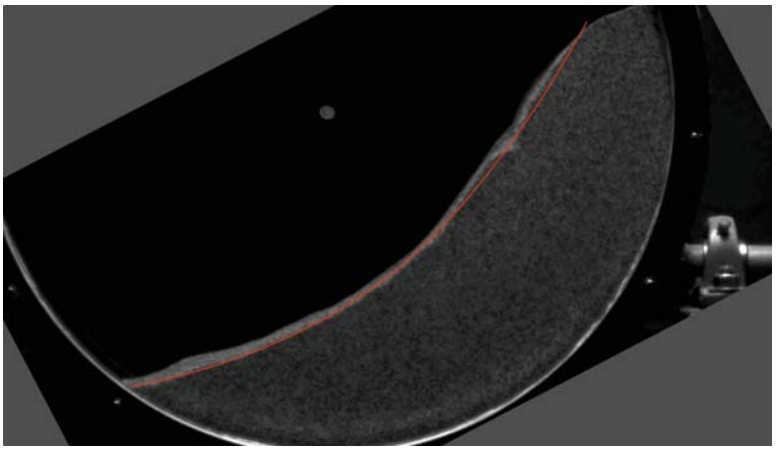

Figure 7.2.2: An image illustrating the curvature of the free surface. The material in this picture is the beach sand, and the drum is rotating at 15 RPM. Unusual cropping due to camera being rotated during filming.

Low-density regions

At high enough velocities, when the system was in the cascading regime and verging on cataracting [Mellmann, 2001], a low-density region formed in the materials. This occurred earliest in the beach (Fig. 7.2.3) and pumice at 21.875 RPM. The ash followed at 25 RPM. The millet never displayed a visible low-density region.

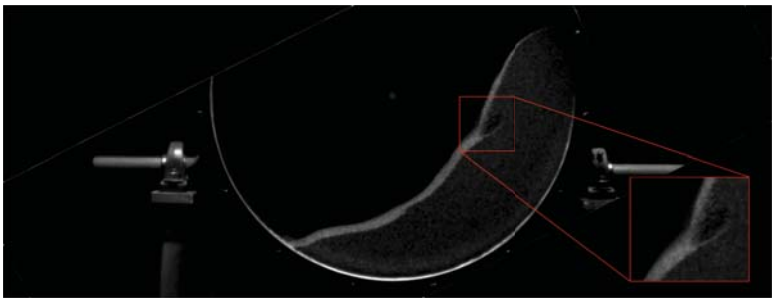

Figure 7.2.3: An example of a low-density region. This image is taken from the beach sand experiments; the drum is rotating at 21.875 RPM. Unusual cropping due to camera being rotated during filming.

Inflections

As the rotational velocity was increased, the free surface curvature increased. Additionally, two distinct sections of the curvature would appear as the rotational velocity increased further - a convex and concave region (Fig. 7.2.4). Where the convex and concave regions of a curved flow meet are referred to in this thesis as inflections. Inflections occur after the onset curvature, and are indicative of the material entering the latter stages of the cascading regime.

The inflections were noted first in the ash at 4.375 RPM. The ash was followed by the pumice at 6.875 RPM, then the millet at 15 RPM. The beach sand displayed this phenomenon last, at 15 RPM.

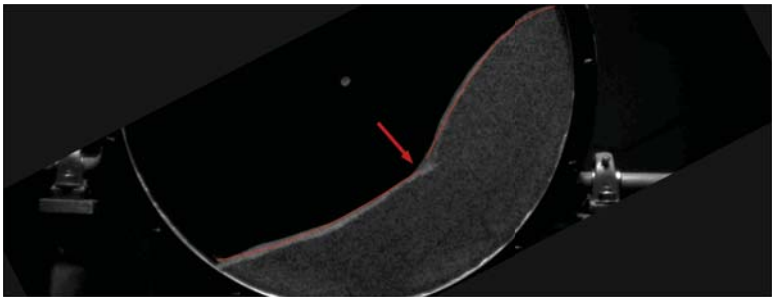

Figure 7.2.4: An example image showing the inflection point phenomenon. Material is the beach sand, and rotational velocity is 18.125 RPM. Where the convex (right side of image) and concave (left side of image) regions meet is referred to in this study as the inflection point (highlighted by an arrow). Unusual cropping due to camera being rotated during filming.

7.3 Measured Variables

In this section measurements taken of the beach sand are presented along side the equivalents for the volcanic ash, allowing for cross material comparisons. Measurements taken include velocities, layer dimensions, and the dynamic angle of friction (see Section 5.2.6).

7.3.1 Example Velocity Profiles

Velocity profiles for the beach sand were obtained, in addition to the profiles already made for the ash. The PIV data for 1000 frames (two seconds of real-time footage) was interrogated in two-frame pairs along the radial line that passes through the drum centre and the centre of mass for the material at the velocity in question. Presented below (Fig 7.3.1 and 7.3.2) are the results from these measurements.

The centre of mass line was chosen as it represents a common point across all the materials that has some basis in the properties of the material itself, rather than being an arbitrary point in space, perhaps defined by a point in the drum equipment.

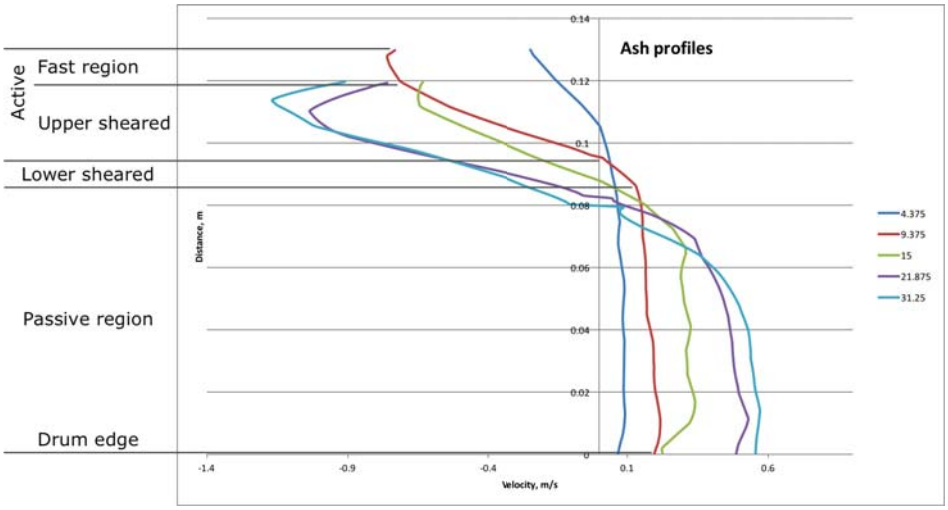

Figure 7.3.1: Velocity profiles for the ash, along the radial line that passes through the material's centre of mass. Legend gives the rotational velocities in RPM. Note the general lack of slippage at the drum edge. For this figure, the left-hand side has been labelled to illustrate which part of the material the velocity profile is taken from.

7.3.2 Avalanche Velocity Profiles

The velocity profiles presented here to illustrate avalanche behaviour are across two frames of video footage. The results are shown in Figures 7.3.3 to 7.3.8.

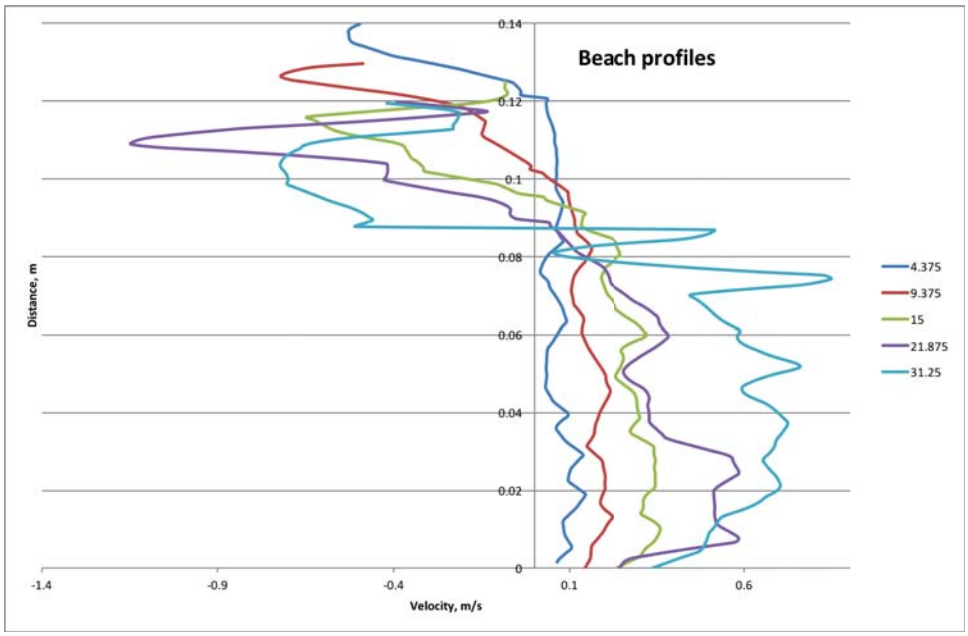

Figure 7.3.2: Velocity profiles for the beach sand, along the radial line that passes through the material's centre of mass. Legend gives the rotational velocities in RPM.

7.3.3 Layer Thicknesses

The dimensionless layer thicknesses for the beach sand were found in the same manner as those for the ash (Fig. 5.2.4). The results are presented in Figure 7.3.9.

7.3.4 Area of Passive and Active Regions

As well as one-dimensional layer thicknesses, the area of the active and passive regions was calculated by manipulating the layer velocity data.

In general, the coarser ash material presents a much more distinct change in the active and passive regions. As may be expected, in both materials, the passive region gets smaller with increasing rotational velocity, and *vice versa* for the active. In both cases the total areas is relatively constant, as one may expect. However, there is some variation in the total. Data on this and the implications for this variability are explored in the discussion for this chapter, Section 7.6.

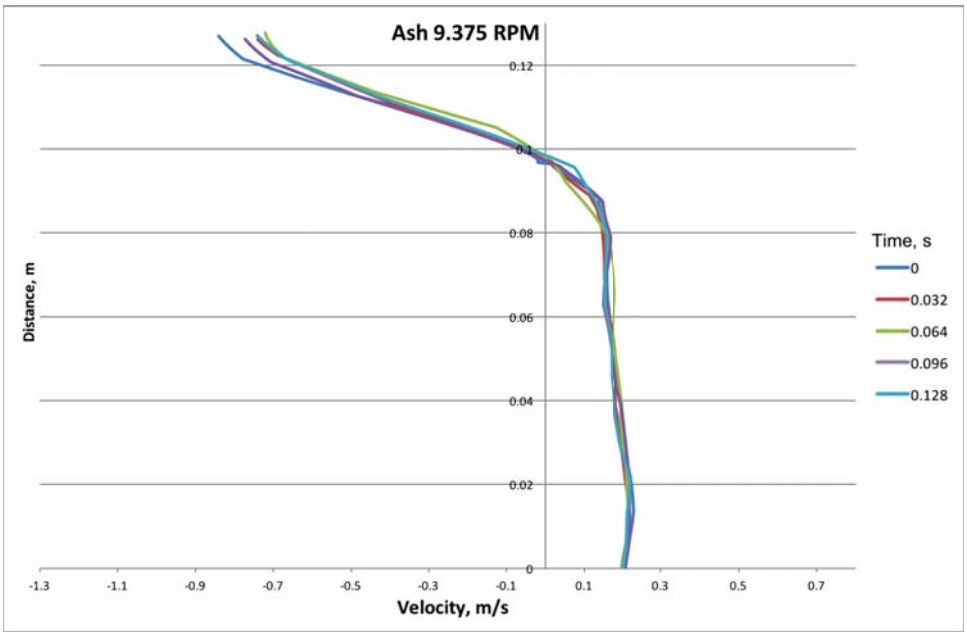

Figure 7.3.3: Instantaneous velocity profiles across the centre of mass line for the ash at 9.375 RPM. Legend gives time in seconds at which the profiles were taken. Time zero is the point at which the body of the avalanche meets the centre of mass line. This is figure is identical to Figure 5.2.6 and is presented here for the reader's convenience.

Active Region Dilation

It is well known that for a granular material to flow, there needs to be some dilation of the bulk material to allow individual particulates to move past each other (*e.g.*, Reynolds [1885, 1886]). In a rotating drum is seems reasonable to assume that the material in the passively rotating region maintains the bulk density of the material in question [Orpe and Khakhar, 2004]. It is the flowing region that must dilate in order for it to flow down-hill on top of the passive region.

As can be seen from Figures 7.3.10 and 7.3.11, there is some variability in the total area of the drum window occupied by the two main regions in a flowing material. However, the dilation of the active region cannot be found from the change in area occupied by the active region alone, as there is no baseline area to compare it to. But the changes in the total area occupied by the material, assuming that the passive region does not dilate, can give us a place to estimate how much the flowing region dilates by.

Two dilations were calculated for each of the ash and beach sand materials. The first

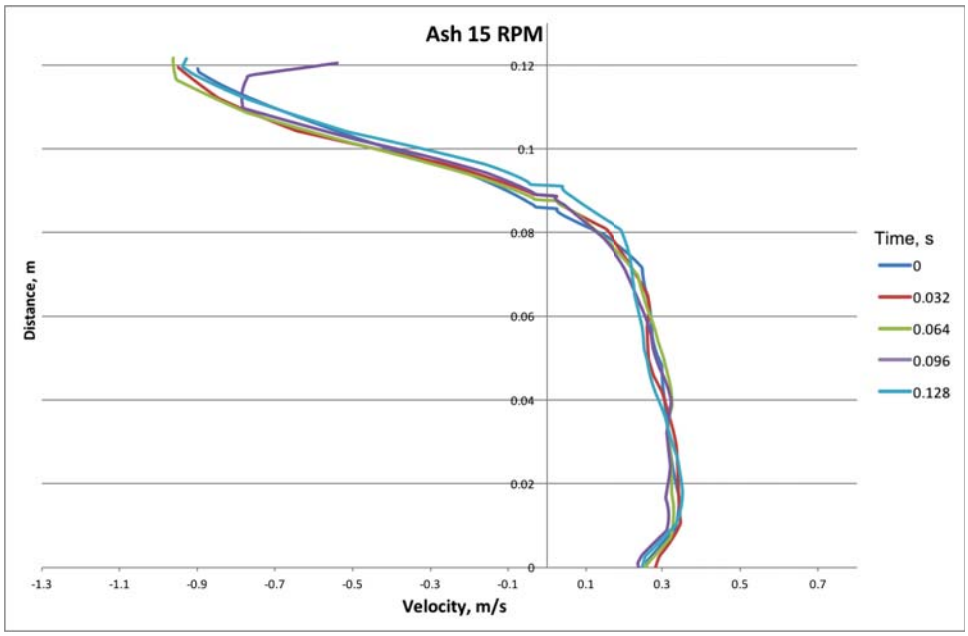

Figure 7.3.4: Instantaneous velocity profiles across the centre of mass line for the ash at 15 RPM. Legend gives time in seconds at which the profiles were taken. Time zero is the point at which the body of the avalanche meets the centre of mass line. This is figure is identical to Figure 5.2.7 and is presented here for the reader's convenience.

takes the change in total area occupied by the material from the *lowest* to *fastest* rotational velocities measured. The second took the *largest* total occupied area and the *smallest*, to calculate a maximum dilation. (As can be seen in Figure 7.3.11, the beach sand had quite a variable maximum occupied area, and it did not necessarily reach its maximum at the highest velocity.) Data for the dilation of the beach sand and ash are presented in Table 7.1.

Table 7.1: The dilations of the beach sand and the ash, as percentages of total volume. "Maximum to minimum" uses the largest and smallest areas from Figures 7.3.10 and 7.3.11, while "Start to finish" uses the first and last, *i.e.*, from the lowest and highest rotational velocities.

Material	Maximum to minimum, %	Start to finish, %
Beach sand	4.6	1.7
Ash	6.7	2.1

7.3.5 Collapse Periodicity

Presented in Figure 7.3.12 are the collapse periodicities for both the ash and the beach sand.

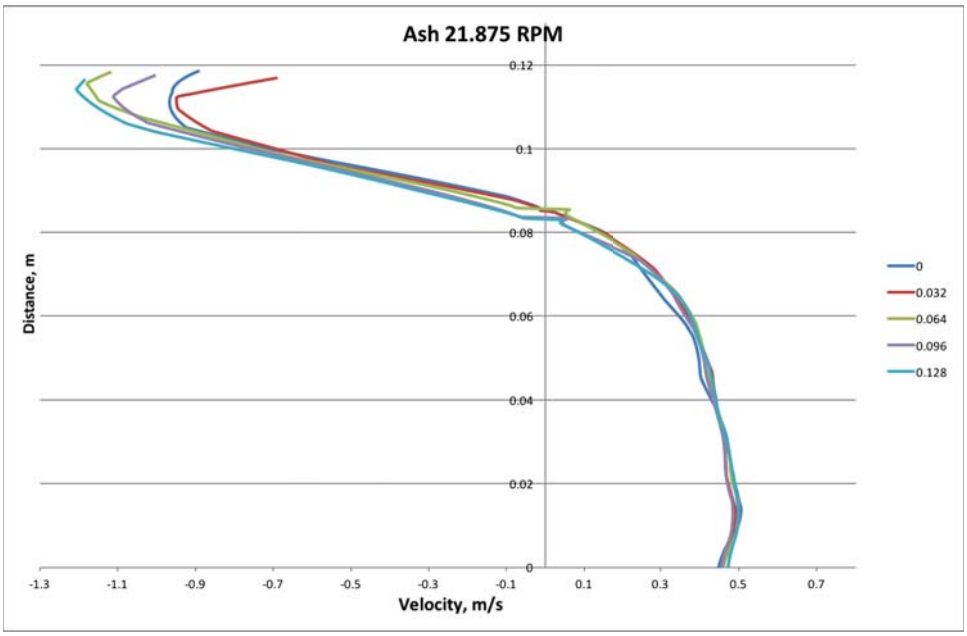

Figure 7.3.5: Instantaneous velocity profiles across the centre of mass line for the ash at 21.875 RPM. Legend gives time in seconds at which the profiles were taken. Time zero is the point at which the body of the avalanche meets the centre of mass line. This is figure is identical to Figure 5.2.8 and is presented here for the reader's convenience.

7.3.6 Dynamic Angle of Friction

The dynamic angle of friction is one of the data outputs of the MATLAB PIV analysis code. This angle is the displacement from vertical of the centre of mass of the material in the drum while the drum is turning (Fig. 5.2.12). The code finds this angle by looking for the point at which the area of the material as measured by the PIV is divided by two. Note that this makes no assumptions about the dilation of the active region as this increase in area will be automatically taken into account.

The results for the two main materials in this study are presented in Figure 7.3.13.

7.4 The Effect of a Passing Avalanche

The passing avalanche measurements undertaken for the ash were repeated on the beach sand. For three velocities (9.375 RPM, 15 RPM, and 21.875 RPM), particularly distinct avalanches were visually identified in the footage. The frame number at which

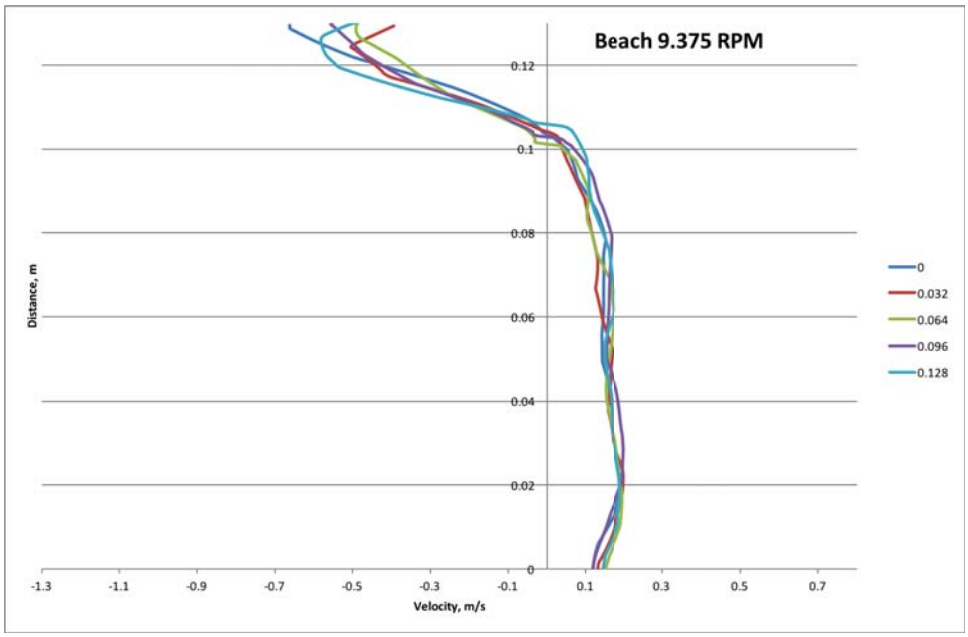

Figure 7.3.6: Instantaneous velocity profiles across the centre of mass line for the beach sand at 9.375 RPM. Legend gives time in seconds at which the profiles were taken. Time zero is the point at which the body of the avalanche meets the centre of mass line.

the avalanche reached the average centre of mass line was noted, and PIV analysis was run on five groups of two frames, over a total duration of 80 frames (0.16 seconds). The centre of mass line was found using the MATLAB code written by Dr. Luke Fullard. Velocity profiles were constructed for each of these two-frame groups across all three velocities, and are presented in Figure 7.4.1 and 7.4.2.

7.5 Mass Flux

Mass flux, *i.e.*, the rate at which material is transported downhill by the active layer, was calculated from the data obtained for the passing avalanches. The velocities profiles were manipulated to give an area with the units $m^2\ s^{-1}$. Multiplying this by the depth (*i.e.*, the width of the drum) and then by the bulk density of the material gives a mass flux, in $kg\ s^{-1}$. (This assumes that the dilation is minimal.) This means that the mass fluxes presented (both here and later in the thesis) are the fluxes across the centre of mass line found by the MATLAB code. Usage of the centre of mass line means the

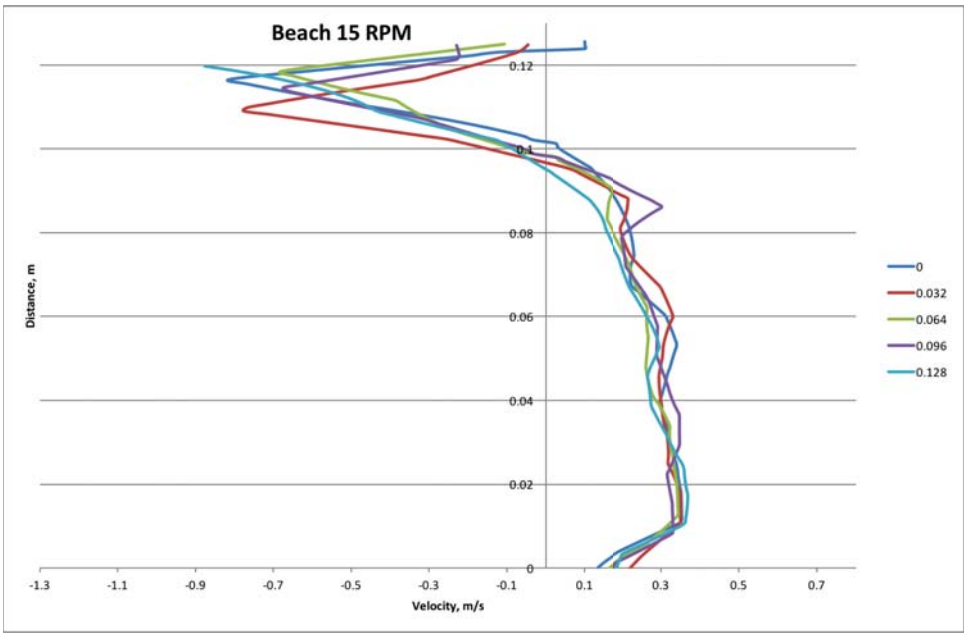

Figure 7.3.7: Instantaneous velocity profiles across the centre of mass line for the beach sand at 15 RPM. Legend gives time in seconds at which the profiles were taken. Time zero is the point at which the body of the avalanche meets the centre of mass line.

mass fluxes are calculated across a line which has the same meaning to all velocities, as opposed to an arbitrary angle from horizontal, for example. The results are presented in Figures 7.5.1 and 7.5.2.

7.6 Discussion

In this chapter, materials with different particulate size distributions, angles of repose, and densities are compared. This comparison comprised both qualitative descriptions across all four materials (pumice, millet, beach sand and volcanic ash) and quantitative measurements (beach sand, volcanic ash).

7.6.1 Qualitative Observations

Qualitative descriptions across all four experimental materials reveals some striking differences in behaviour; see Appendix A for details. The millet differs most from the

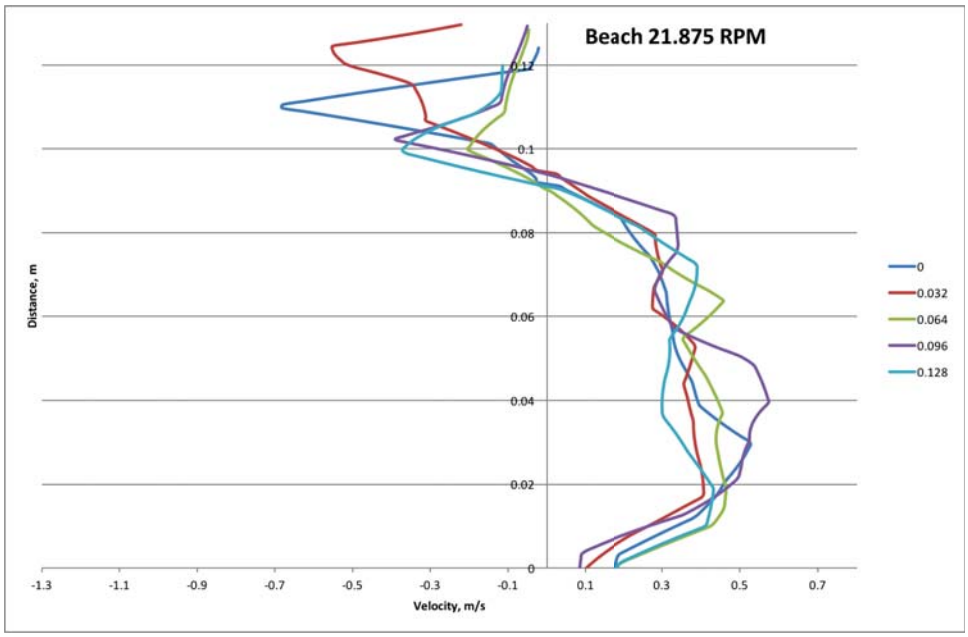

Figure 7.3.8: Velocity profiles across the centre of mass line for the beach sand at 21.875 RPM. Legend gives time in seconds at which the profiles were taken. Time zero is the point at which the body of the avalanche meets the centre of mass line.

other materials, never displaying several phenomenon almost universally present in the other materials, namely LDRs, collapses (i.e, avalanche on-set), and the putative Kelvin-Helmholtz instabilities. The millet differs physically from the other materials in two key ways: it has one of the largest mean diameters, and is close to monodisperse. No link between the physical properties of the millet and its behaviour is suggested here, but it may be worth investigating in the future.

The pumice never displays SECCs, which is unique across the four materials. Why this may be so is not immediately apparent. The pumice is a particularly problematic material in that it is the most self-destructive of the materials used. The increase in fine material as experiments continued were obvious even to visual observation. This is why the pumice was never subjected to more rigorous numerical investigation, as it was subject to a changing parameter that was beyond our control.

The beach sand and ash display generally similar behaviour patterns, though the ash shows free surface curvature at very low rotational velocities. This may be due to the ash's generally more coarse grained nature compared to the beach sand - the ash is less

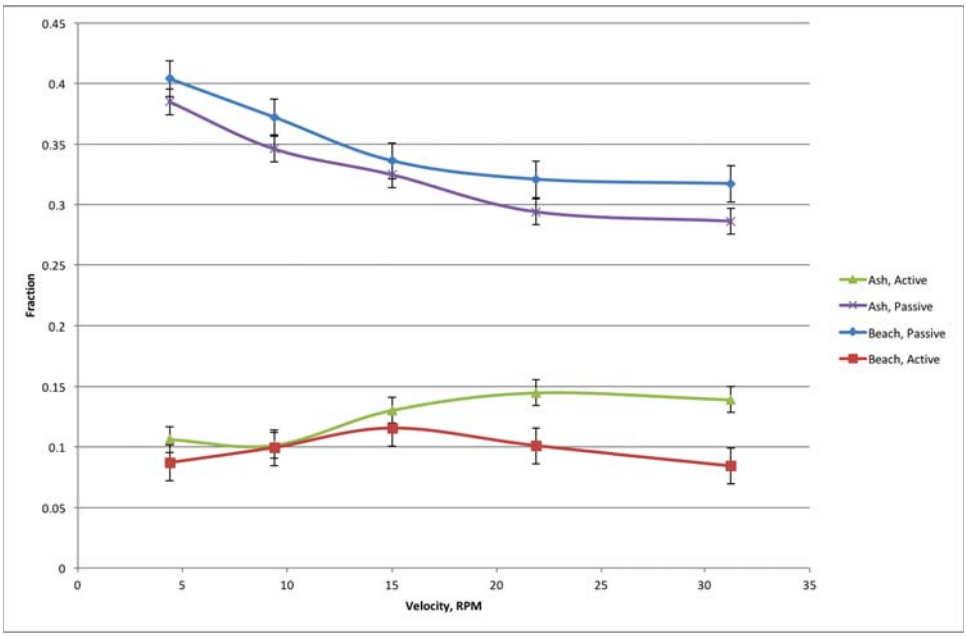

Figure 7.3.9: The dimensionless layer thicknesses for both the beach sand and the ash, found using the methodology given in Section 4.3. Layer depths are non-dimensionalised by the radius of the drum. Green is the active layer for the ash, with purple denoting the ash passive layer. The beach active layer is shown in blue, and the related passive layer in red. Vertical error bars are the standard deviation. Horizontal error bars are smaller than the point.

easy flowing than the beach sand, and as such has to compensate for the increased rotational velocity with free surface curvature earlier than the beach sand.

7.6.2 Active Region Fraction

The active region data (see Figures 7.3.10 and 7.3.11) shows that the ash has more material in the active region than the beach, at least as a function of length or area. The area measurements in particular display a much stronger changing layer structure in the ash than the beach sand. It is also possibly related to the grain size distributions of the two materials. The ash is coarser than the beach sand, and the literature (*e.g.*, [Abdullah and Geldart, 1999; Alexander et al., 2002; Liao et al., 2013]) does state that size plays a critical role in determining the flowing nature of a granular material.

The beach sand displays some interesting behaviour, in that the active region and the sum (*i.e.*, the material a as whole) seems to expand before contracting again. This is

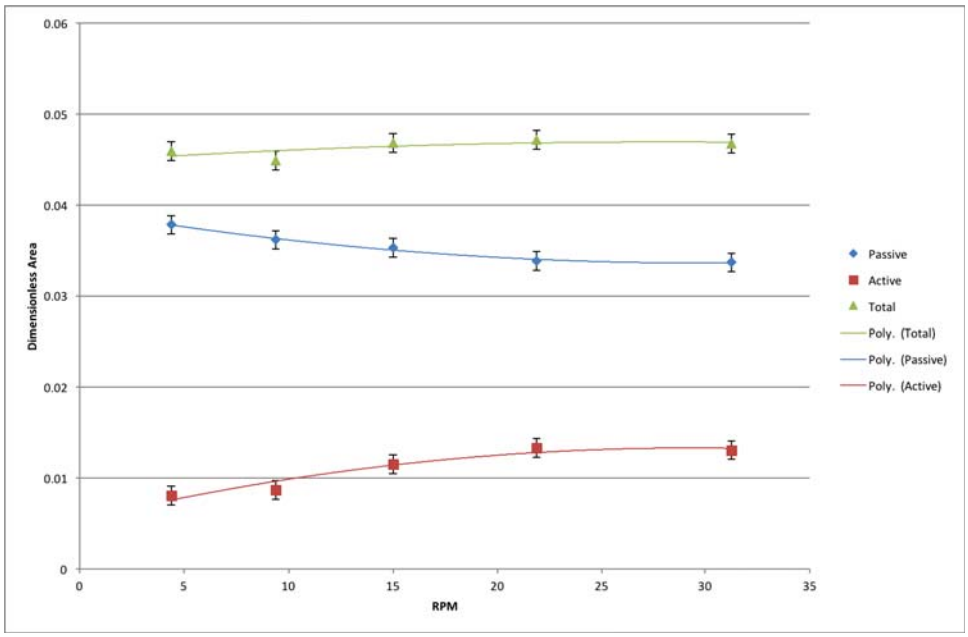

Figure 7.3.10: The area of the active and passive region of the ash at various velocities (x axis). On the y axis is the dimensionless area of the passive region (blue diamonds), the active (red squares), and the total of the two regions (green triangles). Area is non-dimensionalised by the sum of the two areas. Error in the vertical axis is the standard deviation. Error in horizontal axis is smaller than the point (see Table 3.5). Solid lines are polynomial best fit. This figure is identical to Figure 5.2.9.

extremely counter-intuitive. It could be down to the increased rotational velocity applying a centripetal force to the material, causing a concentration of the particulates. This would presumably happen preferentially in the active region, as that part of the granular material has to be at a lower particulate density than the passive region in order to be able to flow. This effect would be less marked in the sum of the two regions, as the passive region, which would be relatively well packed, would not undergo this centripetal concentration to the same degree. Indeed, this is what is displayed in the graph of the data (Fig. 7.3.11). However, it seems unlikely that centripetal force would be able to produce such a marked effect in the size of the active region. A more likely explanation is simply down to error. It is possible to fit linear relationships onto the data if one makes use of the error bars - see Figure 7.6.1.

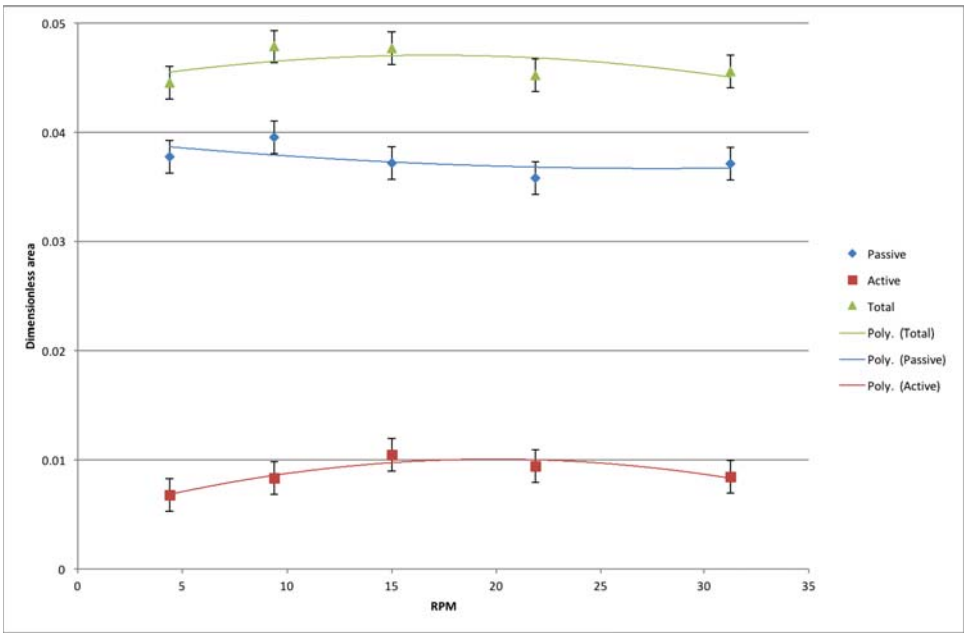

Figure 7.3.11: The area of the active and passive region of the beach sand at various velocities (x axis). On the y axis is the dimensionless area of the passive region (blue diamonds), the active (red squares), and the total of the two regions (green triangles). Area is non-dimensionalised by the sum of the two areas. Error in the vertical axis is the standard deviation. Error in horizontal axis is smaller than the point (see Table 3.5). Solid lines are polynomial best fit.

7.6.3 Dynamic Angles of Friction

The beach sand displays a generally higher dynamic angle of friction than the volcanic ash. This is possibly due to its lower flow function (Table 4.1), and as such it is forced higher up the drum wall during rotation: as the material finds it "easier" to flow, the beach sand is more susceptible to centrifugal forces, which pushes the material further up the drum wall, increasing the dynamic angle of friction. Both ash and beach sand display a general upward trend with a head at around the 10 RPM mark. This is possibly related to the other phenomena that appear to have a limit around the 10 to 12 RPM velocity region, such as the frequency of collapse minimum value explored earlier in this thesis, or to changes in Mellmann regime.

Additionally, the beach sand shows more dynamic mass flux graphs. There is generally a much greater increase in mass flux for the beach sand when an avalanche passes than in the ash. Predictably, the greater velocities, in both material cases, present higher

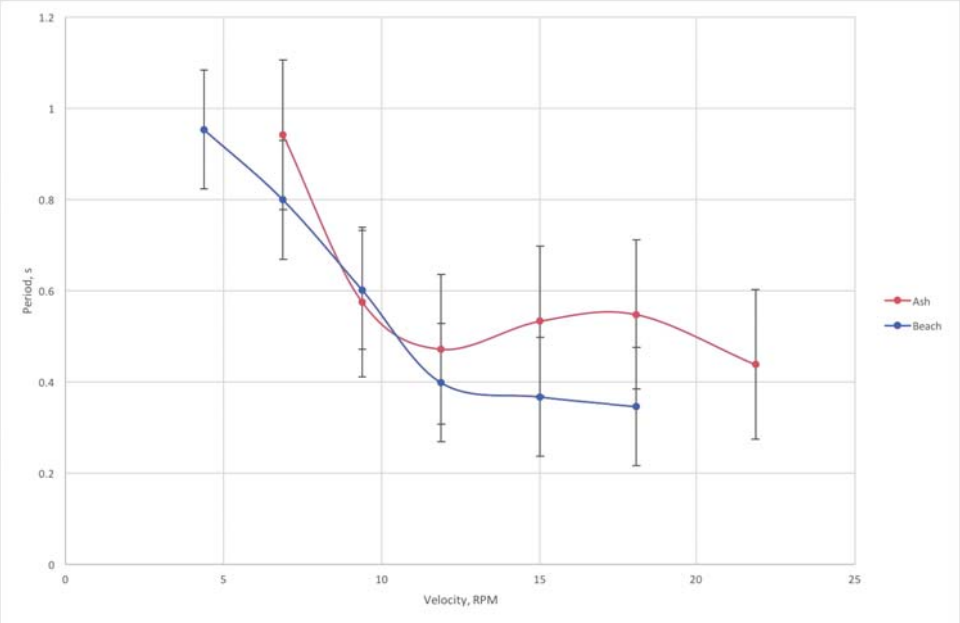

Figure 7.3.12: This is the collapse periodicity versus motor RPM for the ash (blue) and beach sand (orange). At around the 12 RPM mark the periodicity levels off (within the error bars), after which the frequency of collapse on set no longer changes significantly. Error bars for vertical data (period) represent the standard deviation. Error for the rotational velocity is smaller than the point. For each velocity, four seconds of footage was observed to find the number of collapses. Note that while some velocities do display collapse behaviour, it was not always measurable, so data presented here may not match presented velocity ranges for collapses presented elsewhere in the thesis. (For example, Figure 7.2.1 and Appendix A.)

mass fluxes.

7.6.4 Collapse Periodicity

The collapse periodicity for the beach sand follows the same general trend for the ash, in that the time between collapse events gets shorter with increasing rotational velocity. It also displays the same levelling off, but this is more pronounced than the ash, with no "hump" in the middle of the "level" section of the graph. However, the beach sand has generally shorter amounts of time between the events than the ash. This is probably related to the more easily flowing nature of the beach sand compared to the ash - the beach sand has a lower flow function (f_f) and a lower internal angle of friction (θ_i) (Table 4.1).

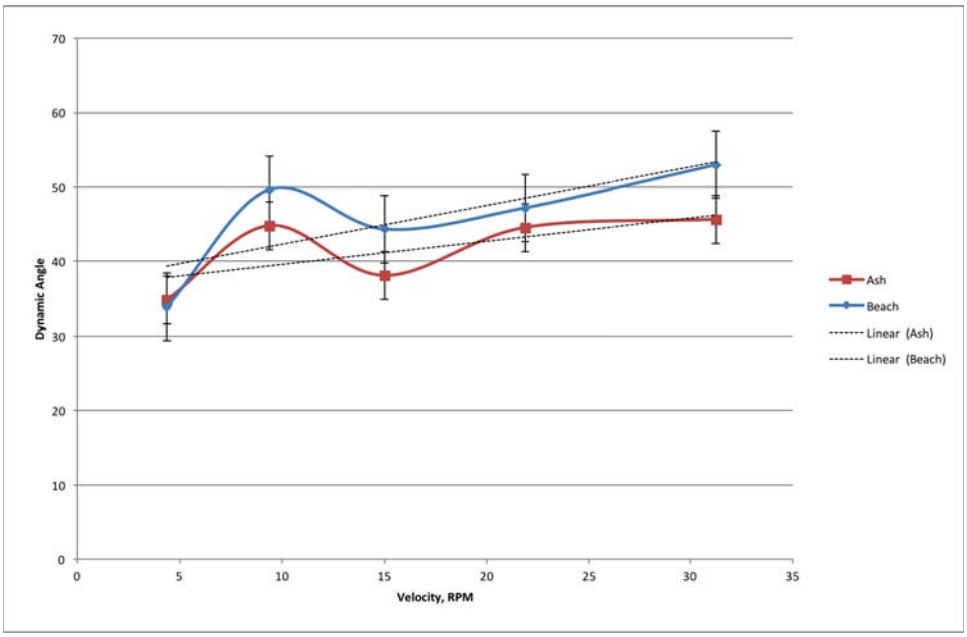

Figure 7.3.13: The dynamic angle of friction for the beach sand and ash. Blue data points are the beach sand, while the red are the ash. Dashed lines are linear best-fit, intended to show a general trend rather than a true mathematical relationship. The curved lines are software interpolations. Error bars represent the standard deviation.

7.6.5 The Effect of a Passing Avalanche

One interesting point of comparison between the ash and the beach sand are the respective velocity profiles of a passing avalanche, and example profiles. The beach sand displays much more noisy data than the ash does. This is possibly related to the difference in flow function between the two materials, and as such the beach sand moves in a more stuttering manner than the ash. However, the flow functions for the two materials, though different, are relatively similar. Would such a narrow difference be able to explain the difference in the velocity profiles collective smoothness?

7.6.6 Pumice Radial Stripes

Observed in the pumice experiments were a phenomena which will be referred to in this thesis as "radial stripes". These were most visible between velocities 1.875 and 11.875 RPM, and were completely gone by 18.125 RPM. The radial stripes can be seen below in Figure 7.6.2.

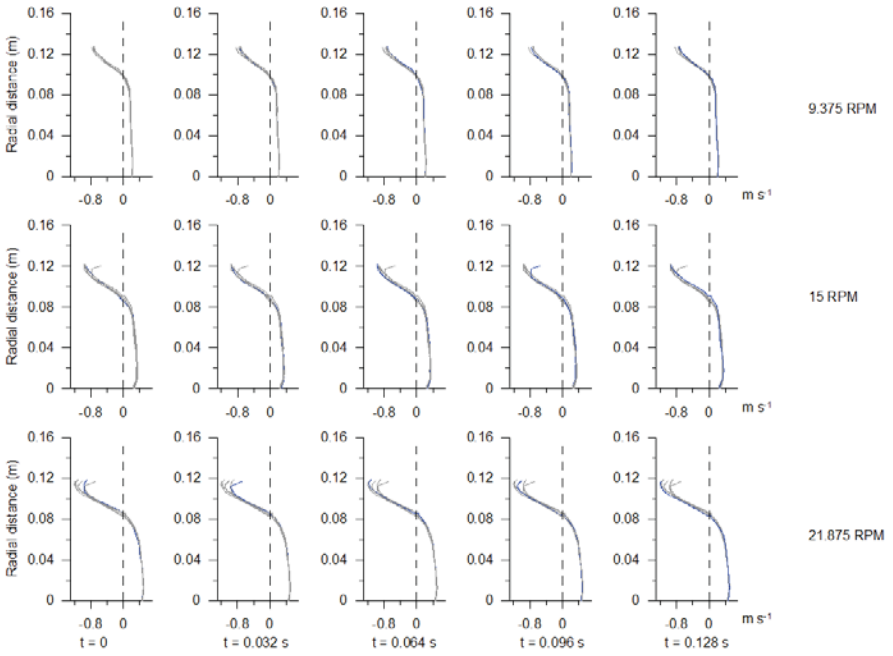

Figure 7.4.1: Velocity profiles for the ash through the centre of mass line as an avalanches passes, for a variety of velocities (rows). Time is from left to right. The profiles show the passive region (positive velocity) and active region (negative velocities). All profiles are shown on each graph. The profile for the time in question is highlighted in blue.

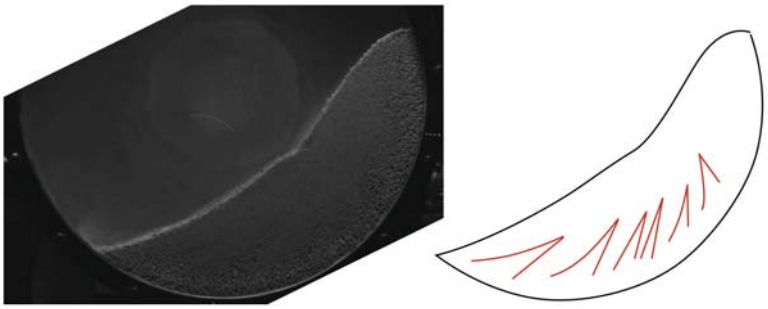

Figure 7.6.2: On the left can be seen an image taken from the 6.875 RPM experiments involving the pumice material. On the right is a sketch highlighting the stripes that formed during the experiments.

As mentioned in the Introduction chapter (1.1), segregation is a common process in granular materials. An everyday example is the separation of ingredients in a breakfast cereal (Section 1.1.1). Segregation also occurs in industrial processes, and can be extremely problematic if it occurs when homogeneous blends of materials are required,

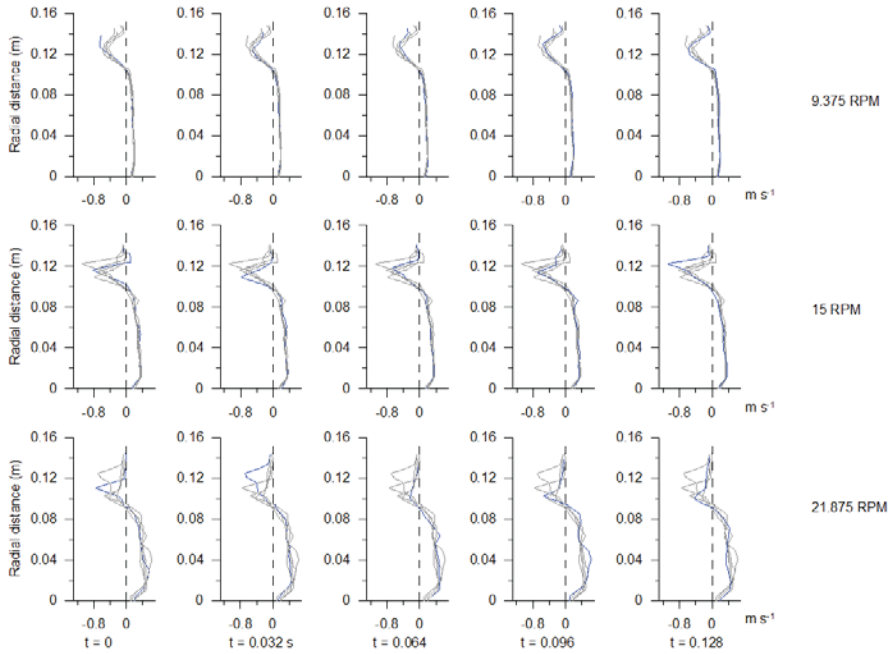

Figure 7.4.2: Velocity profiles for the beach sand through the centre of mass line as an avalanches passes, for a variety of velocities (rows). Time is from left to right. The profiles show the passive region (positive velocity) and active region (negative velocities). All profiles are shown on each graph. The profile for the time in question is highlighted in blue.

such as in the pharmaceutical industry [Hill et al., 2001]. In industrial applications using a rotating drum, the segregation presents in the manner shown in Figure 7.6.3, known as axial segregation, or axial banding [Alexander et al., 2004; Finger and Stannarius, 2007; Hill and Kakalios, 1995; Hill et al., 2001; Santos et al., 2016; Zik et al., 1994], which was first observed by Oyama [1939]. Segregation occurs due to two main processes: percolation (in which smaller particulates fall between the larger, *e.g.*, [Chou et al., 2010]), and buoyancy (in which denser particles "sink" towards the bottom of the container, *e.g.*, [Finger and Stannarius, 2007]). In the literature, axial banding is given as an extension of either of the above effects (see references for axial segregation, above). Any areas that are, by chance [Hill and Kakalios, 1995], already richer in one particulate type over the other (assuming a binary mixture), will have a different dynamic angle. One of the two member materials will find it easier to flow at this angle than the other, resulting in a region in the material that has a preference for one ma-

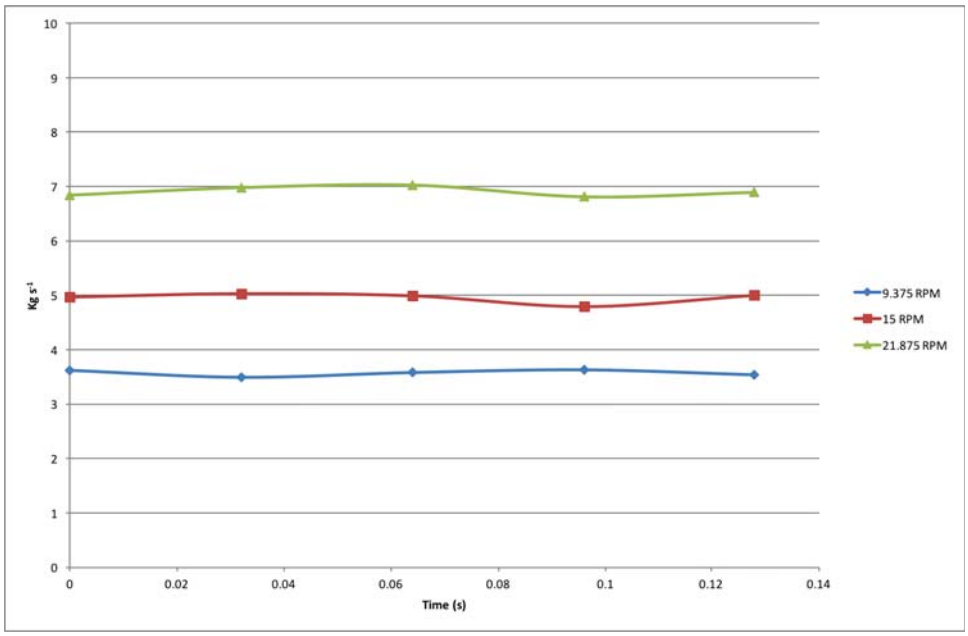

Figure 7.5.1: The mass fluxes, in kg s^{-1} for the ash for three key velocities.

terial. This results in the material splitting into bands, generally within a hundred or so rotations of the drum Richard and Taberlet [2008]. However, this explanation has been shown to be imperfect, and discussion continues in the literature (*e.g.*, Hill and Kakalios [1995]; Hill et al. [2001]; Richard and Taberlet [2008]).

The other type of segregation in a rotating drum presented in the literature is called radial banding, in which the coarser fraction of the material ends up surrounding the finer, which is concentrated at the core of the bulk material. This can be seen in the pumice experiments above 11.875 RPM, becoming particularly distinct at velocities greater than 15 RPM (Figure 7.6.4).

As far as the author is aware, the radial stripes as observed in the pumice are not reported in the literature. The radial stripes occur in the pumice before the radial banding (stripes at 6.875 RPM, and the banding at 11.875 - see Appendix A). The author suggests that perhaps the radial stripes are the proto form of the axial banding, with the drum simply not being wide enough in this experimental set up to allow the axial bands to form. This is suggested as an explanation because the radial stripes and axial banding seem to share similar formation mechanics - differences in dynamic angle for the different material sizes. As can be seen in Figure 7.6.5, the pumice builds

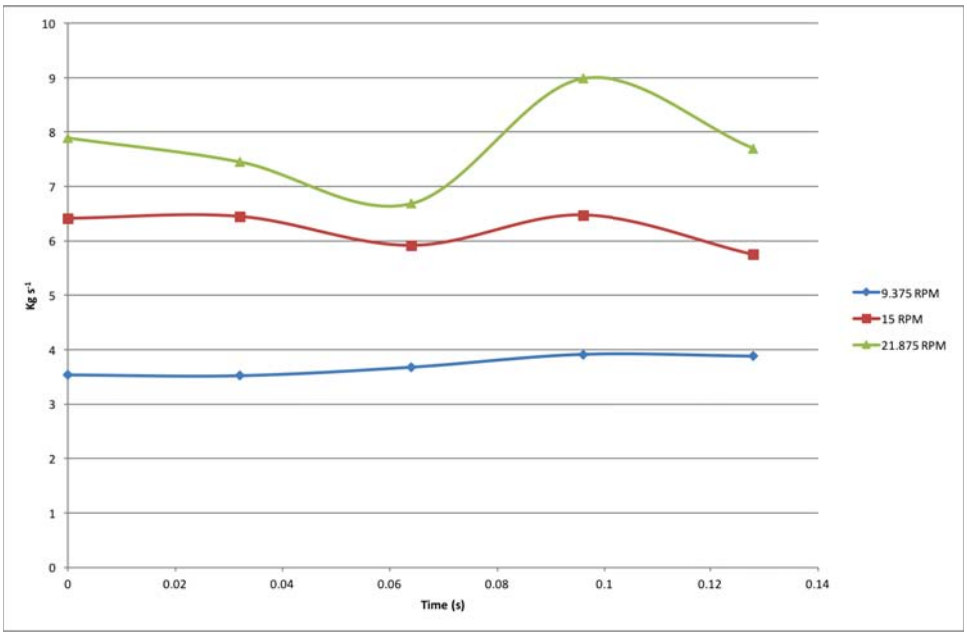

Figure 7.5.2: The mass fluxes, in kg s^{-1} for the beach sand for three key velocities.

small raised regions towards the bottom of the flowing region. While it would be a gross oversimplification to say that the pumice has a binary size distribution of member particles, it would not be too much of a stretch to divide the pumice into two size families, one above and one below a critical particulate diameter. Each of these groups would have a different dynamic angle (admittedly with some range in each group, due to each group not being monodisperse). One material is, then, presumably finding it difficult to overcome the buildup of material at the end, while the other flows over it with minimal difficulty. This results in the loss of the raised region as the preferred material over tops it. This again changes the dynamic angle of the situation, allowing either a mixture of the two groups or preferentially selecting the other. The two groups of material are then separated as a result of the raised area cycle, resulting in the stripes.

It is possible that if the drum were wider, the two groups of materials would move laterally to accommodate each other, resulting in the axial banding prevalent in the literature. It is also possible that this lateral movement would not happen, and the radial stripes are a new form of segregation that can occur in a rotating drum.

Eventually it is observed that the radial stripes disappear, to be replaced with radial

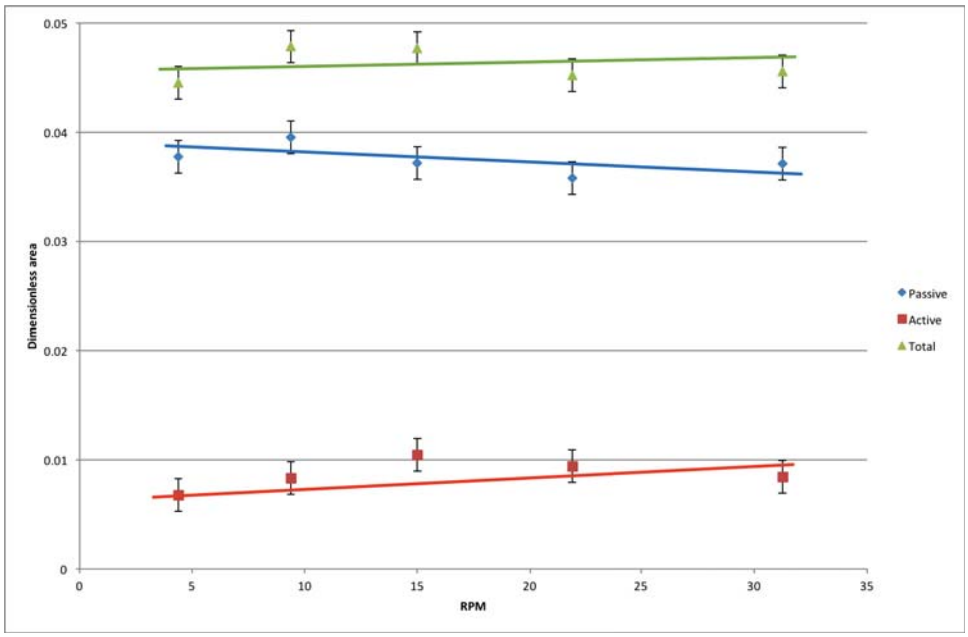

Figure 7.6.1: The area of the active and passive region of the beach sand at various velocities (x axis). On the y-axis is the dimensionless area of the passive region (blue diamonds), the active (red squares), and the total of the two regions (green triangles). Error in the vertical axis is the standard deviation. Error in horizontal axis is smaller than the point (see Table 3.5). In this version of the graph (the original is Figure 7.3.11, the polynomial best fit lines have been removed, and linear relationships that fall within the error bars are presented.

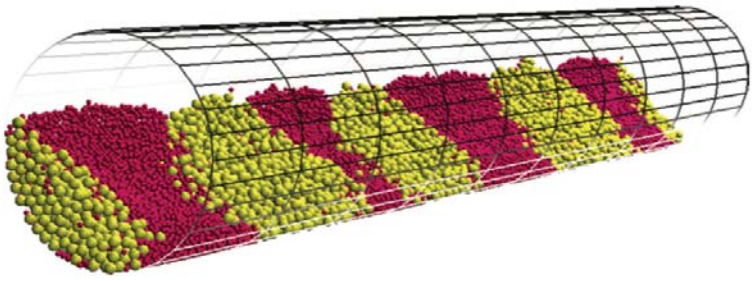

Figure 7.6.3: An example of axial segregation in a long rotating drum, partially filled with two populations of granular materials. As the drum has been rotated, the two types of particulates have segregated along the axis of rotation. Based on a figure originally published by Richard and Taberlet [2008].

banding. If the coarser group of grains simply disappeared, it could be said that the pumice, which is already known to be extremely self-destructive, has just lost its coarser grains as they are broken up to become successively more fine. However, the coarse group is visible towards the centre of the drum, as per the standard formation of radial banding, so while it is reasonable to assume some of the coarse group is lost to the

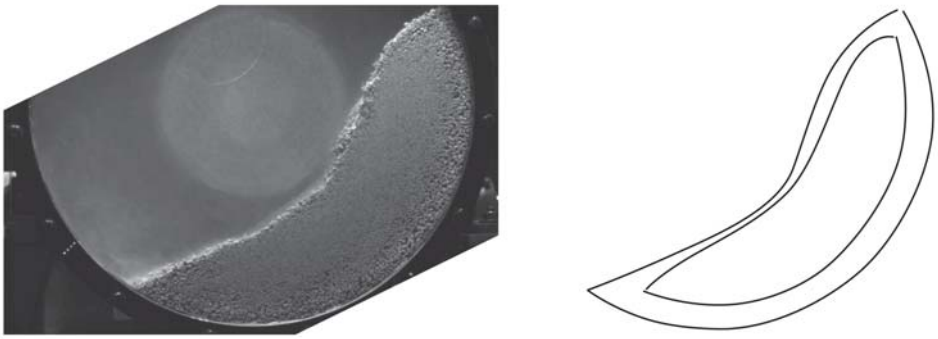

Figure 7.6.4: An example of radial segregation. Under this phenomenon, in a rotating drum, the coarser materials move to the outside of the bulk of the material, with the finer fraction moving towards the core. This image was taken from the pumice experiments at 18.125 RPM. Cartoon on the right demonstrates the suggested boundaries of the finer and coarser fractions.

pumice's friability, not all of it is gone.

The pumice then seems to be presenting a new form of segregation followed by an already observed one. Why does one end to be replaced by the other? While at lower velocities the flowing part of a material in a rotating drum can be said to be rolling downhill simply due to gravity, once the rotational velocity is high enough, the flowing material is also moving with the momentum gained during its journey from the passive region to the active. At this point, even part of the pumice that would struggle with the raised regions is now able to surmount this obstacle. As such, another form of segregation is able to take over.

Of course, the explanations presented above are conjecture only, and are given only as potential starting points for future workers in this area.

7.6.7 Implications for Natural Flows

Assuming that dry experiments have some applicability to water-based natural granular flows, this chapter does demonstrate that the physical characteristics of the solid fraction of a flow does have an influence on the overall subsequent behaviour. Com-

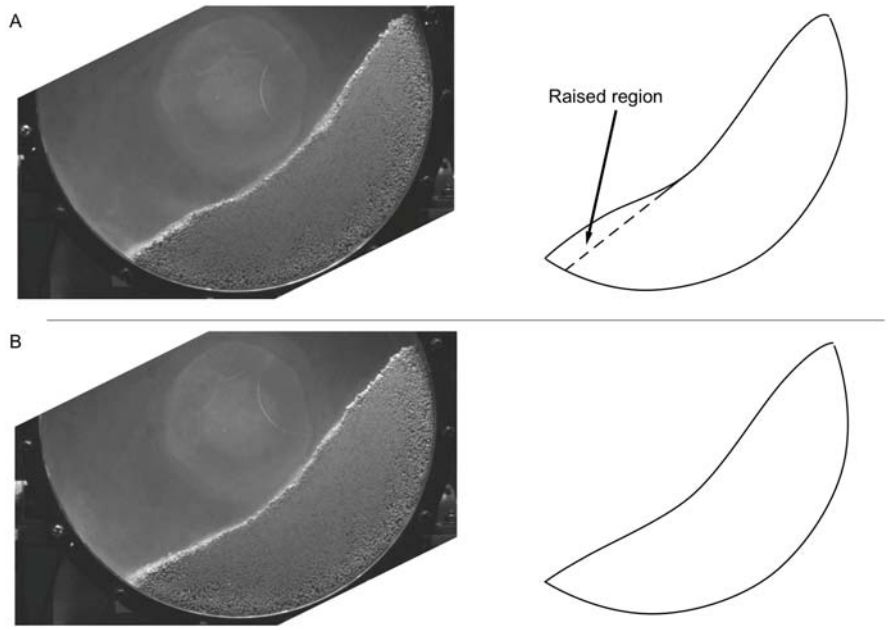

Figure 7.6.5: An example of the raised region in the pumice material. In situation A, the pumice has built up raised section of material ("raised" compared to the proposed projected free surface, shown as a dashed line). In situation B, which occurs some 0.2 seconds later, the raised region has disappeared. This raised region is proposed to be the origin of the radial stripes (see main text). Images taken from the 9.375 RPM experiment.

pare, for example, the early onset of various phenomena in the pumice (multiple layers, collapses, free surface curvature) to the complete absence of certain behaviours in the millet (LDRs, SECCs, and KHIs).

However, it would be a stretch to try and draw qualitative predictions on lahar behaviour from these results. While it would be reasonable to assume that an ash-heavy flow would behave differently to an otherwise identical ash-light flow, there would remain a great number of uncertainties when trying to accurately predict flow characteristics. There remains a significant amount of work to be done before lab-based measurements like these could be used to make predictions. This work, should it be done, would hopefully prove very illuminating, should a large enough body of granular material types be thoroughly studied.

These future endeavours could be aided with comparison to field-based measurements of lahars - before, during, and after any events. In addition, the more information that

can be gathered about the solid materials available to a flow should help with future prediction efforts. (For example, the amount of ash involved in a volcanic eruption, and any sources of rocks/sand, *etc.*, in a potential lahar flow area.) However, these measurements would be afflicted by the same problems discussed in the opening chapters of this thesis Ð predictions of when and where a lahar would occur are extremely difficult, and as such obtaining thorough measurements before and during an event would be rare.

There is an indication from this work that the constituents of a natural flow would have a significant impact on its behaviour, but much work remains to be done before a laboratory-based approach can provide enough information that would be useful for hazard planners and other stake holders.

Chapter 8

Results IV - Wet Materials under Constant Velocities

8.1 Introduction

This chapter presents the results of the experiments in which the air was replaced, partially or fully, with water. This step was undertaken to create an artificial system that could be examined in the laboratory that would be closer to what is observed in natural debris flows, such as lahars. (In lahars, the fluid phase is water, rather than air. Geological flows with air as the fluid phase do exist - see pyroclastic flows, for example. But these are not addressed in this thesis.)

The substitution of air with water changes the mechanics of the system in a few key ways. The inter-particulate friction will be reduced due to the lubricating effects of the fluid. Additionally, the ratio of densities between the solid particles and the fluid phase changes dramatically, allowing the system to more easily fluidise. Finally, the increased viscosity of the fluid phase will reduce the velocity of the particles, changing the rate at which the system can accomodate changes in rotational velocity of the drum.

Presented here are the results for layer thicknesses and dynamic angles of friction in the steady velocity ash experiments, with the drum completely filled with air and water. Additionally, qualitative observations of the beach sand across various water fills are also given in this chapter.

8.2 Layer Thicknesses and Dynamic Angles of Friction in Wet Experiments

Though the PIV struggled with the wet experiments due to dust in the water or chaotic flow patterns, particularly the ones in which the drum was completely filled with water, some data were able to be obtained. Results are presented here. The ash, with its larger particulate size, was more tractable in the PIV software. As such it was possible to obtain layer thickness and dynamic angle of friction measurements for these sets of

experiments. The results are presented in Figures 8.2.1 and 8.2.2.

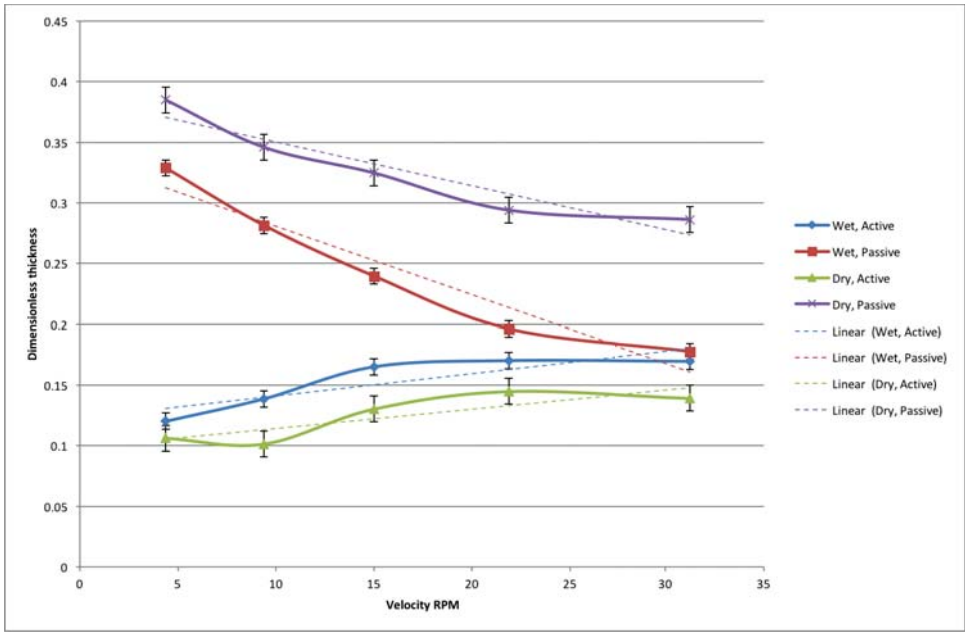

Figure 8.2.1: Dimensionless layer thicknesses for the ash, measured across dry and wet constant velocity experiments. Here, a wet experiment means that the air has been completely replaced with water. Layer thicknesses are non-dimensionalised by the radius of the drum. Layer thicknesses found from an average of several profile lines spaced 5° apart. Vertical error is the standard deviation for that experiment; horizontal is smaller than the point. Linear (dashed) relationships are shown to demonstrate general trends, rather than suggest a specific mathematical relationship. Curved lines between points are software interpolated by Microsoft Excel 2016.

8.3 Observation of the Varied Water Fill Level Experiments

The methodology for finding the saturation level of the coarse beach sand was presented in Section 3.4.5. Results here are only for the coarse beach sand. The various levels of water used are given in Table 8.1. Ash was not used for the varied fill levels as it was very difficult to remove all the air bubbles when calculating saturation for the material. As such, ash is only used in the wet experiments in which the entirety of the drum not taken up by the solid fraction is filled with water.

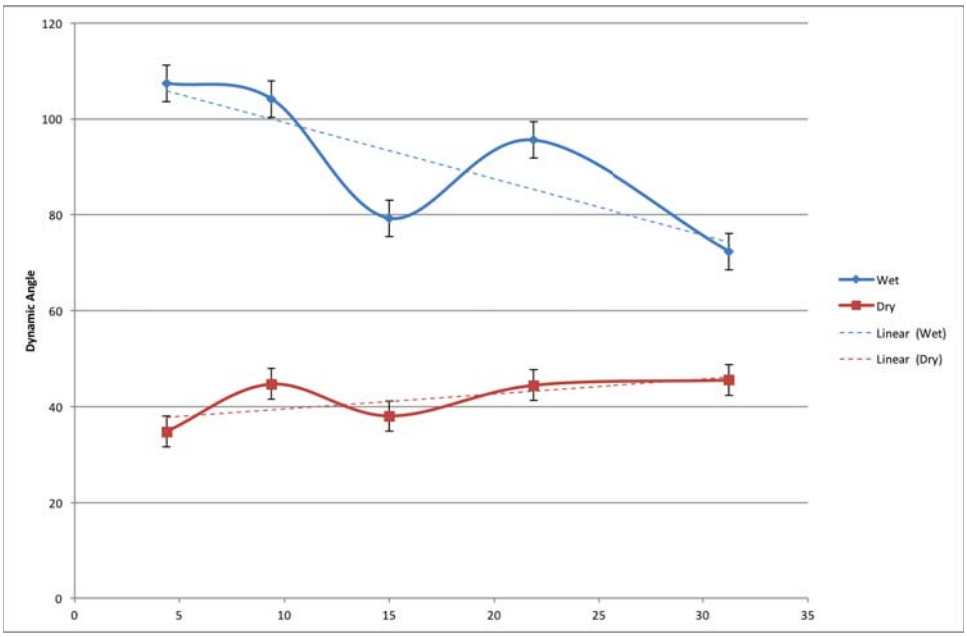

Figure 8.2.2: The dynamic angle (angle through which the centre of mass has been displaced) at various rotational velocities for the ash, in wet and dry constant velocity experiments. Here, a wet experiment means that the air has been completely replaced with water. Vertical error is the standard deviation for that experiment; horizontal is smaller than the point. Linear (dashed) relationships are shown to demonstrate general trends, rather than suggest a specific mathematical relationship. Curved lines between points are software interpolated by Microsoft Excel 2016.

8.3.1 Low Water Content

At the lower water levels (-5% below saturation) and exact saturation, the experiments behaved, perhaps predictably, rather differently to the dry cases. Probably due to cohesion forces supplied by the water content, the solid fraction moved essentially as a fragile solid body. The entire body of material would move with the motion of the drum, and once it passed a certain critical angle, a section of the material would shear off and begin to tumble down hill, fragmenting into smaller pieces as it went. This

Table 8.1: The various levels of water used for the qualitative beach sand experiments. The volumes in litres are given to threes significant figures. 0% is the exact volume needed (per one litre of beach sand) to reach saturation.

Percentage	Volume (L)
-5	0.356
0	0.374
50	0.561
100	0.749

shearing would occur earlier (*i.e.*, at a lower angle) in the exactly saturated case compared to the -5% case. The behaviour of these cases in demonstrated in Figure 8.3.1, and similar behaviour was observed by Tegzes et al. [2003].

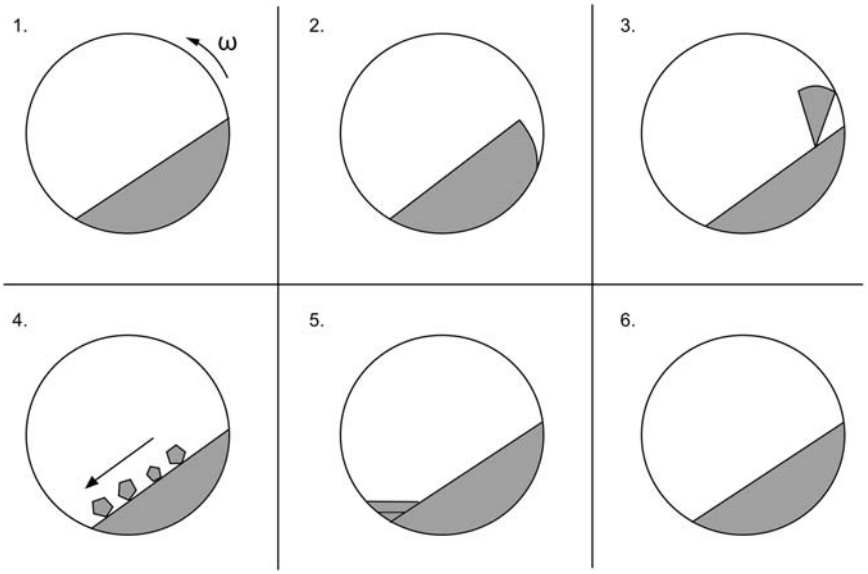

Figure 8.3.1: The behaviour of the material, in diagrammatic form, of the low water level experiments (-5% saturation, and exact saturation). 1) The material moves with the rotation of the drum as a solid body. 2) The material begins to peel away from the drum wall at some critical angle. 3) As the rotation continues, a section of the material shears away. 4) This section of material fractures into smaller sections, which then tumble downhill. 5) The smaller sections, upon reaching the wall of the drum at the toe-end of the main body of the material, are flattened. 6) The smaller sections are incorporated into the main body again, and the process repeats.

It was decided that the lower water level experiments would not be passed through the PIV software, as it no longer behaves as a granular material, as the water content at this level simply acts as a cohesive force between the particulates. While the behaviour displayed in these systems is interesting, it does not aid the particular aims of this project as the ratio of solids to water is much lower than a lahar in nature (Section 2.2.2).

8.3.2 Mid-level Water Content

At the mid-levels of water fill (+50% above saturation and one-to-one), a region of water was observed at the toe-end of the material (Fig. 8.3.2). The author suggests that this is perhaps a lab-scale analogue for the region of "clean" water pushed ahead of the main lahar body, as observed by Cronin et al. [1999] and Lube et al. [2012]. (Further correlation between the observed lab-scale and lahar behaviour is demonstrated by the lack of super fines in both cases as in the experiments these were purposefully removed, and the fact than the solid fraction in these mid-level fill experiments behaves in a non-cohesive manner, in contrast to the lower level water content cases. See Figure 8.3.1.) The water region had suspended fines within it, and predictably was larger at the higher water fill level. At the higher water fill level and faster rotational velocities, the occasional shearing block of granular material would enter the water region with enough momentum to cause a wave to propagate through the water. Where the water region met the granular matter (*i.e.*, the free surface), the interface was much less distinct than in the air experiments - the author suggests that this is due to some particulates being close to the density required to float. Finally, on occasion, air would get trapped in the material body, resulting in regions with a lower density than the main body. These bubbles would make their way out of the solid/water mixture region, before exiting rapidly from the water region.

Presumably lubricated by the water content, there were periods in these sets of experiments in which the body of granular matter simply slid, counter-rotationally, at the same rate as the drum.

8.3.3 Full Drum

Behaviour here is much closer to the dry experimental regimes, though the curved free surface occurs much earlier (Fig. 8.3.3). In contrast to the dry experimental regimes, the interface between the solid materials and the fluid phase is much less distinct, fea-

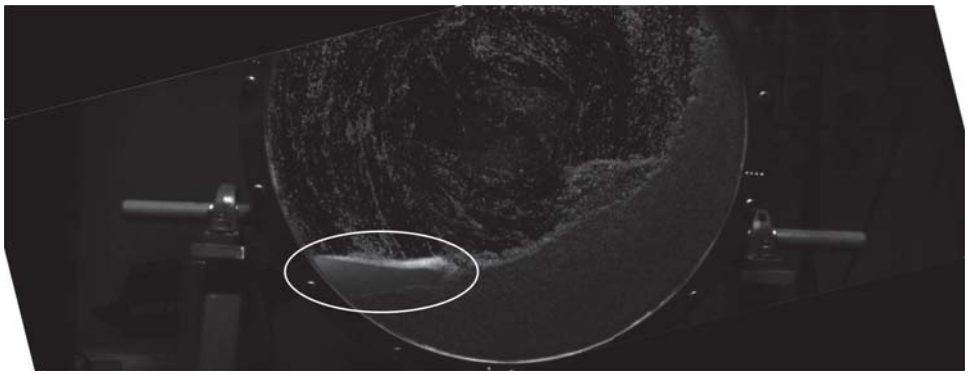

Figure 8.3.2: The "clean" water region (circled) observed in the mid-level water fill experiments (50% above saturation by volume). Drum is rotating at 4.375 RPM in a counter-clockwise direction. The material in this case is the beach sand. Unusual cropping of the image due to camera being rotated during the experiment.

turing billows of backwardly propagating material and plumes of fines from the toe-end of the material. (These "plumes" are assumed to be where the energetic active region meets the drum wall, and ejects the lighter particulates into the water. This is presumably the same process that produces the splashes observed in the dry experiments.) An interesting interface between the material moving passively with the drum rotation and that moving downhill was observed - at this point, it was sometimes observed that a rotating zone of material was established, circulating counter-rotationally to the motion of the drum (Fig. 8.3.4). These occur because the passively rotating region of the solid fraction includes the entirety of the toe-ward end of the solid materials, so that the material flowing downhill in the active region in these experiments does not flow over the passive region, but instead meets it head on, causing an interestingly shaped interface between them. It is at this interface that the counter-rotational zones (CRZs) would appear (Fig. 8.3.4). Note that the CRZs are not the same phenomenon as the SECCs noted earlier. There are two key differences: 1) the SECCs rotate in the same direction as the rotation of the drum (*i.e.*, clockwise or counter-clockwise), while the vortices (Fig. 8.3.4) are are counter rotational to the drum; 2) the SECCs form at the interface of the two main regions, while the vortices form where the active layer intrudes upon the passive.

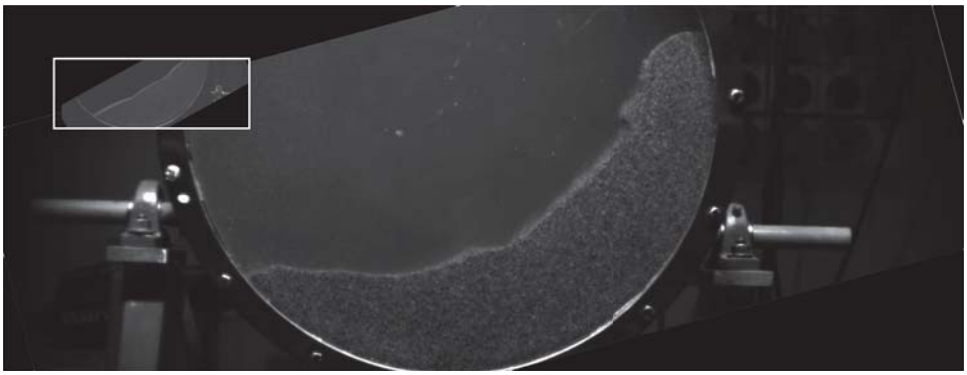

Figure 8.3.3: An illustration of the earlier on-set of free surface curvature in the water-based experiments. Shows the same material (beach sand), at the same rotational velocity (4.375 RPM), in the cases in which the drum is filled with water (main) and air (inset). While the free surface is curved in the water case, the dry case is still flat. In this case, the wet experiment is one in which the air has been completely replaced.

8.4 Temporary Centrifuging of the Granular Material During the Wet Acceleration Experiments

It was observed during the wet acceleration experiments that for high enough acceleration regimes, the granular material would temporarily enter the centrifuging regime before settling back out to cascading or rolling, depending on the target velocity and the length of time the target velocity was maintained for. Investigating this as a force balance question yields a number we designate as Ip, the ratio of the inertial impulse force and the torque impulse reaction force. When acceleration is zero and centrifuging occurs, Ip collapses to the more widely known Froude number, Fr, which can be defined as the ratio of the inertial impulse force and gravity. In this case, $Fr > 1$.

The temporary centrifuging state is not intended to help explain natural debris flow behaviour but is included as it was an interesting phenomenon that was observed, and it was felt it warranted further investigation. It will be of more interest to rotating drum investigators than those interested in natural debris flow mechanics.

The particle will stay at the surface of the drum if the outward centrifugal force is greater than the inward gravity force at the top of the rotation cycle (Fig. 8.4.1). Thus,

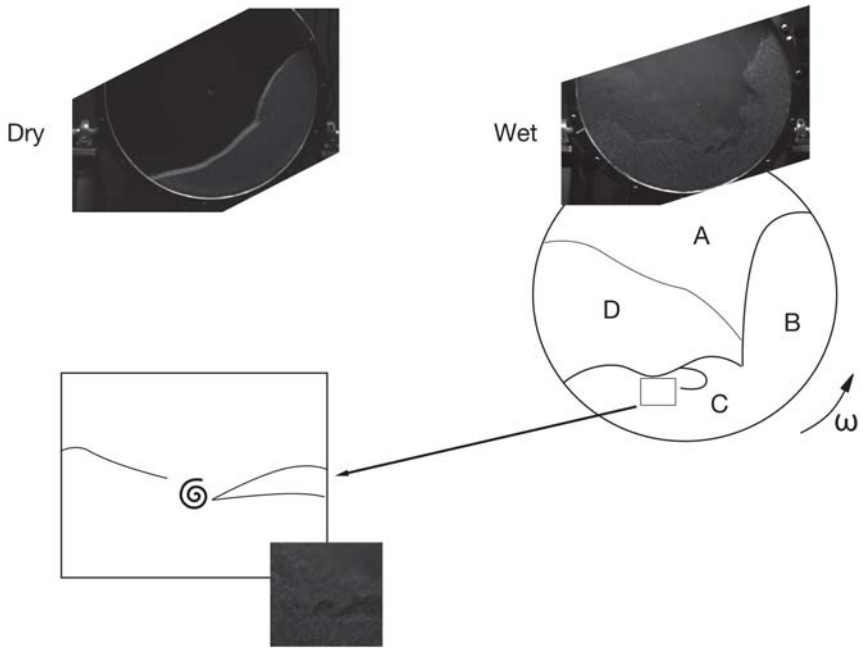

Figure 8.3.4: Comparison of the same material (beach sand) at the same rotational velocity (21.875 RPM), in which the interstitial fluid is air (left photograph) or water (right photograph), i.e, in each case there is only one fluid phase present. The cases are visually very distinct from each other, despite all other variables bar interstitial fluid being identical. The cartoon illustration of the drum shows a simplified structure of the flowing granular material in the wet case. Region (A) has a very low particulate concentration. (B) is the main body of the granular material, while (C) is the location of the subsumed interface between the passive and active regions of the material. The box here is shown in a zoomed cartoon fashion in the lower left of the figure, which illustrates the existence of the counter-rotational zone. (D) is the location of the backwardly propagating billows.

the criterion for falling off the surface of the drum is

$$F_{\text{gravity}} > F_{\text{centrifugal}} \tag{8.4.1}$$

For any position in the rotation cycle this is

$$F_{\text{gravity}} \cos\theta > F_{\text{centrifugal}} \tag{8.4.2}$$

where $\theta = 0$ at the top of the cycle. Substituting the forces, remembering that the centrifugal force has two components (one due to instantaneous rotational velocity, and

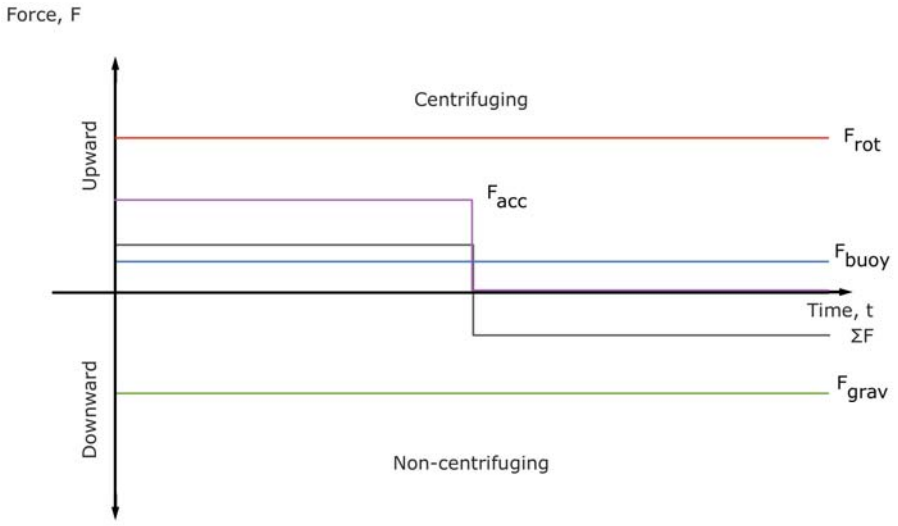

Figure 8.4.1: Forces on an imaginary single particle on the wall at the top of the drum during an accelerated experiment with water as the fluid phase. The criterion for centrifuging is that the forces on the particle in the upward direction are greater than that of gravity, the sole downward force. The forces acting on the particle are F_{rot} (due to linear rotational velocity), F_{acc} (due to rotational acceleration), F_{buoy} (buoyancy), and F_{grav} (gravity). The sum of these forces is ΣF. When ΣF is greater than zero, the upward forces are dominant and centrifuging occurs. In an accelerating experiment, F_{acc} is applied for a certain amount of time - if during this time the acceleration applied is rapid enough, then the particle can temporarily enter the centrifuging state.

the other due to angular acceleration), and simplifying gives

$$g\cos\theta > \omega^2 r + 2\pi\alpha r \tag{8.4.3}$$

Dividing this through by $\omega^2 r$ yields a form of the criterion for a particle to fall away from the drum wall containing the inverse of the Froude number, Fr = $(\omega^2 r)/g$ [Boateng and Barr, 1997] and another dimensionless quantity, which for the purposes of this study is called the inverse of Ip = $(\omega^2)/\alpha$

$$\frac{g}{\omega^2 r}\cos\theta > 1 + \frac{2\pi\alpha r}{\omega^2 r} \tag{8.4.4}$$

or

$$\frac{\cos\theta}{\mathrm{Fr}} > 1 + \frac{2\pi}{\mathrm{Ip}} \tag{8.4.5}$$

The Froude number and Ip are defined as the force ratios

$$\mathrm{Fr} = \frac{\omega^2 r}{g} \tag{8.4.6}$$

$$\mathrm{Ip} = \frac{\omega^2}{\alpha} \tag{8.4.7}$$

When there is no acceleration, $1/\mathrm{Ip} = 0$, and so centrifugation occurs at the well-known $\mathrm{Fr} > 1$. When acceleration does occur (without slippage), it is clear that the particle bed can easily centrifuge even though the angular velocity may be well below that which satisfies $\mathrm{Fr} = 1$.

8.5 Discussion

The active layer was thicker and the passive thinner for the wet experiments, probably due to the lubricating effect of the water and the reduced density ratio between the solid and fluid phases. This reduced density ratio manifests as a greater buoyancy force on the particulates, allowing for easier initiation of flow in the granular material.

The dynamic angle of friction for the wet case was much higher and displayed a reversed linear trend compared to the dry cases. Why would this be? A higher angle is relatively easy to explain - a reduced density ratio means the particulates in these experiments had much greater buoyancy, and would much more readily flow when subjected to external forcing, *i.e.*, the rotation of the drum.

The temporary centrifuging displayed in these experiments was a particularly interesting and unexpected phenomena. While only industrial (artificial) flows, *i.e.*, those in a drum, are likely to display true centrifuging behaviour like this, there could also be lessons learned for natural flows, too. For example, it is possible that a lahar or other water-based debris flow found in nature, when subjected to rapid acceleration (i.e, changes in bed angle or channel direction) that temporarily very chaotic behaviour will occur, and the internal structure of a flow will be completely changed until equilibrium is reached once again. It is possible that the temporary centrifuging, in a lahar setting, is responsible for the stripes of erosion seen in Procter et al. [2010b], though this is left for future studies for verification. Temporary centrifuging is, at the very least, evidence of the great change in flow behaviour of a granular material when the interstitial material is changed, and the density ratio changes with it.

The experiments with varied water fill were hard if not impossible to PIV: as such, this represents a rich vein for potential future research as partially wet granular materials are closest analogue to lahars and many other natural flows. Significant amounts of work may be needed to create a system in which water can be used as the fluid phase, but the imagery remains PIV-tractable at all stages.

Chapter 9

Discussion

Here the results presented in the preceding chapters are discussed in greater detail. Possible explanations for the results and phenomena observed are given, using insight from across all the experiments undertaken, as well as the particulate characterisation.

9.1 Restatement of Aims

The aim of this project was to quantitatively understand erosion and deposition processes in unsteady granular flows. Laboratory experiments were undertaken using a rotating drum. This thesis aimed to cover the three main research objectives:

1. Characterize granular solid-liquid phase transitions for a wide range of naturally occurring flow regimes in dry granular systems using solid phases with a natural range in particle shape, size and roughness.

2. Determine the role of the main parameters that control the phase transitions, and erosion and deposition, in variably unsteady granular flow situations.

3. Quantitatively determine the influence of specific gravity and fluid drag on granular phase transitions by comparing dry and wet systems.

Discussion of these research aims and other findings reached during this research will be covered in this chapter. Over-arching conclusions and possible avenues for future research will be presented in the next chapter.

9.2 Consideration of Material Behaviour

Here are presented thoughts on the behaviour of granular materials within a rotating drum, across multiple experiments. Investigated variables include material type (i.e,

size distribution, roughness, density, etc.), rotational velocity, water content, and accelerated cases.

9.2.1 Overview

The internal structure of a granular material in a rotating drum was studied quantitatively. It was demonstrated that the material has a more complex internal structure than commonly presented in the literature (*e.g.*, Dubé et al. [2013]; Komatsu et al. [2001]; Yamane et al. [1998]). A flowing material will consist of continuous processes, such as active layer, passive layer, sheared boundaries, SECCs, and depending on the velocity, KHIs. Intermittent/pseudo-periodic phenomena, such as avalanches, collapses and splashes were also demonstrated. The SECCs and KHIs, both of which are discussed in more detail later, are proposed to be new phenomena, we believe previously unreported in the literature.

The general behaviour of a granular material can be summarised as follows: as the rotational velocity increases, the thickness of the active layer increases. The opposite occurs for the passive region. Also, the free surface will begin to display curvature once a sufficient rotational velocity has been reached, which confirms findings by Orpe and Khakhar [2001]. Collapses occur at the uphill end of the flow, and result in avalanches flowing down the free surface. If these reach the downhill drum wall with sufficient velocity, a splash can occur, in which particulates are ejected from the flow. As the rotational velocity is increased further, then an LDR (low-density region) can occur, as the material moves towards the cascading Mellmann regime.

Where the active and passive regions meet are the sheared layers. Here the velocity profile is different again. This results from the opposed motion of the two layers. It is at the sheared layers that we propose erosion and deposition takes place, as part of our lahar-flowing-over-an-erodible-bed analogue.

9.2.2 Flow Regimes as Observed and in the Literature

Differences were noted between the flow regimes illustrated in the literature, for example in Mellmann [2001], as illustrated in Figures 9.2.1 for the ash and 9.2.2 for the beach sand.

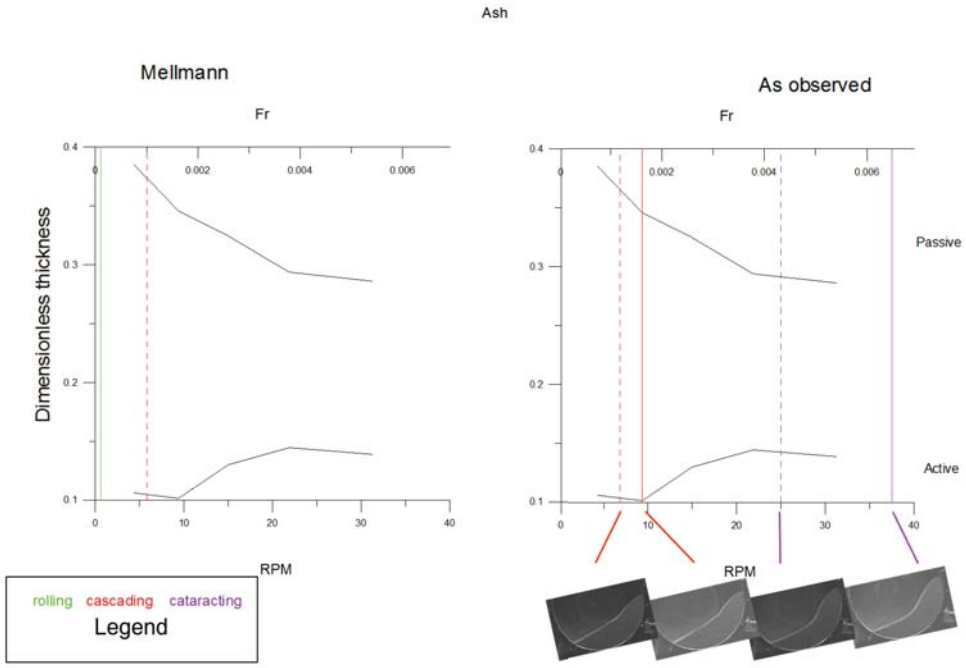

Figure 9.2.1: An illustration of the flow regimes as they were observed in the ash in this study and as they are presented in Mellmann [2001]. The horizontal axis is the velocity, presented as both RPM and the Froude number equivalent. The vertical axis is the dimensionless thickness of the layer in question - the upper line is the passive, the lower the active. Thicknesses were non-dimensionalised by the drum radius. Coloured lines represent the velocities at which the Mellmann regimes in the legend can be said to occur. Dashed lines indicate the regime could be argued to have been reached, while a solid line is definite. Images of the experiments in-progress are presented rotated to true horizontal.

The classical Mellmann regimes are as follows; sliding, surging, slumping, rolling, cascading, cataracting, and centrifuging (Table 1, Mellmann [2001]). The experimental equipment for this study was designed to replicate the rolling and cascading regimes, as these regimes were considered to mostly closely resemble a lahar (or other natural

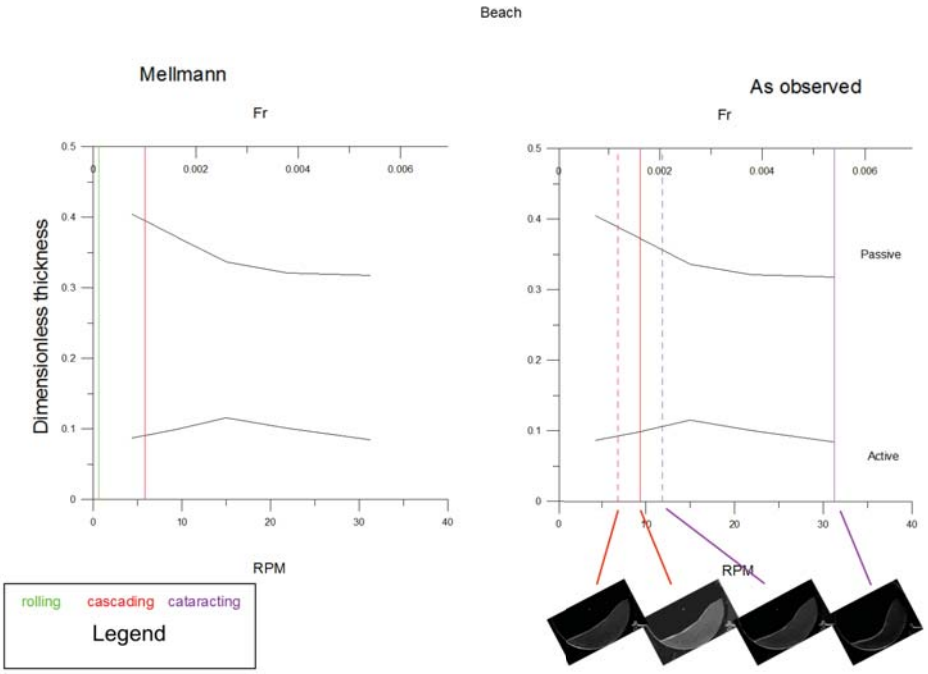

Figure 9.2.2: An illustration of the flow regimes as they were observed in the beach sand in this study and as they are presented in Mellmann [2001].The horizontal axis is the velocity, presented as both RPM and the Froude number equivalent. The vertical axis is the dimensionless thickness of the layer in question - the upper line is the passive, the lower the active. Thicknesses were non-dimensionalised by the drum radius. Coloured lines represent the velocities at which the Mellmann regimes in the legend can be said to occur. Dashed lines indicate the regime could be argued to have been reached, while a solid line is definite. Images of the experiments in-progress are presented rotated to true horizontal.

granular flow). In some cases, at high enough velocities, it was found that the cataracting phase was also possible. Only during the wet experiments was the centrifuging case possible. The implications of this are explored earlier (Section 8.4).

In this study, changes between the regimes were identified by the onset of key phenomena. The rolling regime is said to be in effect when the free surface is flat and smooth, and the two-layer approximation holds. The material was considered to be in the cascading regime when the free surface becomes curved. Also associated with this regime are the onset of SECCs, collapse events and avalanches, the inflection points, and mul-

tiple layers (*i.e.*, the two-layer approximation no longer applies). Finally, the cascading regime is entered when the LDR is extant and continuous. The LDR is associated with a secondary phenomena, the KHIs. The LDRs provide the starting conditions for the proposed KHIs by establishing the two regions of differing densities moving against each other.

Additionally, both the beach sand and the ash show a levelling off of collapse periodicity (Fig. 7.3.12) at the 12 RPM mark, which is associated with the cascading regime (Figs. 9.2.1 and 9.2.2). Both materials also display a peak in the dynamic angle of friction at around the 10 RPM mark (Fig. 7.3.13), suggesting that the increased rotational velocity is compensated for by the material moving further up the drum wall until it enters the next (*i.e.*, the cascading) regime.

It is possible for a material to be flowing in a way that puts it between two regimes. For example, at 31.25 RPM, the ash displays occasional LDRs as well as the indicators of being in the cascading regime, and as such could be considered to be in a transitional regime.

9.2.3 Collapse Periodicity

As displayed earlier in this thesis (Sections 5.2.5 and 7.3.5), the amount of time between subsequent collapses reduces as a function of velocity, but reaches a minimum value around the 12 RPM mark. This happens in both the ash and the beach sand. We propose that this is due to mechanical limits of a granular material. As the rotational velocity increases, the material is forced to flow at greater rates. Its own mechanical and physical properties, however, presumably coupled with the limitations imposed by the flow channel, means that there is a maximum rate at which mass can be forced to flow in a granular system. Once this maximum rate is achieved, other systems have to come into place to compensate for any further forcing of the system, *i.e.*, increased rotational velocity. One possible mechanism is the free surface curvature.

The free surface curvature hypothesis is far from confirmed, however. In Figure 7.2.1, the free surface curvature occurs much earlier than around the 12 RPM mark in both of the materials; at 6.875 RPM in the beach sand, and 9.375 RPM for the ash. In Figure 9.2.2, it is proposed that the beach sand enters the cascading regime at roughly the 10 RPM mark. Of course, it is possible that two mechanisms for compensating for increasing rotational velocity are capable of occurring at the same time, *i.e.*, while the increased thickness for the active region begins first, the free surface curvature also comes into play before the active region becomes unable to cope with the rotational velocity. One mechanism follows another, but with an interim period in which both are active.

9.2.4 Dynamic Angle of Friction

The dynamic angle of friction is a measurement of the centre of mass for a moving system, and is particularly relevant to a granular material within a rotating drum. The dynamic angle of friction was found for both materials across multiple velocities (see Sections 5.2.6, 7.3.6, and 8.2.).

In general, the beach sand shows higher dynamic angles of friction for the same rotational velocity when compared with the ash. We ascribe this to the difference in flow function (f_f), which is 1.15 for the ash and 1.03 for the beach sand (Table 4.1). The lower flow function for the beach sand means that it finds it easier to flow. As such, when the drum begins to turn, this increased ability to react to changes in drum velocity means the material moves further around the outside of the drum.

Both the ash and the beach sand display a hump in the dynamic angle of friction at around the 10 RPM mark. We ascribe this to a change in flow regime, similar to how the collapse periodicity reaches a minimum value at 12 RPM. As the rotational velocity is increased, the material is forced further around the drum from the resulting centrifugal forces. However, when the material moves from the rolling to cascading phases, *i.e.*,

the free surface curvature begins to be displayed by the material, part of the mass flux forcing by the rotation of the system is compensated for by this new mechanism. As such, the dynamic angle of friction drops slightly, before continuing to rise again.

9.2.5 Material Dilation

It was observed in the graphs (see Section 7.3.4) that show the area of the active and passive layers and their sum that, with some variation, the general trend is that the material expands as the rotational velocity increases. We assumed that this would be limited to the flowing region, as the passive region would have the flowing on top of it, as well as centrifugal forces. As such, we were able to come up with measurements for the dilation of the active region as the rotational velocity increases, see Table 9.1.

Table 9.1: The dilations of the beach sand and the ash, as percentages of total volume. "Maximum to minimum" uses the largest and smallest areas from the beach sand and ash, while "Start to finish" uses the first and last, *i.e.*, from the lowest and highest rotational velocities.

Material	Maximum to minimum, %	Start to finish, %
Beach sand	4.6	1.7
Ash	6.7	2.1

We present two dilation factors for each of the ash and beach sand. This is due to both materials displaying a maximum dilation that didn't necessarily coincide with the fastest velocity, and *vice versa*. The two dilation factors presented show the maximum dilation, *i.e.*, the largest possible dilation factor using the data to hand, and the "start to finish" dilation, in which the dilation is calculated from the slowest to fastest rotational velocity data sets.

Material dilation in the flowing region was measured as it allows us to quantitively describe a key behaviour of granular materials in a non-invasive way. As dilation increases, the number of collisions will decrease, leading to a different friction factor.

Material dilation has another bonus, in that it helps, perhaps in a small way, for a rotat-

ing drum to simulate a natural granular flow. In such a situation, the flowing region will intuitively be less densely packed than the material in the bed over which it flows. Having the active region in a rotating drum also dilate to accommodate for motion means the material in a drum more closely resembles that which is found in nature.

9.2.6 Mass Flux

Both materials display an increased mass flux when the rotational velocity is increased. (See Figures 7.5.1 and 7.5.2.) The beach sand shows more dynamic mass flux graphs than the ash, and there is generally a much greater increase in mass flux for the beach sand when an avalanche passes when compared with the ash.

9.2.7 Temporary Centrifuging

It was observed during the wet acceleration experiments that for high enough acceleration regimes, the granular material would temporarily enter the centrifuging regime before settling back out to cascading or rolling, depending on the target velocity and the length of time the target velocity was maintained (see Section 8.4). We studied this problem under the paradigm of a force balance question, and this gave a number Ip, which is the ratio of the inertial impulse force and the torque impulse reaction force. Ip simplifies to the more widely known Froude number (Fr) when there is no acceleration applied to the system.

The temporary centrifuging is interesting from a granular mechanics point of view as it suggests that granular materials have a time dependence to their behaviour. It was demonstrated that it is possible to force a wet granular system into the centrifuging regime despite the instantaneous rotational velocity not being at a high enough value. After time had passed, the system returns to a state that has been described in the literature before. While this finding may not be particularly applicable to natural flows, it

should be of interest to industrial applications, and gives important insight into granular mechanics. At the very least, it should be a consideration for future granular material research, that the current state of a granular system in a drum depends on more than just the current rotational velocity.

9.2.8 Differences Between Materials

There were clearly discernible differences between the materials used in this study, even from a purely qualitative point of view. For example, the millet never displayed low-density regions, KHIs, or periodic collapses. This is perhaps due the material's high smoothness, as indicated by the fact it has the lowest angle of repose of all four materials (26.6°, Table 3.2). The material is smooth enough that particulates do not catch on their neighbours in the same way as the other materials. This leads to no collapses, and perhaps means the material enters the cataracting phase (*i.e.*, when the low-density region becomes apparent) much later than the other materials.

The millet contrasts strongly with the pumice. The pumice has the highest angle of repose of the four materials, at 33.4°. This high roughness, which allows the material to be more self-supporting, also means that the friction during a flow is higher. The pumice displays free surface curvature even from the lowest rotational velocity studied. The material is less easy-flowing than the others, and therefore other mass flux mechanisms have to compensate for increased rotational velocity earlier than the other materials. Like the millet, the pumice has a phenomenon that it does not display - the SECCs. The lack of the circulation cells is a mystery to the author, and perhaps represents an area for future investigation as SECCs are probably relevant for mixing efficiency questions; which materials display SECCs, and under what conditions?

Layer Thickness Differences

The ash displays generally thicker active regions and thinner passive regions than the beach sand. This could be due to the differences in size between the two materials, *i.e.*, a material with larger particulates forms a larger active region, though why the active region would be preferred to the passive in this case is not clear.

Noise on Velocity Profiles

Multiple velocity profiles were constructed for this study, for both the ash and the beach sand. It was observed that the beach sand velocity profiles were generally noisier than the ash counter-parts (Figures 7.3.2, 7.3.1, and 7.3.3 to 7.3.8). It is possible that this is due to the beach sand being a finer material than the ash, which results in the ash being easier for the PIV software to track, which as a result mean the data is less prone to errors. However, the beach sand, unlike the ash, has a good colour variation, with some particles presumably acting as tracers, which would aid in PIV accuracy. It could be due to the lower flow function of the beach sand (1.03 compared to the ash's 1.15). But why would a material which is more receptive to flow be more prone to stops and starts, presumably as the material catches on itself? Additionally, is a difference of only 0.12 (1.15 - 1.03) high enough to explain the much nosier velocity profiles shown by the beach sand? This is especially troublesome when the flow funtion is subject to an amount of error that is difficult to quantify. This is an area that would benefit from future research.

Mass Flux Comparisons

Similar to the increased noise on the velocity profiles of the beach sand, the sand's mass flux presents much greater variation at the point where an avalanche is passing by. The mass flux for the sand is also, in general, greater than the ash flux for the comparable

velocity, barring the near identical mass flux of around 3.5 kg s^{-}1 for 9.375 RPM. (See Section 7.5.)

While the similar mass fluxes for both materials at the lowest investigated rotational velocity, the greater mass fluxes for the beach sand is readily explained. While the beach sand has the lower density, which would incline one to thinking it would also therefore have the lower mass flux, the beach sand is more inclined to flow. The beach sand has a lower flow function (f_f), a lower internal angle of friction (Table 4.1), generally lower dynamic angles of friction (Table 7.3.13), and a lower angle of repose (Table 3.2). This all points to a material with a good ability to flow, which compensates for its lack of density when compared to the volcanic ash.

9.2.9 Changes in Behaviour with Interstitial Fluid

Changing the fluid phase from air to water resulted in noticeably different behaviour in the flowing granular material. One way in which the system is greatly changed by the fluid phase switch is the density ratio between host fluid and the granular material in question. This is demonstrated by Table 9.2. The densities of the solid materials are presented earlier in this thesis (Table 3.3).

Table 9.2: The ratios of the densities of the main materials used in this study, granular material over fluid phase. Changing the fluid phase from air to water shows a markedly reduced ratio. Data are presented to three significant figures. The densities of water and air were taken as 1000 kg m^{-3} and 1.275 kg m^{-3}, respectively, as they'll be presented in any scientific reference text.

Solid / Fluid	Air	Water
Beach sand	2320	2.96
Ash	2380	3.03

The replacement of air with water produced measurable effects on the dynamic angle of friction and the layer thicknesses. As discussed earlier, (see Section 8.2), the ash displayed a much higher dynamic angle of friction in the wet experiments (Figure 8.3.1), with a generally reversed trend when compared with the dry case. The higher

dynamic angle of friction of the wet experiments is probably explained by the density ratio change; the increase in buoyancy due to the lower density ratio means that the particulates will more easily start to flow.

A similar buoyancy effect can also be used to explain the differences in layer thicknesses between the wet and dry experiments. When water replaces air as the fluid phase, the passive region gets thinner and the active thicker. With their increased buoyancy, the particulates find it easier to flow, and as such the active region is larger than the same material with air.

Low amounts of added water stopped the material flowing as a granular material. Low water content experiments move in a shearing/slumping motion, and as such cannot be analysed with PIV. As such, results are presented in this thesis for completeness' sake (see Section 8.3.1), but are not explored further. However, larger water content experiments do move in a similar fashion to granular material. If the cloudiness issue could be overcome, mid- to high-level water content granular material experiments could present extensive research possibilities, especially as they are the closest analogy to natural flows. Indeed, the mid-level experiments presented in this thesis even display a clean water region at the head of the granular flow, as lahars do in nature (Fig. 2.2.1).

Finally, the addition of water enabled the temporary centrifuging, as explored in Section 8.4.

9.3 Relating Findings to Natural Flows

Here is discussed potential applications of the findings to natural flows, particularly lahars, and with a focus on the implications for hazard planning. For example, the accelerating cases displayed a hysteresis with the constant velocity cases (see Section 6.2.1). Could this finding be incorporated into danger mitigation efforts? Indeed, would a

serpentine overflow channel help reduce the destructive capability of a lahar or other natural mass flow? A serpentine channel, placed correctly before a lahar event, would cause a lahar to have to constantly slow down and re-accelerate. The hysteresis between steady state cases and the accelerating equivalents should mean the lahar does less damage. While even the best defences may be swamped by a sufficiently large lahar, these are very difficult to predict - however, in locations in which small-but-frequent lahars occur, this finding may be of more interest to stakeholders.

9.3.1 Clean Water Region Analogue

Regarding the "clean water" region in Figure 8.3.2 - could this be an analogue for the clean water region observed preceding lahars [Cronin et al., 1999]? The author is sceptical, as the phenomenon in a rotating drum is likely an artefact of the separation of the solid and liquid phases due to the rotation of the drum, rather than a true clean water region being pushed ahead of the main body. However, this is left to future researchers. If it could be shown to act as analogue for the clean water region, then the rotating drum would cement itself as a very useful piece of equipment in experimental volcanology and lahar mechanics studies. One could imagine a rotating drum study for a system with a clean water region, in which the inner lining of the drum is changed. The researcher would then study the differences in behaviour between the main body of the flowing material and the clean region as they pass over the different inner linings. This, then, would hopefully illuminate the mechanics of a lahar, complete with the preceding clean water region, as it meets various types of obstacles in a flow channel. In turn, this could inform the shape and structure of sabo dams in the future (Fig. 2.3.2).

9.3.2 Implications for Hazard Planning

Hazard mitigation efforts may have to take into account a much larger range of variables than previously thought. As well as debris type and availability [Doyle et al., 2010; Major, 1997; Pierson, 2005], along with channel gradient, hazard planners may want to consider the sinuosity of a potential channel, the water availability and whether or not this could change (rain, lake outbreak, lahar meeting a river, etc. [Lecointre et al., 2004]), and the history of a lahar as it moves downhill. True estimates of a lahar's destructive capability as it flows downhill may require multiple monitoring stations [Vazquez et al., 2014].

For example, it has been observed that the collapse periodicity of a granular material in a rotating drum reaches a maximum value and then levels out (Fig. 5.2.11, see also Sections 5.2.5 and 5.4.3); if this is true for natural phenomena as well, would it imply that a lahar (of a certain water and solid content, and a given topographical layout) would have a maximum destructive capability? This is suggested because the collapse periodicity, which initially starts out decreasing with velocity eventually levels out. This implies that a granular material has a mechanical limit to the rate at which it can be forced to flow. (This could be considered similar to the way in which a granular material can choke in a hopper.) If a natural granular flow also has a certain mechanical limit, then a lahar of certain physical characteristics would have a maximum velocity - with a known density, and hence mass flux, this maximum velocity could indicate a maximum destructive capability. Hazard planners, with sufficiently detailed knowledge of water availability and the types of solid fraction available in a specific location could advise other stake holders (residents, governments, charities, etc.) on the maximum likely lahar event.

Further evidence for this mechanical limit to granular flow is given by the different rates at which the active and passive regions change thicknesses. (See, for example, Figure 6.2.1.) The active layer gains thickness slower than the passive layer loses it -

as such, the increased rotational velocity of the drum is being compensated for by the material in another way, *i.e.*, by spreading around the drum interior. Applying this to a natural flow, without another way to compensate for an increased channel angle (analogous to the increased rotational velocity of the drum), the velocity of a lahar would reach and maximum and stall.

However, while this study took steps to make the laboratory analogue as close as possible to the natural case, care must be taken when applying the results of this study to research into natural equivalents. A rotating drum will never be a perfect analogue for a flow on a mountainside. For example, while the author uses collapse periodicity as evidence for a mechanical limit to a granular material's ability to compensate for increased rotational velocity in a rotating drum, and hence a similar limit to a lahar's destructive capability, collapse periodicity itself only occurs because of the repetitive and enclosed nature of the experimental set up used. Further study is required to verify the veracity of the extrapolation presented here.

The author suggests the term "unconstrained choking" to cover the suggested phenomena of a mechanical limit to granular flow. This comes from choking, well known in industrial uses of granular materials, and the fact that in this case the choking (*i.e.*, the point the material cannot be forced beyond) occurs in open channels rather than closed.

9.4 New Phenomena

Here I discuss the three of the new phenomena found in this study, the Kelvin-Helmholtz instabilities (KHIs, Section 6.3.2), self-enclosed circulation cells (SECCs, Section 6.3.1), and the counter-rotational zones (CRZs, Section 8.3.3). The other potentially new phenomena, the radial striping and pumice jets, were not subject to the same level of investigation. They are covered in Section 7.6.6 and Appendix B, respectively.

9.4.1 Kelvin-Helmholtz Instabilities

These phenomena appear in two different ways; as a laterally propagating wave, and as a fluctuating interface between the dense passive region of rotating drum granular material flow, and the low-density region (LDR) of material that occurs as the material starts to enter the cascading regime [Mellmann, 2001]. There are several of the laterally propagating waves between each occurrence of a fluctuating interface. This interface fluctuates whilst maintaining an average position, then forms a peak at its centre, forming what may approximately be called a bell curve. This curve will eventually "burst", a colloquialism that we use to describe the moment at which the clearly defined interface boundary rapidly (perhaps near instantaneously) becomes indistinct. The clearly defined fluctuating interface that was the starting point of this description then reforms, and the sequence begins again. We refer to these phenomena as Kelvin-Helmholtz instabilities because they occur at the interface between two regions of differing density which are moving at different velocities, which is the classic scenario for a KHI to take place.

The main trend within the KHI behaviour in the beach sand is as the rotational velocity is increased from 25 to 31.25 RPM, the instabilities become larger and more energetic in their motions. However, when the velocity is increased to 37.5 RPM, the instabilities become slower and smaller in extent, though still over all larger than they were at 25 RPM. The exception to this is the size ratio (circularity) which drops even further (Fig. 6.3.9) due to the general decrease in vertical extent. It seems reasonable to assume that the higher velocity cases are being dampened by the increased rate of material turn over.

The area occupied by a KHI event increases and then decreases again with increasing rotational velocity. It is possible that this is due to a change in flow regime, and part of the increased mass flux required by the increased velocity is being compensated for by the shift from the rolling to cascading regimes.

A much stronger relationship, in this case linear, is shown by the rate at which KHI events occur as a function of rotational velocity.

The phenomena appear to be unobserved in granular materials, presumably this is because most work on rotating drums focus on relatively low rotational velocities [Bonamy et al., 2002; Chou et al., 2010]. Workers that do look at higher rotational velocities tend to be interested in heat flow through the material [Gui et al., 2013; Komossa et al., 2014; Ngako et al., 2014], rather than its flow. In many of the KHI measurements, only three sets of data were analysed for these graphs due to time constraints - expanded data sets in this area may be a valid area for further exploration.

The phenomena could have several explanations; a) de-aeration event; b) shockwave; c) or the granular flow equivalent of a Kelvin-Helmholtz instability, or possibly d) a completely new phenomena that requires its own description.

9.4.2 Self-Enclosed Circulation Cells

Whilst running the experiments, it was visually observed that there were zones of enclosed circulation with along the flowing/passive boundary (see Section 6.3.1). These zones were initially expected to be observational artefacts, or optical illusions. However, after running PIV analysis on the experiment footage, zones of circulation could be clearly seen along the boundary, as were observed by eye.

Self-enclosed circulation cells are usually elliptical in appearance. They are not static, but appear oscillate in a pseudo-random/pseudo-periodic manner around a mean position. On average, an elliptical self-enclosed circulation cell measures around 1.75 cm in height (minor axis) and is approximately 4.3 cm in length (major axis). Their average area is 2.5×10^{-3} m^2. See Table 9.3, below. The figures were found using the same coarse beach sand as detailed earlier, with a standard fill factor of 0.25.

The mechanics and nature of these "self-enclosed circulation cells" remains a mys-

tery to the authors. Initial findings are presented here stimulate discussion and further study of these cells among the community. As a transfer of mass between layers, are they the mechanism by which Ding et al. [2001b]'s mass transfer rate E is enacted?

If, in the cases where there appears to be multiple self-enclosed circulation cells, the areas are totalled, then the graph as presented in Figure 9.4.1 is obtained.

9.4.3 Counter-Rotational Zones

The CRZs were observed in the high-level water experiments (see Section 8.3.3). They occurred where the energetically over-turning material (which would become the active region) met the passively rotating region. The result is a small region in which the material rotates counter to the rotation of the drum.

As the wet experiments were difficult to analyse with PIV, no quantitative data is available in this study for the counter-rotational zones. However, if this difficulty could be overcome, then these zones could present an illuminating study in themselves. It seems reasonable to suppose that the CRZs would be analogous to the behaviour of a natural flow as it tumbles over a lip, or hits a rock, for example. Such counter-flow motion in nature would presumably lead to interesting implications for the channel bed at that location.

It is reasonable to assume, given the fact that the CRZs only occur in the water-based experiments, that these phenomena will be of particular interest to those studying underwater granular flows.

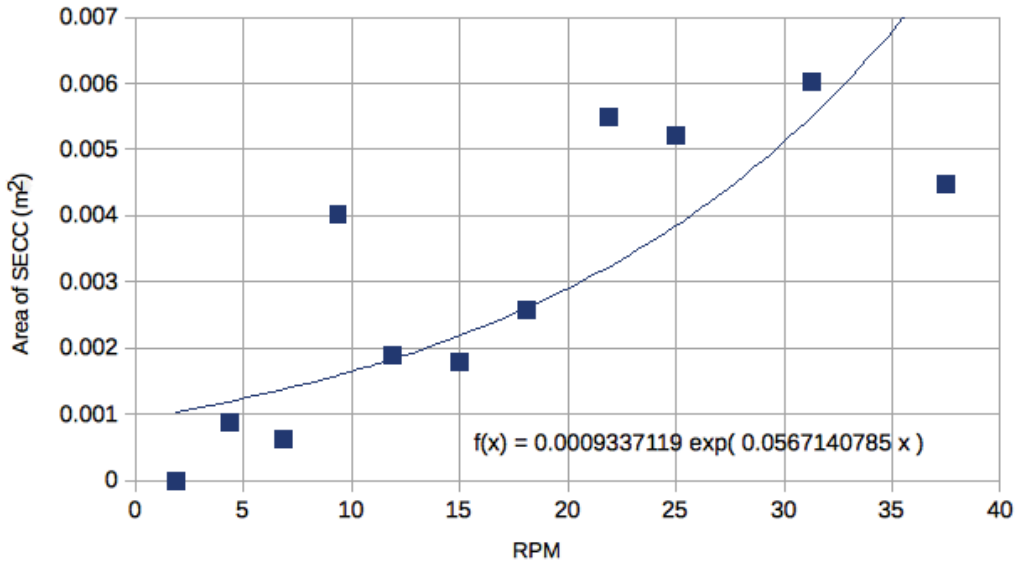

Figure 9.4.1: Plotting the rotational velocity versus the total area of all the self-enclosed circulation cells (SECCs) found in the PIV vector map for that velocity. Error for the rotational velocity is smaller than the point. Equation for the line of best fit is presented on the figure.

9.5 Unsuitability of Hydrodynamic Models

"If the bulk solid were to behave like a Newtonian fluid, the stresses in the horizontal and vertical direction (and in all other directions) would be of equal magnitude. In reality, the behaviour of a bulk solid is quite different from that of a fluid, so the assumption of analogies is often misleading." From Powders and Bulk Solids *(Springer, Berlin, 2008) by D. Schulze.*

One thing that has become clear during this project is that the granular matter community would find it beneficial to move away from treating granular materials as a type of liquid; there has been some discussion about this in the literature [Boudet et al., 2007; Bougie et al., 2002] but no consensus has been achieved [Abrahamsson et al., 2014]. This idea is not a new one - see the quote from Titus Carus at the start of this thesis.

The problem with liquid analogues for granular materials arises, in part, because granular materials are neither micro- nor macroscopic in nature; they are best described as

Table 9.3: The attributes of the self-enclosed circulation cells, as they appeared for the rotational velocities undertaken in this work. No data are presented for 1.875 RPM, as no cells appeared at this rotational velocity. Note that 15 and 18.125 RPM have multiple self-enclosed circulation cells (two and three, respectively). Also note the increased circularity of these multiple cell velocities.

RPM	Minor (m)	Major (m)	Area (m^2)	Circularity
4.375	0.0105	0.0269	0.0009	0.3889
6.875	0.0085	0.0231	0.0006	0.3667
9.375	0.0114	0.1121	0.0040	0.1020
11.875	0.0122	0.0493	0.0019	0.2483
15.000	0.0194	0.0187	0.0011	0.9649
15.000	0.0146	0.0139	0.0006	0.9535
18.125	0.0162	0.0165	0.0008	0.9800
18.125	0.0159	0.0165	0.0008	0.9600
18.125	0.0169	0.0172	0.0009	0.9808
21.875	0.0225	0.0780	0.0055	0.2882
25.000	0.0293	0.0565	0.0052	0.5192
31.250	0.0282	0.0679	0.0060	0.4150
37.500	0.0223	0.0640	0.0045	0.3485
Mean	0.0175	0.0431	0.0025	0.5781

mesoscopic [Song et al., 2014; Wu et al., 2014]. Campbell [2006] is quite correct when mentioning that typical continuum mechanics models rely on reducing particulates to an infinitesimal point, which is incorrect when considering granular materials. While good results have been obtained by considering granular materials under a hydrodynamic model, these can quickly diverge from what is observed in experiment or nature [Abrahamsson et al., 2014; Bonamy et al., 2002, 2009; Qi et al., 2015; Savage, 1984; Warnett et al., 2014] because continuum models treat granular systems in an idealised way [Bougie et al., 2002], and lack explicit terms for the peculiarities of granular materials [Song et al., 2014] such as multi-scale heterogeneity [Lu et al., 2014], the dissipative nature of particulate interactions [Bonamy et al., 2009], collisions over multiple time-scales [Ancey et al., 1999], and non-homogeneous flow regimes [Liao et al., 2013] [1].). For example, success has been achieved by treating granular flows as visco-plastic materials, but this model struggles with handling higher flow velocities [Abrahamsson et al., 2014]. This trend continues, with Motlagh et al. [2014] noting that a range of

[1] Remember that granular materials can behave like all three of classical states of matter, and at the same time - see Section 1.1.1

methods "require tuning for each case of specific operating conditions", such as the model presented in Mellmann et al. [2004]. Problems with assumptions made in many granular studies have also been highlighted in the literature - Campbell [2006] points out that it may not be correct to consider the internal angle of friction of a material as a constant, and that continuum models consider collisions between particulates as instantaneous, while modelling granular materials relies on a long duration contact assumption. This leads to a situation in which model predictions contradict their own assumptions and as such may struggle to model any realistic materials [Ancey et al., 1999; Campbell, 2006].

Another area in which true fluids diverge in behaviour when compared to granular materials is in their history dependance. Assuming that the ambient conditions are the same, water will behave the same way when poured from a cup, no matter how much the liquid was agitated beforehand. A granular material's behaviour once put in motion, however, is strongly dependant on the material's history - how a grain hopper is filled will effect how the same hopper system evacuates its particulates once flow is initiated [Fullard et al., 2017]. In addition, the mass flow rate of a granular material from a hopper has been shown to be independent of the pressure inside of the vessel - an interesting and only recently discovered result of the Janssen effect [Aguirre et al., 2010].

While some authors acknowledge the complexity of granular flows [Liu et al., 2013; Qi et al., 2015] and the unsuitability of hydrodynamic models [Castro-Orgaz et al., 2015; Taberlet et al., 2004; Wu et al., 2014], in general (for example, Ding et al. [2001b]; Komossa et al. [2014]; Ngako et al. [2014]; Orpe and Khakhar [2001]; Sunkara et al. [2015]) granular materials in a rotating drum have been treated as having two layers, an active region and a passive region . It has been seen that granular materials in a rotating drum display much more complex layer structures. Some workers (see, for example, Gomes and Mesquita [2013]) acknowledge the existence of a third (sheared) layer, but assume that it is thin enough to be ignored. The author suggests that this is a potential er-

ror; if granular flows are treated as complex Newtonian problems, then it is potentially problematic to ignore a region which will play a part in force transfer within a granular flow. Each layer, no matter its dimensions relative to its neighbours, plays a role in the mechanics of a granular flow [Iverson and Ouyang, 2015]. To ignore one is to introduce discontinuities between the layers that are considered. Understanding granular materials requires understanding the mechanisms controlling individual particles first [Ancey et al., 1999; Dong et al., 2015], before trying to describe bulk behaviour.

Particularly problematic to the author's mind is the concept of granular temperature, first introduced by Ogawa [1978]. It is frequently used in the literature (*e.g.*, Chou and Hsiau [2012]; Chou et al. [2014]; Hsiau and Shieh [1999, 2000]; Yin et al. [2013]), and considered a key variable in understanding granular mechanics [Hsiau and Shieh, 1999]. It is a measure of the range of variation of the velocity of particulates from the mean, and is given by Hsiau and Shieh [2000] as

$$T = \langle u'^2 + v'^2 \rangle / 2$$

where T is the granular temperature, u' is the fluctuation of velocity in the horizontal and v' the vertical. (Though there are different ways of calculating the granular temperature which produce very different results [Abrahamsson et al., 2014], which is one of the problems with the concept. See, for example, the definition given by Campbell [2006] and compare it with Hsiau and Shieh [2000], above.) Campbell [2006] also points out that the granular temperature, as a measurement of deviation from mean velocity, is then sensitive to the fluctuations of said mean velocity - care must be taken not to measure this as part of the granular temperature. As has been mentioned before, part of the problem with describing granular materials with fluid dynamics concepts is that the former are mesocopic, while the latter are microscopic - this also applies to granular temperature [Wang et al., 2014b]. As [Ding et al., 2001a] mentions, at the rotational velocities that are undertaken in this and most rotating drum studies, the granular temperature can be neglected in any case.

While the study of bulk properties of granular materials can illuminate internal mechanics (a strong example would be the various material properties found using an annular shear cell), the author would suggest that granular temperature either be used with great care in the future, or at the least re-named to avoid further confusion (in regards to treating granular materials as liquids). The difficulty with the concept is that it is not, in reality, a temperature: if whatever is causing the granular matter to flow is stopped, then the material enters its pseudo-solid state. Applying this to actual fluid flow, it would be analogous to a fluid instantly reaching absolute zero whenever there was no shearing force applied to it - this is clearly not the case. Additionally, granular temperature is unable to take into account the occurrence of turbulence within a granular flow [Campbell, 2006]; it seems counter-intuitive that a highly turbulent granular flow could have the same granular temperature as a non-turbulent flow with comparable internal velocities. Campbell [2006] also mentions that, at low particulate concentrations, it is possible for the granular temperature to tend towards infinity. In perhaps a slightly flippant objection, the units of granular temperature are m^2s^{-2} [Hsiau and Shieh, 2000], which is not a temperature in the traditional sense. Finally, temperature is a scalar measurement, while velocity (despite often being treated as a scalar) is a vector; for example Hsiau and Shieh [1999] acknowledge that granular temperature is only extant in the direction of bulk motion - a true temperature does not depend on the direction from which it is being observed.

In the literature, analogies (or sometimes exact parallels, for example by Chou and Hsiau [2012]) are drawn between the granular temperature and the temperature of classical gasses; this is misleading, because the motions of a grain within a granular material are *not* random (*i.e.*, *not* Brownian) [Ancey et al., 1999; Campbell, 2006] as they are in a gas, though they may appear to be at first pass. They are an example of a multitude of simple Newtonian processes creating a complex and counter-intuitive system [Rosato et al., 1987]. It is fair to describe them as "chaotic", in the Lorenzian [Lorenz, 1963] sense of the word (*i.e.*, "*deterministic* chaotic"), but they are not truly random [Campbell, 2006].

While I am averse to the granular temperature measurement, I do recognise a degree of usefulness within the literature (see, for example, Chou and Hsiau [2012]; Chou et al. [2014]; Hsiau and Shieh [1999, 2000]; Yin et al. [2013]). I suggest that the term "granular temperature" be replaced with the more accurate "kinetic noise", *i.e.*, the variability of the velocities of the particulates in the material in question. Another possibility would be "velocity variance", but I prefer kinetic noise as it avoids unnecessary alliteration and reduces the chances of confusion (is the velocity under consideration that of the granular material as a whole as a function of time, or that of its particles as a function of space?). At the very least, a set definition of the concept needs to be agreed upon by the granular materials community to avoid further problems. As Campbell [2006] says, "[g]ranular temperature is one of the most confusing concepts in granular flow".

9.6 Difficulties and Limitations

9.6.1 Difficulties

This study was, as may be expected, not without its problems or limitations. For example, finding suitable granular materials took much longer than expected. Even the materials that were used in the end had problems further down the line - the pumice was much more self-destructive than hoped, for example.

The experimental equipment, though in concept rather simple, took longer to construct than anticipated. The steel drum required a level of engineering above that attainable by most local companies, but one was found eventually that could build the drum to the required level of accuracy. The motor that turns the drum had stringent demands placed upon it, and as such was also quite difficult to source. In the end the motor from SEW Eurodrive performed admirably, though the difficulties with extracting torque data was frustrating (more on this later). We leave this avenue of exploration open for future studies.

As the motor was not, in and of itself, capable of producing acceleration regimes, this had to be added by SEW Eurodrive engineer Nav Prasad. Iterating upon his software produced an easy to use interface for user-definable acceleration profiles. Future work can also be done using this program, as it does provide the ability to define deceleration profiles. On the subject of code, Luke Fullard's MATLAB code that automated the process of finding layer thicknesses etc., also took a few iterations before it was able to both perform consistently and produce the data that was required. However, this should be seen as a reflection of the complexity of the data sets, rather than on Dr. Fullard's prodigious programming capabilities.

One of the novelties of this experiment was the high-speed full-drum video recording. This required a lighting solution after the equipment was moved from a dusty but well-lit environment to a clean but relatively dark area. With the aid of Massey University photographer David Wiltshire and engineer David Feek, a lighting rig was constructed using off-the-shelf garden halogen lamps and part of the frame for an office bookshelf. The remaining problem was the flickering of the lamps, not usually visible to the naked eye but quite apparent in the high-speed footage. However, careful testing of the PIV results between frames revealed that the lighting was sufficiently stable between frames to ignore the flickering problem. To be on the safe side, future studies may wish to invest in high-end photography lights (*i.e.*, flicker-free), if the budget will allow.

After the footage of the experiment was obtained, the next step was to pass the individual frames through PIV analysis. Finding a feature-complete PIV suite that was not extremely costly also took a surprising amount of time. Certain PIV programs offered free (zero-cost) versions but, with limited functionality compared to the full version. There are a number of open-source PIV applications that are command-line only, which would be fine for mass-processing of footage with well-known parameters, but less useful when considering our experiments in which the region of interest could be quite different between experiments. The PIVlab plug-in for MATLAB proved to tick

all the relevant boxes: a user-friendly GUI, an open source license, and all the required features. The only cost was in obtaining a copy of MATLAB, but that was covered by a Massey University site license. Indeed, the Student version of MATLAB is around NZ$100, which is still much cheaper than the other commercial PIV suites available, which could run into the hundreds or thousands of dollars.

On a related note, while the amount of data that would be generated by an experiment was anticipated, this was still underestimated. An experiment that was four seconds long in real time could generate 50 GB of footage. When this is combined with the PIV analysis and resultant spreadsheet files, the total amount of data storage required for this research tops 9 TB. Storage and back-up of all this data become troublesome, though this was solved with kind permission to use a department server as a back-up location. Simply storing all the data required several external hard drives, the management of which became its own almost Sisyphean task.

Similarly, creating 100% air-free water experiments took some trial and error to solve. The original plan of over-filling the part of the drum which would contain the material, then inserting the glass door to force the water out, turned out to be insufficient. (Remember that the drum is filled and emptied in the horizontal position.) To avoid significant bubbles in experiments, it was found that the water would have to be left in the drum overnight to allow for the air trapped in the particulates to escape. For the ash, which was especially good at trapping air, gentle agitation of the substance periodically the day before the planned experiment was found to help reduce the air content.

Mass Flux Imbalance

During this research, as well as the mass flux for the active region, the mass flux for the passive region was also measured. It was noticed that the mass fluxes didn't balance, which is a physical impossibility. (While it's possible that instantaneous measurements

across an arbitrary profile may not balance, when considering time-averaged data for entire regions, basic physics suggests that mass fluxes must balance.)

Whilst investigating the source of this error, the following possible explanation was found. During this research, the interface between the passive and active regions has been assumed to be the point at which the relative velocity hits zero, *i.e.*, the point at which the material goes from flowing up hill to down hill. However, in the literature a different definition of this point is frequently used, and the interface is said to be at the point at which the velocity profile goes linear. (A linear velocity profile would occur at the point at which the velocity of the material is simply the rotational velocity multiplied by the radial position of the particulate in question, *i.e.*, the material is simply moving with the rotation of the drum, which may be considered the very definition of the passive region.)

This linear velocity profile point occurs lower than the point at which the velocity changes sign. As the error in mass fluxes was that the active region was smaller than the passive, this change in boundary position would help redress the mass flux imbalance problem. See Figure 9.6.1 for a demonstration, and Figure 5.2.5 for good examples of the linear profile region in reality.

It must be remembered that the mass fluxes that are presented in this study are correct, the only problem is that they don't balance, and this is presumably because the interface point between the two main regions in a flowing granular material has been erroneously chosen. However, corrections for this problem are not presented for the following reasons: the mass flux of the active region above the zero velocity point still gives a picture of the erosion and deposition mechanics, and these were the main focus of the project; the zero velocity point gives a much more readily identifiable layer cut-off point than the start of the linear velocity point (which would be especially difficult to identify consistently, in automated fashion or not, in the noisy beach sand data); re-calculation of the data would take several months, and not actually aid the aims of this research.

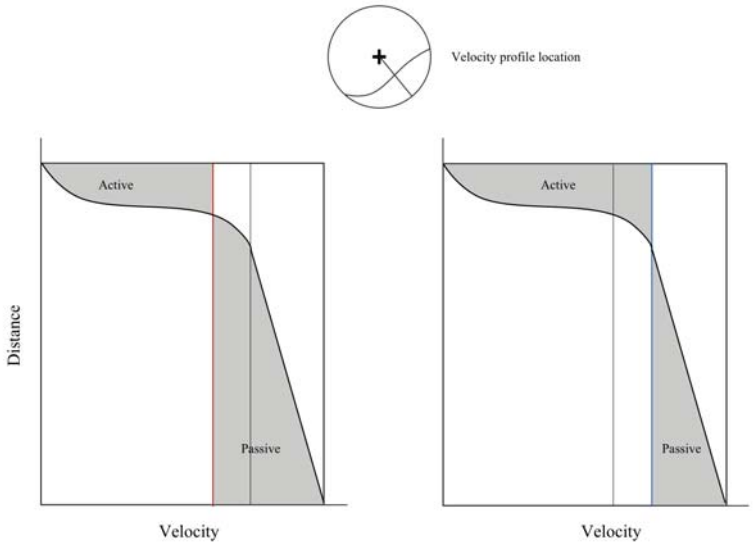

Figure 9.6.1: A demonstration of the mass flux imbalance problem. The mass fluxes were found by summing the areas of the passive and active regions, then multiplying by the depth of the drum and the density of the material. Using the point at which the horizontal velocity component changes sign (left, red line) gives a different pair of areas than the point at which the velocity profile becomes linear (right, blue line). In left and right hand figures, the vertical black line represents the position of the coloured line in the adjacent figure.

This troublesome finding is presented in the spirit of openness, and under the scientific paradigm that negative results are still results. Future researchers can use this finding to properly define the interface between the passive and active regions. While the zero velocity point does give an easily identifiable point, it is not the true point at which the change from active to passive occurs. Additionally, as can be seen in the velocity profiles for the beach sand (*e.g.*, Figure 7.3.5), the data can be extremely noisy; finding the point at which the linear velocity region occurs will take a significant amount of work.

In the remainder of this thesis, wherever the active/passive boundary is discussed, it refers to the point of zero velocity, as was used in the calculations, rather than the point at which the velocity profile becomes linear.

9.6.2 Limitations

The wet experiments, as well as being difficult to render fully air-free, were also the most difficult to measure with PIV. Most of the footage obtained from these experiments was only analysable from a qualitative perspective. If future researchers can create wet rotating drum experiments in which the dust problem is overcome, they should prove data-rich and greatly help with the interpretation of natural granular flow mechanics [Tegzes et al., 2003].

While the particulates used in this study were not monodisperse, as often seen in the literature, the small laboratory scale necessarily limits the range of particulates that can be used. For example, natural lahars can contain everything from silt to boulders. In order to avoid edge effects and inter-particulate forces, the largest and smallest particulates that can be used in this study were limited to within a few ϕ-scale steps of each other (0.25 to 4 mm). It may be interesting to expand the range of particulate sizes in future studies, if a large enough drum can be constructed to avoid edge effects. Nullifying the inter-particulate forces of small grains may prove more problematic, especially while maintaining the PIV-tractability of the resultant footage.

The experimental set up was capable of outputting torque data, but the data was limited in accuracy and in the frequency with which it could be obtained. Either a new rotating drum or the current one fitted with a torque transducer could generate extremely detailed quantitative data. This is because, as the material moves around inside the drum, say due to slumping, collapse, or avalanching, the centre of mass' location will also change. This will result in a change in the amount of torque required from the motor to maintain the current rotational velocity. Using a Fast Fourier Transform on the resultant data should allow us to extract the various periodicities involved in the material's flow to a much more accurate and quantifiable level than collapse observation alone.

As can be seen from the imagery in this thesis, the flowing material within a rotating

drum displays different layer structure at each end, especially when compared with the centre. As such, only the middle portion of the flow is relevant to natural events, though the entirety will be interesting to engineering studies.

9.7 Addressing the Aims

The three aims of the study (listed in Section 9.1) are completed with a varied of levels of success.

The first aim ("Characterize granular solid-liquid phase transitions...") is satisfactorily covered by Section 9.2.2, and the sections and figures referred to within. This section covers the differences between the granular material behaviours as presented in the literature, comparing that with what was found in this study. It also covers which phenomena and system behaviour is associated with which flow regime(s).

The second aim ("Determine the role of the main parameters...") is discussed in Section 9.2.8. This section illustrates how the two main materials (the beach sand and the volcanic ash) and their properties affects the resulting flow.

The third aim ("...comparing dry and wet systems") is not as well addressed as the first two, as the wet systems were more difficult to successfully PIV than was anticipated. However, some valuable numerical data was gleaned, and this is covered in Chapter 7 (starting on page 158) and Section 9.2.9. As discussed in the previous section, the wet experiments present a rich area for potential future research.

Chapter 10

Conclusions

10.1 Summary

A number of conclusions can be drawn from this research. The frequently cited model of flows in a rotating drum as two-layer phenomena does not describe the true complexity of these flows (we identify two layers only in the slowest flows, while faster ones include a minimum of three). As the rotational velocity of the drum increases, the curvature of the free surface increases, the number of layers in the flow increases, as does the number of SECCs, or self-enclosed circulation cells (the name we use for points of rotation along the flowing/passively rotating interface). The centre of mass' deflection from normal is weakly and linearly dependent on rotational velocity, whilst showing no dependency on the typical rotating drum flow regimes as identified by Mellmann [2001]. The frequency of avalanches increases with velocity up to a critical value, after which the avalanche frequency remains constant.

Finally, also observed and described in this thesis are what is believed to be previously unknown phenomena. These are the SECCs, mentioned above, and what may be the granular flow equivalent of a Kelvin-Helmholtz instability (KHI) [von Helmholtz, 1868; Thomson, 1871]. Additionally observed but not investigated to the same degree are the counter-rotational zones (CRZs), radial stripes, and pumice jet streams (see Appendix B).

10.2 Broader Implications

As well as Mellmann's regime changes at a wide range of Froude numbers that are generally identified only by the shape of the material in the drum, we can further pin down regime membership using other factors, such as a drop in dynamic angle of friction, when collapse periodicity meets its maximum, and when dynamic angle of friction reaches an early peak.

Wet materials display a very different set of flow behaviours, such the crumbling mo-

tion of the solid fraction in the lowest water content experiments. This will be related to buoyancy effects (*i.e.*, density ratio between fluid and solid phases), and changes in inter-particulate forces (suppression of van der Waals and electrostatics).

Dynamic angle of friction for the beach sand and ash has a reversed trend when comparing the wet to the dry experiments. Layer thicknesses are different - flowing region is larger and the passive smaller, and the rate at which they change is different.

The observed temporary centrifuging during the wet cases probably only has industrial applications, as lahars will never centrifuge. It does, however, strengthen the conclusion reached in the literature that the addition of a liquid over a gas to a granular material greatly changes the resultant behaviour.

There is the possibility for regions of rapidly recycled particulates in granular flows in rotating drums, and possibly again for other (potentially natural) situations. This was observed as rotating cells (SECCs) and shown to be a possibility with the velocity profiles drawn through the cells' major axis.

There is a new phenomenon that resembles a Kelvin-Helmholtz instability. They are suspected to be KHIs due to the density ratio across the regions of the granular flow where they occur. Measurements of this phenomenon, along with observations, are presented. They represent a rich vein for potential future study. They display behaviour in which their size, etc., increase with rotational velocity, then drop again. This is possibly due to them being suppressed by the greater mass flux incident upon them.

10.3 Implications for Lahars

Bearing in mind the above, when considering the erosive capabilities of lahars, investigators must remember the accelerating hysteresis - on-the-spot measurements of a natural mass flow's velocity must take into account the amount of time the material

has been at this velocity. In the field, this will probably incorporate measurement of surface elevation and estimates of lahar energy via geophones (for example, Keys and Green [2008]; Marcial et al. [1996]; Worni et al. [2012]).

Super-imposed avalanches within a granular mass flow do not have a strong effect on the erosive capability of the flow (see Section 5.4.4). As such, lahars and other debris flows are at their most erosive during acceleration, followed closely by when they are allowed to reach a steady velocity and remain there. Extra pulses of material, be they avalanches or from another source, that travel down the body of the flow will have more impact on super-surface objects (vegetation, buildings, etc.) than they will on the channel bed.

Of the new phenomena (SECCs, KHIs, and CRZs) the one most applicable to lahars in this author's opinion are the SECCs. A natural flow is unlikely to be subject to the steady forcing required to create the conditions necessary for the KHIs or CRZs. The SECCs, however, were observed perpetually during the experiments in which they were extant. It is easy to imagine a SECC being created in a natural flow, perhaps after a sudden drop in the elevation of flow channel. Perhaps a SECC like phenomena in nature is responsible for the striped erosion patterns of lahars as observed in Procter et al. [2010a]?

It was demonstrated earlier that the dilation of the active region is greatest not at the highest velocity, but at an intermediate one. This has implications for lahars and other natural flows - the amount of material colliding with a structure per surface area will not increase linearly with the incident velocity of the lahar. The area of a structure that will be exposed to a lahar or another natural flow will also be of interest to hazard mitigation efforts - what will be most damaging to this particular structure: having more of its facing exposed to a lahar, or having less exposed but to a lahar of greater density?

As has been shown both in this thesis and in the literature, a change in interstitial fluid

has a great effect on the behaviour of a granular material. The water experiments, as well as varying from what was observed in the dry, varied between each other as a function of water content. At the lowest water contents, the material didn't behave as a granular material at all, shearing off large chunks that would then roll downhill. Mid-level water fills lubricated this process, allowing smaller chunks to break off. Full-drum water experiments produced results closest to the dry, but with marked differences in measurable factors, such as dynamic angle of friction, etc. If we consider all this from the perspective of application to natural phenomena, it becomes a distinct possibility that a hazard mitigation effort must take into account the amount of water available to a potential lahar, as well as the granular material it may pick up on its journey. Low water availability will result in a lahar with potentially reduced destructive ability, as the water simply acts to bind the fine particulates together, retarding the flow's overall velocity (*i.e.*, increasing the effective viscosity of the granular material). Increasing the water available to a lahar enables it to enter more energetic flow regimes at lower velocities, possibly increasing the lahar's ability to do damage.

10.4 Future Directions

This research suggests several ways forward for the rotating drum and granular material communities. A simple starting point would be to repeat the experiments presented here with varied fill levels; everything in this thesis, for the purposes of cross-comparison between data sets, was set to a fill factor, f, of 0.25. Expanding beyond this would allow for simulation of larger and smaller natural debris flows and comparisons between the two.

10.4.1 Water-based Experiments

It is reasonable to assume that the nearer an experimental analogue can get to describing the natural phenomena in question, the more applicable the results will be. It is the author's opinion, therefore, that future research projects in the rotating drum area with application to natural granular flows should concentrate on over-coming the cloudiness issue when using water as the interstitial fluid. At low enough velocities and with careful PIV, these experiments could be very helpful in understanding the internal mechanics of natural granular flows.

It would be interesting to see if future work is able to create a "synthetic-natural" granular material - one that shares the properties of a natural material such as the pumice or ash, but is completely dust-free and resilient to breakage.

10.4.2 Other Fluids

There are, of course, other fluids that could be used in a rotating drum experiment, other than air and water. As well as allowing the investigator to study the effects of changed density ratio, the role that viscosity plays (for example, Seiden and Thomas [2011]) can also be studied.

An added bonus of density ratio changes is the ability to study different gravitational regimes. For a fluid with similar properties to water, but with a different density, the end effect is analogous to a change in the resultant acceleration due to gravity. For example, Finger and Stannarius [2007] use glycerol and sodium iodide solutions to create liquids with properties similar to water but with different densities and viscosities. The author is aware that the mineral industries exploit buoyancy with fluids of differing densities - if one exists that is near identical to water bar the density, this material could be very useful indeed. This would allow for the study of lahars and other natural granular flows on other terrestrial bodies, such as Mars which has recently been

confirmed to be subject to periodic temporary water flow[1].

10.4.3 Deceleration

This study used acceleration as its non-steady state. However, in both nature and industry, granular materials may often be subject to decelerations. Study of the behaviour of granular materials under decelerations should prove illuminating. It may also be interesting to compare the results of deceleration and acceleration of the same material - if the deceleration regime is the same as the acceleration (but reversed), what differences can be seen in the behaviour of material? Expanding the experimental regime to decelerations will allow the future investigator to study what happens to a natural flow when it meets an obstacle.

10.4.4 Torque Measurements

Another possible avenue for future interrogation of the mechanics of a granular flow in a rotating drum involves the measurement of the torque required as a function of time. Using a Fast Fourier Transform on the torque measurements should allow for the extraction of the various periodicities involved in the material's flow. (See Section 9.6.2 for original discussion of this topic.) This will allow for greater understanding of the internal mechanics via a previously unexplored avenue (as far as the author is aware), and may provide interesting results.

10.5 Synopsis

This study attempted to gain insight into the flow of natural phenomena, in this case lahars, by use of an experimental analogue. This analogue was created inside a rotating

[1] `https://tinyurl.com/ow8k53d`, last accessed 24th March, 2016.

drum, a common piece of equipment in industry and related fields of research. The "lahar" with in the drum was created using a variety of natural materials, intended to be the experimental equivalents of the solid fraction within a lahar. While the fluid phase in a lahar is exclusively water, the fluid phase in the experiments was either air or water, with the latter being investigated at a variety of fill levels. This was to simulate lahars with different water content.

This study differentiates itself from those that have come before in a number of key ways. It uses equipment usually reserved for industrial purposes to investigate natural phenomena. It also makes use of natural-like materials, opposed to the near-spherical materials commonly employed. Additionally, it is perhaps the first project to measure the effects of acceleration on a granular material within a rotating drum. Finally, the presentation of admittedly limited data from water-based experiments is also novel.

The research was partially successful. Valuable data was collected from the dry experiments (i.e., the ones in which the fluid phase was air). These runs showed that the commonly accepted two-layer approximation for a granular material within a rotating drum is probably too simplistic a model to correctly describe reality. Measurements were also taken of the collapse periodicity, showing that there is a potential mechanical limit to the rate at which granular materials can flow; this is presumably applicable to natural flows as well. When accelerating the dry materials, it was found that there was a hysteresis between the steady state velocity experiments and the equivalent velocities found within the accelerating cases. This, too, could perhaps be applied to lahars, in that hazard planners and other stake holders should consider the history of a potential lahar as well as it's current state when calculating a destructive potential.

Adding water to the system showed that, as expected, the interstitial fluid phase plays a large role in the final behaviour of a fluid/granular solid system. However, measuring these experiments proved more problematic than was hoped, and a full suite of data that could be compared to the dry experiments was not obtained. However, some data

was obtained, and interesting behaviour observed in the temporary centrifuging.

Not everything that occurred that was unexpected was negative, though. Several phenomena were observed that were potentially new to the literature. These were the SECCs (self-enclosed circulation cells), regions of rotating material located along the passive/active interface; the KHIs (Kelvin-Helmholtz instabilities), though further research will be required to confirm or deny whether what was observed is truly a KHI event; the CRZs (counter-rotational zones), areas of material rotating *against* the rotation of the drum, located at the interface between the main body of the granular material and the low-density regions; radial striping, observed in the pumice, which is distinct to the lateral striping described in the rotating drum literature; and finally, jets of ejected material, also observed in the pumice.

It is clear that there is still much to learn about the behaviour of granular materials, especially if we want to be able to describe them accurately enough to model the behaviour of lahars and other natural granular flows. This thesis gives some ideas of where the author thinks both experimental and theoretical descriptions should head in future in order to answer some of the questions posed here and in the literature at large. Where this future research will take us, I look forward to with no small measure of excitement.

References

References

EC Abdullah and D Geldart. The use of bulk density measurements as flowability indicators. *Powder Technology*, 102(2):151–165, 1999.

P J Abrahamsson, S Sasic, and A Rasmuson. On the continuum modeling of dense granular flow in high shear granulation. *Powder Technology*, 268(C):1–8, Jan 2014. doi: 10.1016/j.powtec.2014.08.057. URL `http://dx.doi.org/10.1016/j.powtec.2014.08.057`.

R J Adrian. Twenty years of particle image velocimetry. *Experiments in Fluids*, 39(2):159–169, Aug 2005. doi: 10.1007/s00348-005-0991-7.

M A Aguirre, J G Grande, A Calvo, L A Pugnaloni, and J-C Géminard. Pressure independence of granular flow through an aperture. *Physical Review Letters*, 104(23):238002, 2010.

H Ahn, Z Başaranoğlu, M YÄślmaz, A Buğutekin, and M Gül. Experimental investigation of granular flow through an orifice. *Powder Technology*, 186(1):65–71, 2008.

A Alexander, T Shinbrot, and F J Muzzio. Scaling surface velocities in rotating cylinders as a function of vessel radius, rotation rate, and particle size. *Powder Technology*, 126(2):174–190, 2002.

A Alexander, F J Muzzio, and T Shinbrot. Effects of scale and inertia on granular banding segregation. *Granular Matter*, 5(4):171–175, 2004.

C Ancey, P Coussot, and P Evesque. A theoretical framework for granular suspensions in a steady simple shear flow. *Journal of Rheology (1978-present)*, 43(6):1673–1699, 1999.

A Aradian, E Raphael, and P G de Gennes. Surface flows of granular materials: a short introduction to some recent models. *Comptes Rendus Physique*, 3(2):187–196, 2002.

ASTM. D6773-02: Standard shear test method for bulk solids using the Schulze ring shear tester, ASTM International. 2008.

RA Bagnold. The shearing and dilatation of dry sand and the 'singing' mechanism. 295 (1442):219–232, 1966.

O Baran, D Ertas, T Halsey, and G Grest.... Velocity correlations in dense gravity-driven granular chute flow. *Physical Review E (...*, Jan 2011. URL `http://www.citeulike.org/group/13900/article/8651435`.

R Berger, C Kloss, A Kohlmeyer, and S Pirker. Hybrid parallelization of the LIGGGHTS open-source DEM code. *Powder Technology*, 278(C):234–247, Apr 2015. doi: 10.1016/j.powtec.2015.03.019. URL `http://dx.doi.org/10.1016/j.powtec.2015.03.019`.

Y Bernabé and B Evans. Pressure solution creep of random packs of spheres. *Journal of Geophysical Research Solid Earth*, pages n/a–n/a, May 2014. doi: 10.1002/2014JB011036.

WA Beverloo, HA Leniger, and J van de Velde. The flow of granular solids. 1960.

T Bhattacharya and J J Mccarthy. Chute flow as a means of segregation characterization. *Powder Technology*, 256:126–139, Oct 2013. doi: 10.1016/j.powtec.2014.01.092. URL `http://dx.doi.org/10.1016/j.powtec.2014.01.092`.

R J Blong. *Volcanic hazards. A sourcebook on the effects of eruptions*. Academic Press, Inc., Orlando, FL, 1984.

AA Boateng and PV Barr. Granular flow behaviour in the transverse plane of a partially filled rotating cylinder. *Journal of Fluid Mechanics*, 330:233–249, 1997.

D Bonamy, F Daviaud, and L Laurent. Experimental study of granular surface flows via a fast camera: a continuous description. *Physics of Fluids (1994-present)*, 14(5): 1666–1673, 2002.

D Bonamy, P.-H Chavanis, P.-P Cortet, F Daviaud, B Dubrulle, and M Renouf. Euler-like modelling of dense granular flows: application to a rotating drum. *European Physical Journal B*, 68(4):619–627, Apr 2009. doi: 10.1140/epjb/e2009-00123-6.

J. F Boudet, Y Amarouchene, B Bonnier, and H Kellay. The granular jump. *Journal of Fluid Mechanics*, 572:413, Feb 2007. doi: 10.1017/S002211200600365X.

J Bougie, S J Moon, J B Swift, and H L Swinney. Shocks in vertically oscillated granular layers. *Physical Review E*, 66(5):051301, Nov 2002. doi: 10.1103/PhysRevE.66.051301.

R Brown. A brief account of microscopical observations made in the months of June, July and August 1827, on the particles contained in the pollen of plants; and on the general existence of active molecules in organic and inorganic bodies. *The Philosophical Magazine, or Annals of Chemistry, Mathematics, Astronomy, Natural History and General Science*, 4(21):161–173, 1828.

L Caballero, D Sarocchi, E Soto, and L Borselli. Rheological changes induced by clast fragmentation in debris flows. *Journal of Geophysical Research Earth Surface*, pages n/a–n/a, Aug 2014. doi: 10.1002/2013JF002942.

B Cagnoli and G P Romano. Vertical segregations in flows of angular rock fragments: Experimental simulations of the agitation gradient within dense geophysical flows. *Journal of Volcanology and Geothermal Research*, pages 1–39, Sep 2013. doi: 10.1016/j.jvolgeores.2013.08.017. URL `http://dx.doi.org/10.1016/j.jvolgeores.2013.08.017`.

C Campbell. Granular material flows–an overview. *Powder Technology*, 162(3):208–229, 2006.

P Canuti, N Casagli, F Catani, and G Falorni. Modeling of the Guagua Pichincha volcano (Ecuador) lahars. *Physics and Chemistry of the Earth*, 27(36):1587–1599, Jan 2002.

JF Carr and DM Walker. An annular shear cell for granular materials. *Powder Technology*, 1:369–373, Aug 1967.

RE Carter. Torque transducer improves workability test. *Concrete-Camberley*, 46(7):25, 2012.

O Castro-Orgaz, K Hutter, J V Giraldez, and W H Hager. Nonhydrostatic granular flow over 3-d terrain: New Boussinesq-type gravity waves? *Journal of Geophysical Research Earth Surface*, pages n/a–n/a, Jan 2015. doi: 10.1002/2014JF003279.

Phairot Chatanantavet and Michael P Lamb. Sediment transport and topographic evolution of a coupled river and river plume system: An experimental and numerical study. *Journal of Geophysical Research Earth Surface*, Jun 2014. doi: 10.1002/2013JF002810.

J Chen, Y Wang, X Li, R He, S Han, and Y Chen. Erosion prediction of liquid-particle two-phase flow in pipeline elbows via CFD–DEM coupling method. *Powder Technology*, 275(C):182–187, Feb 2015. doi: 10.1016/j.powtec.2014.12.057. URL `http://dx.doi.org/10.1016/j.powtec.2014.12.057`.

N-S Cheng. Scaling law for velocity profiles of surface granular flows observed in rotating cylinders. *Powder Technology*, 218:11–17, 2012.

H T Chou, S H Chou, and S S Hsiau. The effects of particle density and interstitial fluid viscosity on the dynamic properties of granular slurries in a rotating drum. *Powder*

Technology, 252:42–50, Jan 2014. doi: 10.1016/j.powtec.2013.10.034. URL http://dx.doi.org/10.1016/j.powtec.2013.10.034.

S H Chou and S S Hsiau. Dynamic properties of immersed granular matter in different flow regimes in a rotating drum. *Powder Technology*, 226(C):99–106, May 2012. doi: doi:10.1016/j.powtec.2012.04.024. URL http://dx.doi.org/10.1016/j.powtec.2012.04.024.

S H Chou, C C Liao, and S S Hsiau. An experimental study on the effect of liquid content and viscosity on particle segregation in a rotating drum. *Powder Technology*, 201(3):266–272, Aug 2010. doi: 10.1016/j.powtec.2010.04.009. URL http://dx.doi.org/10.1016/j.powtec.2010.04.009.

S. H Chou, C. C Liao, and S. S Hsiau. The effect of interstitial fluid viscosity on particle segregation in a slurry rotating drum. *Physics of Fluids*, 23(8):083301, Jan 2011. doi: 10.1063/1.3623275.

S Cloete, S T Johansen, and S Amini. Grid independence behaviour of fluidized bed reactor simulations using the two fluid model: Effect of particle size. *Powder Technology*, 269(C):1–13, Sep 2014. doi: 10.1016/j.powtec.2014.08.055. URL http://dx.doi.org/10.1016/j.powtec.2014.08.055.

M-J Colbert, M Grandbois, and N Abatzoglou. Identification of inter-particular forces by atomic force microscopy and how they relate to powder rheological properties measured in shearing tests. *Powder Technology*, 2015.

C Coulomb. Memoires de mathematiques et de physique presentes a l'academie royale des sciences par divers savans et lus dans les assemblees. 1773a.

C Coulomb. Test on the applications of the rules of maxima and minima to some problems of statics related to architecture. *Mem. Math. Phys*, 7:343, 1773b.

S J Cronin, V E Neall, J A Lecointre, and A S Palmer. Unusual "snow slurry" lahars from

Ruapehu volcano, New Zealand, september 1995. *Geology*, 24(12):1107, 1996.

S J Cronin, K A Hodgson, V E Neall, A S Palmer, and J A Lecointre. 1995 Ruapehu lahars in relation to the late Holocene lahars of Whangaehu River, New Zealand. *New Zealand Journal of Geology and Geophysics*, 40(4):507–520, Dec 1997a. doi: 10.1080/00288306.1997.9514780.

S J Cronin, V E Neall, J A Lecointre, and A S Palmer. Changes in Whangaehu River lahar characteristics during the 1995 eruption sequence, Ruapehu volcano, New Zealand. *Journal of Volcanology and Geothermal Research*, 76(1-2):47–61, 1997b.

S J Cronin, V E Neall, J A Lecointre, and A S Palmer. Dynamic interactions between lahars and stream flow: A case study from Ruapehu volcano, New Zealand. *Bulletin of the Geological Society of America*, 111(1):28, 1999.

P A Cundall and O D L Strack. A discrete numerical model for granular assemblies. *Géotechnique*, 29:47–65(18), 1979. URL `http://www.icevirtuallibrary.com/content/article/10.1680/geot.1979.29.1.47`.

F da Cruz, S Emam, M Prochnow, and J Roux.... Rheophysics of dense granular materials: Discrete simulation of plane shear flows. *Physical Review E (...*, Jan 2008. URL `http://www.citeulike.org/group/13900/article/8651198`.

Frédéric da Cruz, Sacha Emam, Michaël Prochnow, Jean-Noël Roux, and François Chevoir. Rheophysics of dense granular materials: Discrete simulation of plane shear flows. *Physical Review E*, 72(2):021309, 2005.

A Daerr and S Douady. Two types of avalanche behaviour in granular media. *Nature*, 399(6733):241–242, 1999.

C Davies, A Williams, S J Tallon, K Fenton, and N Brown. A new approach to monitoring the movement of particulate material in rotating drums. *Developments in Chemical Engineering and Mineral Processing*, 12(3âĂŘ4):263–275, 2004.

E de Bélizal, F Lavigne, D S Hadmoko, J-P Degeai, G A Dipayana, B W Mutaqin, M A Marfai, M Coquet, B Le Mauff, A-K Robin, C Vidal, N Cholik, and N Aisyah. Rain-triggered lahars following the 2010 eruption of Merapi volcano, Indonesia: A major risk. *Journal of Volcanology and Geothermal Research*, 261(C):330–347, Jul 2013. doi: doi:10.1016/j.jvolgeores.2013.01.010. URL `http://dx.doi.org/10.1016/j.jvolgeores.2013.01.010`.

PG de Gennes. Granular matter: a tentative view. *Reviews of Modern Physics*, 71(2): 374–382, 1999.

M Debacq, S Vitu, D Ablitzer, J-L Houzelot, and F Patisson. Transverse motion of cohesive powders in flighted rotary kilns: experimental study of unloading at ambient and high temperatures. *Powder Technology*, 245:56–63, Sep 2013. doi: 10.1016/j.powtec.2013.04.007. URL `http://dx.doi.org/10.1016/j.powtec.2013.04.007`.

N G Deen, E A J F Peters, J T Padding, and J A M Kuipers. Review of direct numerical simulation of fluid–particle mass, momentum and heat transfer in dense gas–solid flows. *Chemical Engineering Science*, 116(C):710–724, Sep 2014. doi: 10.1016/j.ces.2014.05.039. URL `http://dx.doi.org/10.1016/j.ces.2014.05.039`.

Y L Ding, R N Forster, J P K Seville, and D J Parker. Scaling relationships for rotating drums. *Chemical Engineering Science*, 56(12):3737–3750, 2001a.

Y L Ding, J P K Seville, R Forster, and D J Parker. Solids motion in rolling mode rotating drums operated at low to medium rotational speeds. *Chemical Engineering Science*, 56(5):1769–1780, 2001b.

Y L Ding, R Forster, J P K Seville, and D J Parker. Granular motion in rotating drums: bed turnover time and slumping-rolling transition. *Powder Technology*, 124(1-2):18–27, 2002.

F Dioguardi and D Mele. A new shape dependent drag correlation formula for non-spherical rough particles. experiments and results. *Powder Technology*, 277(C):222–

230, Mar 2015. doi: 10.1016/j.powtec.2015.02.062. URL http://dx.doi.org/10.1016/j.powtec.2015.02.062.

K Dong, C Wang, and A Yu. A novel method based on orientation discretization for discrete element modeling of non-spherical particles. *Chemical Engineering Science*, 126(C):500–516, Apr 2015. doi: 10.1016/j.ces.2014.12.059. URL http://dx.doi.org/10.1016/j.ces.2014.12.059.

S Douady, B Andreotti, and A Daerr. On granular surface flow equations. *The European Physical Journal B-Condensed Matter and Complex Systems*, 11(1):131–142, 1999.

E E Doyle, H E Huppert, G Lube, H M Mader, and R S J Sparks. Static and flowing regions in granular collapses down channels: Insights from a sedimenting shallow water model. *Physics of Fluids*, 19(10):106601, Jan 2007. doi: 10.1063/1.2773738.

E E Doyle, S J Cronin, S E Cole, and J C Thouret. The challenges of incorporating temporal and spatial changes into numerical models of lahars. *Proceedings of the 18th World IMACS Congress and MODSIM09 International Congress on Modelling and Simulation: Modelling and Simulation Society of Australia and New Zealand and International Association for Mathematics and Computers in Simulation*, pages 2665–2671, 2009.

E E Doyle, S J Cronin, S E Cole, and J C Thouret. The coalescence and organization of lahars at Semeru volcano, Indonesia. *Bulletin of Volcanology*, 72(8):961–970, Oct 2010. doi: 10.1007/s00445-010-0381-8.

E E Doyle, S J Cronin, and J C Thouret. Defining conditions for bulking and debulking in lahars. *Geological Society of America Bulletin*, 123(7-8):1234–1246, Jul 2011. doi: 10.1130/B30227.1.

O Dubé, E Alizadeh, J Chaouki, and F Bertrand. Dynamics of non-spherical particles in a rotating drum. *Chemical Engineering Science*, 101(C):486–502, Sep 2013. doi: 10.1016/j.ces.2013.07.011. URL http://dx.doi.org/10.1016/j.ces.2013.07.011.

A Einstein. *Investigations on the Theory of the Brownian Movement*. Dover publications, 1956.

SA Fagents and SM Baloga. Toward a model for the bulking and debulking of lahars. *Journal of Geophysical Research*, 111(B10):B10201, Oct 2006. doi: 10.1029/2005JB003986.

AN Faqih, B Chaudhuri, A Mehrotra, MS Tomassone, and F Muzzio. Constitutive model to predict flow of cohesive powders in bench scale hoppers. *Chemical Engineering Science*, 65(10):3341–3351, May 2010. doi: 10.1016/j.ces.2010.02.028. URL `http://dx.doi.org/10.1016/j.ces.2010.02.028`.

B Ferdowsi, M Griffa, R A Guyer, and P A Johnson. Microslips as precursors of large slip events in the stick-slip dynamics of sheared granular layers: A discrete element model analysis. *Geophysical Research Letters*, Jan 2013. URL `http://onlinelibrary.wiley.com/doi/10.1002/grl.50813/abstract`.

S. J Fiedor and J. M Ottino. Mixing and segregation of granular matter: multi-lobe formation in time-periodic flows. *Journal of Fluid Mechanics*, 533:1–14, Jun 2005. doi: 10.1017/S0022112005003952.

T Finger and R Stannarius. Influences of the interstitial liquid on segregation patterns of granular slurries in a rotating drum. *Physical Review E*, 75(3):031308, 2007.

Y Forterre and O Pouliquen. Flows of dense granular media. *Annual Review of Fluid Mechanics*, 40(1):1–24, Jan 2008. doi: 10.1146/annurev.fluid.40.111406.102142.

LA Fullard, CE Davies, G Lube, AC Neather, ECP Breard, and BJ Shepherd. The transient dynamics of dilation waves in granular phase transitions during silo discharge. *Granular Matter*, 19(1):6, 2017.

P Gauer, M Kern, K Kristensen, K Lied, L Rammer, and H Schreiber. On pulsed doppler

radar measurements of avalanches and their implication to avalanche dynamics. *Cold Regions Science and Technology*, 50(1):55–71, 2007.

D Geldart. Types of gas fluidization. *Powder Technology*, 7(5):285–292, Jan 1973.

D Gidaspow and V Chandra. Unequal granular temperature model for motion of platelets to the wall and red blood cells to the center. *Chemical Engineering Science*, 117(C):107–113, Sep 2014. doi: 10.1016/j.ces.2014.06.025. URL http://dx.doi.org/10.1016/j.ces.2014.06.025.

J C Gill and B D Malamud. Reviewing and visualizing the interactions of natural hazards. *Reviews of Geophysics*, pages n/a–n/a, Aug 2014. doi: 10.1002/2013RG000445.

L Girolami, O Roche, T H Druitt, and T Corpetti. Particle velocity fields and depositional processes in laboratory ash flows, with implications for the sedimentation of dense pyroclastic flows. *Bulletin of Volcanology*, 72(6):747–759, Aug 2010. doi: 10.1007/s00445-010-0356-9.

L Girolami, T H Druitt, and O Roche. Towards a quantitative understanding of pyroclastic flows: Effects of expansion on the dynamics of laboratory fluidized granular flows. *Journal of Volcanology and Geothermal Research*, 296(C):31–39, Apr 2015. doi: 10.1016/j.jvolgeores.2015.03.008. URL http://dx.doi.org/10.1016/j.jvolgeores.2015.03.008.

L M Gomes and A L Amarante Mesquita. Effect of particle size and sphericity on the pickup velocity in horizontal pneumatic conveying. *Chemical Engineering Science*, 104(C):780–789, Dec 2013. doi: 10.1016/j.ces.2013.08.055. URL http://dx.doi.org/10.1016/j.ces.2013.08.055.

I Gómez-Arriaran, I Ippolito, R Chertcoff, M Odriozola-Maritorena, and R De Schant. Characterization of wet granular avalanches in controlled relative humidity conditions. *Powder Technology*, 279(C):24–32, Apr 2015. doi: 10.1016/j.powtec.2015.03.050. URL http://dx.doi.org/10.1016/j.powtec.2015.03.050.

P Gopalakrishnan and D Tafti. Development of parallel DEM for the open source code MFIX. *Powder Technology*, 235(C):33–41, Jan 2013. doi: doi:10.1016/j.powtec.2012.09.006. URL http://dx.doi.org/10.1016/j.powtec.2012.09.006.

J Grattan and R Torrence. *Natural disasters and cultural change*. Routledge, 2002.

R Greve, T Koch, K Hutter, R Greve, T Koch, and K Hutter. Unconfined flow of granular avalanches along a partly curved surface. i. theory. *Proceedings of the Royal Society of London. Series A: Mathematical and Physical Sciences*, 445(1924):399–413, 1994.

N Gui, J Yan, W Xu, L Ge, D Wu, Z Ji, J Gao, S Jiang, and X Yang. DEM simulation and analysis of particle mixing and heat conduction in a rotating drum. *Chemical Engineering Science*, 97(C):225–234, Jun 2013. doi: 10.1016/j.ces.2013.04.005. URL http://dx.doi.org/10.1016/j.ces.2013.04.005.

M Halidan, G R Chandratilleke, S L I Chan, A B Yu, and J Bridgwater. Prediction of the mixing behaviour of binary mixtures of particles in a bladed mixer. *Chemical Engineering Science*, 120(C):37–48, Dec 2014. doi: 10.1016/j.ces.2014.08.048. URL http://dx.doi.org/10.1016/j.ces.2014.08.048.

S Havens, H-P Marshall, J B Johnson, and B Nicholson. Calculating the velocity of a fast-moving snow avalanche using an infrasound array. *Geophysical Research Letters*, pages n/a–n/a, Sep 2014. doi: 10.1002/2014GL061254.

J Havlica, K Jirounkova, T Travnickova, and M Kohout. The effect of rotational speed on granular flow in a vertical bladed mixer. *Powder Technology*, 280(C):180–190, May 2015. doi: doi:10.1016/j.powtec.2015.04.035. URL http://dx.doi.org/10.1016/j.powtec.2015.04.035.

YR He, HS Chen, YL Ding, and B Lickiss. Solids motion and segregation of binary mixtures in a rotating drum mixer. *Chemical Engineering Research and Design*, 85(7):963–973, 2007.

Lara B Hedrick, James T Anderson, Stuart A Welsh, and Lian-Shin Lin. Sedimentation in mountain streams: a review of methods of measurement. 2013.

H Henein, JK Brimacombe, and AP Watkinson. Experimental study of transverse bed motion in rotary kilns. *Metallurgical and Materials Transactions B*, 14(2):191–205, 1983a.

H Henein, JK Brimacombe, and AP Watkinson. Experimental study of transverse bed motion in rotary kilns. *Metallurgical Transactions B*, 14(2):191–205, 1983b.

K M Hill and J Kakalios. Reversible axial segregation of rotating granular media. *Physical Review E*, 52(4):4393, 1995.

K M Hill, N Jain, and J M Ottino. Modes of granular segregation in a noncircular rotating cylinder. *Physical Review E*, 64(1):011302, 2001.

D Höhner, S Wirtz, and V Scherer. A study on the influence of particle shape and shape approximation on particle mechanics in a rotating drum using the discrete element method. *Powder Technology*, pages 1–25, Nov 2013. doi: 10.1016/j.powtec.2013.11.023. URL `http://dx.doi.org/10.1016/j.powtec.2013.11.023`.

D Höhner, S Wirtz, and V Scherer. A study on the influence of particle shape on the mechanical interactions of granular media in a hopper using the discrete element method. *Powder Technology*, 278(C):286–305, Apr 2015. doi: 10.1016/j.powtec.2015.02.046. URL `http://dx.doi.org/10.1016/j.powtec.2015.02.046`.

R D Holtz and W D Kovacs. *An introduction to geotechnical engineering*. Number Monograph. 1981.

AJ Holyoake and JN McElwaine. High-speed granular chute flows. *Journal of Fluid Mechanics*, 710:35–71, Dec 2012. doi: 10.1017/jfm.2012.331.

S-S Hsiau and Y-M Shieh. Fluctuations and self-diffusion of sheared granular material flows. *Journal of Rheology*, 43:1049, 1999.

S-S Hsiau and Y-M Shieh. Effect of solid fraction on fluctuations and self-diffusion of sheared granular flows. *Chemical Engineering Science*, 55(11):1969–1979, 2000.

L Hsu, W. E Dietrich, and L. S Sklar. Mean and fluctuating basal forces generated by granular flows: laboratory observations in a large vertically rotating drum. *Journal of Geophysical Research Earth Surface*, pages n/a–n/a, May 2014. doi: 10.1002/2013JF003078.

H E Huppert. Gravity currents: a personal perspective. *Journal of Fluid Mechanics*, 554 (-1):299, May 2006. doi: 10.1017/S002211200600930X.

M Ishii and K Mishima. Two-fluid model and hydrodynamic constitutive relations. *Nuclear Engineering and Design*, 82(2):107–126, 1984.

R Iverson, S Schilling, and J Vallance. Objective delineation of lahar-inundation hazard zones. *Geological Society of America Bulletin*, 110(8):972–984, 1998.

R M Iverson. The physics of debris flows. *Reviews of Geophysics*, 35(3):245–296, Jan 1997.

R M Iverson and C Ouyang. Entrainment of bed material by earth-surface mass flows: Review and reformulation of depth-integrated theory. *Reviews of Geophysics*, 53(1): 27–58, Feb 2015. doi: 10.1002/2013RG000447.

R M Iverson, M Logan, R G Lahusen, and M Berti. The perfect debris flow? Aggregated results from 28 large-scale experiments. *Journal of Geophysical Research*, 115(F3): F03005, Jul 2010. doi: 10.1029/2009JF001514.

HM Jaeger, SR Nagel, and RP Behringer. Granular solids, liquids, and gases. *Reviews of Modern Physics*, 68(4):1259–1273, 1996.

N Jain, J M Ottino, and R M Lueptow. An experimental study of the flowing granular layer in a rotating tumbler. *Physics of Fluids (1994-present)*, 14(2):572–582, 2002.

N Jain, J M Ottino, and R M Lueptow. Effect of interstitial fluid on a granular flowing layer. *Journal of Fluid Mechanics*, 508:23–44, Jun 2004. doi: 10.1017/S0022112004008869.

HA Janssen. Versuche über getreidedruck in silozellen. *Zeitschr. d. Vereines deutscher Ingenieure*, 39(35):1045–1049, 1895.

A C Jenike. Gravity flow of bulk solids. *Utah University Engineering Experiment Station Bulletin*, (123), 1964a.

A W Jenike. Storage and flow of solids, bulletin no. 123. *Bulletin of the University of Utah*, 53(26), 1964b.

A W Jenike. Quantitative design of mass-flow bins. *Powder Technology*, 1(4):237–244, 1967.

S F Jenkins, J C Phillips, R Price, K Feloy, P J Baxter, D S Hadmoko, and E de Bélizal. Developing building-damage scales for lahars: application to merapi volcano, indonesia. *Bulletin of Volcanology*, 77(9):1–17, 2015.

Y-J Jiang, Y Zhao, I Towhata, and D-X Liu. Influence of particle characteristics on impact event of dry granular flow. *Powder Technology*, 270(PA):1–15, Jan 2014. doi: 10.1016/j.powtec.2014.10.005. URL `http://dx.doi.org/10.1016/j.powtec.2014.10.005`.

J Jones, C Davies, and A Williams. Slumping in a rotating drum. *Chemeca 2003: Products and Processes for the 21st Century: Proceedings of the 31st Australasian Chemical Engineering Conference*, Jan 2003. URL `http://search.informit.com.au/documentSummary;dn=914693540213397;res=IELENG`.

P Jop, Y Forterre, and O Pouliquen. Crucial role of sidewalls in granular surface flows: consequences for the rheology. *Journal of Fluid Mechanics*, 541:167–192, 2005.

P Jop, Y Forterre, and O Pouliquen. A constitutive law for dense granular flows. *Nature*, 441(7094):727–730, Jun 2006. doi: 10.1038/nature04801.

A Jovanović, M Pezo, L Pezo, and L Lević. DEM/CFD analysis of granular flow in static mixers. *Powder Technology*, 266:240–248, Nov 2014. doi: 10.1016/j.powtec.2014.06.032. URL http://dx.doi.org/10.1016/j.powtec.2014.06.032.

R Kaitna and D Rickenmann. Flow of different material mixtures in a rotating drum. *Fourth International DFHM Conference*, pages 10–13, 2007.

Toshihiro Kawaguchi. MRI measurement of granular flows and fluid-particle flows. *Advanced Powder Technology*, 21(3):235–241, May 2010. doi: 10.1016/j.apt.2010.03.014. URL http://dx.doi.org/10.1016/j.apt.2010.03.014.

G Kawashima and WJ Yang. Unsteady flow in rotating drums using laser doppler velocimetry. *Experiments in Fluids*, 6(3):165–171, 1988.

E G Kelly and D J Spottiswood. Introduction to mineral processing. 1982.

K A Kempter and G L Rowe. Leakage of active crater lake brine through the north flank at rincón de la vieja volcano, northwest costa rica, and implications for crater collapse. *Journal of Volcanology and Geothermal Research*, 97(1):143–159, 2000.

H J R Keys and P M Green. Ruapehu lahar New Zealand 18 march 2007: lessons for hazard assessment and risk mitigation 1995–2007. *Journal of Disaster Research*, 3(4):284–296, 2008.

Mohammad Khalilitehrani, Per J Abrahamsson, and Anders Rasmuson. Modeling dilute and dense granular flows in a high shear granulator. *Powder Technology*, 263:45–49, Sep 2014. doi: 10.1016/j.powtec.2014.04.088. URL http://dx.doi.org/10.1016/j.powtec.2014.04.088.

T A Kingston and T J Heindel. Optical visualization and composition analysis to quantify continuous granular mixing processes. *Powder Technology*, 262(C):257–264, Jan

2013. doi: 10.1016/j.powtec.2014.04.071. URL http://dx.doi.org/10.1016/j.powtec.2014.04.071.

T A Kingston and T J Heindel. Granular mixing optimization and the influence of operating conditions in a double screw mixer. *Powder Technology*, 266(C):1–12, Jan 2014. doi: 10.1016/j.powtec.2014.06.016. URL http://dx.doi.org/10.1016/j.powtec.2014.06.016.

T A Kingston, T A Geick, T R Robinson, and T J Heindel. Characterizing 3D granular flow structures in a double screw mixer using x-ray particle tracking velocimetry. *Powder Technology*, 278(C):211–222, Apr 2015. doi: 10.1016/j.powtec.2015.02.061. URL http://dx.doi.org/10.1016/j.powtec.2015.02.061.

D Knighton. *Fluvial forms and processes: a new perspective. Ed. 2.* Arnold, Hodder Headline, PLC, 1998.

M Kodam, R Bharadwaj, J Curtis, B Hancock, and C Wassgren. Cylindrical object contact detection for use in discrete element method simulations, Part II—experimental validation. *Chemical Engineering Science*, 65(22):5863–5871, Nov 2010a. doi: 10.1016/j.ces.2010.08.007. URL http://dx.doi.org/10.1016/j.ces.2010.08.007.

M Kodam, R Bharadwaj, J Curtis, B Hancock, and C Wassgren. Cylindrical object contact detection for use in discrete element method simulations. Part I – contact detection algorithms. *Chemical Engineering Science*, 65(22):5852–5862, Nov 2010b. doi: 10.1016/j.ces.2010.08.006. URL http://dx.doi.org/10.1016/j.ces.2010.08.006.

Ma H Köhl, G Lu, J R Third, M Häberlin, L Kasper, K P Prüssmann, and C R Müller. Magnetic resonance imaging (MRI) study of jet formation in packed beds. *Chemical Engineering Science*, 97(C):406–412, Jun 2013. doi: 10.1016/j.ces.2013.04.046. URL http://dx.doi.org/10.1016/j.ces.2013.04.046.

M Koken, G Constantinescu, and K Blanckaert. Hydrodynamic processes, sediment

erosion mechanisms, and reynolds-number-induced scale effects in an open channel bend of strong curvature with flat bathymetry. *Journal of Geophysical Research Earth Surface*, pages n/a–n/a, Nov 2013. doi: 10.1002/2013JF002760.

T S Komatsu, S Inagaki, N Nakagawa, and S Nasuno. Creep motion in a granular pile exhibiting steady surface flow. *Physical Review Letters*, 86(9):1757–1760, 2001.

H Komossa, S Wirtz, V Scherer, F Herz, and E Specht. Transversal bed motion in rotating drums using spherical particles: Comparison of experiments with DEM simulations. *Powder Technology*, 264(C):96–104, Jul 2014. doi: doi:10.1016/j.powtec.2014.05.021. URL `http://dx.doi.org/10.1016/j.powtec.2014.05.021`.

V Kumaran. The constitutive relation for the granular flow of rough particles, and its application to the flow down an inclined plane. *Journal of Fluid Mechanics*, 561:1, Aug 2006. doi: 10.1017/S0022112006000279.

K Kuwagi, A Kogane, H Hirano, A B Alias, and T Takami. Non-dimensionalization and three-dimensional flow regime map for fluidization analyses. *Chemical Engineering Science*, 119(C):199–211, Nov 2014. doi: 10.1016/j.ces.2014.08.006. URL `http://dx.doi.org/10.1016/j.ces.2014.08.006`.

F Lavigne and JC Thouret. Sediment transportation and deposition by rain-triggered lahars at Merapi Volcano, Central Java, Indonesia. *Geomorphology*, 49(1-2):45–69, 2002.

F Lavigne, JC Thouret, B Voight, H Suwa, and A Sumaryono. Lahars at Merapi volcano, Central Java: an overview. *Journal of Volcanology and Geothermal Research*, 100(1-4):423–456, 2000.

J Lecointre, K Hodgson, V E Neall, and S J Cronin. Lahar-triggering mechanisms and hazard at Ruapehu volcano, New Zealand. *Natural Hazards*, 31(1):85–109, 2004.

C-C Liao, S-S Hsiau, and P-S Chang. Bottom wall friction coefficients on the dynamic

properties of sheared granular flows. *Powder Technology*, 270(C):1–10, Jan 2013. doi: 10.1016/j.powtec.2014.10.043. URL http://dx.doi.org/10.1016/j.powtec.2014.10.043.

S Y Lim, J F Davidson, R N Forster, D J Parker, D M Scott, and J P K Seville. Avalanching of granular material in a horizontal slowly rotating cylinder: PEPT studies. *Powder Technology*, 138(1):25–30, 2003.

H Liu, D K Tafti, and T Li. Hybrid parallelism in MFIX CFD-DEM using OpenMP. *Powder Technology*, 259(C):22–29, Jan 2014. doi: 10.1016/j.powtec.2014.03.047. URL http://dx.doi.org/10.1016/j.powtec.2014.03.047.

S D Liu, Z Y Zhou, R P Zou, D Pinson, and A B Yu. Flow characteristics and discharge rate of ellipsoidal particles in a flat bottom hopper. *Powder Technology*, pages 1–45, Nov 2013. doi: 10.1016/j.powtec.2013.11.001. URL http://dx.doi.org/10.1016/j.powtec.2013.11.001.

E Lorenz. Deterministic nonperiodic flow. *Journal of the Atmospheric Sciences*, 20(2):130–141, 1963.

H Louati, D Oulahna, and A de Ryck. Apparent friction and cohesion of a partially wet granular material in steady-state shear. *Powder Technology*, 278(C):65–71, Jan 2015. doi: 10.1016/j.powtec.2015.03.011. URL http://dx.doi.org/10.1016/j.powtec.2015.03.011.

G Lu, J R Third, and C R Müller. Discrete element models for non-spherical particle systems: From theoretical developments to applications. *Chemical Engineering Science*, 127(C):425–465, May 2015. doi: 10.1016/j.ces.2014.11.050. URL http://dx.doi.org/10.1016/j.ces.2014.11.050.

L Lu, J Xu, W Ge, Y Yue, X Liu, and J Li. EMMS-based discrete particle method (EMMS–DPM) for simulation of gas–solid flows. *Chemical Engineering Science*, 120(C):67–87,

Dec 2014. doi: 10.1016/j.ces.2014.08.004. URL `http://dx.doi.org/10.1016/j.ces.2014.08.004`.

G Lube, H E Huppert, R Stephen J Sparks, and M A Hallworth. Axisymmetric collapses of granular columns. *Journal of Fluid Mechanics*, 508:175–199, Jun 2004. doi: 10.1017/S0022112004009036.

G Lube, H E Huppert, R Sparks, and A Freundt. Collapses of two-dimensional granular columns. *Physical Review E*, 72(4):041301, Oct 2005. doi: 10.1103/PhysRevE.72.041301.

G Lube, S J Cronin, V Manville, J N Procter, S E Cole, and A Freundt. Energy growth in laharic mass flows. *Geology*, 40(5):475–478, May 2012. doi: 10.1130/G32818.1.

Zheng Yuan Luo and BoFeng Bai. Dynamics of biconcave vesicles in a confined shear flow. *Chemical Engineering Science*, 2015.

J J Major. Depositional processes in large-scale debris-flow experiments. *The Journal of Geology*, 105(3):345–366, 1997.

J J Major and L E Mark. Peak flow responses to landscape disturbances caused by the cataclysmic 1980 eruption of Mount St. Helens, Washington. *Geological Society of America Bulletin*, 118(7-8):938–958, Jul 2006. doi: 10.1130/B25914.1.

H Makse, N Gland, D Johnson, and L Schwartz. Granular packings: Nonlinear elasticity, sound propagation, and collective relaxation dynamics. *Physical Review E*, 70(6):061302, 2004.

A Mangeney-Castelnau. On the use of Saint Venant equations to simulate the spreading of a granular mass. *Journal of Geophysical Research*, 110(B9):B09103, Jan 2005. doi: 10.1029/2004JB003161.

V Mansard and A Colin. Local and non local rheology of concentrated particles. *Soft Matter*, 8(15):4025, Jan 2012. doi: 10.1039/c2sm25306b.

V Manville and S J Cronin. Breakout lahar from new zealand's crater lake. *Eos, Transactions American Geophysical Union*, 88(43):441–442, 2007.

S Marcial, A A Melosantos, K C Hadley, R G LaHusen, and J N Marso. Instrumental lahar monitoring at Mount Pinatubo. *Fire and Mud: Eruptions and Lahars of Mt. Pinatubo, Philippines*, 1996.

M C Marinack Jr and C F Higgs III. Three-dimensional physics-based cellular automata model for granular shear flow. *Powder Technology*, 277(C):287–302, Mar 2015. doi: 10.1016/j.powtec.2015.02.057. URL `http://dx.doi.org/10.1016/j.powtec.2015.02.057`.

B Marks and I Einav. A mixture of crushing and segregation: the complexity of grainsize in natural granular flows. *Geophysical Research Letters*, pages n/a–n/a, Jan 2015. doi: 10.1002/2014GL062470.

M Massoudi, J Kim, and J F Antaki. Modeling and numerical simulation of blood flow using the theory of interacting continua. *International Journal of Non-Linear Mechanics*, 47(5):506–520, Jun 2012. doi: 10.1016/j.ijnonlinmec.2011.09.025. URL `http://dx.doi.org/10.1016/j.ijnonlinmec.2011.09.025`.

D Mateo-Ortiz, F J Muzzio, and R Méndez. Particle size segregation promoted by powder flow in confined space: The die filling process case. *Powder Technology*, 262(C):215–222, May 2014. doi: doi:10.1016/j.powtec.2014.04.023. URL `http://dx.doi.org/10.1016/j.powtec.2014.04.023`.

S W McCoy, G E Tucker, J W Kean, and J A Coe. Field measurement of basal forces generated by erosive debris flows. *Journal of Geophysical Research Earth Surface*, 118(2):589–602, May 2013. doi: 10.1002/jgrf.20041.

A Mehring. Factors affecting the drillability of fertilizers. *Industrial & Engineering Chemistry*, 21(12):1219–1223, 1929.

J Mellmann. The transverse motion of solids in rotating cylinders—forms of motion and transition behavior. *Powder Technology*, 118(3):251–270, 2001.

J Mellmann, E Specht, and X Liu. Prediction of rolling bed motion in rotating cylinders. *AIChE journal*, 50(11):2783–2793, 2004.

G V Middleton and M A Hampton. Subaqueous sediment transport and deposition by sediment gravity flows. *Marine sediment transport and environmental management: New York, Wiley*, pages 197–218, 1976.

GDR MiDi. On dense granular flows. *The European Physical Journal E*, 14(4):341–365, Jan 2004. doi: 10.1140/epje/i2003-10153-0.

Y Miyabuchi, F Maeno, and S Nakada. The October 16, 2013 rainfall-induced landslides and associated lahars at Izu Oshima Volcano, Japan. *Journal of Volcanology and Geothermal Research*, 302:242–256, 2015.

O Mohr. Über die bestimmung und die graphische darstellung von trägheitsmomenten ebener flächen. *Civiling*, 33:43, 1887.

A H Ahmadi Motlagh, J R Grace, M Salcudean, and C M Hrenya. New structure-based model for Eulerian simulation of hydrodynamics in gas–solid fluidized beds of Geldart group "A" particles. *Chemical Engineering Science*, 120(C):22–36, Dec 2014. doi: 10.1016/j.ces.2014.08.042. URL `http://dx.doi.org/10.1016/j.ces.2014.08.042`.

W O Moughrabiah, J R Grace, and X T Bi. Electrostatics in gas–solid fluidized beds for different particle properties. *Chemical Engineering Science*, 75(C):198–208, Jun 2012. doi: 10.1016/j.ces.2012.02.041. URL `http://dx.doi.org/10.1016/j.ces.2012.02.041`.

E Muñoz-Salinas, V C Manea, D Palacios, and M Castillo-Rodriguez. Estimation of

lahar flow velocity on Popocatepetl volcano (Mexico). *Geomorphology*, 92(1-2):91–99, Jan 2007.

M Nakagawa, S A Altobelli, A Caprihan, E Fukushima, and E-K Jeong. Non-invasive measurements of granular flows by magnetic resonance imaging. *Experiments in Fluids*, 16(1):54–60, 1993. ISSN 0723-4864. doi: 10.1007/BF00188507. URL http://dx.doi.org/10.1007/BF00188507.

J L Naranjo, H Sigurdsson, S N Carey, and W Fritz. Eruption of the Nevado del Ruiz volcano, Colombia, on 13 November 1985: tephra fall and lahars. *Science*, 233(4767): 961, 1986.

S M Nascimento, D A Santos, M A S Barrozo, and C R Duarte. Solids holdup in flighted rotating drums: An experimental and simulation study. *Powder Technology*, 280(C): 18–25, May 2015. doi: doi:10.1016/j.powtec.2015.04.038. URL http://dx.doi.org/10.1016/j.powtec.2015.04.038.

V Neall. Lahars as major geological hazards. *Bulletin of Engineering Geology and the Environment*, Jan 1976. URL http://www.springerlink.com/index/860727077516V2G1.pdf.

R M Nedderman. *Statics and kinematics of granular materials*. Cambridge University Press, 2005.

C G Newhall and R Punongbayan. *Fire and mud: eruptions and lahars of Mount Pinatubo, Philippines*. Philippine Institute of Volcanology and Seismology Quezon City, 1996.

S Ngako, R Mouangue, S Caillat, A Kuitche, and E Saragba. Numerical investigation of bed depth height, axial velocity and mean residence time of inert particles in steady state industrial cement rotary kiln: Case of Figuil Plant in Cameroon. *Powder Technology*, 271(C):1–7, Jan 2014. doi: 10.1016/j.powtec.2014.11.007. URL http://dx.doi.org/10.1016/j.powtec.2014.11.007.

D Nguyen, A Rasmuson, K Thalberg, and I N Björn. Numerical modelling of breakage and adhesion of loose fine-particle agglomerates. *Chemical Engineering Science*, 116 (C):91–98, Sep 2014. doi: 10.1016/j.ces.2014.04.034. URL `http://dx.doi.org/10.1016/j.ces.2014.04.034`.

D O Njobuenwu and M Fairweather. Dynamics of single, non-spherical ellipsoidal particles in a turbulent channel flow. *Chemical Engineering Science*, 123(C):265–282, Feb 2015. doi: 10.1016/j.ces.2014.11.024. URL `http://dx.doi.org/10.1016/j.ces.2014.11.024`.

S Ogawa. Multitemperature theory of granular materials. *Proc. of US-Japan Symp. on Continuum Mechanics and Statistical Approaches to the Mechanics of Granular Media*, 1978.

A Orpe and D Khakhar. Scaling relations for granular flow in quasi-two-dimensional rotating cylinders. *Physical Review E*, 64(3):031302, Aug 2001. doi: 10.1103/PhysRevE.64.031302.

A V Orpe and D V Khakhar. Solid-fluid transition in a granular shear flow. *Physical Review Letters*, 93(6):068001, 2004.

B E O'Shea. Ruapehu and the Tangiwai disaster. *New Zealand Journal of Science and Technology B*, 36:174–189, 1954.

Y Oyama. Mixing of solids. *Bull Inst Phys Chem Res Rep*, 5:600, 1939.

F Pacheco-Vázquez, F Ludewig, and S Dorbolo. Dynamics of a grain-filled ball on a vibrating plate. *Physical Review Letters*, 113(11):118001, Sep 2014. doi: 10.1103/PhysRevLett.113.118001.

T Pähtz, A Omeradžić, M V Carneiro, Nuno A M Araújo, and H J Herrmann. Discrete element method simulations of the saturation of aeolian sand transport. *Geophysical Research Letters*, pages n/a–n/a, Feb 2015. doi: 10.1002/2014GL062945.

D J Parker, C J Broadbent, P Fowles, M R Hawkesworth, and P McNeil. Positron emission particle tracking-a technique for studying flow within engineering equipment. *Nuclear Instruments and Methods in Physics Research Section A: Accelerators, Spectrometers, Detectors and Associated Equipment*, 326(3):592–607, 1993.

D J Parker, M R Hawkesworth, C J Broadbent, P Fowles, T D Fryer, and P A McNeil. Industrial positron-based imaging: principles and applications. *Nuclear Instruments and Methods in Physics Research Section A: Accelerators, Spectrometers, Detectors and Associated Equipment*, 348(2):583–592, 1994.

D J Parker, A E Dijkstra, T W Martin, and J P K Seville. Positron emission particle tracking studies of spherical particle motion in rotating drums. *Chemical Engineering Science*, 52(13):2011–2022, Jan 1997.

D J Parker, R N Forster, P Fowles, and P S Takhar. Positron emission particle tracking using the new Birmingham positron camera. *Nuclear Instruments and Methods in Physics*, 477(1):540545, Jan 2002.

J M Pastor, A Garcimartín, P A Gago, J P Peralta, C Martín-Gómez, L M Ferrer, D Maza, D R Parisi, L A Pugnaloni, and I Zuriguel. Experimental proof of faster-is-slower in multi-particle systems flowing through bottlenecks. *arXiv preprint arXiv:1507.05110*, 2015.

B R Paterson et al. The hazard of lahars to the Tongariro power development, New Zealand. 1980.

J D Pelletier. Controls on the large-scale spatial variations of dune-field properties in the barchanoid portion of White Sands dune field, new mexico. *Journal of Geophysical Research Earth Surface*, pages n/a–n/a, Jan 2015. doi: 10.1002/2014JF003314.

R H Perry and C H Chilton. 1973, chemical engineers handbook. *McGraw–Hill, New York. In article*, 1973.

P G C Petean and M L Aguiar. Determining the adhesion force between particles and rough surfaces. *Powder Technology*, 274(C):67–76, Jan 2013. doi: 10.1016/j.powtec.2014.12.047. URL http://dx.doi.org/10.1016/j.powtec.2014.12.047.

T C Pierson. Hyperconcentrated flow—transitional process between water flow and debris flow. *Debris-flow Hazards and Related Phenomena*, pages 159–202, 2005.

T C Pierson, R J Janda, J C Thouret, and C A Borrero. Perturbation and melting of snow and ice by the 13 November 1985 eruption of Nevado del Ruiz, Colombia, and consequent mobilization, flow and deposition of lahars. *Journal of Volcanology and Geothermal Research*, 41(1-4):17–66, 1990.

T C Pierson, A S Daag, P J Delos Reyes, M T M Regalado, R U Solidum, and B S Tubianosa. Flow and deposition of posteruption hot lahars on the east side of Mount Pinatubo, July–October 1991. *Fire and Mud: eruptions and lahars of Mount Pinatubo, Philippines*, pages 921–950, 1996.

TC Pierson. Initiation and flow behavior of the 1980 Pine Creek and Muddy river lahars, Mount St. Helens, Washington. *Geological Society of America Bulletin*, 96(8):1056–1069, 1985.

TC Pierson and JE Costa. *A rheologic classification of subaerial sediment-water flows*. US Geological Survey, 1986.

M Pistolesi, R Cioni, M Rosi, and E Aguilera. Lahar hazard assessment in the southern drainage system of Cotopaxi volcano, Ecuador: Results from multiscale lahar simulations. *Geomorphology*, 207(C):51–63, Feb 2014. doi: doi:10.1016/j.geomorph.2013.10.026. URL http://dx.doi.org/10.1016/j.geomorph.2013.10.026.

E B Pitman, C C Nichita, A Patra, A Bauer, M Sheridan, and M Bursik. Computing granular avalanches and landslides. *Physics of Fluids*, 15:3638, 2003a.

E B Pitman, C C Nichita, A K Patra, A C Bauer, M Bursik, and A Weber. A model of

granular flows over an erodible surface. *Discrete and Continuous Dynamical Systems Series B*, 3(4):589–600, 2003b.

M Pore, G H Ong, C M Boyce, M Materazzi, J Gargiuli, T Leadbeater, A J Sederman, J S Dennis, D J Holland, A Ingram, P Lettieri, and D J Parker. A comparison of magnetic resonance, X-ray and positron emission particle tracking: Measurements of a single jet of gas entering a bed of particles. *Chemical Engineering Science*, pages 1–25, Sep 2014. doi: 10.1016/j.ces.2014.09.029. URL `http://dx.doi.org/10.1016/j.ces.2014.09.029`.

O Pouliquen. Scaling laws in granular flows down rough inclined planes. *Physics of Fluids*, 11(3):542–548, Jan 1999a.

O Pouliquen. On the shape of granular fronts down rough inclined planes. *Physics of Fluids*, 11:1956, 1999b.

O Pouliquen and F Chevoir. Dense flows of dry granular material. *Comptes Rendus Physique*, 3(2):163–175, 2002.

O Pouliquen, C Cassar, P Jop, Y Forterre, and M Nicolas. Flow of dense granular material: towards simple constitutive laws. *Journal of Statistical Mechanics: Theory and Experiment*, 2006(07):P07020–P07020, Jul 2006. doi: 10.1088/1742-5468/2006/07/P07020.

J Procter, S J Cronin, I C Fuller, G Lube, and V Manville. Quantifying the geomorphic impacts of a lake-breakout lahar, Mount Ruapehu, New Zealand. *Geology*, 38(1):67–70, Jan 2010a. doi: 10.1130/G30129.1.

J Procter, S J Cronin, I C Fuller, G Lube, and V Manville. Quantifying the geomorphic impacts of a lake-breakout lahar, mount ruapehu, new zealand. *Geology*, 38(1):67–70, 2010b.

H Qi, J Xu, G Zhou, F Chen, W Ge, and J Li. Numerical investigation of granular flow

similarity in rotating drums. *Particuology*, pages 1–9, Mar 2015. doi: 10.1016/j.partic.2014.10.012. URL http://dx.doi.org/10.1016/j.partic.2014.10.012.

S Radl and S Sundaresan. A drag model for filtered Euler–Lagrange simulations of clustered gas–particle suspensions. *Chemical Engineering Science*, 117(C):416–425, Sep 2014. doi: 10.1016/j.ces.2014.07.011. URL http://dx.doi.org/10.1016/j.ces.2014.07.011.

C V Raman. The photographic study of impact at minimal velocities. *Physical Review*, 12(6):442–447, 1918.

J E Reber, N W Hayman, and L L Lavier. Stick-slip and creep behavior in lubricated granular material: insights into the brittle-ductile transition. *Geophysical Research Letters*, pages n/a–n/a, May 2014. doi: 10.1002/2014GL059832.

K Reddy, Y Forterre, and O Pouliquen. Evidence of mechanically activated processes in slow granular flows. *Physical Review Letters*, 106(10):108301, Mar 2011. doi: 10.1103/PhysRevLett.106.108301.

I Reiweger, J Gaume, and J Schweizer. A new mixed-mode failure criterion for weak snowpack layers. *Geophysical Research Letters*, pages n/a–n/a, Jan 2015. doi: 10.1002/2014GL062780.

M Renouf, D Bonamy, F Dubois, and P Alart. Numerical simulation of 2D steady granular flows in rotating drum: On surface flows rheology. *arXiv preprint cond-mat/0506796*, 2005.

O Reynolds. LVII. On the dilatancy of media composed of rigid particles in contact. With experimental illustrations. *The London, Edinburgh, and Dublin Philosophical Magazine and Journal of Science*, 20(127):469–481, 1885.

O Reynolds. Experiments showing dilatancy, a property of granular material, possibly

connected with gravitation. In *Proc. Royal Institution of Great Britain, Read*, volume 12, 1886.

P Richard and N Taberlet. Recent advances in dem simulations of grains in a rotating drum. *Soft Matter*, 4(7):1345–1348, 2008.

O Roche, S Montserrat, Y Niño, and A Tamburrino. Pore fluid pressure and internal kinematics of gravitational laboratory air-particle flows: Insights into the emplacement dynamics of pyroclastic flows. *Journal of Geophysical Research*, 115(B9): B09206, Sep 2010. doi: 10.1029/2009JB007133.

K S Rodolfo. Rain-lahar generation and sediment delivery systems at Mayon Volcano, Philippines. 1991.

K S Rodolfo, J V Umbal, R A Alonso, C T Remotigue, M L Paladio-Melosantos, J H G Salvador, D Evangelista, and Y Miller. Two years of lahars on the western flank of Mount Pinatubo: Initiation, flow processes, deposits, and attendant geomorphic and hydraulic changes. *Fire and Mud: Eruptions and Lahars of Mount Pinatubo, Philippines*, pages 989–1013, 1996.

S S Rodrigues, A Forret, F Montjovet, M Lance, and Th Gauthier. Riser hydrodynamic study with different Group B powders. *Powder Technology*, 272(C):300–308, Jan 2014. doi: 10.1016/j.powtec.2014.12.014. URL `http://dx.doi.org/10.1016/j.powtec.2014.12.014`.

A Rosato, K J Strandburg, F Prinz, and R H Swendsen. Why the Brazil nuts are on top: Size segregation of particulate matter by shaking. *Physical Review Letters*, 58(10): 1038, 1987.

P J Rowley, O Roche, T H Druitt, and R Cas. Experimental study of dense pyroclastic density currents using sustained, gas-fluidized granular flows. *Bulletin of Volcanology*, 76(9):855, Sep 2014. doi: 10.1007/s00445-014-0855-1.

R Rutgers. Longitudinal mixing of granular material flowing through a rotating cylinder—: Part I. Descriptive and theoretical. *Chemical Engineering Science*, 20(12): 1079–1087, 1965a.

R Rutgers. Longitudinal mixing of granular material flowing through a rotating cylinder: Part II. Experimental. *Chemical Engineering Science*, 20(12):1089–1100, 1965b.

A C Santomaso, Y L Ding, J R Lickiss, and D W York. Investigation of the granular behaviour in a rotating drum operated over a wide range of rotational speed. *Chemical Engineering Research and Design*, 81(8):936–945, 2003.

D A Santos, I J Petri, C R Duarte, and M A S Barrozo. Experimental and CFD study of the hydrodynamic behavior in a rotating drum. *Powder Technology*, 250:52–62, Oct 2013. doi: 10.1016/j.powtec.2013.10.003. URL `http://dx.doi.org/10.1016/j.powtec.2013.10.003`.

D A Santos, C R Duarte, and M A S Barrozo. Segregation phenomenon in a rotary drum: Experimental study and CFD simulation. *Powder Technology*, 294:1–10, 2016.

S B Savage. In J W Hutchinson and T Y Wu, editors, *The Mechanics of Rapid Granular Flows*, volume 24 of *Advances in Applied Mechanics*, pages 289 – 366. Elsevier, 1984. doi: http://dx.doi.org/10.1016/S0065-2156(08)70047-4. URL `http://www.sciencedirect.com/science/article/pii/S0065215608700474`.

S B Savage and K Hutter. The motion of a finite mass of granular material down a rough incline. *Journal of Fluid Mechanics*, 199(1):177–215, 1989.

C P Schlick, Y Fan, P B Umbanhowar, J M Ottino, and R M Lueptow. Granular segregation in circular tumblers: theoretical model and scaling laws. *Journal of Fluid Mechanics*, 765:632–652, Feb 2015. doi: 10.1017/jfm.2015.4.

Stanislaw F Scieszka and Daniel Adamecki. The importance of wall friction between particulate solids and elastomeric belt. *Powder Technology*, 245(C):1–9, Jan 2013.

doi: 10.1016/j.powtec.2013.04.031. URL http://dx.doi.org/10.1016/j.powtec.2013.04.031.

G Seiden and P J Thomas. Complexity, segregation, and pattern formation in rotating-drum flows. *Reviews of Modern Physics*, 83(4):1323, 2011.

S S Sharpe, S A Koehler, R M Kuckuk, M Serrano, P A Vela, J Mendelson, and D I Goldman. Locomotor benefits of being a slender and slick sand-swimmer. *The Journal of Experimental Biology*, pages jeb–108357, 2014.

T Shinbrot, A Alexander, M Moakher, and F J Muzzio. Chaotic granular mixing. *Chaos: An Interdisciplinary Journal of Nonlinear Science*, 9(3):611–620, 1999a.

T Shinbrot, A Alexander, and F Muzzio. Spontaneous chaotic granular mixing. *Nature*, 397(6721):675–678, 1999b.

T Shinbrot, K Lamarche, and B Glasser. Triboelectrification and razorbacks: Geophysical patterns produced in dry grains. *Physical Review Letters*, 96(17):178002, May 2006. doi: 10.1103/PhysRevLett.96.178002.

C Small and T Naumann. The global distribution of human population and recent volcanism. *Global Environmental Change Part B: Environmental Hazards*, 3(3):93–109, 2001.

G Smith and D Lowe. Lahars: Volcano hydrologic-events and deposition in the debris flow—hyperconcentrated flow continuum. *archives.datapages.com*, Jan 1991. URL http://archives.datapages.com/data/sepm_sp/SP45/Lahars_Volcano_Hydrologic_Events.pdf.

G A Smith and W J Fritz. Volcanic influences on terrestrial sedimentation. *Geology*, 17 (4):375–376, 1989.

F Song, W Wang, K Hong, and J Li. Unification of EMMS and TFM structure-dependent analysis of mass, momentum and energy conservation. *Chemical Engineering Sci-*

ence, 120(C):112–116, Dec 2014. doi: 10.1016/j.ces.2014.08.057. URL http://dx.doi.org/10.1016/j.ces.2014.08.057.

M Sperl. Experiments on corn pressure in silo cells–translation and comment of Janssen's paper from 1895. *Granular Matter*, 8(2):59–65, 2006.

M K Stanford and C Dellacorte. Effects of humidity on the flow characteristics of a composite plasma spray powder. *Journal of Thermal Spray Technology*, 15(1):33–36, Mar 2006. doi: 10.1361/105996306X92550.

C C A Starheim, C Gomez, T Davies, F Lavigne, and P Wassmer. In-flow evolution of lahar deposits from video-imagery with implications for post-event deposit interpretation, Mount Semeru, Indonesia. *Journal of Volcanology and Geothermal Research*, 256:96–104, 2013.

W F Stilwell, H J Hopkins, and W Appleton. Tangiwai railway disaster. *Report of the Board of Inquiry. Wellington, Government Printer*, 1954.

K Rao Sunkara, F Herz, E Specht, and J Mellmann. Transverse flow at the flight surface in flighted rotary drum. *Powder Technology*, 275(C):161–171, Feb 2015. doi: 10.1016/j.powtec.2015.01.058. URL http://dx.doi.org/10.1016/j.powtec.2015.01.058.

S L F Sutton, C Mckenna Neuman, and W Nickling. Avalanche grainflow on a simulated aeolian dune. *Journal of Geophysical Research Earth Surface*, pages n/a–n/a, Aug 2013. doi: 10.1002/jgrf.20130.

N Taberlet, P Richard, E Henry, and R Delannay. The growth of a super stable heap: An experimental and numerical study. *EPL (Europhysics Letters)*, 68(4):515, 2004.

P Tegzes, T Vicsek, and P Schiffer. Development of correlations in the dynamics of wet granular avalanches. *Physical Review E*, 67(5):051303, 2003.

W Thielicke and E J Stamhuis. PIVlab - Time-Resolved Digital Particle Image Velocime-

try Tool for MATLAB (version: 1.35). 07 2014. URL http://dx.doi.org/10.6084/m9.figshare.1092508.

W Thomson. Hydrokinetic solutions and observations. (Lord Kelvin). *Proceedings of the Royal Society*, 7:63, 1871.

J-C Thouret, K E Abdurachman, J-L Bourdier, and S Bronto. Origin, characteristics, and behaviour of lahars following the 1990 eruption of Kelud volcano, eastern Java (Indonesia). *Bulletin of Volcanology*, 59(7):460–480, 1998.

R Torres, P Mouginis-Mark, S Self, H Garbeil, K Kallianpur, and R Quiambao. Monitoring the evolution of the Pasig–Potrero alluvial fan, Pinatubo Volcano, using a decade of remote sensing data. *Journal of Volcanology and Geothermal Research*, 138(3): 371–392, 2004.

M Tost, S. J Cronin, and J. N Procter. Transport and emplacement mechanisms of channelised long-runout debris avalanches, Ruapehu volcano, New Zealand. *Bulletin of Volcanology*, 76(12):881, Dec 2014. doi: 10.1007/s00445-014-0881-z.

S Uesawa. A study of the Taisho lahar generated by the 1926 eruption of Tokachidake Volcano, central Hokkaido, Japan, and implications for the generation of cohesive lahars. *Journal of Volcanology and Geothermal Research*, 270:23–34, Jan 2014. doi: 10.1016/j.jvolgeores.2013.11.002. URL http://dx.doi.org/10.1016/j.jvolgeores.2013.11.002.

R Vazquez, L Capra, L Caballero, R Arambula-Mendoza, and G Reyes-DaVila. The anatomy of a lahar: Deciphering the 15th September 2012 lahar at Volcán de Colima, Mexico. *Journal of Volcanology and Geothermal Research*, 272(C):126–136, Feb 2014. doi: doi:10.1016/j.jvolgeores.2013.11.013. URL http://dx.doi.org/10.1016/j.jvolgeores.2013.11.013.

H L F von Helmholtz. XLIII. on discontinuous movements of fluids. *The London, Edin-*

burgh, and Dublin Philosophical Magazine and Journal of Science, 36(244):337–346, 1868.

D M Walker. A basis for bunker design. *Powder Technology*, 1(4):228–236, 1967.

M Wang, W Zhu, Q Sun, and X Zhang. A DEM simulation of dry and wet particle flow behaviors in riser. *Powder Technology*, 267(PA):221–233, Jan 2014a. doi: 10.1016/j.powtec.2014.07.026. URL http://dx.doi.org/10.1016/j.powtec.2014.07.026.

S Wang, Y Shen, Y Ma, J Gao, X Lan, Q Dong, and Q Cheng. Study of hydrodynamic characteristics of particles in liquid–solid fluidized bed with uniform transverse magnetic field. *Powder Technology*, 245:314–323, Sep 2013. doi: 10.1016/j.powtec.2013.04.049. URL http://dx.doi.org/10.1016/j.powtec.2013.04.049.

T Wang, Y He, and D R Kim. Granular temperature and rotational characteristic analysis of a gas–solid bubbling fluidized bed under different gravities using discrete hard sphere model. *Powder Technology*, 271(C):1–14, Nov 2014b. doi: 10.1016/j.powtec.2014.11.005. URL http://dx.doi.org/10.1016/j.powtec.2014.11.005.

J M Warnett, P Denissenko, P J Thomas, and M A Williams. Collapse of a granular column under rotation. *Powder Technology*, 262:249–256, Jan 2014. doi: 10.1016/j.powtec.2014.04.030. URL http://dx.doi.org/10.1016/j.powtec.2014.04.030.

N S Weerasekara, M S Powell, P W Cleary, L M Tavares, M Evertsson, R D Morrison, J Quist, and R M Carvalho. The contribution of DEM to the science of comminution. *Powder Technology*, 248(C):3–24, Sep 2013. doi: doi:10.1016/j.powtec.2013.05.032. URL http://dx.doi.org/10.1016/j.powtec.2013.05.032.

C Wentworth. A scale of grade and class terms for clastic sediments. *The Journal of Geology*, pages 377–392, 1922.

A C Wilcox, J E O'Connor, and J J Major. Rapid reservoir erosion, hyperconcentrated flow, and downstream deposition triggered by breaching of 38 m tall Condit Dam,

White Salmon River, Washington. *Journal of Geophysical Research Earth Surface*, pages n/a–n/a, Jun 2014. doi: 10.1002/2013JF003073.

W L Wilkinson. *Non-Newtonian fluids: fluid mechanics, mixing and heat transfer*. Pergamon Press London, 1960.

CS Witham. Volcanic disasters and incidents: A new database. *Journal of Volcanology and Geothermal Research*, 148(3):191–233, 2005.

R Worni, C Huggel, M Stoffel, and B Pulgarín. Challenges of modeling current very large lahars at Nevado del Huila Volcano, Colombia. *Bulletin of Volcanology*, 74(2): 309–324, 2012.

C L Wu, O Ayeni, A S Berrouk, and K Nandakumar. Parallel algorithms for CFD–DEM modeling of dense particulate flows. *Chemical Engineering Science*, 118(C):221–244, Oct 2014. doi: 10.1016/j.ces.2014.07.043. URL `http://dx.doi.org/10.1016/j.ces.2014.07.043`.

K Yamane, M Nakagawa, S A Altobelli, T Tanaka, and Y Tsuji. Steady particulate flows in a horizontal rotating cylinder. *Physics of Fluids (1994-present)*, 10(6):1419–1427, 1998.

RY Yang, AB Yu, L McElroy, and J Bao. Numerical simulation of particle dynamics in different flow regimes in a rotating drum. *Powder Technology*, 188(2):170–177, 2008.

V M Yarushina, D Bercovici, and C Michaut. Two-phase dynamics of volcanic eruptions: Particle size distribution and the conditions for choking. *Journal of Geophysical Research Solid Earth*, 120(3):1503–1522, Mar 2015. doi: 10.1002/2014JB011195.

H Yin, M Zhang, and H Liu. Numerical simulation of three-dimensional unsteady granular flows in rotary kiln. *Powder Technology*, pages 1–40, Nov 2013. doi: 10.1016/j.powtec.2013.10.044. URL `http://dx.doi.org/10.1016/j.powtec.2013.10.044`.

Y Yu, S Jia, G Zhu, W Tan, and X Chen. Numerical study of frictional model for dense

granular flow. *Powder Technology*, 272(C):1–13, Jan 2014. doi: 10.1016/j.powtec.2014.12.001. URL `http://dx.doi.org/10.1016/j.powtec.2014.12.001`.

MT Zen and D Hadikusumo. The future danger of Mt. Kelut (Eastern Java-Indonesia). *Bulletin of Volcanology*, 28(1):275–282, 1965.

Y Zhang, Z An, H Bai, Q Li, and Z Guo. Characterization and measurement of apparent viscosity of solid particles in fixed beds under high temperature. *Powder Technology*, 2015.

Z Zhang and Q Chen. Comparison of the eulerian and lagrangian methods for predicting particle transport in enclosed spaces. *Atmospheric Environment*, 41(25):5236–5248, 2007.

O Zik, D Levine, S G Lipson, S Shtrikman, and J Stavans. Rotationally induced segregation of granular materials. *Physical Review Letters*, 73(5):644, 1994.

Appendix A

Observations by Velocity

A.1 Introduction

Presented here are qualitative observations of the dry ash, beach sand, pumice, and millet as the rotational velocity was stepped up from its lowest to highest values (1.875 to 37.5 RPM). Froude numbers given here are the rotational (global) variant.

A.2 Ash

1.875 RPM, Fr = 2.49×10^{-5} As with previous (sand) experiments, the lowest velocity experiment with the sieved Taranaki ash sample produces a very thin flowing layer, with the majority of the material being in the passive region.

If a "splash" does occur, they involve single particulates. As such, in order to make sure that a splash is a definite event, rather than the random ejection of a single particulate, a splash is defined as a multi-particulate event. The free surface of the material is flat. (The free surface is observed as Mellmann et al. [2004] and Tegzes et al. [2003] highlights its importance in determining the granular material's current flow regime.)

4.375 RPM, Fr = 1.36×10^{-4} The active region has increased in thickness. The active region moves in a tumbling motion at the top of the flow, while towards the centre it more closely resembles a sliding motion. The free surface is thickest towards the middle of the free surface, and tapers towards either end. While the free surface is not curved at this velocity, there are undulations.

6.875 RPM, Fr = 3.34×10^{-4} Mostly similar to 4.35 RPM with increased active region thickness. In addition, any splashes that do occur are starting to involve multiple particulates.

The free surface is mostly flat, but there appears to be an inflection at around one third of the total length of the free surface, measured downhill from the top of the flow.

9.375 RPM, Fr = 6.23 $\times 10^{-4}$ The inflection previously noted at 6.875 RPM is now more apparent; the free surface is starting to become curved - this indicates a transition from the Mellmann rolling to cascading regimes. The active region thickness has increased again, and the sliding motion region has increased its share of the layer. Small avalanches could be argued to exist at this velocity.

11.875 RPM, Fr = 9.99 $\times 10^{-4}$ The free surface curvature increases again, with some undulation becoming apparent. Multiple inflections in the free surface. Here collapse events are clearly occurring. At this velocity, the ash has entered the cascading regime.

15 RPM, Fr = 1.59 $\times 10^{-3}$ Further increase to free surface curvature, with decreased undulation. Is this due to the material moving more decidedly from one flow regime to another? It will be possible to confirm this using our knowledge of the Froude number and fill factor, coupled with the known Mellmann regimes.

18.125 RPM, Fr = 2.33 $\times 10^{-3}$ The active region depth has increased further, as has the curvature.

In addition, dust is beginning to be ejected from the bottom end of the active region; it is possible that the regime is energetic enough to begin communition of the ash.

At this rotational velocity the sheared layers, also observed in the other experiments, have become visible.

21.875 RPM, Fr =3.38 $\times 10^{-3}$ Increased amounts of dust (fines suspended in the air) are appearing at the front of the active region. The free surface curvature has increased again. The inflection at a point one-third of the distance downhill from the head of the material is more distinct.

25 RPM, Fr = 4.43 $\times 10^{-3}$ At this velocity, a "curtain" region has formed, that is to say a low-density region (LDR). The curtain is not present continuously, however; as such, at this velocity, the ash is in a hybrid/transitional cascading/cataracting regime.

Also, the inflection point is becoming more pronounced, and even greater amounts of dust are being ejected from the front of the active region.

31.25 RPM, Fr = 6.92×10^{-3} Even more dust appearing. The LDR is present continuously now, and the ash can be said to have entered the cataracting regime.

37.5 RPM, Fr = 9.96×10^{-3} The inflection point is very sharp at this maximum velocity. Dust has reached large enough amounts that it is rotating within the drum separately from the main body of the material.

A.3 Beach Sand

1.875 RPM, Fr = 2.49×10^{-5} At this velocity there is a very thin active region with an undulating free surface. The free surface is approximately flat, however, with no discernible curvature (The difference between an undulating and curved free surface is demonstrated in Figure A.3.1). There is no head that builds and collapses at the head end of the flowing material. While the material appears to be moving in segments, hence the undulations of the free surface, the active region is moving continuously, as opposed to a stick-slip regime. At this low velocity, the two-layer approximation as presented in the literature holds.

4.375 RPM, Fr = 1.36×10^{-4} The active region has increased in depth as the velocity is stepped up. At this velocity, small splashes are observable when the free surface undulations meet the downhill drum wall. The free surface may also be slightly curved at this point, but there is still no clearly defined collapsing head at the flow head.

6.875 RPM, Fr = 3.34×10^{-4} The free surface is now clearly displaying a slight curvature, and a small head is visible at the head-end of the flow, though no collapse events can be ascertained visually from the footage.

9.375 RPM, Fr = 6.23×10^{-4} Collapse events are now clearly visible at this velocity. The

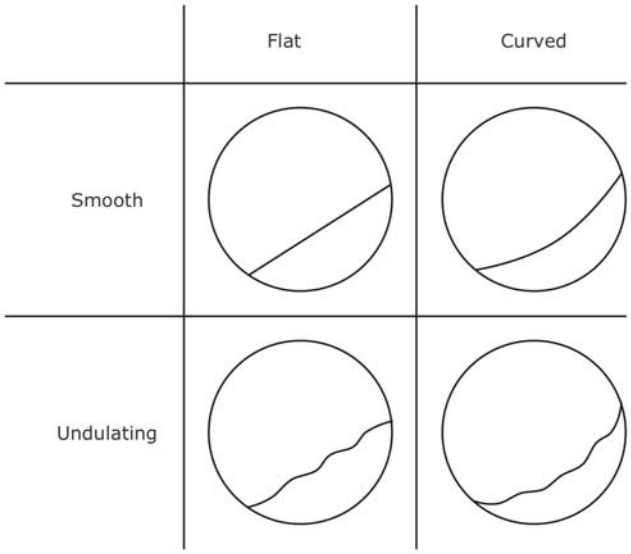

Figure A.3.1: A simple figure to demonstrate the difference between what is referred to as a curved free surface, and one which is undulating. It is entirely possible for a free surface to also demonstrate both, and neither.

free surface has increased curvature, and the active region is thicker again. Any splashes that do occur involve low numbers of particulates. At this velocity we begin to see evidence of a sheared region (see Figure 5.2.1), and the accepted two-layer model of granular flows in a rotating drum begins to break down. It is at this velocity that the beach sand has moved into the cascading regime.

11.875 RPM, Fr = 9.99×10^{-4} At this velocity, the active region is clearly moving downhill via a tumbling motion. It is possible that this method of material transport is responsible for the free surface undulations, as we can treat each region of tumbling as a low-energy and low-mass avalanche. It is at this velocity that clearly discernible splashes occur, with several particulates ejected.

15 RPM, Fr = 1.59×10^{-3} An inflection point appears in a pseudo-periodic fashion at this velocity, suggesting that the material is nearing the cataracting phase of motion. The tumbling mini-avalanches appear to destroy the inflection point as they pass over it. In addition, the collapsing head is now displaying the expected pseudo-periodic behaviour, and splashes at the toe-end of the material are now much more energetic,

expelling a higher number of particles a greater distance.

18.125 RPM, Fr = 2.33 $\times 10^{-3}$ The undulating surface has been getting smoother (*i.e.*, fewer undulations) with increasing velocity, and at this stage of the experiment the heads are much reduced in amplitude indeed. The author suspects that this is due to the increased kinetic energy of these higher velocity experiments, which overcomes the internal friction of the material. The inflection point is now present more often than it is absent. In addition, it is here that we begin to see the low-density region (LDR) form.

21.875 RPM, Fr =3.38 $\times 10^{-3}$ At this velocity highly energetic splashes are observed. Up to four avalanches can be seen propagating at the same time. The LDR is clearly visible in this velocity and higher, though the LDR is not continuously present as yet. As such, the beach sand is in a hybrid cascading/cataracting regime.

25 RPM, Fr = 4.43 $\times 10^{-3}$ Here the splashes are larger still, and free surface curvature has continued to increase.

31.25 RPM, Fr = 6.92 $\times 10^{-3}$ The head has climbed to a remarkable height up the uphill side of the drum. Avalanches are now so frequent that they are starting to overlap with one another. The LDR is present continuously from this velocity - the beach sand has fully moved into the cataracting regime.

37.5 RPM, Fr = 9.96 $\times 10^{-3}$ The head is larger than before, and splashes are even more energetic. Individual avalanches have become so frequent as to be indistinguishable from each other; they must be still extant, however, to account for the splash events.

A.4 Pumice

The pumice was chosen as a material for this study as it has a very low density compared to the other materials, with a value of 1600 kg m−3 (Table 3.3). The particulates

have an angle of repose of 33.4 °(Table 3.2).

1.875 RPM, Fr = 2.49×10^{-5} Unusually, even at this low velocity, the free surface is not flat; there appear to be hillocks that periodically form and collapse. There is a radial stratification of the materials (see Section 7.6.6). In addition, the active region appears to mostly consist of larger particulates. The author suggests that the very finest parts of the pumice are acting in a cohesive manner, and clumping together on their journey downhill, causing the hillocks to form. Eventually these hillocks collapse as the angle of repose of the material is overcome as the drum rotates.

A noticeable dust circulation is already apparent, due to the pumice being a more friable material than the ash. This friability is primarily why the pumice experiment analysis is limited to mainly qualitative observations.

4.375 RPM, Fr = 1.36×10^{-4} Increased free surface curvature.

6.875 RPM, Fr = 3.34×10^{-4} Increased free surface curvature, coupled with distinct avalanches. The inflection point noticeable in the ash case appears here, but with noticeable differences; there are multiple inflections rather than just one, and they are mobile, rather than static, is it was with the ash experiments. It is possible that the mobile inflections are a different phenomenon with a similar appearance in the pumice case. Perhaps they are related to the collapsing hillocks, as previously mentioned. This clumping/-collapse behaviour could go some way to explaining the appearance of the radial segregation stripes.

It is at this velocity that we observe the collapse of the standard two layer model, and observe the fast flowing, sheared and passive regions. The pumice has entered the cascading regime.

This velocity also displays the collapse behaviour observed in other materials (i.e., the collapse of the head of the flow leading to distinct avalanche events).

9.375 RPM, Fr = 6.23×10^{-4} Further increase to free surface curvature. In addition, the

radial stripes of alternating particulate size has begun to dissipate. Perhaps the hillocks are forming and collapsing too quickly to allow for the fines and coarse materials to segregate properly.

The avalanches are sometimes returned to motion by the impact of a subsequent avalanche, rather than the hillocks simply overcoming their angle of repose as before.

There are some very large (for the sample) particulates that form a rolling and bouncing region at the very top of the active region, i.e., on top of the free surface.

11.875 RPM, Fr = 9.99×10^{-4} There is now a larger dust plume at the toe of the flow.

Segregation pattern has undergone a distinct change from the lowest velocities; the radial stripes are nearly gone, while the coarse particles are now form a ring around the fines, which sit centrally in the material. The top- and bottom-ends of the flow appear to have a lower density than the main flowing region near the centre of the material.

15 RPM, Fr = 1.59×10^{-3} At this velocity, the radial segregation stripes are completely unobservable by eye. The avalanches are still occuring in pulses, but none are getting stuck and being knocked back into motion by a subsequent avalanche catching up.

18.125 RPM, Fr = 2.33×10^{-3} Splashes involving multiple particulates are now observable at the toe of the flow. An LDR is also observable, but is inconsistent, sometimes disappearing completely. As such, the pumice can be said to be in the hybrid cascading/cataracting regime.

21.875 RPM, Fr =3.38×10^{-3} Very clear LDR. Compared with the other materials studied, this is a very low velocity for the LDR to appear at.

The splashes continue to be observably more energetic than previous lower rotational velocities.

25 RPM, Fr = 4.43×10^{-3} There is a clear and energetic LDR region at this velocity. This could be in part due to the heavy segregation that this material has displayed compared to previous experiments. The fines are central, while the coarser materials collect at the drum walls and form the active region.

Some material is ejected from the LDR region entirely, in what appears to be a ballistic arc that is approximately parallel to the free surface.

31.25 RPM, Fr = 6.92×10^{-3} At this velocity we can observe large, fragmentary LDRs, with very noticeable KHI events.

The free surface is so curved at this point that it is helping to reduce the angle of the wall of the drum incident to the splash events; as such the splashes appear less energetic at this higher rotational velocity than they did before. This is an artefact of the experimental set up, rather than something intrinsic to granular flows. (I.e., splashes in a granular flow down an inclined plane will presumably get more energetic with velocity of the main flow - there's a reduction in number of ejected particulates in a rotated drum because at higher velocities the angle the material meets the downhill drum edge is reduced.)

The radial stripes and larger particulates surrounding the finer have both disappeared at this point. The entire material appears to consist of fines, with some coarser particulates travelling as part of the LDR, and occasionally appearing near the bottom of the passive region, i.e., where it meets the wall of the drum.

As the LDR is now present at all times, the pumice has moved into the pure cataracting regime.

37.5 RPM, Fr = 9.96×10^{-3} Lots of dust at this velocity. The LDR has become enormous and very chaotic, with large amounts of variation in the density. There also appears to be complex behaviour at the LDR region/main body interface, with some events that appear to move up hill.

Almost everything in the drum now appears to be in the fine fraction. It is possible that the experiment has destroyed the larger particulates completely.

The LDR region at this velocity in this material is the most dynamic yet observed. While other materials display LDRs, there are visible variations in the density of the pumice LDR itself. See Figure A.4.1.

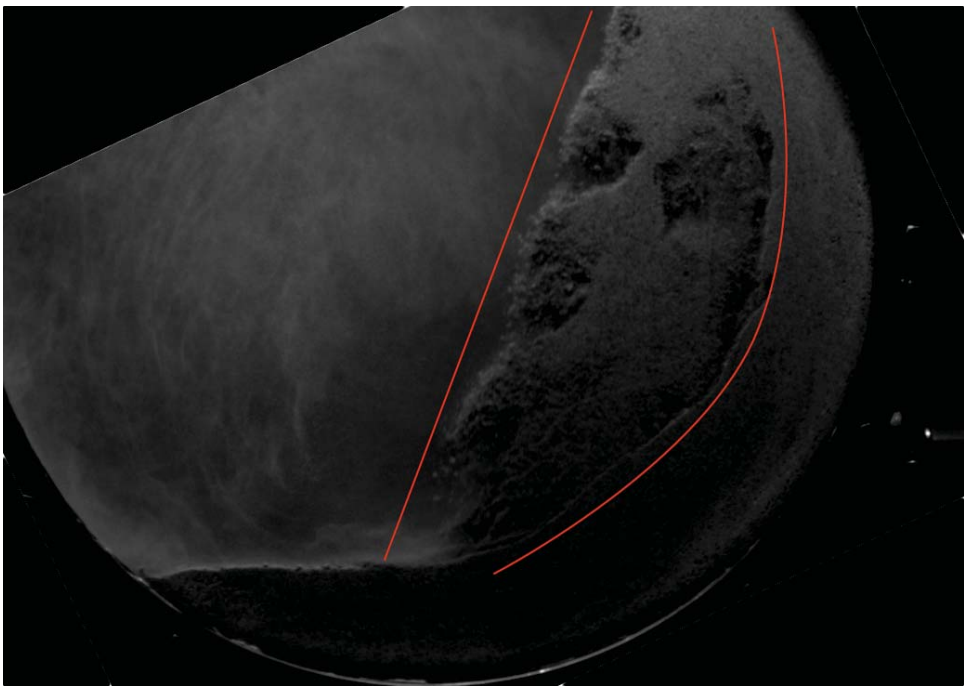

Figure A.4.1: An image of the pumice at 37.5 RPM displaying the dynamic low-density region (highlighted in red), which shows wide variations in material density. Unusual image cropping due to experiment being recorded with a tilted camera.

A.5 Millet

The millet is a material usually used as birdseed. The particulates are the smoothest in this study, with an angle of repose of 26.6 °(Table 3.2). This material also has the narrowest size distribution (Fig. 3.4.2).

1.875 RPM, Fr = 2.49×10^{-5} A very thin active region is visible at this velocity, with a flat free surface. There are some particulates stuck to the glass door, presumably due to electrostatic forces. These putative electrostatic forces are why the millet experiments

are limited to qualitative analysis.

4.375 RPM, Fr = 1.36×10^{-4} The active region has increased slightly in thickness. The motion of this layer is different when compared to the ash; here the motion is more sliding than tumbling. This could be due to the changed inter-particulate friction. While the ash is relatively rough and would perhaps catch on itself, causing the particulates to roll over the ones below, the millet is smooth.

More material is stuck to the glass door. This is possibly due to the increased speed adding further electrostatic effects. However, the amount is still low compared to the total in the drum, and does not appear to be effecting the main body of material.

6.875 RPM, Fr = 3.34×10^{-4} Free surface curvature has started now. However, there are no noticeable splash events.

9.375 RPM, Fr = 6.23×10^{-4} Further increase to the free surface curvature. The active region appears to show what could be considered a typical velocity profile, decreasing non-linearly toward the passive region. Some splash events have started at this velocity, but they have low ejection distances, and typically consist of one particulate.

It may also be argued that at this velocity an inflection point can be observed. Unlike in previous experiments, though, where this appear one-third of the distance from the head to the toe, in this case the position is closer to two-thirds.

11.875 RPM, Fr = 9.99×10^{-4} Here the free surface curvature has increased again, if only mildly. The head of the flow appears indistinct, possibly due to this being the preferred place to lose particulates to the electrostatic forces that are building on the window.

15 RPM, Fr = 1.59×10^{-3} The inflection point is more pronounced than before, and a third sheared layer has become observable.

18.125 RPM, Fr = 2.33×10^{-3} Even at this velocity there are no observable avalanche

events. It is proposed that this is due to the smoothness of this material compared to the others that have been used; the individual pieces of millet simply slide over their neighbours below them, rather than catching and sticking as they would in the rougher materials.

21.875 RPM, Fr =3.38×10^{-3} Though the free surface is increasingly curved, it is still very smooth compared to ash and especially pumice.

Though collapse events are happening (i.e., the pseudo-periodic drop of the head of the active region), there are no discernible avalanches.

25 RPM, Fr = 4.43×10^{-3} Any splashes that do occur, even at this relatively high velocity, are still single particle events. (As such, in Figure 7.2.1, the splashes in the millet are shown for the velocities in which even only single-particle splashes occur - this is different to the other materials presented.) In addition, the material in the passive region at the wall appears to be sliding in a counter-rotational way; perhaps the rotational forces are overcoming the wall/particulate friction forces at this velocity.

37.5 RPM, Fr = 9.96×10^{-3} A further increase to the curvature of the inflection point. Splashes are very small, if observed at all. Avalanches continue to be absent, despite more frequent collapse events. Finally, the amount of material stuck to the glass appears to have been reduced. This may be possible due to the rotation of the drum overcoming the electrostatic forces, or that they have simply been dissipated in some-way.

Appendix B

Pumice Jet Streams

B.1 Introduction

A further new phenomenon was observed in the pumice. However, this was only seen well into the thesis writing process, and only in the pumice, which wasn't subjected to the same interrogation as the ash and the beach sand, due to its self-destructive nature. No mathematical work around this phenomenon has been done, but are presented here for completeness' sake.

The observed processes are referred to as jet streams, as they are narrow and oscillating, and appear to be based on the motion of the air inside the rotating drum. They occurred only at the highest rotational velocity, 37.5 RPM. In general, the pumice displayed very chaotic behaviour, including a low-density region (LDR), similar to the other materials (Section 7.2), but much larger and more active. Inside the pumice LDR could be observed thin streaks of material, which moved in an uphill direction, and appeared to be caused by the expulsion of air from the pumice as the curtain meets the main body of material. These jet streams were not continuous, appearing only from time to time.

An example of a jet stream is given in Figure B.1.1.

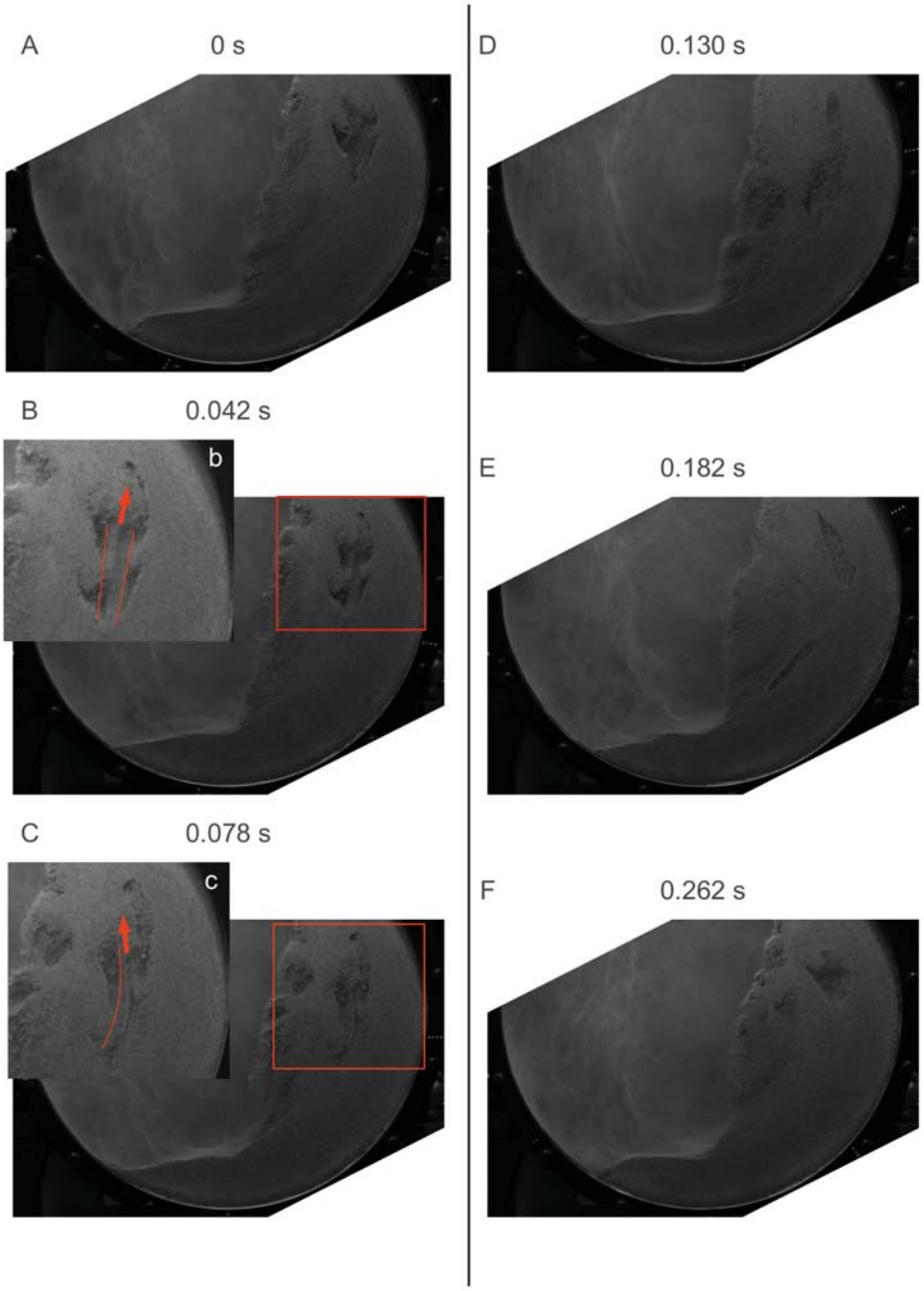

Figure B.1.1: An example of the life time of a pumice jet stream, from the 37.5 RPM footage. In A, starting at zero seconds, a very low-density region ("pocket") forms between the falling material and the passively rotating region. This pocket then narrows in B, causing a plume (the proposed jet stream) of material to be ejected in an upwards direction (see boxout b) The narrowing continues (C), and the density of material in the jet stream increases as the jet stream narrows; see boxout c. The pocket gains a greater amount of material at step D, and the jet stream has ceased. In E, the pocket reduces in volume. In F, another pocket with the extremely low density of material inside, as at step A, has formed. The process then repeats, though not all pockets have associated jet streams. Note that as red lines and arrows in the boxouts are meant to draw the eye, they do not lie on top of the jet stream itself.

Appendix C

Nomenclature

C.1 Introduction

There are a large number of terms and mathematical symbols used in this study. A summary of the most important of these is presented here for references purposes.

C.2 Nomenclature

C.2.1 Roman

Co Coulomb number

D Depth of a linear flow

d Diameter of a typical particle

E Mass transfer rate from work by Ding et al. [2001b]

$F_{centrifugal}$ Force on a single particulate due to centrifugal acceleration

$F_{gravity}$ Force on a single particulate due to gravity

ΔF Difference in force between the steady rotational and accelerating systems upon a single particulate

f Fill factor

f_f Flow function

Fr The Froude number

g Acceleration due to gravity

Ip Ratio of the inertial impulse force and the torque impulse reaction force on a single particulate; a dimensionless impluse

I The inertial number

P Pressure

R Radius of a typical particulate

r Radius of the system

T Granular temperature or kinetic noise

t Time

u' Fluctuation in the horizontal component of velocity

v Velocity of a linear flow

v' Fluctuation in the vertical component of velocity

C.2.2 Greek

α Angular acceleration

$\dot{\gamma}$ Characteristic time

ΔF Difference in force between the steady rotational and accelerating systems upon a single particulate

θ Angle around central position of the drum

θ_i The internal angle of friction

ρ Density of a typical particulate

Σ Effective shear

σ Normal stress

σ_p Pre-consolidation stress

σ_1 Unconfined yield stress (UYS)

σ_3 Major principle stress (MPS)

τ Shear stress

ϕ Geological sieve size

ω Rotational velocity

C.3 Glossary

Active region The part of a granular material in a rotating drum that is not moving with the rotation of the drum.

Active/passive interface The imaginary line between the active and passive regions of a granular material in a rotating drum.

Angle of repose Also known as static angle of repose, this is the angle formed by the flanks of a granular material with horizontal when poured into a pile and allowed to reach equilibrium. See also: Dynamic angle.

Annular shear cell, ASC A piece of equipment used to ascertain the flowability of a powder or granular material.

Avalanche A small body of material travelling down hill, on top of the active layer.

Collapse The process of the head of the flow being no longer able to support any more growth, and collapsing; this is defined as when the head of the material is travelling with gravity on both sides of the peak that forms the head.

Computer fluid dynamics, CFD A mathematical model, used to describe fluid systems. Often coupled with DEM.

Counter-rotational zone, CRZ A region of material, rotating in a manner opposite to that of the drum, that occurs in the wet experiments.

Discrete element method, DEM A way of simulating granular materials, by treating individual particles as springs and dashpots and then solving Newton's second law across the entire system. Sometimes referred to as particle dynamics, or PD.

Dynamic angle The angle the flanks of a granular material forms after it has been agitated and allowed to return to a resting state. See also: Angle of repose

Dynamic angle of friction The angle between the vertical and the centre of mass of a flowing granular material in a rotating drum.

Fast flowing region The uppermost part of the active region, which has a velocity profile which suggests that part of the active region is flowing in a bulk fashion, rather than slowing steadily as the active region approaches the passive region.

Free surface The top most part of a granular material in a rotating drum that is exposed entirely to the fluid phase.

Free surface curvature The bending of the free surface as the rotational velocity in the rotating drum increases.

Granular material A body of material composed of a large number of mesoscopic grains.

Inflection A noticeable bend in the free surface of a flowing granular material in a rotating drum.

Kelvin-Helmholtz instability, KHI An instability which occurs when two materials of differing densities flow past each other. Used in this study as the name for an-

other phenomenon, due to the latter's similarity to a classical KHI.

Lahar A natural granular material phenomenon; a mudflow with a volcanic origin.

Low density region, LDR A region in a granular material flowing in a rotating drum, in which the rotational velocity is fast enough to generate a region of fewer particles per volume between the rest of the active region and the passive region.

Passive region The part of a granular material in a drum that is moving with the rotation of the drum.

Particle image velocimetry, PIV The measurement of velocities inside a granular material by using a computer to automatically process imagery of the material.

Primary interface See active/passive interface.

Radial stripes The stripes which occur in the high velocity experiments for the pumice.

Self-enclosed circulation cell, SECC A region of material along the active/passive interface in which the particulates appear to be at least temporarily trapped.

Sheared regions The layers of a granular material flowing in a rotating drum immediately either side of the passive/active interface, which, due to the opposed motions of the active and passive layers are subject to shear forces.

Splash The ejection of particulates from a granular material as the active region meets the downhill edge of the drum.

Appendix D

Source Code

D.1 Introduction

During the course of this research, two complex programming tasks were undertaken. These were the MATLAB code that processed the PIV data, and a C# program that ran the acceleration experiments. These were written by Dr. Luke Fullard of Massey University, and Nav Prasad of SEW Eurodrive, respectively.

With the permission of both authors of these programs, the source code is presented along with this thesis (see CD attached to the back cover) under the following licenses. Please note that the code was written specifically for this project, and as such may need tweaking before it'll work with other data sets or equipment. The code is presented in the spirit of the Science Code Manifesto[1].

D.2 MATLAB PIV Analysis Code

D.2.1 License

With the permission of Dr. Fullard, the code has been made free software, released under the Simplified BSD License [2]. The license below and the source code are on the compact disc at the back of this thesis.

License Text

Redistribution and use in source and binary forms, with or without modification, are permitted provided that the following conditions are met:

[1] http://sciencecodemanifesto.org/, last accessed 15th October, 2015.
[2] http://opensource.org/licenses/bsd-license.php, last accessed 15th October, 2015.

1. Redistributions of source code must retain the above copyright notice, this list of conditions and the following disclaimer.

2. Redistributions in binary form must reproduce the above copyright notice, this list of conditions and the following disclaimer in the documentation and/or other materials provided with the distribution.

D.3 C# Acceleration Code

D.3.1 License

With the permission of Nav Prasad, the code has been made free software, released under the Simplified BSD License. The license below, the software manual, and the source code are on the compact disc at the back of this thesis.

License Text

Appendix E

Open Source Software

E.1 Introduction

Free and open source software (FOSS) are computer programs which the end user is freely allowed to modify, redistribute, and study the relevant source code. In science, it is the author's opinion that FOSS should be used whenever possible, as it aids with the scientific aims of openness and reproducibility[1]. As such, in the spirit of the FOSS community, this appendix lists the software used in this project that was released under a free software license. (To quote the Free Software Foundation[2], "think of 'free' as in 'free speech', not as in 'free beer'"[3].) This list is presented in the hopes that the software will prove useful to someone studying a similar field as this thesis.

E.1.1 Software Used

Aquamacs Mac OS X port of Emacs text editor, `http://aquamacs.org/`

BibDesk Bibliography manager, `https://www.tug.org/mactex/`

Colloquy IRC client, `http://colloquy.info/`

Excalibur LaTeX-aware spell checker, `https://www.tug.org/mactex/`

export_fig MATLAB figure exporter, `https://github.com/altmany/export_fig`

Fiji Image processing software, `http://fiji.sc/Fiji`

Firefox Web browser, `https://www.mozilla.org/`

GhostScript Post Script file interpreter, `http://www.ghostscript.com/`

GNU Octave High-level mathematical programming language, `https://gnu.org/software/octave/`

[1] http://fiji.sc/Open_Source, last accessed 15th October, 2015.
[2] https://www.fsf.org/, last accessed 15th October, 2015.
[3] https://www.gnu.org/philosophy/free-sw.html, last accessed 15th October, 2015.

HandBrake Converts videos between file formats, `http://handbrake.fr/`

iChm .chm file reader, `https://code.google.com/p/ichm/`

ImageJ Image processing software, `http://imagej.nih.gov/ij/`

Inkscape Vector-based drawing program, `http://www.inkscape.org/`

JPIV Java-based particle image velocimetry package, `http://www.jpiv.vennemann-online.de/`

LibreOffice Office suite, `https://www.libreoffice.org/`

MacPorts Package manager, `https://www.macports.org/`

MacTubes YouTube video downloader, `http://macapps.sakura.ne.jp/mactubes/index_en.html`

Miro Video Converter Converts videos between file formats, `http://getmiro.com/`

Notepad++ Text editor, `http://www.notepad-plus-plus.org/`

PDFView PDF reader. `http://pdfview.sourceforge.net/`

Perian Extra QuickTime components, `http://perian.org/`

PIVlab PIV environment for MATLAB, `http://pivlab.blogspot.co.nz/`

ProjectLibre Project management, `http://www.projectlibre.org/`

R Statistical programming language, `http://r-project.org/`

RSSOwl RSS subscription reader, `http://www.rssowl.org/`

Skim PDF reader, `http://skim-app.sourceforge.net/`

SumatraPDF PDF reader, `http://blog.kowalczyk.info/software/sumatrapdf/free-pdf-reader.html`

TeXShop LaTeX editor, `https://www.tug.org/mactex/`

Vienna RSS subscription reader, `http://www.vienna-rss.org/`

VirtualDub Video editor, `http://www.virtualdub.org/`

Visual Studio Code Source code editor, `https://code.visualstudio.com/`

VLC Video player, `https://www.videolan.org/vlc/`

Waterfox 64-bit version of Firefox, `https://www.waterfoxproject.org/`

Zotero Reference management, `https://www.zotero.org/`

Index